A theoretical study of correlation effects of N electrons in semiconductor nanocrystals : applications to optoelectronic properties of perovskite nanocrystals

Thi Phuc Tan Nguyen

THÈSE

Pour obtenir le grade de

DOCTORAT DE L'UNIVERSITE GRENOBLE ALPES

préparée dans le cadre d'une cotutelle *entre la Communauté Université Grenoble Alpes* et *Nanyang Technological University*

Spécialité: **Physique des matériaux**

Arrêté ministériel: 25 Mai 2016

Présentée par

Thi Phuc Tan NGUYEN

Thèse dirigée par **Steven BLUNDELL (CEA-UGA)**
codirigée par **Tze Chien SUM (NTU)**
co-encadrée par **Claude GUET (NTU)**

préparée au sein du **IRIG/SyMMES au CEA, Grenoble**

dans **l'École Doctorale de Physique**

Une étude théorique des effets de corrélation à N-électron dans nanocristaux semi-conducteurs: Application aux propriétés optoélectroniques des nanocristaux de matériaux pérovskites.

Thèse soutenue publiquement le 03 juillet 2020,
devant le jury composé de:

M. Christophe DELERUE
Directeur de Recherche, IEMN, Villeneuve d'Ascq, Rapporteur
M. Laurent PEDESSEAU
Maître de Conférences (HDR), INSA - FOTON Institute - UMR/CNRS, Rennes, Rapporteur
M. Alexandre SIMIONOVICI
Professeur, ISTerre, Univ. Grenoble Alpes, Grenoble, Président
M. Siew Ann CHEONG
Professeur associé, PAP, SPMS, NTU, Singapore, Examinateur

A theoretical study of correlation effects of N electrons in semiconductor nanocrystals:

Applications to optoelectronic properties of perovskite nanocrystals

NGUYEN Thi Phuc Tan

A thesis prepared for the degree of
Doctorat de l'Université Grenoble Alpes

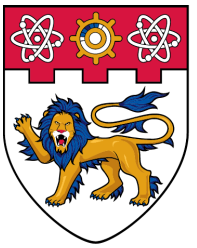

NANYANG TECHNOLOGICAL UNIVERSITY
SINGAPORE

A theoretical study of correlation effects of N electrons in semiconductor nanocrystals:

Applications to optoelectronic properties of perovskite nanocrystals

Nguyen Thi Phuc Tan

Interdisciplinary Graduate School
Energy Research Institute @ NTU (ERI@N)

A thesis submitted to Nanyang Technological University
in partial fulfillment of the requirements for the degree of
Doctor of Philosophy
on a joint PhD program with Université Grenoble Alpes

Résumé

Cette thèse doctorale fait appel à des concepts propres à la physique du solide et la physique atomique. La variété des structures cristallines, des constituants chimiques, des dimensionnalités rencontrées dans les matériaux offre une abondance de phénomènes fascinants qu'explore la physique du solide. De son côté, la physique atomique dont les données expérimentales sont d'une grande précision a permis le développement de méthodes théoriques possédant un haut niveau de rigueur et de contrôle systématique pour l'étude des systèmes finis composés de particules en interaction électromagnétique. L'objectif de cette thèse est d'étendre les méthodes théoriques de physique atomique à l'étude des nanoparticules faites de matériaux semi-conducteurs, un domaine de la physique du solide.

On distingue deux grandes catégories de méthodes théoriques pour l'étude de la structure électronique des nanocristaux semi-conducteurs. D'un part, les méthodes ab initio fondées sur la théorie de la fonctionnelle de densité et l'usage de pseudo-potentiels traitent l'ensemble des atomes présents dans la nanoparticule. Ces méthodes ont l'avantage de pouvoir prendre en compte les impuretés, les défauts, les états de surface, .. En revanche, ces méthodes ab initio sont rapidement limitées par les capacités des ordinateurs actuels les plus performants. Pour des nanocristaux contenant plusieurs milliers d'atomes, les calculs ab-initio deviennent vite prohibitifs. D'autre part, les modèles de type $\mathrm{k}\cdot\mathrm{p}$ permettent de réaliser des calculs beaucoup moins coûteux et bien adaptés à l'étude de phénomènes électroniques au voisinage de la bande interdite, ceci au prix de disposer par les méthodes ab initio ou l'expérience des paramètres fondamentaux que sont les masses effectives (des électrons et des trous), la permittivité diélectrique et aussi le «gap» énergétique. Il est à noter que le modèle $\mathrm{k}\cdot\mathrm{p}$ produit parfois des états fallacieux n'ayant aucune signification physique, dans la bande interdite. Dans cette thèse, nous proposons une solution pour résoudre ce problème d'états fallacieux via un méthode de théorie des perturbations.

Jusqu'à récemment, les études ont été consacrées principalement aux semiconducteurs de groupes II-VI et III-V, comme GaAs ou CdSe. Efros et al. et Ekimov et al. ont pour cela développé le modèle 'non-interacting single-particle' via la méthode $\mathrm{k}\cdot\mathrm{p}$. Plus tard, l'interaction de Coulomb a été incluse avec les fonctions d'onde non-interactives. Pour les matériaux à base de perovskites, les structures de bandes ont été traitées par le théorie de la fonctionnelle de la dénsite (DFT). Becker et al. ont examiné le cas de l'exciton, une paire électron-trou corrélée. Longtemps, les travaux théoriques ont négligé les systèmes multi-excitoniques. Or, grâce à une puissance d'excitation croissante les mesures expérimentales ont permis d'obtenir plus d'une paire électron-trou. L'émission de trions et biexcitons a été observée, révélant une énergie de liaison quantifiable de lumière. Seule la prise en compte des corrélations N-corps, c.-à-d. de l'interaction entre les charges (les électrons et les trous) permet de prédire correctement ces énergies de liaison. La durée de vie de l'exciton dans son état fondamental est sub-nanoseconde pour les perovskites et beaucoup plus courte que celle de CdSe ou d'halogénures métalliques. L'émission rapide est peut-être responsable de la forte luminosité de nanocristaux de perovskites. Les sections efficaces d'absorption expérimentales sont aussi plus fortes que celles d'autres semi-conducteurs de même taille. Pour cette raison, les

perovskites sont des matériaux prometteurs pour les cellules solaires.

Dans cette thèse, nous avons construit une méthode théoretique adaptée a l'étude de systèmes excitoniques avec N_e électrons et N_h trous confinés dans un nanocristal sphérique. Au Chapitre 2, après avoir rappelé les principes des calculs de structure de bandes, nous présentons le Hamiltonien $\mathrm{k} \cdot \mathrm{p}$ pour modéliser l'énergie cinétique du semi-conducteur. En imposant la symétrie sphérique pour la structure de bandes et aussi le potentiel du confinement, le temps de calcul est réduit par environ 10000 fois. Si on permet au paramètre de Kane d'être nul, le modèle $\mathrm{k} \cdot \mathrm{p}$ devient l'approximation parabolique de masse effective.

Pour traiter l'interaction de Coulomb, nous nous plaçons dans l'approximation Hartree-Fock introduite dans le chapitre 3. Nous évaluons alors les énergies de l'exciton pour plusieurs tailles de nanocristaux.

Le chapitre 4 est consacré à la présentation de la théorie des perturbations à N-corps à partir de l'espace modèle Hartree-Fock. Nous calculons le «redshift» du biexciton et celui du trion au deuxième ordre des perturbations à N-corps. Cependant, il est nécessaire d'inclure tous les ordres pour obtenir des prédictions quantitatives. Au bout de ce chapitre, nous présentons la méthode de théorie à N-corps «dégénérée» pour calculer la différence énergétique entre les «dark» et «bright» excitons.

Dans le chapitre 5, one examine l'interaction entre un électron et un photon (processus à un photon). Le taux de recombinaison radiative d'un exciton dans son état fondamental et la section efficace d'absorption sont très mal décrits au niveau de l'approximation Hartree-Fock. La prise en compte de la corrélation électron-trou, ou autrement dit l'interaction dans l'état final, est essentielle pour obtenir un bon accord de la théorie avec les mesures expérimentales. Cet approche complexe à N-corps, qui couple tous les états excités de l'exciton à tous les ordres de corrélation, pour construire le spectre d'absorption, devrait être plus rigoureuse que la méthode se fondant sur un principe variationnel.

Acknowledgement

Here, I would like to express my gratitude towards all the relevant people during the three years of my PhD in Grenoble and Singapore.

First and foremost, I would like to send my deepest thanks to all of my three advisors for the scientific discussions and guidance that have propelled the PhD work forwards. Most of the technical knowledge and foundations related to this project, especially the many-body perturbation theory and relativistic quantum field theory, have been gained under the close supervision by Steven Blundell. Besides, the subroutines in Fortran provided by him have helped make the whole numerical development possible within three years. For these reasons, I am indebted to Steve. Without his instruction, proofreading and comments, the completion of this thesis would be impossible.

I would like to extend my wholehearted thanks to Claude Guet. He was the person who introduced me to this doctoral project and has played an important role in my career development. Claude's ideas and suggestions, which often take quite a significant amount of effort and time for me to realize, have greatly shaped the direction of the thesis as well as influenced crucially the focuses of the PhD work. Again, I thank him for the PhD project having arrived at its current state.

I also wish to thank Sum Tze Chien for the reading materials, the discussion involving numerous experiments as well as for his support, especially during 2018. I truly respect him for his leadership of the big experimental group working on a wide range of topics and for the fact that he has been always encouraging an open and collaborative atmosphere within the group amidst his busy schedule.

Furthermore, there have been always people who were willing to help with the various aspects of the project. The discussions with Le Si Dang, who has been very kind to me, together with the various papers that he recommended have taken the PhD project in an interesting and unexpected direction. Wang Zhe, whom I am impressed by his perseverance to pursue his interests, has been extremely helpful for calculating the dielectric screening factor of the electron-photon interaction for Chapter 5 of this thesis. I also thank Xu Qiang for giving me the materials regarding DFT as well as for being so kind to provide me with the essential instructions to get started with VASP. About the project, I also thank Rafael for much of his help with the numerical details and for correcting and "beautifying" the introduction of the thesis.

I also appreciate very much the fun discussions about the experimental and academic issues over dinners and, sometimes, lunches with Do Thi Thu Ha, one of my really good friends. I thank all the group members at CAMPE (CEA), especially Pascale Maldivi and Lionel Dubois, for their friendliness and keen sense of humour. The postdocs and students from Prof. Sum's group at NTU have also been genuinely kind to me. Akanksha Kapoor and Romain Fons gave their considerable aid with the submission of my thesis during the total lockdown in France due to Covid-19, which is the historical event that the world is living through right now.

Lastly, I wish to mention that I am only able to reach this milestone with the love and emotional support from my family and Rafael. Thanks to them, I have become the person who I am today.

Contents

Chapter 1

Introduction

The research described in this doctoral thesis lies at the interface of two major fields of modern physics: solid-state physics and atomic physics. On the one hand, the former offers a rich playground replete with fascinating phenomena, thanks to the endless possibilities of variation in the lattice structure, chemical compositions, material dimension etc. On the other hand, the theoretical techniques from atomic physics, for dealing with finite systems of multiple interacting particles (i.e. finite many-body systems), have been developed to a high standard of rigour and methodology. The aim of this work is to apply the theoretical formulations from the latter field to solve certain outstanding issues in semiconductor nanoparticles, a branch of solid-state physics. These problems would be extremely time-consuming or even infeasible with the traditional techniques that are normally used in the study of semiconductor nanocrystals.

This chapter serves as an introduction to the later, technical parts of the thesis. We start out by recalling the concept of an exciton, including the Frenkel and Wannier types, in the bulk semiconductor. Subsequently, we explain the reasons for choosing lead halide perovksite nanocrystals as the applications in Section 1.2. In the study of semiconductor nanocrystals, it is important to understand the interplay between the confinement effect and the Coulomb interaction, to which Section 1.3 is devoted. The fundamental parameter here is the ratio between the effective Bohr radius and the nanocrystal size. The existing literature will be reviewed in Section 1.4, which provides the motivation and defines the scope of the current work. Section 1.5 contains an overview of the remaining chapters and is meant to guide the reader through the whole structure of the thesis.

1.1 The concept of a bulk exciton

In a metal, the highest occupied band is a partially filled conduction band and the electrons can freely move around in the crystal lattice. Any amount of excitation, no matter how little energy it carries, can transport an electron from the Fermi level to an unoccupied state. As a result, metals absorb light strongly over an extended frequency range subsuming the entire visible spectrum. Only more than several atomic layers successfully make a metal sheet opaque. On the contrary, a semiconductor stays almost transparent for excitation energy below the electronic

band gap. The band gap is defined as the energy difference between the highest occupied energy level, the valence band maximum, and the lowest unoccupied band (or the conduction band). All bands below the valence band maximum are commonly referred to as valence bands. For most electronic processes, the highest valence band and the lowest conduction band are the most relevant. With the right amount of a quantum of energy (e.g. photon frequency $\hbar\omega$), an electron is promoted from a valence band to a conduction band, leaving a hole, i.e. a missing electron, in the valence band. The Coulomb interaction between these two charge carriers leads to the formation of a correlated electron-hole pair that is called an exciton.

Depending on the semiconductor, an exciton can be classified into one of two types. When the electron and hole wave functions tend to localize around an atomic site, they form a Frenkel exciton [49, 50]. The spatial extent of the electron-hole pair is limited to just one unit cell. Their energy levels resemble those of an atom or a molecule staying at a particular point on the lattice. The Coulomb interaction between the electron and the hole remains largely unscreened. Materials with Frenkel excitons include halide salts and some organic materials, among others. Early calculations for Cu_2O and CuCl, for instance of their exciton and biexciton binding energies, have been given in Ref. [42]. A Frenkel exciton moves around the lattice via the annihilation and recreation of the correlated electron-hole pair under Coulomb interaction of the charged particles at different points throughout the material. In other words, a Frenkel exciton is a coherent superposition of the electron-hole excitations that occupy various sites across the entire lattice.

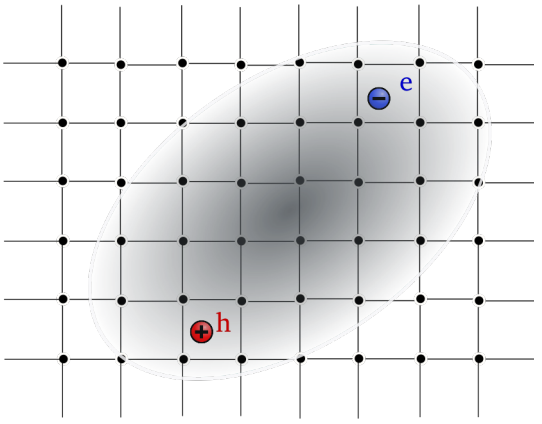

Figure 1.1.1: A Wannier exciton, also referred to as 'an exciton' in the rest of the thesis, spreads over many lattice sites. The averaged electron-hole distance can be characterized by the effective Bohr radius a_B given in (1.1.3).

For materials such as GaAs, CdSe as well as perovskites, the averaged distance between the electron and the hole spans over many unit cells. In this case, the correlated electron-hole pair is called a Wannier exciton [128]. Two factors that contribute to the size of a Wannier exciton are the light effective masses of the

carriers and the large dielectric constant. On the one hand, the electron and hole effective masses m_e^* and m_h^* at the band edge are an order of magnitude smaller than the bare mass m_0 due to the interaction with other bands [98]. The smallness of m_e^* or m_h^* also leads to high carrier mobility [134], which is beneficial for charge transport. On the other hand, the dielectric constants of these semiconductors turn out to be typically on the order of 10, see Table 1.1 and Table 3.1. They are the result of the many-body Coulomb interaction between the charged particles [28].

A Wannier exciton moves across the semiconductor in the center-of-mass motion of a 'hydrogen-like' system. In the 3D crystal, the translational symmetry implies that the center-of-mass wave function is a plane wave with wave number $\vec{k}_{CM}$. In the bulk, a Wannier exciton can be described by the hydrogen-like states with the reduced mass μ, where

$$\frac{1}{\mu} = \frac{1}{m_e^*} + \frac{1}{m_h^*}. \tag{1.1.1}$$

Its bulk binding energy takes the form

$$E_{\text{bind}}^{\text{bulk}} = \frac{\mu}{\varepsilon_{sc}^2} E_H, \tag{1.1.2}$$

in which $E_H = 13.605693122994(26)$ eV is the Rydberg constant. The symbol ε_{sc} represents the dielectric constant of the semiconductor. The spatial extent of a Wannier exciton is captured in the effective Bohr radius a_B.

$$a_B = \frac{\varepsilon_{sc}}{\mu} a_0, \tag{1.1.3}$$

where $a_0 = 5.2917721067(12) \times 10^{-2}$ nm stands for the Bohr radius of a hydrogen atom. We note that the dielectric 'constant' ε_{sc} generally depends on the frequency [43] or on the sample size [125, 67] in the case of a confined system.

Considering the group III-V and II-VI semiconductors, the highest valence band consists of three subbands: the heavy hole band, the light hole and the spin-orbit split-off band. The separation into three subbands comes as a result of the coupling within the valence band and of the spin-orbit coupling. The basic parameters of the band structure as well as the dielectric constant of the three common semiconductors GaAs, CdSe and CdS are listed in Table 1.1. In the bulk, the heavy hole lies at the top of the valence band. Therefore, the effective hole mass that appears in the formula (1.1.1) for the reduced mass μ is equal to m_{hh}^*, the heavy hole mass. Using the value of m_{hh}^* in Table 1.1 for GaAs, we can estimate the binding energy of a bulk exciton in GaAs to be $E_{\text{bind}}^{\text{bulk}} = 4.7 - 5.1$ meV, which agrees with the measured values in Ref. [87]. This implies that the hydrogen-like model provides a reasonable description of the Wannier exciton in the bulk. From now on, we use the word 'exciton' to simply denote the Wannier exciton in a semiconductor, which is the focus of the current thesis.

The hydrogen-like model with the binding energy $E_{\text{bind}}^{\text{bulk}}$ and the effective Bohr radius a_B, given in (1.1.2) and (1.1.3), can be used in the study of a free exciton in the bulk. The value of $E_{\text{bind}}^{\text{bulk}}$ helps to understand the process of thermal dissociation of the exciton, which happens around 60K for GaAs [131]. The exciton Bohr radius is one way of determining the regime of confinement when the exciton was created

inside a nanocrystal. In this thesis, we are particularly interested in understanding the excitons in perovskite nanocrystals. We shall provide the reasons for our focus on these recent materials in the next section.

parameters	GaAs	CdSe	CdS
m_e^*	0.0665	0.11	0.18
m_{hh}^*	0.502	1.000	2.128
m_{lh}^*	0.082	0.313	0.339
m_{soc}^*	0.141	0.476	0.585
$\varepsilon_{\text{static}}$	$12.5 - 13.1$	9.56	8.28
ε_∞	10.9	6.23	5.23
E_{gap} (eV)	1.519	1.84	2.56

Table 1.1: The basic band parameters and the dielectric constants for GaAs (zincblende lattice structure), CdSe and CdS (wurtzite lattice structure). The band parameters include the electron effective mass m_e^*, the heavy hole mass m_{hh}^*, the light hole mass m_{lh}^*, the spin split-off hole mass m_{soc}^* and the bulk energy gap E_{gap}. The hole effective masses were derived from the Luttinger parameters taken from Ref. [98] (GaAs, CdS) and Ref. [41] (CdSe). $\varepsilon_{\text{static}}$ and ε_∞ are the static and high-frequency dielectric constants from Ref. [115, 54] (GaAs), Ref. [94] (CdSe) and Ref. [92] (CdS).

1.2 Why perovskite nanocrystals?

Perovskites represent a wide class of materials with the perovskite structure, which is named after the crystal structure of calcium titanium oxide ($CaTiO_3$). Nonetheless, it was the class of lead halide perovskites $APbX_3$ that has been recently demonstrated to possess superior optoelectronic properties [24]. In $APbX_3$, A represents some cation such as Cs, CH_3NH_3 or FA (formamidinium), while X stands for a halide among Cl, Br or I. For the reason just stated, we focus in this thesis on understanding the optical properties of $APbX_3$. In the remainder of the thesis, the word 'perovskites' refers specifically to $APbX_3$.

As 3D crystals, perovskites show high carrier mobility [134] and long carrier lifetime [13, 141]. These materials also have rather good defect tolerance [65] and the defects generally stay quite close to the band edges [136]. These shallow defects do not severely affect the optical and transport properties of the perovskites. Besides, the solution processability allows for a cheap and economically viable route to the large-scale production of this class of semiconductors [129]. Lead halide perovskites absorb strongly in the optical range and prove to be some of the most promising candidates for photovoltaic applications [77, 116]. The perovskite-perovskite tandem solar cells that use a mixture of various perovskites achieve an excellent efficiency over 20% [44, 56, 63]. These materials have been shown to be

very bright emitters, with potential implications for their usage in light emitting devices [117, 26].

Several years ago, arose the idea of making perovskite nanocrystals for the purpose of further exploiting their optoelectronic properties [111]. Generally, the emitting and absorbing characteristic frequency can be tuned by using the chemical technique of halide exchange [30]. However, nanocrystals can also offer the color tunability through the variation of the nanoparticle sizes, which can be achieved by varying numerous experimental conditions, such as the processing temperature or the choice of ligands of the synthesis. The perovskite nanocrystals have been demonstrated to cover the whole visible range with very high color purity in their photoluminescence spectra [99, 73]. Recent efforts aimed at making highly monodisperse nanocrystals have achieved significant success [60, 35]. With an increasing level of control over the size and shape as well as the chemical composition of the nanocrystals, researchers are getting closer and closer to making bright nanocrystals emitting at the desired frequency. This potentially open the way to creating single-photon sources [123] or even generating entangled photon pairs [22], which will continue to attract additional fundamental research interest in the future.

To study an excitonic system in a perovskite nanocrystal, it is important to understand the quantum-mechanical effect that a nanocrystal creates via its confining potential.

1.3 Confinement and Coulomb interaction

material	phase	μ	$E_{\text{bind}}^{\text{bulk}}$ (meV)	a_B (nm)
$CsPbBr_3$	orthorhombic	0.126	33	3.07
$CsPbI_3$	cubic	0.114	15	4.64
$FAPbBr_3$	orthorhombic	0.115	25	3.87
$FAPbBr_3$	tetragonal	0.13	24	3.50
$FAPbI_3$	orthorhombic	0.09	14	5.50
$FAPbI_3$	tetragonal	0.095	10	6.35
$MAPbBr_3$	orthorhombic	0.117	25	3.39
$MAPbI_3$	orthorhombic	0.104	16	4.78
$MAPbI_3$	tetragonal	0.104	12	5.55

Table 1.2: The measured reduced mass μ, bulk binding energy $E_{\text{bind}}^{\text{bulk}}$ and the estimated Bohr radius from the formula (1.1.3) of the hydrogen-like model for various perovskites. The measurements for μ and $E_{\text{bind}}^{\text{bulk}}$ come from Ref. [132] and Ref. [53].

Upon passing from the bulk crystal to nanocrystals (or eventually quantum

dots), the created electron and hole are confined inside the semiconducting material, which may be surrounded by an outer medium (a solvent or some ligand). The situation of the charged particles is similar to that of a standing wave in a box. The smaller the size of the box, the shorter the wavelength and the higher the wave energy. The confinement comes as a consequence of, for instance, the band misalignment between the semiconductor and the surrounding medium. When an electron-hole pair, or an exciton, lives within a nanocrystal, it experiences a quantization of the kinetic energy.

In the bulk, the translational symmetry guarantees that the particle momentum $\vec{p}$ or the wave vector $\vec{k}$ is a good quantum number. Generally, the confining potential breaks this translational symmetry. Nonetheless, depending on the shape of the nanocrystal and on the properties of the band structure, there may still be some other symmetry exhibited by the excitonic system. For instance, an overall spherical symmetry exists if the band edge kinetic energy is isotropic [55, 8] and the nanocrystal turns out to be a sphere. In this case, the quantum states of the exciton can be classified by the total angular momentum, which is well-known to be a conserved quantity for a spherical system. If the nanocrystal comes out to be cuboidal, we shall show in Section 2.3 that an appropriately chosen spherical confining potential serves as a fair approximation to the cubic case. In brief, the edge length L of a cube can be related to the radius R of the equivalent sphere by $L = \sqrt{3}R$. For this reason, we shall focus in the remainder thesis on the treatment of spherical models.

Let R be the radius of the spherical nanocrystal. The ratio R/a_B characterizes the confinement regime. Table 1.2 provides the effective Bohr radii of a number of perovskites in different phases. Fig. 1.3.1 depicts the various limits for the confining potential. There is no clear threshold between them. Generally, we consider the region where the ratio $R/a_B \leq 1$ to be the strong confinement regime. Here, the wave functions of the charge carriers experience a forced overlap due to the confining potential. Consequently, the Coulomb attraction between the electron and the hole, which is proportional to $1/R$, becomes stronger while, at the same time, their kinetic energy increases much more rapidly as $1/R^2$. As a result, the emission or absorption line shifts to higher energy as one enters more deeply into the strong confinement limit. Moreover, the electron and the hole exhibit more clearly their single-particle characteristics.

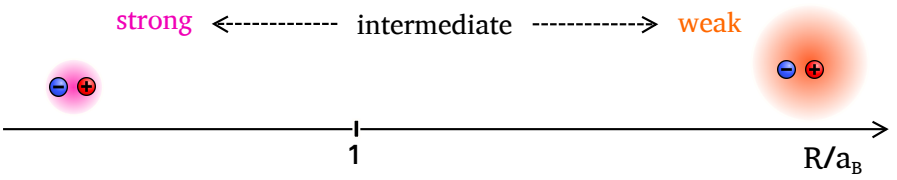

Figure 1.3.1: The confinement regime depending on the ratio R/a_B. The intermediate confinement regime is understood to be the case in which R is equal to several times the Bohr radius a_B. We consider the strong confinement regime to be where $R/a_B \leq 1$. In the weak confinement regime, $R/a_B \gg 1$.

When the nanocrystal radius ranges from slightly above a_B up to several times a_B, we consider the system to be in the intermediate confinement regime. As R/a_B increases, one enters further into the weak confinement. In these regimes, Coulomb interaction becomes relatively more important compared to the kinetic energy. Furthermore, the strong electron-hole correlation also implies that the many-body effects are crucial for computing the long-range exchange interaction and the electron-photon interaction, see subsection 4.2.5 and section 5.4 respectively. Nonetheless, we have to remark that the effect of the confinement on the kinetic energy cannot be neglected. The hydrogen-like model for a bulk exciton does not suffice as a description of an exciton in the intermediate or even weak confinement limit. Here, the kinetic energy of the confined particles must be taken into account to yield the correct exciton energy as shown in Fig. 3.4.3.

1.4 Motivation and objective

Two main lines of theoretical studies exist for investigating the electronic structure of semiconductor nanocrystals. On the one hand, the first-principle calculations [137, 68] or the pseudopotential methods [125, 144] describe the nanoparticles with the full atomistic details. Their advantages remain at providing answers to many issues that would otherwise be intractable if one uses, for instance, the $\mathrm{k}\cdot\mathrm{p}$ approach. These issues include impurities, small and irregular systems, surface bonds etc. Nonetheless, the *ab initio* methods are limited by the computational capability. When the nanocrystal becomes very large with several thousands of atoms or more, an *ab initio* approach becomes extremely expensive or even impractical computationally. On the other hand, the $\mathrm{k}\cdot\mathrm{p}$ model has been employed to study the physics around the band edge. This is possible only when the basic parameters of the bulk band structure, such as the effective masses and the band gap, are known via another method. Then, the $\mathrm{k}\cdot\mathrm{p}$ approach offers a simple and computationally efficient route that can treat nanocrystals of any size in principle. However, there are still issues with the $\mathrm{k}\cdot\mathrm{p}$ model for certain semiconductors, as discussed in Ref. [124]. The $\mathrm{k}\cdot\mathrm{p}$ model in these cases produces spurious, unphysical solution(s) that stay inside the energy gap of the semiconductors. This thesis takes the $\mathrm{k}\cdot\mathrm{p}$ model as the starting point and will deal with the issue that we have just mentioned in the later parts. We shall show in chapters 4 and 5 a way of avoiding the problem of the spurious (or intra-gap) solutions by following the philosophy of perturbation theory.

Past studies have mostly treated the case of nanocrystals from group III-V and II-VI semiconductors. With the $\mathrm{k}\cdot\mathrm{p}$ approach, the non-interacting single-particle picture has been discussed [39, 41]. Later on, the Coulomb interaction was treated by using the non-interacting particle wave functions [72, 7]. Regarding perovskites, the band structure in the bulk has been investigated via the use of density functional theory [45, 46, 10]. Less work was done on the calculations of perovskite nanocrystals [99, 10]. A discussion of the correlated single exciton in nanocrystals can be found in Ref. [10]. So far, all of the theoretical studies on perovskite nanocrystals have not focused on the properties of any electron-hole system other than a single exciton. However, with increasing excitation power,

more than one pair of electron and hole can be created inside a nanocrystal [71, 126]. Many interesting experimental results are available on the emission of the trions (a neutral exciton with an additional charge) [52, 100, 80] as well as the biexciton (two electrons and two holes) [21, 80, 135]. The trion and biexciton emission peaks differ from that of a single exciton due to the correlation between the charge carriers.

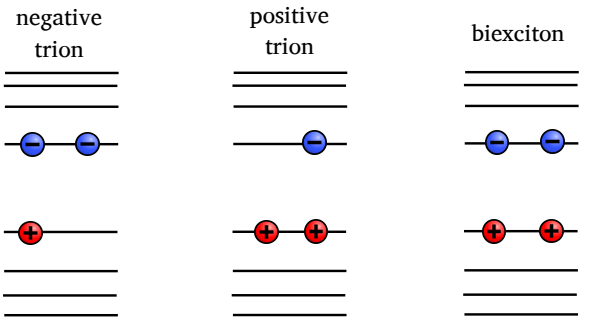

Figure 1.4.1: From left to right: depiction of the negative trion, position trion and biexciton in their respective ground states.

Further motivation for this research comes from the measured lifetime and absorption cross-section of the electron-photon interaction involving one photon. The radiative lifetime of an exciton in its ground state falls in the sub-nanosecond range for perovskites [10, 100, 20], which seems to be similar to that of GaAs [11] and is notably shorter than in many other semiconductors such as CdSe or CuCl [71, 61]. The fast radiative decay might be linked to the brightness of these perovskite nanocrystals. The recorded one-photon absorption cross-section is also quite good compared to the nanocrystals of other materials of the same size [23, 85]. This fact partially explains why perovskites are generally good light absorbers for solar cells [24].

In this thesis, we aim at providing a computationally efficient theoretical method for the study of an excitonic system with N_e electrons and N_h holes in a semiconductor nanocrystal. The main applications of the theory that will be developed in the thesis are

(i) the single exciton binding energy for nanocrystals,

(ii) the long-range exchange contribution to single exciton fine structure,

(iii) the emission energies of trions and biexciton from their ground states,

(iv) the spontaneous radiative decay rate and the one-photon absorption cross-section.

The study of the quantities listed above can be accomplished by using the approach of many-body perturbation theory. Our theoretical formulation will be constructed in stages. They correspond to the various chapters of the thesis. An overview is also given below.

1.5 Outline of the thesis

In Chapter 2, we start the technical discussion with a quick recapitulation of the band structure calculations. The $\mathrm{k}\cdot\mathrm{p}$ Hamiltonian is viewed as a way to model the kinetic energy at the band edge of the semiconductor. To further boost the computational efficiency, we make the assumption of spherical symmetry for the band structure as well as the confining potential. Both the 8×8 and 4×4 models will be discussed. By setting the Kane parameter $E_{\mathrm{p}}=0$ in the $\mathrm{k}\cdot\mathrm{p}$ model, we recover the effective mass model (parabolic approximation).

Only in a nanocrystal with a high dielectric constant in the strong confinement regime such as PbSe or PbS [64], the non-interacting single-particle picture for charge carriers (electrons and holes) adequately describes the exciton binding energy. However, this is no longer true for perovskite nanocrystals: one has to take the Coulomb interaction into account. In Chapter 3, we present the Hartree-Fock formulation as a mean-field level approximation to the exact intercarrier Coulomb interaction. As an application, the calculated single exciton energy will be compared to experimental figures at the end of this chapter. The Hartree-Fock approximation shows to be a reasonable description for a single exciton binding energy in perovskites, see the results of Section 3.4.

It turns out that at a mean-field level, including Hartree-Fock, the emission energy of a trion or a biexciton is basically identical to that of a single exciton. The small but measurable difference between their emission energies come almost purely from correlation effects [113]. Chapter 4 is concerned with the theoretical foundation for obtaining the trion and biexciton shifts. There, we use the second-order many-body perturbation theory approach to clearly demonstrate that some nonzero red-shifts are present for trions as well as the biexciton. The quantitative prediction is less than satisfactory at second-order level, which implies that an all-order method is needed for a better comparison with experiments. To complete the discussion of many-body perturbation theory, we shall apply the second-order degenerate version [75] to calculate the long-range exchange contribution to the dark-bright exciton energy splitting.

Chapter 5 deals with the electron-photon interaction. At Hartree-Fock level, the computed radiative decay rate and one-photon absorption cross-section turn out to be too small compared to the measured values. The electron-hole correlation in the many-body approach greatly improves the theoretical prediction of these quantities, bridging the gap between our theory and the experiments. We conclude that the Coulomb correlation also plays a very important role in the electron-photon interaction. Again, to have a good quantitative agreement with the measurements, this correlation must be included up to all orders. Even though the variational method, which was first given in Ref. [119], can take care of the Coulomb interaction nonperturbatively in principle, it becomes increasingly involved for the calculations of the higher exciton states [118]. We remark that our current approach requires the same level of complexity when applied to these excited states, which is beneficial for correcting the whole absorption spectrum.

Finally, we conclude the thesis in Chapter 6 with a summary of the basic findings and a discussion of some future research directions.

Chapter 2

Non-interacting particles

At the beginning of this chapter, we rapidly recall the concept of an electronic band structure with rather minimal details. More thorough studies on the subject can be found in Ref. [4] and Ref. [70]. We then move on to the $\mathrm{k}\cdot\mathrm{p}$ theory, in combination with envelope function approximation, as a simple and canonical way of modelling the band edge kinetics in Section 2.2. Both the eight-band 8×8 and four-band 4×4 $\mathrm{k}\cdot\mathrm{p}$ models will be discussed. The former is known to work well for the case of group III-V and II-VI semiconductors [69, 78, 71] whereas the latter has been recently used to examine the properties of perovskites [10, 105, 106]. It should be stressed here that all the $\mathrm{k}\cdot\mathrm{p}$ models considered in this thesis are spherical. Regarding the non-spherical (or cubic) corrections in a more general $\mathrm{k}\cdot\mathrm{p}$ approach, the interested readers are directed to Ref. [114], for example. We dedicate the last section to how the spherical confinement, in conjunction with the $\mathrm{k}\cdot\mathrm{p}$ model, can be used to treat cubic-shape nanocrystals.

2.1 Band structure

The semiconductor nanocrystal system can be described by the total Hamiltonian for a system with N_0 valence electrons

$$H_{\mathrm{tot}}^{N_0} = \underbrace{-\frac{1}{2}\sum_{i}^{N_0}\nabla_i^2}_{H_{\mathrm{kin}}^{N_0}} + \sum_{i}^{N_0} V_{\mathrm{ion}}(\vec{r}_i) + \underbrace{\sum_{\langle i,j\rangle}^{N_0} G(\vec{r}_i,\vec{r}_j)}_{V_{\mathrm{Coul}}^{N_0}}. \tag{2.1.1}$$

The N_0 electrons build up the band structure of the semiconductor by filling in the available bulk states up to the valence band maximum (VBM). Clearly, $H_{\mathrm{kin}}^{N_0} = -\frac{1}{2}\sum_i^{N_0}\nabla_i^2$ describes the kinetic energy of these N_0 electrons. The periodic potential $V_{\mathrm{ion}}(\vec{r}_i)$ represents the interaction of the i^{th} electron with the lattice consisting of the positive ionic background and the non-valent electrons. Here, we assume a fix lattice structure, which results in a constant energy added for the ion-ion interaction. Therefore, we shall remove this part from the total Hamiltonian. In principle, the dynamics of the ionic background and the resulting interaction with the valence electrons, in other words, the electron-phonon interaction, should

be also included [142]. By virtue of the Bloch theorem, the single-particle electronic wave function can be written as

$$\psi(\vec{r}) = \eta(\vec{r})\ u_{\lambda,k}(\vec{r}), \tag{2.1.2}$$

where the bulk (3D) envelope function $\eta(\vec{r})$ equals to $e^{i\vec{k}\cdot\vec{r}}$ for the case of a periodic potential and the Bloch function $u_{\lambda,k}(\vec{r})$ of a band indexed λ has the same periodicity as the underlying lattice.

The last term $V_{\text{Coul}}^{N_0} = \sum_{\langle i,j\rangle}^{N_0} G(\vec{r}_i, \vec{r}_j)$ of $H_{\text{tot}}^{N_0}$ contains the Coulomb interaction of the $N_0(N_0-1)/2$ pairs $\langle i,j\rangle$ of electrons. When $V_{\text{Coul}}^{N_0}$ or an external potential is present, which is important for the case of semiconductor, the envelope function $\eta(\vec{r})$ may no longer take the form $e^{i\vec{k}\cdot\vec{r}}$ though the Bloch function $u_{\lambda,k}(\vec{r})$ is still expected to be periodic. The exact solution of the ground state of the Hamiltonian in Eq. (2.1.1) proves a numerical challenge, due not only to the need for a sensible description of $V_{\text{ion}}(\vec{r})$ but also, more importantly, the many-body nature of the Coulomb interaction $V_{\text{Coul}}^{N_0}$. For gaining a good understanding of the semiconductor ground state, one must look for a way of approximating $V_{\text{Coul}}^{N_0}$, sometimes by trial and error.

To use a mean-field potential $U_{\text{mf}}^{N_0}$ is among the most conceptually simple approximations to the many-body Coulomb interaction. One choice of a mean-field $U_{\text{mf}}^{N_0}$ is $U_{\text{mf}}^{N_0} = U_{\text{HF}}^{N_0}$, where the HF potential $U_{\text{HF}}^{N_0}$ is defined as follows

$$\langle i|U_{\text{HF}}^{N_0}|j\rangle = \sum_{a=1}^{N_0}\langle i|U^a|j\rangle = \sum_{a=1}^{N_0}\langle ia|G_{12}|ja\rangle - \langle ai|G_{12}|ja\rangle. \tag{2.1.3}$$

In Eq. (2.1.3), $\sum_{a=1}^{N_0}$ means summing over the N_0 states in the valence bands.

However, the mean-field methods are usually insufficient to predict the correct band structure of most semiconductors. An approach, which somehow includes exchange and correlation effects, must be used instead. In considering the system ground state, the density functional theory (DFT) often provides a reasonable approximation to the electron-electron correlation with a well-chosen effective single-particle exchange-correlation functional. The readers who are interested in knowing more about its theoretical foundation can look for a concise introduction from the book by R. G. Parr and W. Yang [96] or a more comprehensive study in the book of R. Martin [82]. Various software versions that implement DFT to calculate the electronic band structure are available either freely, for instance *Quantum Espresso* and *Abinit*, or commercially such as *VASP*. An exhaustive list of programs for DFT can be found at the following link "en.wikipedia.org/wiki/List_of_quantum_chemistry_and_solid-state_physics_software". Some example calculations of the band structure of $CsPBX_3$, one of the recent promising semiconductors for photovoltaics and light-emitting applications, are shown in Fig. 2.1.1.

There are a number of basic features of the band structures of semiconductors, as seen from Fig. 2.1.1. The lowest unoccupied band right above the VBM, called the conduction band (CB), is separated from the VBM by an energy gap E_{gap}. The values of E_{gap} are in the optical range for the semiconducting materials. To excite

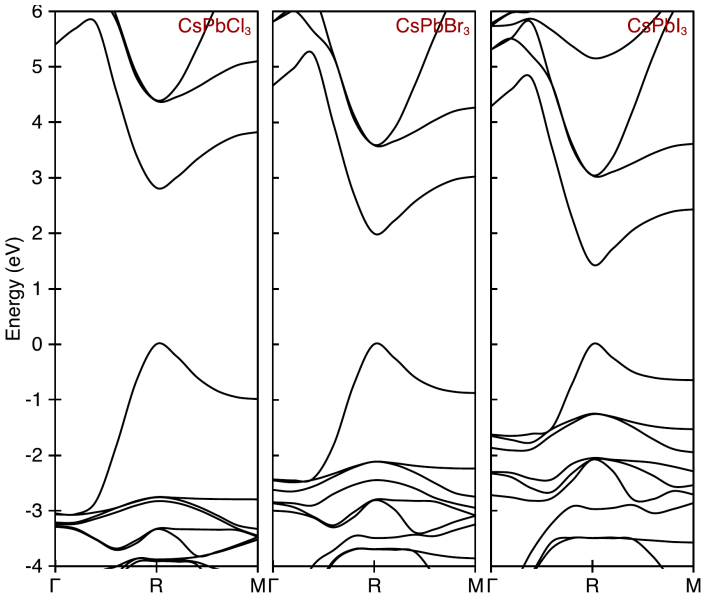

Figure 2.1.1: Example calculations using VASP of the band structures of $CsPbX_3$, where X=Cl, Br or I. The figure is taken from Supp. Info. of Ref. [99]. All N_0 valence electrons fill the electronic levels up to the valence band maximum that is set to be at 0 eV.

an electron from a valence band to a conduction band, one needs to provide an amount of energy of at least E_{gap}. One common problem with DFT is the underestimation of E_{gap}, as for the case of perovskites. In addition to this, around a high symmetry point, for instance the R-point at the band gap of $CsPBX_3$, the curvatures of the electronic bands also incorrectly underestimate the reduced masses in the bulk [99] as compared to the measured values [132, 53, 84]. One way of attempting to deal with these problems is to employ the GW method. Using the wave functions and energy levels from the DFT calculations, the GW approximation takes into account the electronic correlation more properly by using the many-body Green function method. Roughly speaking, a correlation functional Σ^{N_0} will be used, in place of $U_{\text{HF}}^{N_0}$ or any other mean-field potential $U_{\text{mf}}^{N_0}$, for treating the Coulomb interaction. All the software listed above can be extended, in principle, to include GW approximation though at the price of much heavier computations. Example calculations of GW method can be found in [122, 1].

The calculations of the band structure based on DFT or GW methods are referred to as *ab initio* calculations in this thesis. They provide the useful inputs, such as the band gap E_{gap} and the effective masses of the band edge, for the $\mathbf{k} \cdot \mathbf{p}$ theory in the next section to describe an excitonic system in a confined system.

2.2 k · p model

When an electron is promoted from the valence band to the conduction band, an 'exciton' is created where the electron stays in the conduction band and the 'hole', a missing electron, in the valence band. The curvatures of the conduction and valence bands around the band gap are interpreted as the 'effective masses' m_e^* and m_h^* of the electron and hole respectively. Note that VBM has a negative curvature, which implies that m_h^* is positive.

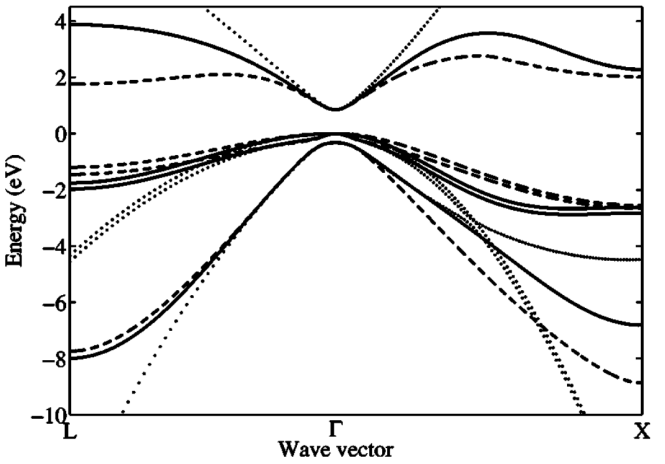

Figure 2.2.1: Calculated band structure of $In_{0.5}Ga_{0.5}As$, taken from Ref. [109], using three different methods: the 8×8 k · p method (dotted lines), the tight-binding like effective bond-orbital method (solid lines) and the empirical sp^3s^* tight-binding method (dashed lines). The 8×8 k · p method works very well around the Γ point where the direct band gap occurs, as typical for GaAs, CdSe etc.

Fig. 2.2.1 shows an example band structure of $In_{0.5}Ga_{0.5}As$ calculated using three different methods. The k · p theory agrees very well with the other two numerical methods in reproducing the band edge structure around the Γ point (i.e. wave vector $\vec{k} = 0$), where there is the direct band gap. Moving away from $\vec{k} = 0$ at the Γ point, some deviations start to appear, which possibly are caused by insufficient number of included bands (since only 8×8 k · p model was used) and other atomistic effects. In an excitonic system, the electron(s) and hole(s) relax to CBm and VBM respectively, after the initial excitation, via phonon emission on the time scale of picoseconds. Therefore, only the valence and conduction band edges at $\vec{k} = 0$ are important and the k · p theory renders a simple and adequate description for the electronic energy levels and relevant processes of the electron-hole system.

Within the scope of the current thesis, we focus on describing the optical properties of colloidal nanocrystals. Due to the confinement from the shape of nanostructure, the full wave function of a particle no longer belongs purely to the bulk conduction or valence band. In other words, the confining potential mixes the various bands at the band edge as well as discretizes the electronic energy levels, which

makes a nanocrystal look like an 'artificial' atom. The full wave function $\psi_a(\vec{r})$ of a particle state $|\psi_a\rangle$ in 2n $\times$ 2n k $\cdot$ p model is

$$\psi_a(\vec{r}) = \sum_{\alpha=1}^{\mathrm{n}} \psi_{a\alpha}(\vec{r}), \text{ where } \psi_{a\alpha}(\vec{r}) = \xi_{a\alpha}(\vec{r})\ u_{a\alpha,0}(\vec{r}). \tag{2.2.1}$$

The wave function $\psi_{a\alpha}(\vec{r})$ can be expressed as in (2.2.1) thanks to the separation of length scale, for which the Bloch part $u_{a\alpha,0}(\vec{r})$ is periodic w.r.t. the unit cells (microscopic, atomic length scale) while $\xi_{a\alpha}(\vec{r})$ varies over the whole mesoscopic nanocrystal. The information about symmetry and degeneracy of the bands at $\vec{k} = 0$ is contained inside the Bloch functions $u_{a\alpha,0}(\vec{r})$. The envelope parts $\xi_{a\alpha}(\vec{r})$ of the full wave function $\psi_a(\vec{r})$ describe the particle at mesoscopic length scale.

The remaining part of this chapter is devoted to deriving the radial form for the k $\cdot$ p Hamiltonian and the envelope functions $\xi_{a\alpha}(\vec{r})$. This will provide a theory for the mesoscopic length scale, which is much more computationally efficient than the atomistic approaches. We shall make the basic assumption that the same bulk parameters can be used for the confined nanocrystal systems. For the very small nanocrystals, especially those having less than 10 atomic layers in each dimension, the assumption about using the bulk parameters may not strictly hold true. This range of sizes may introduce certain atomistic effects, for example the distortions from the bulk lattice crystals, surface defects, etc. Hence, an *ab initio* approach might be desirable here. Nonetheless, for a sizable nanocrystal with more than several thousands of atoms, the band structure parameters get closer to the bulk values throughout the whole nanocrystal while the atomistic-level calculations become too expensive or even infeasible. In this case, the k $\cdot$ p model in combination with the envelope function approximation is extremely advantageous.

In Chapters 2 and 3, we treat both the 8×8 k $\cdot$ p model (for group III-V and II-VI semiconductors) and the 4×4 k $\cdot$ p model (PbS, PbSe and perovskites). After obtaining the radial k $\cdot$ p Hamiltonian $H_{\text{k}\cdot\text{p}}$ in this chapter, we shall derive the radial Hartree-Fock potential, which is a mean-field approximation, in Chapter 3. Then, the Hartree-Fock equations can be utilized to generate a single-particle (mean-field) basis for the many-body perturbation theory in Chapters 4 and 5. In those two chapters, the calculations of the correlation energy and the optical response focus on the 4×4 k $\cdot$ p model having perovskites as the materials for applications.

2.2.1 Eight-band k $\cdot$ p model

As a reminder, the band structure at $\vec{k} = 0$ (the band gap) of the common semiconductors such as GaAs, InAs, CdSe, CdS etc. can be well described using the 8×8 k $\cdot$ p model. The lowest conduction band has an approximate s-wave symmetry, thus called an s-like band, with two-fold degeneracy from spin [41]. Meanwhile, the valence band is p-like and is split further into two subbands due to spin-orbit coupling of the constituent heavy metal (Ga, Cd, ...), see [40, 78] for more details.

Let $\vec{L}$ be the orbital angular momentum and $\vec{S}$ be the electron spin associated with the Bloch functions. The spin-orbit coupling implies that only the Bloch total angular momentum $\vec{J} = \vec{L} + \vec{S}$, also called the pseudospin $\vec{J}$, is the conserved quantity in the bulk. Therefore, the p-like subbands (with $L = 1$) are labelled as

$p_{3/2}$ and $p_{1/2}$ corresponding to $J = 3/2$ and $J = 1/2$. At $\vec{k} = 0$, their degeneracy $(2J + 1)$ equals 4 and 2 respectively. As the wave vector $\vec{k}$ becomes non-zero, the $p_{3/2}$ band splits into a light hole branch with more negative curvature and a heavy hole branch that lies above the light hole. Figure 2.2.2 is a schematic of an 8×8 k·p model of the band structure at around the band edge.

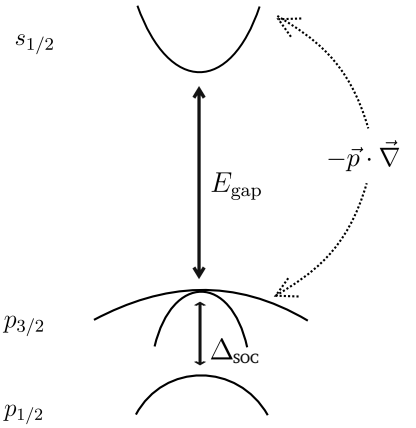

Figure 2.2.2: The schematic of the 8×8 k · p. The $s_{1/2}$ conduction band and the (spin split-off) $p_{1/2}$ valence band are two-fold degenerate. At $\vec{k} = 0$, the $p_{3/2}$ valence band is four-fold degenerate. Away from $|\vec{k}| = 0$, the $p_{3/2}$ band constitutes of two branches with different curvatures. These are called the light and heavy holes. The $p_{3/2}$ and $p_{1/2}$ bands are further coupled to $s_{1/2}$ via $(-\vec{p}\cdot\vec{\nabla})$, where $(-\vec{\nabla})$ is the momentum opertor $\vec{k}$ in position space representation. We have chosen the convention where a momentum operator is real and the complex unit i has been omitted.

The effective Hamiltonian for the kinetic energy of a *hole* can be described by the 8×8 k · p model as [39]

$$H_{\text{kin}} = H_{\text{k·p}}^{8\times8} = -(A_c\nabla^2 + E_{\text{gap}})\ \mathbb{I}_c - \vec{p}\cdot\vec{\nabla} + H_{\text{k·p}}^{6\times6}\ \mathbb{I}_v + H_{\text{soc}}. \tag{2.2.2}$$

In the above, H_{soc} represents the spin-orbit coupling in the p-like valence band. Its effect is to put the $p_{1/2}$ band below the $p_{3/2}$ band by an energy difference Δ_{soc}. The operator $\mathbb{I}_{c/v}$ acts on a conduction/valence state as the identity and equals to 0 otherwise. The block $-(A_c\nabla^2 + E_{\text{gap}})\ \mathbb{I}_c$ captures a portion of the conduction band kinetic energy. The 6×6 block $H_{\text{k·p}}^{6\times6}$ describes the properties of the valence band including the $p_{3/2}$ and $p_{1/2}$ subbands. One has that

$$H_{\text{k·p}}^{6\times6} = \frac{1}{2}\gamma_1\nabla^2 + \gamma(\vec{\nabla}\cdot\vec{L})^2, \tag{2.2.3}$$

where $\vec{L}$ acts on the Bloch function part of the total wave function. The idea behind Eq. 2.2.3 is a Hamiltonian that has quadratic dependence on the momentum operator, in other words quadratic in $\vec{\nabla}$, meanwhile possesses rotational invariance. We note that the coefficients γ_1 and γ in (2.2.3) are precisely the Luttinger parameters of the spherical k · p model used in Ref. [98, 39].

The term $(-\vec{p}\cdot\vec{\nabla})$ is the $\mathrm{k}\cdot\mathrm{p}$ coupling between the $s_{1/2}$ band and the $p_{3/2}$ and $p_{1/2}$ bands. It will become clear later in this chapter that $(-\vec{p}\cdot\vec{\nabla})$ is proportional to $\sqrt{E_{\mathrm{p}}}$, where E_{p} is the Kane parameter. The operator $\vec{\nabla}$ acts on the envelope parts $\xi_{a\alpha}(\vec{r})$ of the total wave function while $\vec{p}=\vec{\nabla}^{(L)}$ acts only on the orbital parts of the Bloch functions $u_{a\alpha,0}(\vec{r})$.

In the bulk, both the pseudospin $\vec{J}$ and the wave vector $\vec{k}$ are conserved quantities. In a confined system, $\vec{J}$ and $\vec{k}$ of the total wave function are no longer good quantum numbers. Instead of $\vec{k}$, the envelope degree of freedom can be more conveniently classified by its orbital angular momentum $\vec{l}$. The total angular momentum $\vec{F}=\vec{J}+\vec{l}$, of a single-particle state, is a good quantum number of the Hamiltonian $H_{\mathrm{k\cdot p}}^{8\times8}$. In other words, the operator $\vec{F}$ commutes with $H_{\mathrm{k\cdot p}}^{8\times8}$, for which we shall now give a proof. For a system with an overall spherical symmetry, the total angular momentum should be a good quantum number in principle. It is obvious that $\vec{F}$ commutes with $-(A_c\nabla^2+E_{\mathrm{gap}})\mathbb{I}_c$. The operator $\vec{l}$ commutes with ∇^2 because the eigen functions $|lm_l\rangle$ of the former are also eigen functions of the Laplacian ∇^2. On the other hand, ∇^2 contains no dependence on $\vec{J}$ and, as a result, must commute with $\vec{J}$.

Therefore, it remains to show that $(-\vec{p}\cdot\vec{\nabla})$ and $H_{\mathrm{k\cdot p}}^{6\times6}$ also commute with $\vec{F}$.

Next, we shall show that $\left[\vec{p}\cdot\vec{\nabla},\vec{F}\right]=0$.

Let ϵ_{ijk} be the Levi-Civita symbol. Note the following commutation identities

$$\begin{aligned}[p_i,L_j]&=i\hbar\sum_k\epsilon_{ijk}\ p_k,\\ [\nabla_i,l_j]&=i\hbar\sum_k\epsilon_{ijk}\nabla_k.\end{aligned}\tag{2.2.4}$$

By applying the identities in (2.2.4) to the commutator $\left[\vec{p}\cdot\vec{\nabla},F_j\right]$, where

$$\left[\vec{p}\cdot\vec{\nabla},F_j\right]=\sum_i\left(p_i\left[\nabla_i,L_j\right]+\left[p_i,l_j\right]\nabla_i\right),\tag{2.2.5}$$

and recalling that ϵ_{ijk} is anti-symmetric upon exchanging any two indices, one has

$$\left[\vec{p}\cdot\vec{\nabla},F_j\right]=\sum_{ik}i\hbar\left(\epsilon_{ijk}\nabla_i p_k+\epsilon_{ijk}\nabla_k p_i\right)=0.\tag{2.2.6}$$

Now, we prove that the commutator $\left[H_{\mathrm{k\cdot p}}^{6\times6},\vec{F}\right]$ is also zero.

In Eq. (2.2.3), the first term $\frac{1}{2}\gamma_1\nabla^2$ commutes with $\vec{F}$. Therefore, to show that $H_{\mathrm{k\cdot p}}^{6\times6}$ commutes with $\vec{F}$, one only needs that $\left[(\vec{\nabla}\cdot\vec{L})^2,\vec{F}\right]=0$.

$$\left[(\vec{\nabla}\cdot\vec{L})^2,F_j\right]=\left[(\vec{\nabla}\cdot\vec{L})^2,l_j\right]+\left[(\vec{\nabla}\cdot\vec{L})^2,J_j\right],\tag{2.2.7}$$

where $\vec{\nabla}\cdot\vec{L}=\sum_k \nabla_k L_k$ and $\left[(\vec{\nabla}\cdot\vec{L})^2, J_j\right]=\left[(\vec{\nabla}\cdot\vec{L})^2, L_j\right]$. Therefore,

$$\begin{aligned}\left[(\vec{\nabla}\cdot\vec{L})^2, F_j\right] &= i\hbar\sum_{i_1 i_2}\left(\sum_{k_2}\epsilon_{i_2 j k_2}\nabla_{i_1}\nabla_{k_2}+\sum_{k_1}\epsilon_{i_1 j k_1}\nabla_{k_1}\nabla_{i_2}\right)L_{i_1}L_{i_2}\\ &+ i\hbar\sum_{i_1 i_2}\nabla_{i_1}\nabla_{i_2}\left(\sum_{k_2}\epsilon_{i_2 j k_2}L_{i_1}L_{k_2}+\sum_{k_1}\epsilon_{i_1 j k_1}L_{k_1}L_{i_2}\right).\end{aligned} \tag{2.2.8}$$

With a change of notation for the sum,

$$\begin{aligned}\sum_{i_1 i_2 k_2}\epsilon_{i_2 j k_2}\nabla_{i_1}\nabla_{k_2}L_{i_1}L_{i_2} &= \sum_{i_1 k_2 i_2}\epsilon_{k_2 j i_2}\nabla_{i_1}\nabla_{i_2}L_{i_1}L_{k_2} = -\sum_{i_1 i_2 k_2}\epsilon_{i_2 j k_2}\nabla_{i_1}\nabla_{i_2}L_{i_1}L_{k_2},\\ \sum_{i_1 i_2 k_1}\epsilon_{i_1 j k_1}\nabla_{k_1}\nabla_{i_2}L_{i_1}L_{i_2} &= \sum_{k_1 i_2 i_1}\epsilon_{k_1 j i_1}\nabla_{i_1}\nabla_{i_2}L_{k_1}L_{i_2} = -\sum_{i_1 i_2 k_1}\epsilon_{i_1 j k_1}\nabla_{i_1}\nabla_{i_2}L_{k_1}L_{i_2}.\end{aligned} \tag{2.2.9}$$

Substituting (2.2.9) to (2.2.8), we get $\left[(\vec{\nabla}\cdot\vec{L})^2, F_j\right]=0$, which completes the proof of $\vec{F}$ being a good quantum number for $H^{8\times 8}_{\mathrm{k\cdot p}}$. Thus, an eigenstates of $H^{8\times 8}_{\mathrm{k\cdot p}}$ can be classified by the total angular momentum $\vec{F}$ and takes the form $|FM\rangle$.

It is also clear from the above derivation that $(\vec{\nabla}\cdot\vec{L})^2$ does not commute with either $\vec{l}$ or $\vec{J}$. Thus, $(\vec{\nabla}\cdot\vec{L})^2$ generally mixes the Bloch states with $J=1/2$ and $J=3/2$.

Consider the ∇^1_q component of $\vec{\nabla}=\nabla^1$, which is a rank-one spherical tensor. ∇^1_q maps $|lm_l\rangle$ to $|l\pm 1\ m_l+q\rangle$. As a consequence, $(-\vec{p}\cdot\vec{\nabla})$ connects $|lm_l\rangle$ to $|l'\ m_{l'}\rangle$, where $l'=l\pm 1$, and $(\vec{\nabla}\cdot\vec{L})^2$ connects $|lm_l\rangle$ to $|l'\ m_{l'}\rangle$, where $l'=l,\ l\pm 2$. It means that within the valence band, the various states $|\,(l,J)\,FM\rangle$ for the same (F,M) with different l and J are coupled to each other. These coupled states can have both $J=1/2$ and $J=3/2$.

Let l be the smallest envelope angular momentum among these coupled states. From the triangle inequality (l,J,F), there is a number of cases, depending on the relation between l and F:

- If $l=F-\frac{3}{2}$ for $F\geq\frac{3}{2}$, there are four coupled states $|\,\big(l,p\tfrac{3}{2}\big)\,FM\rangle$, $|\,\big(l+2,p\tfrac{3}{2}\big)\,FM\rangle$, $|\,\big(l+2,p\tfrac{1}{2}\big)\,FM\rangle$ and $|\,\big(l+1,s\tfrac{1}{2}\big)\,FM\rangle$.
- If $l=F-\frac{1}{2}$ for $F\geq\frac{3}{2}$, the four coupled states are $|\,\big(l,p\tfrac{3}{2}\big)\,FM\rangle$, $|\,\big(l+2,p\tfrac{3}{2}\big)\,FM\rangle$, $|\,\big(l,p\tfrac{1}{2}\big)\,FM\rangle$ and $|\,\big(l+1,s\tfrac{1}{2}\big)\,FM\rangle$.
- If $F=\frac{1}{2}$, there are two sets of three coupled states $|\,\big(l=1,p\tfrac{3}{2}\big)\,F=\tfrac{1}{2}M\rangle$, $|\,\big(l=1,p\tfrac{1}{2}\big)\,F=\tfrac{1}{2}M\rangle$ and $|\,\big(l=0,s\tfrac{1}{2}\big)\,F=\tfrac{1}{2}M\rangle$, $|\,\big(l=0,p\tfrac{3}{2}\big)\,F=\tfrac{1}{2}M\rangle$, $|\,\big(l=0,p\tfrac{1}{2}\big)\,F=\tfrac{1}{2}M\rangle$ and $|\,\big(l=1,s\tfrac{1}{2}\big)\,F=\tfrac{1}{2}M\rangle$.

We would like to remind the readers again that each of the coupled states $|(l,J)FM\rangle$ contains information about the corresponding Bloch function and its transformation properties. In what follows, the Bloch functions $u_{a\alpha,0}(\vec{r})$ in the full wave function $|\psi_a\rangle$ (see Eq. (2.2.1)) will be implicit in the $\mathrm{k}\cdot\mathrm{p}$ components of the so-called *total wave function* $|a\rangle$, which will be defined immediately below.

We conclude that for $F \geq \frac{3}{2}$, the total wave function $|a\rangle$ of an eigenstate can be written explicitly as a sum of four components

$$|a\rangle = \begin{cases} \frac{1}{r}\left[R_{a1}(r)|(l+1,s\frac{1}{2})FM\rangle + R_{a2}(r)|(l,p\frac{3}{2})FM\rangle \right. \\ \left. +R_{a3}(r)|(l+2,p\frac{3}{2})FM\rangle + R_{a4}(r)|(l+2,p\frac{1}{2})FM\rangle\right], & \text{if } l = F-\frac{3}{2}, \\ \\ \frac{1}{r}\left[R_{a1}(r)|(l+1,s\frac{1}{2})FM\rangle + R_{a2}(r)|(l,p\frac{3}{2})FM\rangle \right. \\ \left. +R_{a3}(r)|(l+2,p\frac{3}{2})FM\rangle + R_{a4}(r)|(l,p\frac{1}{2})FM\rangle\right], & \text{if } l = F-\frac{1}{2}. \end{cases} \tag{2.2.10}$$

For the special case $F = \frac{1}{2}$, there are only three coupled components, as establish above, and one has

$$|a\rangle = \begin{cases} \frac{1}{r}\left[R_{a1}(r)|(l-1,s\frac{1}{2})FM\rangle \right. \\ \left. +R_{a3}(r)|(l,p\frac{3}{2})FM\rangle + R_{a4}(r)|(l,p\frac{1}{2})FM\rangle\right], & \text{if } l = F+\frac{1}{2}, \\ \\ \frac{1}{r}\left[R_{a1}(r)|(l+1,s\frac{1}{2})FM\rangle + R_{a2}(r)|(l,p\frac{3}{2})FM\rangle \right. \\ \left. +R_{a4}(r)|(l,p\frac{1}{2})FM\rangle\right], & \text{if } l = F-\frac{1}{2}. \end{cases} \tag{2.2.11}$$

Any missing $\mathrm{k}\cdot\mathrm{p}$ component, which is understood to be zero, in Eq. (2.2.11) is due to the corresponding orbital angular momentum $\vec{l}$ being negative or not satisfying the triangle inequality (l, J, F). By using the convention that α, where $\alpha = 1, \ldots, 4$, indexes the spin-angular basis vector $|(lJ)FM\rangle$, one can write down a vector containing only the radial components $R_{a,\alpha}$.

The radial form of the total wave function $|a\rangle$ can be written as

$$|a\rangle = \frac{1}{r}\begin{pmatrix} R_{a1}(r) \\ R_{a2}(r) \\ R_{a3}(r) \\ R_{a4}(r) \end{pmatrix}, \tag{2.2.12}$$

where the associated angular momentum states are as given in Eqs. (2.2.10) and (2.2.11). For the case of $F = 1/2$, the missing component with either $\alpha = 2$ or $\alpha = 3$, see (2.2.11), is set to zero automatically.

In a confined system, the external potential V_{ext} mixes the various $\mathrm{k}\cdot\mathrm{p}$ components with angular states $|(l, J)FM\rangle$. The total wave function $|a\rangle$ is an eigenstate of the following equation

$$\left(H^{8\times8}_{\mathrm{k\cdot p}} + V_{\text{ext}}\right)|a\rangle = E^0_a|a\rangle. \tag{2.2.13}$$

When the external potential V_{ext} is spherically symmetric, $|a\rangle$ takes the form (2.2.10) or (2.2.11). Next, we aim to work out the radial form of $H^{8\times8}_{\mathrm{k\cdot p}}$ matrix of which the radial wave function (2.2.12) is an eigenvector. Roughly speaking, one can do this by taking the projection $\langle(l, J)FM|H^{8\times8}_{\mathrm{k\cdot p}}|a\rangle$, where the total wave function $|a\rangle$ contains the $|(l', J')FM\rangle$ $\mathrm{k}\cdot\mathrm{p}$ components. To achieve this goal, we can use the spherical tensor algebra in chapters 2 and 3 of Ref. [75].

The $H_{\mathrm{k\cdot p}}^{6\times 6}$ defined in Eq. (2.2.3) can be re-written as a sum of spherical tensors,

$$H_{\mathrm{k\cdot p}}^{6\times 6} = A_0\nabla^2 + A_2\left\{\vec{\nabla}\vec{\nabla}\right\}^2\cdot\mathbb{T}^2. \tag{2.2.14}$$

The rank-zero tensor operator ∇^2 commutes with $\vec{l}$ and does not act on the Bloch part. Therefore, ∇^2 does not mix any of the components in Eq. (2.2.12). From the matrix element $\langle l\ l|\nabla^2|l\ l\rangle$, see Eq. (B.2.10), the action of ∇^2 on each radial component takes the simple expression

$$\langle(l,J)FM|\nabla^2|(l,J)FM\rangle = \frac{1}{r^2}\frac{\partial}{\partial r}(r^2\frac{\partial}{\partial r}) - l(l+1)\frac{1}{r^2}. \tag{2.2.15}$$

About the second term, both $\left\{\vec{\nabla}\vec{\nabla}\right\}^2$ and $\mathbb{T}^2$ are rank-two spherical tensors. While $\left\{\vec{\nabla}\vec{\nabla}\right\}^2$ acts on the envelope degree of freedom, $\mathbb{T}^2$ operates on the Bloch part of the total wave function. From the results of Section B.2 in the appendix, one easily sees that $\left\{\vec{\nabla}\vec{\nabla}\right\}^2\cdot\mathbb{T}^2$ generally mixes the various $\mathrm{k\cdot p}$ components $|(l,J)FM\rangle$ of the total wave function. By applying the results (B.4.4) of the appendix Section B.4, the action of $\left\{\vec{\nabla}\vec{\nabla}\right\}^2\cdot\mathbb{T}^2$ is

$$\begin{aligned}\langle(l,J)\,FM|\left\{\vec{\nabla}\vec{\nabla}\right\}^2\cdot\mathbb{T}^2|\,(l',J')\,FM\rangle =& (-1)^{l+J+F}\begin{Bmatrix} l & l' & 2\\ J' & J & F\end{Bmatrix}\times\\ & \langle J||\mathbb{T}^2||J'\rangle\ \langle l||\left\{\vec{\nabla}\vec{\nabla}\right\}^2||l'\rangle,\end{aligned} \tag{2.2.16}$$

where $l' = l$ or $l\pm 2$.

A complete derivation of the reduced matrix element $\langle l||\left\{\vec{\nabla}\vec{\nabla}\right\}^2||l'\rangle$ are given in appendix Section B.2. It remains to evaluate $\langle J||\mathbb{T}^2||J'\rangle$. We must note that, being a rank-two tensor, $\mathbb{T}^2$ connects only the p-like states, which have $L=1$. We define $\mathbb{T}^2$ such that, for $L=1$,

$$\langle L||\mathbb{T}^2||L\rangle = 1. \tag{2.2.17}$$

From the definition (2.2.17), one can deduce the reduced matrix element $\langle J||\mathbb{T}^2||J'\rangle$ by applying the formulas (B.3.2) and (B.3.3) to get

$$\langle J||\mathbb{T}^2||J'\rangle = (-1)^{L+1/2+J'}\times[J]^{1/2}[J']^{1/2}\times\begin{Bmatrix} 2 & J & J'\\ 1/2 & 1 & 1\end{Bmatrix}. \tag{2.2.18}$$

With this choice of $\mathbb{T}^2$, the coefficient A_0 and A_2 in (2.2.14) are related to the Luttinger parameters γ_1 and γ, see the expression (2.2.3) for $H_{\mathrm{k\cdot p}}^{6\times 6}$, as follows

$$\begin{cases} A_0 = \frac{1}{2}\gamma_1,\\ A_2 = -3\sqrt{5}\gamma.\end{cases} \tag{2.2.19}$$

The relations in (2.2.19) can be derived by relating the parameters A_0 and A_2 to the effective masses m^*_{lh} and m^*_{hh} of the light and heavy holes in the bulk limit at $\vec{k}=0$. One can obtain a similar relation between $\{m^*_{lh},\ m^*_{hh}\}$ and $\{\gamma_1,\ \gamma\}$.

The last remaining term of $H^{8\times 8}_{\text{k}\cdot\text{p}}$ to be expressed in radial form is $(-\vec{p}\cdot\vec{\nabla})$. We need, in particular, the matrix element $\langle (l,\frac{1}{2})FM|\vec{p}\cdot\vec{\nabla}|(l',J)FM\rangle$, where $l'=l\pm 1$. Applying the results of the appendix B.4 leads to

$$\begin{aligned}
\langle (l,\frac{1}{2})FM|\vec{p}\cdot\vec{\nabla}|\,(l',J)\,FM\rangle =&(-1)^{l+3/2+F}\begin{Bmatrix} l & l' & 1\\ J & 1/2 & F\end{Bmatrix}\\
&\times\langle (s,\frac{1}{2})\frac{1}{2}||\vec{p}||(p,\frac{1}{2})J\rangle\ \langle l||\vec{\nabla}||l'\rangle,\\
\langle (l',J)\,FM|\vec{p}\cdot\vec{\nabla}|(l,\frac{1}{2})FM\rangle =&(-1)^{l+J+F}\begin{Bmatrix} l' & l & 1\\ 1/2 & J & F\end{Bmatrix}\\
&\times\langle (p,\frac{1}{2})J||\vec{p}||(s,\frac{1}{2})\frac{1}{2}\rangle\ \langle l'||\vec{\nabla}||l\rangle.
\end{aligned}\tag{2.2.20}$$

The reduced matrix element $\langle l||\vec{\nabla}||l'\rangle$ (or $\langle l'||\vec{\nabla}||l\rangle$) can be found in Eq. (B.1.6), see the appendix Section B.1. Regarding $\langle (s,\frac{1}{2})\frac{1}{2}||\vec{p}||(p,\frac{1}{2})J\rangle$, the spherical tensor $\vec{p}$ acts on the first angular momenta $\vec{L}$, where s and p stand for $L=0$ and $L=1$ respectively. Due to the parity selection rule, $\vec{p}$ connects only between $L=0$ and $L=1$ but not among the $L=1$ states themselves. By using the final result of Section B.3, the explicit expressions for the reduced matrix elements of $\vec{p}$ are given as

$$\begin{aligned}
\langle (s,\frac{1}{2})\frac{1}{2}||\vec{p}||(p,\frac{1}{2})J\rangle &= (-1)^{\frac{3}{2}+J}\sqrt{2[J]}\begin{Bmatrix} 1 & 1/2 & J\\ 1/2 & 1 & 0\end{Bmatrix}\langle 0||\vec{p}||1\rangle,\\
\langle (p,\frac{1}{2})J||\vec{p}||(s,\frac{1}{2})\frac{1}{2}\rangle &= -\sqrt{2[J]}\begin{Bmatrix} 1 & J & 1/2\\ 1/2 & 0 & 1\end{Bmatrix}\langle 1||\vec{p}||0\rangle\\
&= -\sqrt{2[J]}\begin{Bmatrix} 1 & 1/2 & J\\ 1/2 & 1 & 0\end{Bmatrix}\langle 0||\vec{p}||1\rangle.
\end{aligned}\tag{2.2.21}$$

Now, we introduce the following shorthand notations for three radial operators that will appear frequently later on.

$$\mathcal{L}_l = \frac{d^2}{dr^2} - l(l+1)\frac{1}{r^2},\tag{2.2.22}$$

$$\mathcal{M}_l = \frac{d^2}{dr^2} + (2l+3)\frac{1}{r}\frac{d}{dr} + l(l+2)\frac{1}{r^2},\tag{2.2.23}$$

$$\mathcal{D}_l = \frac{d}{dr} - (l+1)\frac{1}{r}.\tag{2.2.24}$$

With the above definitions for $\mathcal{L}_l,\ \mathcal{M}_l$ and $\mathcal{D}_l$, one can write down the radial $H^{8\times 8}_{\text{k}\cdot\text{p}}$ more compactly.

Again, the radial $H_{\mathrm{k\cdot p}}^{8\times 8}$ takes two explicit forms depending on the exact relation between l and F. In Eqs. (2.2.25) and (2.2.26), we provide the radial expressions for $H_{\mathrm{k\cdot p}}^{8\times 8}$ when all four radial components are present, i.e. when $F \geq \frac{3}{2}$. When $(F = \frac{1}{2},\ l = 1)$ and $(F = \frac{1}{2},\ l = 0)$, the rows and columns containing the index $\alpha = 2$ or $\alpha = 3$, see Eq. (2.2.11), are set to zero.

If $l = F - \frac{3}{2}$, the radial form of $H_{\mathrm{k\cdot p}}^{8\times 8}$ can be found to be

$$H_{\mathrm{k\cdot p}}^{8\times 8} = \begin{pmatrix} -A_c\mathcal{L}_{l+1} + E_{\mathrm{gap}} & -c_{l+1,l}^{\frac{3}{2}}\mathcal{D}_l & -c_{l+1,l+2}^{\frac{3}{2}}\mathcal{D}_{l+1}^{\dagger} & -c_{l+1,l+2}^{\frac{1}{2}}\mathcal{D}_{l+1}^{\dagger} \\ -c_{l+1,l}^{\frac{3}{2}*}\mathcal{D}_l^{\dagger} & (A_0 - A_2\delta_l^{\frac{3}{2}\frac{3}{2}})\mathcal{L}_l & A_2\sigma_{l,l+2}^{\frac{3}{2}\frac{3}{2}}\mathcal{M}_l & A_2\sigma_{l,l+2}^{\frac{3}{2}\frac{1}{2}}\mathcal{M}_l \\ -c_{l+1,l+2}^{\frac{3}{2}*}\mathcal{D}_{l+1} & A_2\sigma_{l,l+2}^{\frac{3}{2}\frac{3}{2}}\mathcal{M}_l^{\dagger} & (A_0 - A_2\delta_{l+2}^{\frac{3}{2}\frac{3}{2}})\mathcal{L}_{l+2} & -A_2\delta_{l+2}^{\frac{3}{2}\frac{1}{2}}\mathcal{L}_{l+2} \\ -c_{l+1,l+2}^{\frac{1}{2}*}\mathcal{D}_{l+1} & A_2\sigma_{l+2,l}^{\frac{1}{2}\frac{3}{2}}\mathcal{M}_l^{\dagger} & -A_2\delta_{l+2}^{\frac{1}{2}\frac{3}{2}}\mathcal{L}_{l+2} & A_0\mathcal{L}_{l+2} - \Delta_{\mathrm{soc}} \end{pmatrix}. \tag{2.2.25}$$

Or else, if $l = F - \frac{1}{2}$, one has

$$H_{\mathrm{k\cdot p}}^{8\times 8} = \begin{pmatrix} -A_c\mathcal{L}_{l+1} + E_{\mathrm{gap}} & -c_{l+1,l}^{\frac{3}{2}}\mathcal{D}_l & -c_{l+1,l+2}^{\frac{3}{2}}\mathcal{D}_{l+1}^{\dagger} & -c_{l+1,l}^{\frac{1}{2}}\mathcal{D}_l \\ -c_{l+1,l}^{\frac{3}{2}*}\mathcal{D}_l^{\dagger} & (A_0 - A_2\delta_l^{\frac{3}{2}\frac{3}{2}})\mathcal{L}_l & A_2\sigma_{l,l+2}^{\frac{3}{2}\frac{3}{2}}\mathcal{M}_l & -A_2\delta_l^{\frac{3}{2}\frac{1}{2}}\mathcal{L}_l \\ -c_{l+1,l+2}^{\frac{3}{2}*}\mathcal{D}_{l+1} & A_2\sigma_{l,l+2}^{\frac{3}{2}\frac{3}{2}}\mathcal{M}_l^{\dagger} & (A_0 - A_2\delta_{l+2}^{\frac{3}{2}\frac{3}{2}})\mathcal{L}_{l+2} & A_2\sigma_{l+2,l}^{\frac{3}{2}\frac{1}{2}}\mathcal{M}_l^{\dagger} \\ -c_{l+1,l}^{\frac{1}{2}*}\mathcal{D}_l^{\dagger} & -A_2\delta_l^{\frac{1}{2}\frac{3}{2}}\mathcal{L}_l & A_2\sigma_{l,l+2}^{\frac{1}{2}\frac{3}{2}}\mathcal{M}_l & A_0\mathcal{L}_l - \Delta_{\mathrm{soc}} \end{pmatrix}. \tag{2.2.26}$$

The radial expressions of $H_{\mathrm{k\cdot p}}^{8\times 8}$ above are the ones describing a *hole*, where the valence band consists of the light hole, heavy hole and $p_{1/2}$ hole bands. The $H_{\mathrm{k\cdot p}}^{8\times 8}$ for an *electron* receives just an overall *minus sign* compared to (2.2.25) and (2.2.26).

The coefficients $\delta_l^{JJ'}$, $\sigma_{l,l'}^{JJ'}$ and $c_{l+1,l'}^{J}$, which result from (2.2.14)-(2.2.24), can be given as

$$\delta_l^{JJ'} = (-1)^{l+J+F}\sqrt{\frac{2}{3}\frac{l(l+1)(2l+1)}{(2l-1)(2l+3)}}\begin{Bmatrix} l & l & 2 \\ J' & J & F \end{Bmatrix}\langle J||\mathbb{T}^2||J'\rangle, \tag{2.2.27}$$

$$\sigma_{l,l'}^{JJ'} = (-1)^{l+J+F}\sqrt{\frac{(l_{\min}+1)(l_{\min}+2)}{2l_{\min}+3}}\begin{Bmatrix} l & l' & 2 \\ J' & J & F \end{Bmatrix}\langle J||\mathbb{T}^2||J'\rangle, \tag{2.2.28}$$

$$c^J_{l+1,l'} = (-1)^{l+J+F}\sqrt{2l_{\max}[J]}\begin{Bmatrix} l+1 & l' & 1 \\ J & 1/2 & F \end{Bmatrix}\begin{Bmatrix} 1 & 1/2 & J \\ 1/2 & 1 & 0 \end{Bmatrix}\langle 0||\vec{p}||1\rangle, \tag{2.2.29}$$

where $l_{\min} = \min(l, l')$ and $l_{\max} = \max(l+1, l')$.

The coefficients $\delta^{JJ'}_l$ and $\sigma^{JJ'}_{l,l'}$ originate from the term $\left\{\vec{\nabla}\vec{\nabla}\right\}^2 \cdot \mathbb{T}^2$ whereas $c^J_{l+1,l'}$ comes from $(-\vec{\nabla}\cdot\vec{p})$. Note the following symmetry properties of these coefficients

$$\delta^{JJ'}_l = \delta^{J'J}_l,\ \sigma^{JJ'}_{l,l'} = \sigma^{J'J}_{l'l},\ c^J_{l',l+1} = c^{J*}_{l+1,l'}. \tag{2.2.30}$$

The definitions of $\mathcal{L}_l$, $\mathcal{M}_l$ and $\mathcal{D}_l$ together with the identities in (2.2.30) guarantee that the expressions (2.2.25) and (2.2.26) are hermitian. The current derivation is a generalization of the work of Baldereschi et al. [8] on the $p_{3/2}$ valence band to include the $p_{1/2}$ valence band as well as the $s_{1/2}$ conduction band.

The reduced matrix element of the dipole operator $\vec{p}$ is basically related to the Kane parameter $E_{\rm p}$, as expressed by the formula

$$\langle 0||\vec{p}||1\rangle = \langle 1||\vec{p}||0\rangle = \sqrt{\frac{3}{2}E_{\rm p}}, \tag{2.2.31}$$

where $E_{\rm p}$ is defined in (3.4.1) and (3.4.2). From the matrices (2.2.25) and (2.2.26) of the radial 8×8 $\mathrm{k}\cdot\mathrm{p}$ Hamiltonian $H^{8\times 8}_{\mathrm{k}\cdot\mathrm{p}}$, one expects the magnitude of the $\mathrm{k}\cdot\mathrm{p}$ mixing between the conduction and valence bands to be proportional to $\sqrt{E_{\rm p}}$.

An eigenvector $|a\rangle$, which has been described explicitly in (2.2.12), of $H^{8\times 8}_{\mathrm{k}\cdot\mathrm{p}}$ can be labelled following the convention in Ref. [39, 41]. Let $l' = l+1$ be the orbital angular momentum associated with the $s_{1/2}$ (i.e. top left) block of $H^{8\times 8}_{\mathrm{k}\cdot\mathrm{p}}$. If $|R_{a1}|^2 \gg \sum_{\alpha=2}^4 |R_{a\alpha}|^2$, then the state is named the nl'_F conduction (or electron) state. Or else, we call $|a\rangle$ the nl_F valence (or hole) state, where l appears in (2.2.25) and (2.2.26). In these notations, $n = 1, 2, \ldots$ denotes the principal quantum number. We note that for the various components $R_{a,\alpha}$, where $\alpha = 2, 3$ or 4, in the valence band can have comparable magnitudes.

2.2.2 Four-band $\mathbf{k}\cdot\mathbf{p}$ model

In the group of lead halide perovskites ($APbX_3$), the basic electronic properties stem from the octahedra of PbX_6. Hence, many of the features of the band structure, for instance the band gap $E_{\rm gap}$ and the spin-orbit splitting $\Delta_{\rm soc}$, are roughly independent of the choice of the cation A. The calculated band structures, of which an example is given in Fig. 2.1.1 ($CsPbX_3$), demonstrates the existence of a band gap occurring at the R point of the Brillouin zone. The VBM is $s_{1/2}$ (with R^+_6 symmetry) while generally the CBm is $p_{1/2}$ (with R^-_6 symmetry) [10].

Due to the presence of Pb, which induces a strong spin-orbit coupling, the p-like band splits into two subbands, $p_{1/2}$ and $p_{3/2}$. The $p_{3/2}$ band stays above the lower $p_{1/2}$ band by an energy difference $\Delta_{\rm soc}$. The measured $\Delta_{\rm soc}$ of about 1 eV has been reported in Ref. [57] for $MAPbI_3$ (Fig. 3) and Ref. [101] for $CsPbBr_3$ (Fig. 1). As a comparison to $APbX_3$, let us consider the band structure of GaAs. The spin-orbit splitting of GaAs is $\Delta_{\rm soc} = 0.341$ eV [98]. For an average radius at about

several nanometers of the GaAs quantum dots, the energy of a confined particle would exceed Δ_{soc} [98]. Thereby, the inclusion of both $p_{3/2}$ and $p_{1/2}$ subbands and the use of the 8×8 k $\cdot$ p model become necessary for GaAs.

On the contrary, for a perovskite nanocrystal of edge length $L \geq 4.0$ nm, the confined kinetic energy is normally $\lesssim 200$ meV. Thus, the $p_{3/2}$ band is quite far above the $p_{1/2}$ band. Hence, one expects only a small contribution from $p_{3/2}$ band to the electronic properties of, for instance the single exciton, trions and biexciton, when the particles have relaxed to the lowest levels. As a result, the simplest k $\cdot$ p model that describes the $APbX_3$ perovskites is the 4×4 k $\cdot$ p model that includes the $s_{1/2}$ valence band and a $p_{1/2}$ conduction band.

Nonetheless, the derivation of the radial $H^{8\times8}_{\text{k}\cdot\text{p}}$ turns out to be very useful here since the radial $H^{4\times4}_{\text{k}\cdot\text{p}}$ Hamiltonian can be immediately obtained from (2.2.25) and (2.2.26) by removing the rows and columns involving the $p_{3/2}$ band (i.e. where $J = 3/2$). Let l be the envelope angular momentum of the $p_{1/2}$ band.

The radials expressions for $H^{4\times4}_{\text{k}\cdot\text{p}}$ in (2.2.32) describes the kinetic energy of a *hole* for materials with the same band structure as perovskites ($APbX_3$). We note that the bottom right blocks of these matrices correspond to the $p_{1/2}$ band, which is a conduction band. It explains the overall minus signs in front of the matrices. The energy gap E_{gap} should, therefore, be added to this block of $H^{4\times4}_{\text{k}\cdot\text{p}}$.

$$H^{4\times4}_{\text{k}\cdot\text{p}} = \begin{cases} -\begin{pmatrix} -\gamma_h \mathcal{L}_{l-1} & -c^{\frac{1}{2}}_{l-1,l}\mathcal{D}^{\dagger}_{l-1} \\ -c^{\frac{1}{2}*}_{l-1,l}\mathcal{D}_{l-1} & \gamma_e \mathcal{L}_l + E_{\text{gap}} \end{pmatrix}, & \text{if } l = F + \frac{1}{2}, \\ -\begin{pmatrix} -\gamma_h \mathcal{L}_{l+1} & -c^{\frac{1}{2}}_{l+1,l}\mathcal{D}_{l} \\ -c^{\frac{1}{2}*}_{l+1,l}\mathcal{D}^{\dagger}_{l} & \gamma_e \mathcal{L}_l + E_{\text{gap}} \end{pmatrix}, & \text{if } l = F - \frac{1}{2}. \end{cases} \tag{2.2.32}$$

We have introduced a slight change of notations: $A_c \mapsto \gamma_h$ and $A_0 \mapsto \gamma_e$ to be the same as in the Supp. Info. of Ref. [10]. Let m^*_e and m^*_h be the effective masses of the $p_{1/2}$ band (electron) and the $s_{1/2}$ band (hole) respectively. The off-diagonal blocks in (2.2.32) represent the contribution of the $p_{1/2}$ band to the effective mass of the $s_{1/2}$ band and vice versa. The parameters γ_h and γ_e describe the contribution to m^*_h and m^*_e from the bands that are further away from the band edge, i.e. the ones other than $s_{1/2}$ and $p_{1/2}$.

The coefficient $c^J_{l+1,l'}$ is defined in (2.2.29) as same as for 8×8 k$\cdot$p model. Again, the terms containing $c^J_{l+1,l'}$ bring about the k $\cdot$ p mixing between the conduction and valence bands. Similar to (2.2.12), a 2-component eigenfunction of $H^{4\times4}_{\text{k}\cdot\text{p}}$ can be written as

$$|a\rangle = \frac{1}{r}\begin{pmatrix} R_{a1}(r) \\ R_{a4}(r) \end{pmatrix}, \tag{2.2.33}$$

where the components $\alpha = 2$ and $\alpha = 3$ are removed from (2.2.12). Due to the k $\cdot$ p mixing, the radial components in (2.2.33) are non-zero but one has a bigger norm than the other.

For the purpose of notational consistency, we shall relabel R_{a4} to R_{a2}. The total wave function $|a\rangle$ becomes, with the angular part included,

$$|a\rangle = \begin{cases} \frac{1}{r}\left[R_{a1}(r)|(l-1,s\frac{1}{2})FM\rangle + R_{a2}(r)|(l,p\frac{1}{2})FM\rangle\right], & \text{if } l = F+\frac{1}{2}, \\ \\ \frac{1}{r}\left[R_{a1}(r)|(l+1,s\frac{1}{2})FM\rangle + R_{a2}(r)|(l,p\frac{1}{2})FM\rangle\right], & \text{if } l = F-\frac{1}{2}. \end{cases} \tag{2.2.34}$$

Let $l' = l+1$ be the orbital angular momentum of the $s_{1/2}$ block while n denotes the principal quantum number. If $|R_{a1}|^2 \gg |R_{a2}|^2$, the hole state is labelled nl'_F . Or else, it is called the nl_F electron state. We also use the atomic notation from now onwards, where s, p, d, ... correspond to the angular momenta $l = 0, 1, 2, \ldots$

As the last note, the effective mass model can be obtained from (2.2.32) by letting $E_{\rm p} = 0$. It means that the coefficients $c^{\frac{1}{2}}_{l-1,l}$ and $c^{\frac{1}{2}}_{l+1,l}$ are also zero and there is no coupling between the conduction and the valence band. The effective masses m_e^* and m_h^* are physical parameters and their values must be respected. In the effective mass model, $\gamma_e = m_e^*$ and $\gamma_h = m_h^*$.

2.3 Confinement: spherical approximation

Many of the experimentally synthesized quantum dots, for instance of CdSe, come out roughly as spheres [71]. In these cases, the created carriers (electrons and holes) can be treated as being confined in a spherical potential. For the more recent materials such as perovskites, the nanocrystals are cuboids that are fairly monodisperse [73, 60]. A perfect cube is highly symmetric and is invariant under many discrete rotations and inversion. Therefore, a well-chosen spherical confining potential serves as a good approximation to a given cubic confinement.

Let us consider an infinite spherical well of radius R. The confining potential is given as

$$V_{\rm conf} = \begin{cases} 0, & \text{if } r < R; \\ \infty, & \text{otherwise.} \end{cases} \tag{2.3.1}$$

Consider a single particle, which can either be an electron or a hole, of effective mass m^* trapped in $V_{\rm conf}$. Its wave function can be written as

$$\psi^{\rm sphr}_{n,l,m}(\vec{r}) = R_{n,l}(r)Y^l_m(\theta,\phi). \tag{2.3.2}$$

In (2.3.2), $Y^l_m(\theta,\phi)$ means the spherical harmonics of orbital angular momentum l and magnetic quantum number m while the radial function $R_{n,l}$ is a solution of the spherical Bessel equation

$$\left(\frac{d^2}{dr^2} + \frac{2}{r}\frac{d}{dr} + (k^2 - \frac{l(l+1)}{r^2})\right) R_{n,l} = E^{\rm sphr}_{n,l} R_{n,l}, \tag{2.3.3}$$

where n is the principal quantum number of $\psi^{\rm sphr}_{n,l,m}(\vec{r})$. Let $z_{n,l}$ be the n^{th} zero of the spherical Bessel function $j_l(r)$ (of the first kind). One has $k = z_{n,l}/R$.

The non-interacting single-particle energy $E^{\text{sphr}}_{n,l}$ associated with $\psi^{\text{sphr}}_{n,l,m}(\vec{r})$ is

$$E^{\text{sphr}}_{n,l} = \frac{\hbar^2}{2m^*}\frac{1}{R^2}z^2_{n,l}. \tag{2.3.4}$$

We claim here that the spectrum $\{E^{\text{sphr}}_{n,l}\}$ and the particle wave functions $\{\psi^{\text{sphr}}_{n,l,m}\}$ approximate well those of an infinite square well potential $V^{\text{cube}}_{\text{conf}}$ if

$$L = \sqrt{3}R, \tag{2.3.5}$$

where L denotes the edge length of the $V^{\text{cube}}_{\text{conf}}$ confining potential (2.3.6).

$$V^{\text{cube}}_{\text{conf}} = \begin{cases} 0, & \text{if } \max(|x|,|y|,|z|) < L/2; \\ \infty, & \text{otherwise.} \end{cases} \tag{2.3.6}$$

The tuple (n_x, n_y, n_z) of three integers classifies all single-particle eigen wave functions $\psi^{\text{cube}}_{n_x,n_y,n_z}(\vec{r})$ of V_{cube}. We have

$$\psi^{\text{cube}}_{n_x,n_y,n_z}(\vec{r}) = \left(\frac{2}{L}\right)^{3/2} \cos\left(\pi n_x \frac{x}{L}\right) \cos\left(\pi n_y \frac{y}{L}\right) \cos\left(\pi n_z \frac{z}{L}\right) \tag{2.3.7}$$

with its corresponding eigen energy given by

$$E^{\text{cube}}_{n_x,n_y,n_z} = \frac{\pi^2\hbar^2}{2m^*}\frac{n_x^2+n_y^2+n_z^2}{L^2}. \tag{2.3.8}$$

To model the ground state exciton in a nanocrystal, the lowest energy level, which is an s-wave for a sphere, is the most important. Regarding the s-wave channel ($l = 0$), their energy levels can be given explicitly as

$$E^{\text{sphr}}_{n,0} = \frac{\pi^2\hbar^2}{2m^*}\frac{n^2}{R^2},$$

since the zeros of $j_0(r)$ are simply $z_{n,0} = \pi^2 n^2$. The wave function $\psi^{\text{sphr}}_{n,0,0}$ of the lowest s-wave 1s takes the form

$$\psi^{\text{sphr}}_{n,0,0} = \sqrt{\frac{1}{2\pi R}}\,\frac{1}{r}\sin\left(\pi\frac{r}{R}\right). \tag{2.3.9}$$

For an arbitrary integer n, the state $\psi^{\text{cube}}_{n,n,n}$ has the same energy $E^{\text{cube}}_{n,n,n} = E^{\text{sphr}}_{n,0}$ as the spherical s-state $\psi^{\text{sphr}}_{n,0}$. For this reason, the states $\psi^{\text{cube}}_{n,n,n}$ are referred to as the s-like states of a cube. The whole s-like spectrum of a cube of length L is exactly reproduced by the s-waves of a sphere of radius $R = L/\sqrt{3}$.

The lowest p-like states of $\psi^{\text{cube}}_{n_x,n_y,n_z}$ correspond to the case where $(n_x, n_y, n_z) = (2,1,1)$ and the other two permutations. Their eigen energy is $E^{\text{cube}}_{n_x,n_y,n_z} = \frac{\pi^2\hbar^2}{2m^*}\frac{2}{R^2}$ assuming that $L = \sqrt{3}R$. On the other hand, the lowest spherical p-wave $\psi^{\text{sphr}}_{1,1,m}$ has $z_{1,1} = 4.493$ and $E^{\text{sphr}}_{1,0} = \frac{\pi^2\hbar^2}{2m^*}\frac{2.0458}{R^2}$. The relative error $|E^{\text{cube}}_{2,1,1} - E^{\text{sphr}}_{1,0}|/E^{\text{cube}}_{2,1,1}$ is about 2.3%. The three permutations of $(2,1,1)$ mean that the degeneracy of the lowest p-like states of a cube is equal to 3, which reproduces that of the spherical p-waves.

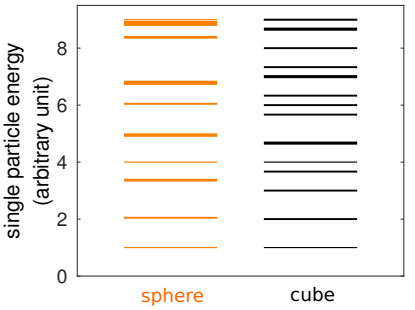

Figure 2.3.1: The single-particle energy spectra of a particle confined in V_{conf} (Eq. (2.3.1)) and in $V_{\text{conf}}^{\text{cube}}$ (Eq. (2.3.6)). The thickness of the lines represents the degeneracy of the energy levels. The two lowest spherical states are the s-wave and p-wave of principle quantum number $n = 1$. The s-like and p-like spectra, for many n, of a cube are approximately reproduced by the correponding ones of a sphere.

When going into the higher energy states, i.e. larger l and n, the spectra start to show more significant differences. Despite this fact, there remains some correspondence between the eigen states of the cubic and spherical confining potentials. The cubic states $\psi^{\text{cube}}_{n_x,n_y,n_z}$ can be thought of as being split from the spherical states due to the former having a (much) smaller symmetry group than the latter.

Nonetheless, the above observations show that the use of V_{conf} in (2.3.1) still serves as a good approximation for the purpose of understanding the electronic and optical properties of the lowest exciton state. For instance, the overlap integral between the wave functions $\psi^{\text{sphr}}_{1,0,0}$ in (2.3.9) and $\psi^{\text{cube}}_{1,1,1}$ in (2.3.7) is equal to 0.98727. From this high degree of overlapping, we expect the Coulomb interaction in a cube to be within a few percent error compared to the equivalent sphere, Eq. (2.3.5). For a more detailed calculation of the Coulomb interaction for a cube and a sphere, see Ref. [89].

In the calculation of the correlation energy, we need the whole basis set of $\{\psi^{\text{sphr}}_{n,l,m}\}$ of a sphere, (or $\{\psi^{\text{cube}}_{n_x,n_y,n_z}\}$ for a cube), up to some cut-offs $l_{\text{cut-off}}$ for the orbital angular momentum and $n_{\text{cut-off}}$ for the principal quantum number. The computation, in Chapter 4 for example, converges rapidly w.r.t. $n_{\text{cut-off}}$. By setting $n_{\text{cut-off}} = 3$, we capture about 98% of the total correlation energy compared to using $n_{\text{cut-off}} = 9$ (with $l_{\text{cut-off}} = 10$). When $l_{\text{cut-off}} = 1$ and $n_{\text{cut-off}} = 2$, about 80% of the total correlation energy is obtained. This means that the two lowest p-waves dominate the contribution to the total correlation energy. As established above, the energy levels of these spherical p-waves are within an error of a few percent from those of the equivalent p-like states of a cubic potential.

When the external potential V_{ext} deviates from a spherical one, let us define the nonspherical potential V_{nsph} to be

$$V_{\text{nsph}} = V_{\text{ext}} - V_{\text{conf}}, \tag{2.3.10}$$

see (2.3.1) for the definition of V_{conf}. In general, V_{nsph} can be treated as a perturbation in the calculation procedure at a later stage if the nonspherical effect may turn out to be important in some way. The spherical basis, see Eq. (4.1.3) for more details, combining with the angular algebra offers a computationally efficient method for treating the nonspherical perturbations. For many physical quantities of interest in the current thesis, the contribution from V_{nsph} is rather small numerically and we shall omit this term for simplicity.

In conclusion, the spherical potential V_{conf} is expected to provide an adequate approximation to describe a cubic nanocrystal of length $L = \sqrt{3}R$. The advantage of using spherical symmetry over cubic symmetry is the reduction of dimensionality. A three-dimensional problem becomes a radial problem, after performing the angular reduction. This brings about a significant computational speed-up, which shows to be extremely useful in the calculations of correlation energy in Chapter 4 and of the electron-photon matrix elements in Chapter 5. With this in mind, we move on to derive the radial Hartree-Fock equations in Chapter 3.

Chapter 3

Hartree-Fock approximation

The previous chapter was concerned with the description of the non-interacting single-particle states in the semiconducting ground state of a nanocrystal. After an external excitation with an energy exceeding E_{gap}, an excitonic system with N_e electrons and N_h holes is created inside the nanocrystal. The particles will be assumed to have relaxed to the lowest occupied states. Using the Hartree-Fock (HF) formulation [75, 96], we aim at understanding the intercarrier interaction in a mean-field approximation in this case.

In the first two sections, we discuss the origin of the HF approximation of the electron-hole system and the dielectric screening of the Coulomb interaction as well as the surface polarization charge. In Section 3.3, the radial HF equations will be derived while, at the same time, one defines the various contributions to the HF energy. Section 3.4 is devoted to calculations of the single exciton binding energy, which comes after a rather careful survey of the fundamental parameters of perovskite materials.

Regarding the notations, $|a\rangle,\ |b\rangle, \dots$ denote the occupied states of the excitonic system, with their total angular momenta and magnetic quantum numbers $(F_a, M_a),\ (F_b, M_b), \dots$ The Greek letters $\alpha,\ \beta, \dots$ represent the $\mathrm{k}\cdot\mathrm{p}$ components of their total wave functions. The capital letters $A, B, \dots$ label the shells (with $F_a,\ F_b, \dots$) containing the states $|a\rangle,\ |b\rangle, \dots$ The words 'shell' and 'level' (or 'energy level') will be used interchangeably. Given an integer or a half-integer f, the shorthand symbol $[f]$ stands for $2f + 1$.

3.1 Hartree-Fock approximation

Consider a system with N_e electrons and N_h holes. It is important for the readers to keep in mind the two parallel-running points of view, which we shall now explain. On the one hand, we may think of electrons and holes as belonging to separate species of particles with different effective masses and opposite charges. This point of view offers the ease of visualizing the interaction between these charge carriers. We call it the viewpoint no. 1. On the other hand, a hole is effectively the absence of an electron in a valence state (in the case of a semiconductor). A system with 'N_e electrons and N_h holes', in fact, contains N_e electrons above the VBM and $N_v = N_0 - N_h$ electrons deeper in the valence bands. Consequently, the creation

and annihilation operators of an electron and a hole must anti-commute. Let us call this the viewpoint no. 2.

As an approximation from the viewpoint no. 1, an electron orbital (occupied or virtual) experiences a mean-field potential U created by all the occupied electrons and holes. The general matrix element $\langle i|U|j\rangle$ of U, between two arbitrary electron states $|i\rangle$ and $|j\rangle$, can be written as

$$\langle i|U|j\rangle = \sum_c \langle i|U^c|j\rangle - \sum_v \langle i|U^v|j\rangle, \tag{3.1.1}$$

where the sums $\sum_c$ and $\sum_v$ are over N_e electrons and N_h holes respectively. In the HF approximation, the various terms in (3.1.1) take the following expression

$$\langle i|U^a|j\rangle = \langle ia|G_{12}|ja\rangle - \langle ia|G_{12}|aj\rangle, \tag{3.1.2}$$

where U^a is the contribution to the HF potential due to an occupied state $|a\rangle$ in which a can denote either an electron or a hole state. The first term $\langle ia|G_{12}|ja\rangle$, called the *direct potential*, embodies the classical charge density interaction. The second term in (3.1.2) is the *exchange potential* coming from the Slater determinant of the many-particle fermionic wave function [96].

Let $N = N_v + N_e$ be the total number of electrons in the system, including the conduction and valence bands. Similar to the formula (2.1.1), the total Hamiltonian describing a system of N electrons can be written as

$$H^N_{\rm tot} = \underbrace{-\frac{1}{2}\sum_i^N \nabla_i^2}_{H^N_{\rm kin}} + \sum_i^N V_{\rm ion}(\vec{r}_i) + \underbrace{\sum_{\langle i,j\rangle}^N G(\vec{r}_i,\vec{r}_j)}_{V^N_{\rm Coul}}. \tag{3.1.3}$$

We define $U^N_{\rm HF}$ to be the HF approximation to the Coulomb interaction $V^N_{\rm Coul}$ between the N_e electrons in the CB and N_v electrons in the VB. Analogous to $U^{N_0}_{\rm HF}$ in (2.1.3), the matrix element $\langle i|U^N_{\rm HF}|j\rangle$ can be given as

$$\langle i|U^N_{\rm HF}|j\rangle = \sum_{a=1}^{N_e}\langle i|U^a|j\rangle + \sum_{a=1}^{N_v}\langle i|U^a|j\rangle, \tag{3.1.4}$$

where $\langle i|U^a|j\rangle$ that is defined in (3.1.2) describes the HF potential U^a generated by an occupied state $|a\rangle$.

As an approximation to the Hamiltonian $H^N_{\rm tot}$ (3.1.3), we construct the following Hamiltonian at the HF level

$$\begin{aligned} H^N_{\rm HF} &= H^N_{\rm kin} + \sum_i^N V_{\rm ion}(\vec{r}_i) + U^N_{\rm HF} \\ &= H^N_{\rm kin} + \sum_i^N V_{\rm ion}(\vec{r}_i) + U^{N_0}_{\rm HF} + U, \end{aligned} \tag{3.1.5}$$

where the difference $U^N_{\rm HF} - U^{N_0}_{\rm HF}$ between the HF approximations in Eqs. (3.1.4) and (2.1.3) is precisely the HF potential U as defined in (3.1.1) and (3.1.2). We recover

the fact that U is the HF approximation to the effective Coulomb interaction for the N_e electrons and N_h holes system.

Apart from the correction U, the one-body term for the kinetic energy plus interaction with the ionic background will be modelled by using the $\mathrm{k}\cdot\mathrm{p}$ theory in envelope function approximation. The total energy $E_{\mathrm{tot}}^{N_0}$ of the N_0-electron ground state is usually taken to be zero though one can choose another conventional value for convenience. The difference between the expectation value of $(H_{\mathrm{HF}}^{N} - U)$ of the N_e conduction and N_v valence electron system and $E_{\mathrm{tot}}^{N_0}$ is the total kinetic energy of the N_e electrons and N_h holes.

Let us define the HF approximation to the Hamiltonian (2.1.1) to be

$$H_{\mathrm{HF}}^{N_0} = H_{\mathrm{kin}}^{N_0} + \sum_{i}^{N_0} V_{\mathrm{ion}}(\vec{r}_i) + U_{\mathrm{HF}}^{N_0}. \tag{3.1.6}$$

Generally, it is necessary to use other approximations that go beyond mean-field level and contain the correlation effects from the Coulomb interaction $V_{\mathrm{Coul}}^{N_0}$, see more the discussion at the beginning of Chapter 2. By using Σ^{N_0} (GW method) instead of $U_{\mathrm{HF}}^{N_0}$, for instance as in Ref. [122], we get the $\mathrm{k}\cdot\mathrm{p}$ Hamiltonian $H_{\mathrm{k\cdot p}}$ that describes the kinetic energy of the N_e electron and N_h holes system with the correct effective masses [84]. From the point of view of correlation, the potential U in (3.1.1) is the lowest-order (Hartree-Fock) approximation to the correlated effective Coulomb potential between the electrons and the holes.

We claim that one can obtain from U the binding energy of the excitonic system. As an example, we look at the case of a single exciton, in which the electron occupies the conduction state $|c\rangle$ while the hole stays in the valence state $|v\rangle$. Explicitly, the potential U, see Eq. (3.1.1), becomes

$$\langle i|U|j\rangle = \langle i|U^c|j\rangle - \langle i|U^v|j\rangle, \tag{3.1.7}$$

which implies the HF Coulomb potential felt by the electron and the hole are, respectively,

$$\begin{cases} \langle c|U|c\rangle = -\langle c|U^v|c\rangle, \\ \langle v|U|v\rangle = +\langle v|U^c|v\rangle. \end{cases} \tag{3.1.8}$$

One retrieves the attractive interaction that gives rise to the exciton binding energy. We remark here that the hole energy spectrum is a reverse of that of an electron. (In the electron description, the curvature of the VBM is negative and the effective kinetic energy of a valence electron is negative.) Therefore, the 'positive' sign of $+\langle v|U^c|v\rangle$, in actuality, signifies a 'negative' binding energy for the hole.

However, the potential U in (3.1.1) is not spherically symmetric. In principle, the matrix element $\langle i|U|j\rangle$ depends on the magnetic substates of the shells containing $|i\rangle$ and $|j\rangle$. In the systems with existing spherical symmetry such as spherical nanocrystals, constructing a spherical HF (or mean-field) potential that still captures the basic physics proves to be useful. Not only that one obtains an elegant classification of the quantum states with the help of the angular algebra [37, 75], the computational efficiency also improves owing to transforming from the full three-dimensional to a radial problem.

The *configuration-averaged* HF potential $V_{\rm HF}$, which is spherically symmetric, can be defined here by its action on the state $|j\rangle$ as follows

$$\langle j|V_{\rm HF}|j\rangle = \sum_C w_C \langle j|U^c|j\rangle - \sum_V w_V \langle j|U^v|j\rangle, \tag{3.1.9}$$

where the sum $\sum_C$ (or $\sum_V$) means summing over all of the magnetic substates $|F_c M_c\rangle$ (or $|F_v M_v\rangle$) in all fully or partially occupied electron (or hole) levels with the total angular momentum F_c (or F_v).

The *configuration-averaged* weight factor w_A in (3.1.9) for an occupied shell A can be given as

$$w_A = \begin{cases} \frac{n_A}{N_A}, & \text{if } j \notin A, \\ \frac{n_A - 1}{N_A - 1}, & \text{if } j \in A. \end{cases} \tag{3.1.10}$$

In the above, n_A is the actual occupation of shell A (i.e. the number of particles in shell A) whereas N_A denotes the maximum occupation (or the degeneracy) of A. If the level A is fully occupied with all magnetic substates filled, $w_A = 1$ always. Interested readers can find out the argument leading to w_A in (3.1.10) from Chapter 6 of Ref. [75].

3.2 Coulomb interaction: Dielectric screening

Similar to the computation of the electronic band structure, one can from first-principle calculate the dielectric function $\varepsilon(\vec{r}, \omega)$ using linear response theory. The details of such computation go beyond the scope of the current study. For further references, please see Ref. [31].

For the current thesis, we assume that each nanocrystal is a sphere with a dielectric constant $\varepsilon_{\rm in}$ submerged in an outside medium of dielectric constant $\varepsilon_{\rm out}$. The dielectric constant $\varepsilon_{\rm in}$ is taken to be the dielectric constant in the bulk that can be derived from the measured reduced mass and the bulk exciton binding energy by using a hydrogen-like model for the exciton in 3D crystals [132, 53, 84]. This value of $\varepsilon_{\rm in}$ is called the *effective* dielectric constant $\varepsilon_{\rm eff}$. The sizes of a typical nanocrystal, for instance of perovskites, are comparable to the length scale of a bulk exciton, which justifies the use of the effective dielectric constant.

For materials with lots of polar bonds like perovskites, the dielectric function $\varepsilon(\vec{r}, \omega)$ is strongly ω-dependent [46]. The high-frequency dielectric constant ε_∞ is the response of the valence electrons to an external field where the relevant energy scale falls in the optical range or higher. In contrast, the static dielectric constant also includes the response of heavy ions and other vibrational modes [9]. Normally, the static $\varepsilon_{\rm static}$ is much bigger than the high-frequency ε_∞ in the ionic materials [104, 83, 74]. The value $\varepsilon_{\rm eff}$ often stays in between ε_∞ and $\varepsilon_{\rm static}$.

In a homogenous medium of dielectric constant $\varepsilon_{\rm eff}$, the screened interaction between two electrons at positions $\vec{r}_1$ and $\vec{r}_2$ is ($q_1 = q_2 = 1$ and $4\pi\varepsilon_0 = 1$ in a.u.)

$$G(\vec{r}_1, \vec{r}_2) = \frac{1}{\varepsilon_{\rm eff}} r_{12}^{-1}, \ r_{12} = |\vec{r}_1 - \vec{r}_2|. \tag{3.2.1}$$

When a spherical nanocrystal lives inside a solvent, the screening of the inter-carrier interaction is further modified. We treat the screening of Coulomb interaction to be that of a dielectric sphere inside a medium of ε_{out}. In Subsection 3.2.1, an explicit formula for this case will be provided. Afterwards, we discuss the self-energy of a particle in an inhomogeneous dielectric medium in Subsection 3.2.2.

3.2.1 Dielectric sphere

The Coulomb interaction in a system with spherical symmetry can be conveniently expressed as a product of angular and radial parts in multipole expansion [62].

Let $G(\vec{r}_1, \vec{r}_2)$ be the screened Coulomb potential between two electrons at $\vec{r}_1$ and $\vec{r}_2$ that are inside a dielectric sphere of ε_{in} surrounded by a solvent with ε_{out}. The multipole expansion of $G(\vec{r}_1, \vec{r}_2)$ is

$$G(\vec{r}_1, \vec{r}_2) = \sum_k \gamma^k(r_1, r_2) \, \frac{4\pi}{[k]} \sum_{m=-k}^{k} Y_m^k(\Omega)^* Y_m^k(\Omega). \tag{3.2.2}$$

In Eq. (3.2.2), when both charges are confined inside the nanocrystal, which means $\max(r_1, r_2) < R$, the radial Green function $\gamma^k(r_1, r_2)$ of the multipole k, sometimes referred to as the k-pole, takes the form

$$\gamma^k(r, r') = \frac{1}{\varepsilon_{\text{in}}} \left[\frac{r_<^k}{r_>^{k+1}} + \frac{(\varepsilon_{\text{in}} - \varepsilon_{\text{out}})(k+1)}{\varepsilon_{\text{in}} k + \varepsilon_{\text{out}}(k+1)} \frac{(rr')^k}{R^{2k+1}} \right], \tag{3.2.3}$$

where $r_< = \min(r, r')$ and $r_> = \max(r, r')$.

The first term on the RHS of (3.2.3) describes the screening in a homogeneous medium of dielectric constant ε_{in}. The second term originates from the interaction with the bound polarization charge induced at the interface between the dielectric sphere and the outside medium. If $\varepsilon_{\text{out}} = \varepsilon_{\text{in}}$, the second term disappears as expected. To calculate many of the interesting excitonic quantities, for example the exciton binding energy or the biexciton and trion shifts, we choose $\varepsilon_{\text{in}} = \varepsilon_{\text{eff}}$ [132, 53, 84].

Following the notations in Chapter 2 of Ref. [75], let us define the $\mathbb{C}$-tensor to be

$$\mathbb{C}_m^k = \sqrt{\frac{4\pi}{[k]}} Y_m^k, \tag{3.2.4}$$

which is a spherical tensor of rank-k. We can rewrite $G(\vec{r}_1, \vec{r}_2)$ in terms of the tensor products of $\mathbb{C}^k$'s.

$$G(\vec{r}_1, \vec{r}_2) \equiv G_{12} = \sum_k \gamma^k(r_1, r_2) \;\; \mathbb{C}^k(1) \cdot \mathbb{C}^k(2). \tag{3.2.5}$$

In the above formula, $\mathbb{C}^k(1)$ and $\mathbb{C}^k(2)$ denote the $\mathbb{C}^k$ spherical tensors acting on the wave functions of the first and second positions respectively. The form of G_{12} in (3.2.5) makes it clear that G_{12} is preserved under spatial rotation and is therefore spherically symmetric.

To compute of the configuration-averaged HF potential $V_{\rm HF}$ in (3.1.9), one needs to derive the general matrix element $\langle ab|G_{12}|cd\rangle$ of the Coulomb interaction. Here, the states $|a\rangle,\ |b\rangle,\ |c\rangle$ and $|d\rangle$ are the n-component $\mathrm{k}\cdot\mathrm{p}$ total wave functions, see formulas (2.2.10), (2.2.11) and (2.2.34),

$$\begin{aligned} |a\rangle &= \sum_{\alpha} \frac{1}{r} R_{a\alpha} |(l_{a\alpha} J_{a\alpha}) F_a M_a\rangle,\ |c\rangle = \sum_{\mu} \frac{1}{r} R_{c\mu} |(l_{c\mu} J_{c\mu}) F_c M_c\rangle, \\ |b\rangle &= \sum_{\beta} \frac{1}{r} R_{b\beta} |(l_{b\beta} J_{b\beta}) F_b M_b\rangle,\quad |d\rangle = \sum_{\nu} \frac{1}{r} R_{d\nu} |(l_{d\nu} J_{d\nu}) F_d M_d\rangle. \end{aligned} \tag{3.2.6}$$

The indices α, β, μ and ν denote the $\mathrm{k}\cdot\mathrm{p}$ components of the total wave functions $|a\rangle, |b\rangle, |c\rangle$ and $|d\rangle$. The expression (3.2.5) for G_{12}, of which $\gamma^k(r_1, r_2)$ is given in (3.2.3), will be used for the derivation of $\langle ab|G_{12}|cd\rangle$ with its radial and angular parts separated.

Let us define the functional $\mathcal{Y}^k[\rho]$ as follows

$$\mathcal{Y}^k[\rho](r) = \int \gamma^k(r, r') \rho(r')\ dr'. \tag{3.2.7}$$

The general Coulomb matrix element $\langle ab|G_{12}|cd\rangle$ can be written as

$$\begin{aligned} \langle ab|G_{12}|cd\rangle = &\sum_{k} \sum_{\alpha\beta,\mu\nu} \int \rho_{a\alpha,c\mu}(r)\ \mathcal{Y}^k[\rho_{b\beta,d\nu}](r)\ dr\ \times \\ &\langle (l_{a\alpha} J_{a\alpha}) F_a M_a; (l_{b\beta} J_{b\beta}) F_b M_b | \mathbb{C}^k(1) \cdot \mathbb{C}^k(2) | (l_{c\mu} J_{c\mu}) F_c M_c; (l_{d\nu} J_{d\nu}) F_d M_d\rangle, \end{aligned} \tag{3.2.8}$$

where the cross-densities are $\rho_{a\alpha,c\mu}(r) = R_{a\alpha}(r) R_{c\mu}(r)$ and $\rho_{b\beta,d\nu}(r) = R_{b\beta}(r) R_{d\nu}(r)$.

The radial part of $\langle ab|G_{12}|cd\rangle$ on the first line in (3.2.8) is an integral over the radial functions $\rho_{a\alpha,c\mu}(r)$ and $\rho_{b\beta,d\nu}(r)$. The second line contains the angular expression of which an explicit formula will be derived in Subsection 3.3.1.

Generalized Poisson equation:

To have a more realistic description of the dielectric screening, one can start by assuming that the dielectric function $\varepsilon(r)$ takes the bulk value $\varepsilon_{\rm in}$ of the semiconducting material around $r = 0$ (i.e. the center of the sphere) and equals to $\varepsilon_{\rm out}$ of the medium at a position far enough from the nanocrystal, i.e. as $r \to \infty$. At the interface between the nanocrystal and the medium outside, $\varepsilon(r)$ makes a continuous transition from $\varepsilon_{\rm in}$ to $\varepsilon_{\rm out}$.

$$\varepsilon(r) = \varepsilon_{\rm in} + t(r)(\varepsilon_{\rm out} - \varepsilon_{\rm in}), \tag{3.2.9}$$

where $t(r)$ is a smoothly varying function such that $t(r = 0) = 0$ and $t(r \gg R) = 1$. The exact functional form of $t(r)$ can be also chosen to model the situations in which there are more than two dielectric media.

In (3.2.9), $\varepsilon(r)$ depends only on the radial position r and the dielectric function still possesses the full rotational symmetry. Therefore, the expression (3.2.5) for G_{12} remains valid, except that $\gamma^k(r_1, r_2)$ should be now solved for by using the following generalized Poisson equation

$$\nabla \cdot (\varepsilon(r)\ \nabla V(\vec{r})) = -4\pi\rho(\vec{r}). \tag{3.2.10}$$

In the above, $\rho(r)$ is the density of some free charge, for instance from the charge carriers.

For a more general dielectric medium, the function $\mathcal{Y}^k[\rho_{b\beta,d\nu}](r)$, which was defined in (3.2.7) for the case of a single dielectric sphere, can be obtained from solving the equation (3.2.10) with $\rho(r) = \rho_{b\beta,d\nu}(r)$. In this way, we can also treat the problem of a nanocrystal having a semiconducting core coated with various shells. The $\mathrm{k}\cdot\mathrm{p}$ formulation for a core-shell system [17, 18] and the derivation of the radial equations for the generalized Poisson equation will be the subject for future publications.

3.2.2 Self-energy

Given a free charge distribution $\rho(\vec{r})$, there is an energy cost that one needs to pay to assemble $\rho(\vec{r})$. Let us consider a charge particle occupying the quantum state $|a\rangle$. The aforementioned energy cost is $\frac{1}{2}\langle aa|G_{12}|aa\rangle$.

All the indices α, β, μ and ν in (3.2.11)-(3.2.15) refer to the $\mathrm{k}\cdot\mathrm{p}$ components of $|a\rangle$. In an homogenous medium with dielectric constant $\varepsilon_{\mathrm{in}}$, the energy for creating a charge occupying $|a\rangle$ is

$$\begin{aligned}\langle a|V_{\mathrm{self}}^{\mathrm{hom}}|a\rangle = \frac{1}{2}\sum_k \sum_{\alpha\beta,\mu\nu} \int \rho_{\alpha,\mu}(r)\ \mathcal{Y}_0^k[\rho_{\beta,\nu}](r)\ dr\ \times \\ \langle (l_\alpha J_\alpha)F_a M_a; (l_\beta J_\beta)F_a M_a|\mathbb{C}^k(1)\cdot\mathbb{C}^k(2)|(l_\mu J_\mu)F_a M_a; (l_\nu J_\nu)F_d M_d\rangle,\end{aligned} \tag{3.2.11}$$

where $\rho_{\alpha,\mu}(r) = R_{a\alpha}(r)R_{a\mu}(r)$ and $\rho_{\beta,\nu} = R_{a\beta}(r)R_{a\nu}(r)$. The subscript a has been omitted for notational simplicity since only one total wave function $|a\rangle$ is involved in this subsection.

We define $\mathcal{Y}_0^k[\rho](r)$ for the homogenous medium as

$$\mathcal{Y}_0^k[\rho](r) = \int \frac{1}{\varepsilon_{\mathrm{in}}} \frac{r_<^k}{r_>^{k+1}} \rho(r')\ dr'. \tag{3.2.12}$$

In the case of a dielectric sphere $\varepsilon_{\mathrm{in}}$ submerged in an external medium $\varepsilon_{\mathrm{out}}$, the energy cost becomes

$$\begin{aligned}\langle a|V_{\mathrm{self}}^{\mathrm{het}}|a\rangle = \frac{1}{2}\sum_k \sum_{\alpha\beta,\mu\nu} \int \rho_{\alpha,\mu}(r)\ \mathcal{Y}^k[\rho_{\beta,\nu}](r)\ dr\ \times \\ \langle (l_\alpha J_\alpha)F_a M_a; (l_\beta J_\beta)F_a M_a|\mathbb{C}^k(1)\cdot\mathbb{C}^k(2)|(l_\mu J_\mu)F_a M_a; (l_\nu J_\nu)F_d M_d\rangle.\end{aligned} \tag{3.2.13}$$

The definition of the radial function $\mathcal{Y}^k[\rho](r)$ can be found in (3.2.7).

As can be seen from (3.2.11) and (3.2.13), $\langle a|V_{\mathrm{self}}^{\mathrm{hom}}|a\rangle$ and $\langle a|V_{\mathrm{self}}^{\mathrm{het}}|a\rangle$ have the same angular structure and differ only in their radial parts. The difference $\mathcal{Y}^k[\rho_{a\beta,a\nu}](r) - \mathcal{Y}_0^k[\rho_{a\beta,a\nu}](r)$ represents the interaction between the charged particle in $|a\rangle$ and the boundary charge at the interface between the dielectric sphere and its outer medium. This boundary charge, associated with the particle in $|a\rangle$, results from the surface polarization that was created due to the inhomogeneity of the entire medium.

Define the potential V_{self} to be such that

$$\langle a|V_{\text{self}}|a\rangle = \langle a|V_{\text{self}}^{\text{het}}|a\rangle - \langle a|V_{\text{self}}^{\text{hom}}|a\rangle. \tag{3.2.14}$$

Note that $\langle a|V_{\text{self}}^{\text{hom}}|a\rangle$ is just a constant amount of energy added in the case of a homogeneous medium. This energy is also present in $\langle a|V_{\text{self}}^{\text{het}}|a\rangle$ as a result of the first term in (3.2.3). Only the energy difference $\langle a|V_{\text{self}}|a\rangle$ has some physical importance. It describes the interaction between a particle and its induced boundary charge. For this reason, $\langle a|V_{\text{self}}|a\rangle$ is called the '*self-energy*' of the particle occupying a quantum state $|a\rangle$ [32, 9].

By using the radial-angular forms of $\langle a|V_{\text{self}}^{\text{het}}|a\rangle$ (Eq. (3.2.13)) and $\langle a|V_{\text{self}}^{\text{hom}}|a\rangle$ (Eq. (3.2.11)), one gets

$$\begin{aligned}\langle a|V_{\text{self}}|a\rangle = \frac{1}{2}\sum_k \sum_{\alpha\beta,\mu\nu} \int \rho_{\alpha,\mu}(r)\left(\mathcal{Y}^k[\rho_{\beta,\nu}](r) - \mathcal{Y}_0^k[\rho_{\beta,\nu}](r)\right) dr \times \\ \langle (l_\alpha J_\alpha)F_a M_a; (l_\beta J_\beta)F_a M_a|\mathbb{C}^k(1)\cdot\mathbb{C}^k(2)|(l_\mu J_\mu)F_a M_a; (l_\nu J_\nu)F_d M_d\rangle.\end{aligned} \tag{3.2.15}$$

Regarding the case of a single dielectric sphere, the Coulomb Green function (3.2.3) describes the screening due to the dielectric constant ε_{in} as well as the interaction with the image charges, see Ref. [62]. Without spilling out of the wave functions, i.e. when the confinement is as given in (2.3.1), $\langle a|V_{\text{self}}|a\rangle$ can be viewed as the interaction between the free charge in $|a\rangle$ and its own image charge. The self-energy term V_{self} is nonzero even for a single electron or hole and, thus, is a one-body potential, contrary to the two-body term (3.2.8) that exists only when at least two particles are present.

By using the final expression (3.2.15), it is possible to study a more general case than the infinite spherical well (2.3.1), for instance a core-shell system with potentially multi-shells or a potential barrier of finite height and width. In these cases, one can obtain the function $\mathcal{Y}^k$ by solving the generalized Poisson equation (3.2.10) whereas the 'homogeneous' counterpart $\mathcal{Y}_0^k$ is an analogue of $\mathcal{Y}^k$ for the following equation

$$\varepsilon(r)\ \nabla^2 V_0(\vec{r}) = -4\pi\rho(\vec{r}). \tag{3.2.16}$$

Due to the level of details involved, we leave this generalization to future publications.

As a summary of the Hartree-Fock formulation, there are two modifications to the non-interacting single-particle equation, see Eqs. (2.2.13) and (4.1.2). The first one arises as a result of the screened intercarrier interaction that is the two-body Coulomb potential (3.2.8). The second modification originates from the one-body self-energy potential that captures the interaction between a confined charge and its induced surface charge at the interface between the nanocrystal and the exterior medium.

3.3 Radial Hartree-Fock equations

To take full advantage of the spherical symmetry imposed earlier in Chapter 2, we also need to express the configuration-averaged HF interaction V_{HF} (3.1.9) as a

product of radial and angular parts. In Subsection 3.3.1, we lay down the derivation for the general Coulomb matrix element $\langle ab|G_{12}|cd\rangle$, which will accomplish at the same time the evaluation of the angular parts of (3.2.8) and (3.2.15). One will come to the explicit radial expressions for the HF equations towards the end of this section.

3.3.1 Angular reduction for a general Coulomb matrix element

Given two spherical tensors $\mathbb{C}^k(1)$ and $\mathbb{C}^k(2)$, we recall the following relation between the dot product and the addition into the scalar tensor $\left\{\mathbb{C}_1^k\mathbb{C}_2^k\right\}_0^0$,

$$\mathbb{C}^k(1)\cdot\mathbb{C}^k(2) = (-1)^k\sqrt{[k]}\ \left\{\mathbb{C}_1^k\mathbb{C}_2^k\right\}_0^0. \tag{3.3.1}$$

The general Coulomb matrix element $\langle ab|G_{12}|cd\rangle$ in (3.2.8) can be rewritten as

$$\begin{aligned}\langle ab|G_{12}|cd\rangle = &\sum_k \sum_{\alpha,\beta,\mu,\nu} (-1)^k\sqrt{[k]}\times R^k(a\alpha\ b\beta, c\mu\ d\nu)\times \\ &\langle (l_{a\alpha}J_{a\alpha})F_aM_a, (l_{b\beta}J_{b\beta})F_bM_b|\left\{\mathbb{C}_1^k\mathbb{C}_2^k\right\}_0^0|(l_{c\mu}J_{c\mu})F_cM_c, (l_{d\nu}J_{d\nu})F_dM_d\rangle,\end{aligned} \tag{3.3.2}$$

where we have introduced the shorthand notation $R^k(a\alpha\ b\beta, c\mu\ d\nu)$ for the radial integral

$$R^k(a\alpha\ b\beta, c\mu\ d\nu) = \int \rho_{a\alpha,c\mu}(r)\ \mathcal{Y}^k[\rho_{b\beta,d\nu}](r)\ dr. \tag{3.3.3}$$

With $\mathcal{Y}^k[\rho_{b\beta,d\nu}](r)$ as given in (3.2.7), the radial integral $R^k(a\alpha\ b\beta, c\mu\ d\nu)$ can be easily calculated. We remind the readers that the spherical tensor $\mathbb{C}^k(1)$ or $\mathbb{C}^k(2)$ individually acts on the pairs of the orbital angular momenta $(l_{a\alpha},\ l_{c\mu})$ and $(l_{b\beta},\ l_{d\nu})$ respectively. There remains the angular part (on the second line) of (3.3.2) to be evaluated.

Consider the matrix element $\langle (l_{a\alpha}J_{a\alpha})F_aM_a|\mathbb{C}_m^k|(l_{c\mu}J_{c\mu})F_cM_c\rangle$, where it is implicitly understood that $\mathbb{C}_m^k \equiv \mathbb{C}_m^k(1)$. The tensor $\mathbb{C}_m^k$ operators on the total angular momenta F_a and F_c via its action on $l_{a\alpha}$ and $l_{c\mu}$. Hence, we can use the results of Section B.3 in the appendix and arrive at

$$\langle (l_{a\alpha}J_{a\alpha})F_aM_a|\mathbb{C}_m^k|(l_{c\mu}J_{c\mu})F_cM_c\rangle = \langle F_a||\mathbb{C}^k||F_c\rangle \times$$

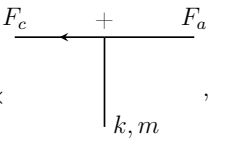

, (3.3.4)

where $\langle F_a||\mathbb{C}^k||F_c\rangle$ on the RHS is the reduced-matrix element of $\mathbb{C}^k$. In fact, one can obtain Eq. (3.3.4) as a direct application of Wigner-Eckart Theorem, see Chapter 3 of Ref. [75]. As a direct application of (B.3.2)-(B.3.3), one has

$$\langle F_a||\mathbb{C}^k||F_c\rangle = \delta_{J_{a\alpha}J_{c\mu}}(-1)^{l_{a\alpha}+J_{a\alpha}+F_c+k}\sqrt{[F_a][F_c]}\begin{Bmatrix} k & F_a & F_c \\ J_{a\alpha} & l_{c\mu} & l_{a\alpha}\end{Bmatrix}\langle l_{a\alpha}||\mathbb{C}^k||l_{c\mu}\rangle. \tag{3.3.5}$$

The explicit expression for the reduced-matrix element $\langle l_{a\alpha}||\mathbb{C}^k||l_{c\mu}\rangle$ between the orbital angular momenta can be found at the end of Chapter 2, Ref. [75].

Repeating the same derivation for $\langle(l_{b\beta}J_{b\beta})F_bM_b|\mathbb{C}^k_m|(l_{d\nu}J_{d\nu})F_dM_d\rangle$ and making use of the angular expression for Coulomb matrix element (see Chapter 3, Ref. [75]), the angular part in (3.3.2) becomes

$$\langle(l_{a\alpha}J_{a\alpha})F_aM_a;(l_{b\beta}J_{b\beta})F_bM_b|\left\{\mathbb{C}^k_1\mathbb{C}^k_2\right\}^0_0|(l_{c\mu}J_{c\mu})F_cM_c;(l_{d\nu}J_{d\nu})F_dM_d\rangle =$$

$$c^k(a\alpha\ b\beta,c\mu\ d\nu)\ \times\frac{1}{\sqrt{[k]}}\times$$

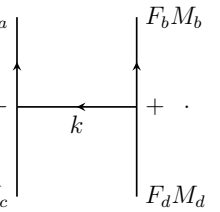

(3.3.6)

The angular coefficient $c^k(a\alpha\ b\beta,c\mu\ d\nu)$ is

$$c^k(a\alpha\ b\beta,c\mu\ d\nu)=\sqrt{[F_a][F_b][F_c][F_d]}\ c^k_\chi(lJ_{a\alpha}F_a;lJ_{c\mu}F_c)\ c^k_\chi(lJ_{b\beta}F_b;lJ_{d\nu}F_d) \quad (3.3.7)$$

where each $c^k_\chi(lJ_lF_l;lJ_rF_r)$ comes from the reduced matrix element $\langle F_l||\mathbb{C}^k||F_r\rangle$ as given in (3.3.5),

$$c^k_\chi(lJ_lF_l;lJ_rF_r)=\delta_{J_l,J_r}(-1)^{l_l+J_l+F_r}\begin{Bmatrix}F_l & F_r & k\\ l_r & l_l & J_l\end{Bmatrix}\langle l_l||\mathbb{C}^k||l_r\rangle. \quad (3.3.8)$$

One notes that k is an integer for the Coulomb multipole. Thus, $(-1)^{2k}=1$ and the $(-1)^k$, which occurs twice in (3.3.7), disappears from the phase factor of the crossed coefficient $c^k_\chi(lJ_lF_l;lJ_rF_r)$ between the left and right states.

As a reminder, the angular momentum $\vec{J}$ is the sum of the Bloch angular momentum $\vec{L}$ and the spin $\vec{S}$. The selection rule δ_{J_l,J_r} in (3.3.8) also means $L_l=L_r$, which is the selection rule of band index resulting from the orthogonality of Bloch functions. Therefore, each δ_{J_l,J_r} in $c^k_\chi(lJ_lF_l;lJ_rF_r)$ implies that (i) $J_l=J_r$ and (ii) the $\mathrm{k}\cdot\mathrm{p}$ components of the left and right wave functions belong to the same band. In other words, it means that, for example, $c^k_\chi(lJ_{a\alpha}F_a;lJ_{c\mu}F_c)$ is non-zero if and only if $\alpha=\mu$.

The coefficient $c^k(a\alpha\ b\beta,c\mu\ d\nu)$ can be factored out from the angular part in (3.3.6) since the H-shape angular diagram is independent of the angular momenta of the $\mathrm{k}\cdot\mathrm{p}$ components. In fact, this H-shape angular diagram is the values of $\langle F_aM_a;F_bM_b|\left\{\mathbb{C}^k_1\mathbb{C}^k_2\right\}^0_0|F_cM_c;F_dM_d\rangle$. For the convenience of later usage, let us define

$$X^k(ab,cd)=(-1)^k\sum_{\alpha\beta,\mu\nu}R^k(a\alpha\ b\beta,c\mu\ d\nu)\times c^k(a\alpha\ b\beta,c\mu\ d\nu). \quad (3.3.9)$$

$X^k(ab,cd)$ can be thought of as the reduced matrix element of the multipole k of the Coulomb matrix element.

Finally, the full Coulomb matrix element (3.3.2) can be compactly written as

$\langle ab|G_{12}|cd\rangle = \sum_k X^k(ab,cd) \times$ 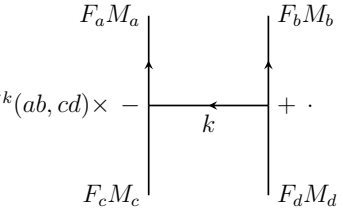

(3.3.10)

Using the expression (3.3.10) for $\langle ab|G_{12}|cd\rangle$, we can now derive the angular reduction for the configuration-averaged HF potential $V_{\rm HF}$ and the self-energy $V_{\rm self}$.

3.3.2 Angular reduction for Hartree-Fock equations

For a particle in $|a\rangle$ (either an electron or a hole) confined in a spherical nanocrystal, its kinetic energy can be described by the $\mathrm{k}\cdot\mathrm{p}$ Hamiltonian $H_{\mathrm{k}\cdot\mathrm{p}}$ together with the confining potential $V_{\rm conf}$ as defined in (2.3.1). The HF Coulomb interaction with other particles is given by the potential $V_{\rm HF}$ (3.1.9). The self-energy $V_{\rm self}$ (due to polarization of the surrounding medium) can be found in (3.2.15).

The Hartree-Fock equation for an *electron* in the occupied orbital $|a\rangle$ is

$$\left(H_{\mathrm{k}\cdot\mathrm{p}} + V_{\rm conf} + V_{\rm HF} + V_{\rm self}\right)|a\rangle = E_a|a\rangle. \tag{3.3.11}$$

Here, the Hamiltonian $H_{\mathrm{k}\cdot\mathrm{p}}$ for an electron equals to $-H_{\mathrm{k}\cdot\mathrm{p}}^{4\times4}$ in (2.2.32) for the 4×4 $\mathrm{k}\cdot\mathrm{p}$ model since those matrices describe the $\mathrm{k}\cdot\mathrm{p}$ Hamiltonian of a hole. (Similarly, $H_{\mathrm{k}\cdot\mathrm{p}} = -H_{\mathrm{k}\cdot\mathrm{p}}^{8\times8}$, formulas (2.2.25) and (2.2.26). For more discussion, see Section 2.2.) The confining potential $V_{\rm conf}$ in (2.3.1) with an infinite barrier implies that the total wave function is zero outside the nanocrystal. For $r < R$, because $V_{\rm conf} = 0$, the contribution to the total energy from $V_{\rm conf}$ is also zero. The numerical effect that the confinement has on the state $|a\rangle$ is really the restriction of the solution on a finite range (i.e. between $r = 0$ and $r = R$). By solving Eq. (3.3.11), we obtain the HF wave function and the HF energy of an electron in $|a\rangle$.

The equation for a hole has the same structure as (3.3.11) except that $H_{\mathrm{k}\cdot\mathrm{p}} = H_{\mathrm{k}\cdot\mathrm{p}}^{8\times8}$ (eight-band $\mathrm{k}\cdot\mathrm{p}$ model) or $H_{\mathrm{k}\cdot\mathrm{p}} = H_{\mathrm{k}\cdot\mathrm{p}}^{4\times4}$ (four-band $\mathrm{k}\cdot\mathrm{p}$ model). Besides, its HF potential receives a minus sign compared to the definition of $V_{\rm HF}$ in (3.1.9). This minus sign results from the hole charge being opposite to an electron charge. One has the following HF equation for a hole in state $|b\rangle$

$$\left(H_{\mathrm{k}\cdot\mathrm{p}} + V_{\rm conf} - V_{\rm HF} + V_{\rm self}\right)|b\rangle = E_b|b\rangle. \tag{3.3.12}$$

From the definitions (3.1.2) and (3.1.9), the direct and exchange contributions to the configuration-averaged HF potential $V_{\rm HF}$ are

$$\langle a|V_{\rm dir}|a\rangle = \sum_C w_C\langle ac|G_{12}|ac\rangle - \sum_V w_V\langle av|G_{12}|av\rangle, \tag{3.3.13}$$

$$\langle a|V_{\rm exc}|a\rangle = -\sum_C w_C\langle ac|G_{12}|ca\rangle + \sum_V w_V\langle av|G_{12}|va\rangle. \tag{3.3.14}$$

An occupied orbital $|a\rangle$ of an electron (or a hole) appears among the conduction (or valence) states $|c\rangle$ (or $|v\rangle$) in the sum $\sum_C$ (or $\sum_V$). When $|c\rangle^* = |a\rangle$ (or $|v\rangle^* = |a\rangle$), there exists a term in $V_{\rm exc}$ that cancels exactly with the corresponding term in $V_{\rm dir}$. Therefore, $\langle a|V_{\rm HF}|a\rangle = \langle a|V_{\rm dir}|a\rangle + \langle a|V_{\rm exc}|a\rangle$ represents only the interaction between a particle $|a\rangle$ and other particles.

Next, we define the non-zero contributions to the HF energy E_a of $|a\rangle$ originating from the various terms on the LHS of (3.3.11).

$$\begin{cases} E_{{\rm kin},a} = \langle a|H_{\rm k\cdot p}|a\rangle, \\ E_{{\rm dir},a} = \langle a|V_{\rm dir}|a\rangle,\ E_{{\rm exc},a} = \langle a|V_{\rm exc}|a\rangle, \\ E_{{\rm self},a} = \langle a|V_{\rm self}|a\rangle, \end{cases} \tag{3.3.15}$$

which means that the HF energy is $E_a = E_{{\rm kin},a} + E_{{\rm dir},a} + E_{{\rm exc},a} + E_{{\rm self},a}$. The term $E_{{\rm kin},a}$ can be understood as the kinetic energy of a confined particle in $V_{\rm conf}$. For an electron, $E_{{\rm kin},a}$ also includes the band gap energy.

One can easily obtain the total HF energy of the N_e electrons and N_h holes to be

$$E_{\rm HF}(N_e, N_h) = \sum_{a=1}^{N_e,N_h} \left(E_{{\rm kin},a} + \frac{1}{2}(E_{{\rm dir},a} + E_{{\rm exc},a}) + E_{{\rm self},a} \right), \tag{3.3.16}$$

where a denotes either an occupied electron or hole. Thus, the sum $\sum_{a=1}^{N_e,N_h}$ runs over all electrons and holes present in the excitonic system. The first term $E_{\rm kin} = \sum_{a=1} E_{{\rm kin},a}$ is the total kinetic energy (including the band gap energy $N_e E_{\rm gap}$). The factor $(\frac{1}{2})$ in front of the direct and exchange energy avoids double counting since the Coulomb interaction should be between the pairs of particles. Roughly speaking,

$$E^{(1)} = \sum_{a=1}^{N_e,N_h} \left(\frac{1}{2}(E_{{\rm dir},a} + E_{{\rm exc},a}) + E_{{\rm self},a} \right) \tag{3.3.17}$$

gives the binding energy at HF level, which is up to the first-order MBPT. In other words, the HF equations provide the first-order MBPT approximation to the true total energy of the system of N_e electrons and N_h holes.

The single-particle HF equation (3.3.11) can be solved by numerical iteration to self-consistency. To start the iteration process, one needs a set $\{|a\rangle^0,\ E_a^0\}$ of approximate wave functions and energy values. The choice of $\{|a\rangle^0,\ E_a^0\}$ has to be close enough to the final HF wave functions and energy values in order to achieve convergence.

In the strong confinement limit, the non-interacting particle equation

$$(H_{\rm k\cdot p} + V_{\rm conf})\,|a\rangle^0 = E_a^0 |a\rangle^0 \tag{3.3.18}$$

serves as a good approximation for obtaining the transition peaks [41]. The solution $\{|a\rangle^0,\ E_a^0\}$ of equation (3.3.18) seems a good practical choice for the starting orbitals and energy levels for the HF iteration since the convergence can be obtained in all cases examined so far.

In going from the strong confinement to the intermediate and eventually weak confinement regime, Coulomb interaction becomes progressively more important.

The non-interacting particle solutions of Eq. (3.3.18) no longer suffice to obtain the binding energy of a single exciton, for instance. Fortunately, the HF energy $E_{\rm HF}$ shows to be a good approximation for the single exciton binding energy for a wide range of experimental sizes, see Subsection 3.4.2. When multi-carriers are present, the HF energy in (3.3.16) has already captured some Physics by accounting for the inter-carrier Coulomb interaction up to first-order MBPT. Furthermore, the HF equation (3.3.11) can be used to generate a basis set for the calculations of the many-body corrections to the energy of the excitonic system. An example of such calculations can be found in the next chapter and serves also as an additional motivation for the HF formulation.

Under the assumption of spherical symmetry, equation (3.3.11) can be reduced from a full three-dimensional to a one-dimensional radial problem. This fact allows a remarkable improvement in the numerical efficiency of solving the HF equation of a system with any practical number of electrons and holes. One can reduce the computational time to not more than a few seconds on one computing core. The computational speed-up shows to be even more advantageous for the MBPT calculations later in Chapter 4 and Chapter 5. It is therefore important to work out the radial HF equations of (3.3.11).

The radial expressions of the $\mathbf{k}\cdot\mathbf{p}$ Hamiltonian have been given in (2.2.25), (2.2.26) and (2.2.32). There remains the task of finding the radial formulas for the direct $V_{\rm dir}$ and exchange $V_{\rm exc}$ potentials as well as the self-energy $V_{\rm self}$. The detailed derivations of equations (3.3.21)–(3.3.22), (3.3.24)–(3.3.26) and (3.3.27)–(3.3.28) are given in Chapter C of the appendix. In what below, we summarize the basic results and provide some physical understanding of the terms that will appear.

Let q_a be the charge of a particle in an occupied orbital $|a\rangle$. We adopt the usual convention where

$$q_a = \begin{cases} -1, & \text{for an electron,} \\ +1, & \text{for a hole.} \end{cases} \tag{3.3.19}$$

Let $V^b_{\rm dir}$ be the configuration-averaged *direct* potential created by a shell B having a total angular momentum F_b. Clearly,

$$\langle a|V_{\rm dir}|a\rangle = \sum_{F_b} q_a \langle a|V^b_{\rm dir}|a\rangle. \tag{3.3.20}$$

For an n-component vector (n=4 or 2), for example radial wave function $|a\rangle$ in (2.2.12), we define the α-component of $|a\rangle$ to be $|a\rangle_\alpha = R_{a\alpha}(r)$. Given an n-component wave function $|a\rangle$, $V^b_{\rm dir}|a\rangle$ is also an n-component vector. The α-component $(V^b_{\rm dir}|a\rangle)_\alpha$ of $V^b_{\rm dir}|a\rangle$ is

$$(V^b_{\rm dir}|a\rangle)_\alpha = \sum_\alpha \mathcal{Y}^0[\rho^d_b](r)\ R_{a\alpha}(r), \tag{3.3.21}$$

where the direct charge density $\rho^d_b(r)$ can be written as

$$\rho^d_b(r) = w_b \times q_b[F_b] \times \sum_\beta R_{b\beta}(r) R_{b\beta}(r)\ . \tag{3.3.22}$$

In fact, $[F_b] = 2F_b+1$ is the total degeneracy of shell B and $q_b[F_b]$ represents the maximum amount of charge that shell B can accommodate. Hence, the prefactor $w_b \times q_b[F_b]$ is the configuration-averaged total charge of an occupied shell B. The product $R_{b\beta}(r)R_{b\beta}(r)$ stands for the charge density created by one of the particles in shell B. The function $\mathcal{Y}^0[\rho_b^d](r)$ symbolizes the monopole Coulomb potential created by the configuration-averaged charge density $\rho_b^d(r)$. The direct interaction $\langle a|V_{\rm dir}^b|a\rangle$ recovers the classical interaction energy between a charge in the quantum state $|a\rangle$ (belonging to shell A) and the charge distribution created by all the occupied orbitals in shell B, after spherically averaging.

Similarly, the configuration-averaged *exchange* potential created by a shell B (with total angular momentum F_b) is $V_{\rm exc}^b$. Again, we have

$$\langle a|V_{\rm exc}|a\rangle = \sum_{F_b} q_a \langle a|V_{\rm exc}^b|a\rangle, \tag{3.3.23}$$

in which $V_{\rm exc}^b|a\rangle = \sum_\alpha (V_{\rm exc}^b|a\rangle)_\alpha$ is an n-component vector with

$$(V_{\rm exc}^b|a\rangle)_\alpha = \sum_\nu [v_X^b]_{\alpha,\nu} R_{a\nu}(r). \tag{3.3.24}$$

One can write the expression on the RHS above explicitly as

$$\sum_\nu [v_X^b]_{\alpha,\nu} R_{a\nu}(r) = (-1)^{F_b-F_a} \sum_k \mathcal{Y}^k[\rho_{ba}^\chi](r) \left(\sum_\mu c_\chi^k(lJ_{a\alpha}F_a; lJ_{b\mu}F_b)\ R_{b\mu}(r) \right). \tag{3.3.25}$$

Here, the cross-density $\rho_{ba}^\chi(r)$ between the two state $|a\rangle$ and $|b\rangle$ takes the following form

$$\rho_{ba}^\chi(r) = w_b \times q_b[F_b] \times \sum_{\beta,\nu} c_\chi^k(lJ_{b\beta}F_b; lJ_{a\nu}F_a)\ R_{b\beta}(r)R_{a\nu}(r). \tag{3.3.26}$$

Just as before, the prefactor $w_b \times q_b[F_b]$ is the configuration-averaged total charge of shell B. The coefficient $c_\chi^k(lJ_{b\beta}F_b; lJ_{a\nu}F_a)$ results from an exchange Coulomb vertex and its expression can be found in (3.3.8).

In (3.3.25), the allowed multipoles k do not need to be the monopole $k = 0$, contrary to the case of direct interaction in which only the monopole term is present. Note also that the direct density $\rho_b^d(r)$ in (3.3.22) contains the overlap of the wave function $|b\rangle$ with itself and is formally on the order $\mathcal{O}((\mathrm{k}\cdot\mathrm{p})^0)$. For a single exciton, the product $R_{b\beta}(r)R_{a\nu}(r)$ contained in the cross-density $\rho_{ba}^\chi(r)$ of the exchange interaction is the overlap between a big and a small component, which is of the order $\mathcal{O}((\mathrm{k}\cdot\mathrm{p})^1)$. The direct interaction is therefore expected to be the main contribution to the single exciton binding energy.

Regarding the self-energy $V_{\rm self}$, one needs to evaluate the angular expression in (3.2.15). This can be done easily by plugging (3.3.6) with $F_b = F_c = F_d = F_a$ into (3.2.15). In general, the value of the H-shape angular diagram in (3.3.6) depends on the magnetic quantum number M_a. To obtain a configuration-averaged *self-energy* potential, one again needs to average over the magnetic substates $|F_aM_a\rangle$, i.e. doing $\frac{1}{[F_a]}\sum_{M_a}$. Interested readers can look up the derivation in the appendix

Chapter C. Here, we quickly quote the final result. The configuration-averaged self-energy potential $V_{\rm self}|a\rangle = \sum_\alpha (V_{\rm self}|a\rangle)_\alpha$ has its α-component to be

$$(V_{\rm self}|a\rangle)_\alpha = \frac{[F_a]}{[k]} \sum_k \left(\mathcal{Y}^k[\rho_a^\chi](r) - \mathcal{Y}_0^k[\rho_a^\chi](r) \right) \left(\sum_\mu c_\chi^k(lJ_{a\alpha}F_a; lJ_{a\mu}F_a)\ R_{a\mu}(r) \right), \tag{3.3.27}$$

where

$$\rho_a^\chi(r) = \sum_{\beta,\nu} c_\chi^k(lJ_{a\beta}F_a; lJ_{a\nu}F_a)\ R_{a\beta}(r) R_{a\nu}(r). \tag{3.3.28}$$

Using the radial potentials above, Eq. (3.3.11) (and also Eq. (3.3.12)) can be solved iteratively to obtain the HF total wave function $|a\rangle$ and energy level E_a for a given occupied state.

3.4 Application to single exciton binding energy

One of the most important applications of the HF formulation is the evaluation of the single exciton binding energy. In this section, we focus on discussing the properties of perovskites, which are the materials of recent intense research [24, 136, 73]. We first will summarize the basic parameters of the k · p model. As it turns out, there is a substantial disagreement between the measured reduced mass and the calculated DFT values [10, 132]. Next, we provide some calculation of the single exciton binding energy $E_{\rm bind}$ for the case of a homogenous medium $\varepsilon_{\rm out} = \varepsilon_{\rm in} = \varepsilon_{\rm eff}$ in Subsection 3.4.2. At HF level, $E_{\rm bind} = E_{\rm HF}$ with $N_e = N_h = 1$. Lastly, we shall discuss the effect of the surface polarization of a single dielectric sphere, in which $\varepsilon_{\rm out}$ differs from $\varepsilon_{\rm in}$ in (3.2.3).

3.4.1 Input parameters for perovskites

Frankly, one of the biggest difficulties working with perovskites is the uncertain nature of many basic parameters, such as the effective masses of electron and hole in the bulk, the exact value of the Kane parameter $E_{\rm p}$ that determines the optical transition strength, etc. Additionally, the 3-D crystal structure [58] and the band gap $E_{\rm gap}$ [110] also show an evident temperature dependence.

The *ab initio* calculation in Ref. [10] of the electronic band structure of $CsPbBr_3$ give $m_e^* = 0.134$ and $m_h^* = 0.128$, which is in close agreement with Ref. [99]. The calculated values of the effective masses, using DFT, generally underestimate the reduced mass μ by a factor of 2 compared to the experimental value [132, 53]. Using magneto-optical measurement at low T [132], the reduced mass μ and the binding energy $E_{\rm bind}$ have been directly measured. From them, the effective dielectric constant $\varepsilon_{\rm eff}$ can be deduced, using the hydrogen model.

As a reminder for perovskites, the VB is an s-like band while the CB is p-like. Due to the spin-orbit coupling, the p-like CB splits into $p_{1/2}$ and $p_{3/2}$ bands, where the latter is higher than the former by $\Delta_{\rm soc} \approx 1$ eV [138]. The momentum operator $\vec{p}$ connects the s-like band to p-like bands via the following matrix elements

$$P = \langle S|p_z|Z\rangle = \langle S|p_x|X\rangle = \langle S|p_y|Y\rangle. \tag{3.4.1}$$

As a result, one expects that both the $p_{1/2}$ and $p_{3/2}$ bands are connected to the $s_{1/2}$ valence band, under the $\mathrm{k}\cdot\mathrm{p}$ perturbation, to a similar extent. It seems likely that they both contribute to the effective mass of $s_{1/2}$ band. The Kane parameter is defined as

$$E_{\mathrm{p}} = 2P^2. \tag{3.4.2}$$

Material (phase)	$\varepsilon_{\mathrm{eff}}$	μ	E_{gap} (eV)	$E_{\mathrm{p}}^{4\times4}$ (eV)	m_h^*	m_e^*
$CsPbBr_3$ (orthorhombic)	7.3	0.126	2.342	27.88	0.337	0.201
$CsPbI_3$ (cubic)	10.0	0.114	1.723	22.67	0.295	0.186
$FAPbBr_3$ (orthorhombic)	8.42	0.115	2.233	29.12	0.299	0.187
$FAPbBr_3$ (tetragonal)	8.6	0.13	2.294	26.47	0.351	0.206
$FAPbI_3$ (orthorhombic)	9.35	0.09	1.501	25.01	0.220	0.153
$FAPbI_3$ (tetragonal)	11.4	0.095	1.521	24.02	0.235	0.160
$MAPbBr_3$ (orthorhombic)	7.5	0.117	2.292	29.38	0.306	0.190
$MAPbI_3$ (orthorhombic)	9.4	0.104	1.652	23.83	0.263	0.172
$MAPbI_3$ (tetragonal)	10.9	0.104	1.608	23.19	0.263	0.172

Table 3.1: The reduced mass μ and the bulk band gap E_{gap} are measured using magneto-optical measurements. The effective dielectric constant $\varepsilon_{\mathrm{eff}}$ is derived from the bulk binding energy [132, 53]. $E_{\mathrm{p}}^{4\times4}$ was estimated from equation (3.4.8), m_e^* and m_h^* estimated from (3.4.4).

From (2.2.32) and the definitions of γ_h and γ_e underneath, we have

$$\begin{aligned} \frac{1}{m_h^*} &= \gamma_h + \frac{1}{3}\frac{E_{\mathrm{p}}}{E_{\mathrm{gap}}} \\ \frac{1}{m_e^*} &= \gamma_e + \frac{1}{3}\frac{E_{\mathrm{p}}}{E_{\mathrm{gap}}} \end{aligned} \tag{3.4.3}$$

To obtain an estimate of E_{p}, we assume that, except $s_{1/2}$ and $p_{1/2}$ bands, the other bands that are further away do not contribute to the effective masses at the band edge. Thus, one has $\gamma_h = -1$ and $\gamma_e = 1$ in (3.4.3). The same approximation was adopted in Ref. [106], which leads to

$$\begin{aligned} \frac{1}{m_h^*} &= -1 + \frac{1}{3}\,\frac{E_{\mathrm{p}}^{4\times4}}{E_{\mathrm{gap}}}, \\ \frac{1}{m_e^*} &= \quad 1 + \frac{1}{3}\,\frac{E_{\mathrm{p}}^{4\times4}}{E_{\mathrm{gap}}}. \end{aligned} \tag{3.4.4}$$

By using the relation between the reduced mass μ and the effective masses m_e^* and m_h^*, where

$$\frac{1}{\mu} = \frac{1}{m_e^*} + \frac{1}{m_h^*}, \tag{3.4.5}$$

we get from (3.4.4) that

$$\frac{1}{\mu} = \frac{2}{3}\frac{E_{\rm p}^{4\times4}}{E_{\rm gap}} \ . \tag{3.4.6}$$

By knowing the measured μ, we can calculate $E_{\rm p}^{4\times4}$, which serves as a point of reference for the true value of $E_{\rm p}$ for various materials, see Table 3.1. m_e^* and m_h^* can be approximated by plugging $E_{\rm p}^{4\times4}$ just obtained to (3.4.4).

However, as argued before, the $p_{3/2}$ band likely contributes to m_e^* of the $s_{1/2}$ band. Again, by neglecting the contribution from the bands other than $s_{1/2}$, $p_{1/2}$ and $p_{3/2}$, one should have $\gamma_h = -1 + \frac{2}{3}\frac{E_{\rm p}^{8\times8}}{E_{\rm gap}+\Delta_{\rm soc}}$. This means that

$$\begin{aligned} \frac{1}{m_h^*} &= -1 + \frac{1}{3}\left(\frac{E_{\rm p}^{8\times8}}{E_{\rm gap}} + \frac{2E_{\rm p}^{8\times8}}{E_{\rm gap}+\Delta_{\rm soc}}\right), \\ \frac{1}{m_e^*} &= \ \ 1 + \frac{1}{3}\ \ \frac{E_{\rm p}^{8\times8}}{E_{\rm gap}}, \end{aligned} \tag{3.4.7}$$

which leads to

$$\frac{1}{\mu} = \frac{2}{3}\left(\frac{E_{\rm p}^{8\times8}}{E_{\rm gap}} + \frac{E_{\rm p}^{8\times8}}{E_{\rm gap}+\Delta_{\rm soc}}\right) \ . \tag{3.4.8}$$

We use the fact that $\Delta_{\rm soc}$ is about 1.0 eV [101, 57] to estimate $E_{\rm p}$ as well as m_e^* and m_h^* from (3.4.7) and (3.4.8). When the spin-orbit coupling is so strong that $\Delta_{\rm soc} \gg E_{\rm gap}$, the expression on the right of (3.4.6) reduces to that of (3.4.8).

The values of $E_{\rm p}^{8\times8}$ (or $E_{\rm p}^{4\times4}$), m_e^* and m_h^* above may be subjected to some further errors when, for instance, there exists a nearby (higher-lying) band that strongly connect to the $s_{1/2}$ or $p_{1/2}$ bands, similar to the situation of PbSe [2].

Undoubtedly, the relations in (3.4.6) and (3.4.8) produce different estimates for $E_{\rm p}$. The value of $E_{\rm p}$ from the same calculations [10] that produces the reduced mass to be half of the experimental μ also differs from these estimations ($E_{\rm p}^8 \times 8$ and $E_{\rm p}^4 \times 4$) using the n $\times$ n k $\cdot$ p models. We are led to the opinion that the actual values of $E_{\rm p}$, m_e^* and m_h^* are uncertain. This motivates one to also check how the relevant physical quantities, for example the single-exciton binding energy $E_{\rm bind}$ and the biexciton/trion shift, depend on the various possible choices for $E_{\rm p}$, m_e^* and m_h^*.

Tables 3.1 and 3.2 summarize the following:

- The experimentally measured parameters that are (a) the crystal structure, (b) the reduced mass μ, (c) the bulk band gap $E_{\rm gap}$ and (d) the effective dielectric constant $\varepsilon_{\rm eff}$.

- The estimated quantities are (i) the Kane parameter, (ii) the electron and hole effective masses m_e^* and m_h^* respectively.

Material (phase)	ε_{eff}	μ	E_{gap} (eV)	$E_{\text{p}}^{8\times8}$(eV)	m_h^*	m_e^*
$CsPbBr_3$ (orthorhombic)	7.3	0.126	2.342	16.39	0.217	0.300
$CsPbI_3$ (cubic)	10.0	0.114	1.723	13.89	0.197	0.271
$FAPbBr_3$ (orthorhombic)	8.42	0.115	2.233	17.23	0.195	0.280
$FAPbBr_3$ (tetragonal)	8.6	0.13	2.294	15.60	0.226	0.306
$FAPbI_3$ (orthorhombic)	9.35	0.09	1.501	15.63	0.151	0.224
$FAPbI_3$ (tetragonal)	11.4	0.095	1.521	14.98	0.160	0.233
$MAPbBr_3$ (orthorhombic)	7.5	0.117	2.292	17.32	0.199	0.284
$MAPbI_3$ (orthorhombic)	9.4	0.104	1.652	14.68	0.177	0.252
$MAPbI_3$ (tetragonal)	10.9	0.104	1.608	14.35	0.177	0.252

Table 3.2: The parameters μ, E_{gap} and ε_{eff} are taken from Ref. [132] and Ref. [53]. $E_{\text{p}}^{8\times8}$ was estimated from equation (3.4.6), m_e^* and m_h^* from (3.4.7).

The parameters (a)–(d) are taken as certain (measured) and have the same values in both tables. The values of the quantities (i)–(ii) depend on the choice of the $\mathrm{k}\cdot\mathrm{p}$ model.

For $CsPbBr_3$, we use two parameter sets listed below (in the 4×4 $\mathrm{k}\cdot\mathrm{p}$ model) for the subsequent calculations in the next subsection as well as in Chapter 4 and Chapter 5.

Parameter set 1:

$$\begin{cases} \varepsilon_{\text{eff}} = 7.3,\ E_{\text{gap}} = 2.342 \text{ eV} \\ m_h^* = m_e^* = 2\mu = 0.252 \\ E_{\text{p}} = 20.00 \text{ eV} \end{cases} \tag{3.4.9}$$

Parameter set 2:

$$\begin{cases} \varepsilon_{\text{eff}} = 7.3,\ E_{\text{gap}} = 2.342 \text{ eV} \\ m_h^* = 0.217,\ m_e^* = 0.300 \\ E_{\text{p}} = E_{\text{p}}^{8\times8} = 16.39 \text{ eV} \end{cases} \tag{3.4.10}$$

For $CsPbI_3$, we use parameter set 3 below, where $m_e^* = m_h^*$. The Kane parameter E_{p} is taken to be 17.0 eV, which is intermediate between $E_{\text{p}}^{8\times8}$ and $E_{\text{p}}^{4\times4}$.

$$\begin{cases} \varepsilon_{\text{eff}} = 10.0,\ E_{\text{gap}} = 1.723 \text{ eV} \\ m_h^* = m_e^* = 2\mu = 0.228 \\ E_{\text{p}} = 17.00 \text{ eV} \end{cases} \tag{3.4.11}$$

In parameter set 1, the values of m_h^* and m_e^* are set to be the same. It has been indicated that m_e^* and m_h^* should be approximately equal [51]. For $CsPbBr_3$, we

compare the calculated binding energy E_{bind}, biexciton and trion shifts for the two parameter sets (3.4.9) and (3.4.10), see Fig. 3.4.5 and Fig. 4.3.8. These results imply that the precise values of m_e^* and m_h^* are not absolutely important to study most quantities of interest within the scope of this thesis.

However, the exact value of E_{p} is crucial for the understanding of the long-range exchange interaction, see Section 4.2, and the electron-photon interband transitions in Chapter 5. Obviously, the interband matrix element (see (5.2.10)–(5.2.12)) is proportional to E_{p}. The long-range exchange interaction relies on the conduction-valence band $\mathrm{k}\cdot\mathrm{p}$ mixing that fundamentally is controlled by E_{p}. In studying these physical quantities, we shall let E_{p} vary in the range $(0, 40)$ eV, where the 'expected maximum' $E_{\text{p}}^{\max} = 40$ eV is the value that the actual E_{p} likely does not exceed. We also take a middle point of this range, for example $E_{\text{p}} = 20$ eV for $CsPbBr_3$, as a 'typical' value of the Kane parameter. This value should be treated as the one that may be close to the actual E_{p}, which can be eventually determined by a first-principle approach or by some measurement.

The problem with the uncertainty of the basic input parameters necessitates the need for a high-quality band-structure calculation, which goes beyond the DFT approach, for instance the relativistic GW method [122], to correctly obtain the individual effective masses of the $s_{1/2}$ and $p_{1/2}$ bands as well as the Kane parameter E_{p}.

3.4.2 Single exciton binding energy

Here, we calculate the HF energy E_{HF} in (3.3.16) for the system with $N_e = N_h = 1$. Two perovskite materials, $CsPbBr_3$ and $CsPbI_3$, will be considered. As discussed before, E_{HF} is the first-order MBPT approximation to the energy of an exciton. The lowest absorption peak of a single exciton, of which the energy approximately equals to the emission energy, is assumed to results from the lowest exciton $1\mathrm{s}^e_{1/2} - 1\mathrm{s}^h_{1/2}$. The calculated E_{HF} versus edge length L can be found in Fig. 3.4.1 for $CsPbBr_3$ and Fig. 3.4.2 for $CsPbI_3$.

We note two basic features in Fig. 3.4.1 and 3.4.2. On the one hand, the theoretical predictions are a bit lower than the experimental PL peaks when $L > 7$ nm, i.e. at the large size end. On the other hand, at small sizes $L < 3$ nm, the HF energy E_{HF} generally overestimates the emission peaks. We propose the following explanations for these discrepancies.

The input parameters listed in Tables 3.2 and 3.1 were all measured at $T = 2K$ [132, 53]. When the temperature rises from cryogenic temperature $T = 2K$ to room temperature $T = 250K$, the bulk band gap increases by about $\Delta E_{\text{gap}} = 60$ meV for $CsPbBr_3$ and $\Delta E_{\text{gap}} = 80$ meV for $CsPbI_3$ [132]. Hence, one expects also that the $1\mathrm{s}^e_{1/2} - 1\mathrm{s}^h_{1/2}$ exciton has higher energy as T increases. Canneson et al., Ref. [20] ($CsPbBr_3$) and Yin et al., Ref. [135] ($CsPbI_3$) conducted their measurements at cryogenic temperature, which explains their reasonable agreement with our theory. The remaining experimental PL peaks in Fig. 3.4.1 and 3.4.2 were measured at room conditions. For these experiments, we assume the energy gap to be $E_{\text{gap}}(250K) = E_{\text{gap}}(2K) + \Delta E_{\text{gap}}$. In Fig. 3.4.3, we show the theoretical $(E_{\text{HF}} - E_{\text{gap}})$ against the experimental excitation energy, which is defined to be the

emission energy minus $E_{\rm gap}(T)$. A marked improvement in the theory-experiment agreement from Fig. 3.4.1 and Fig. 3.4.2.

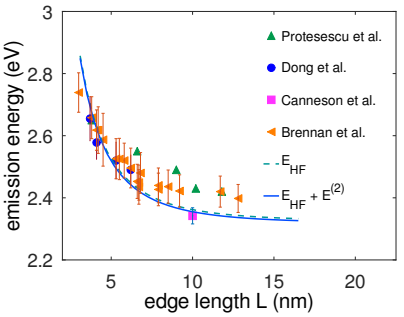

Figure 3.4.1: $CsPbBr_3$, theoretical calculations for $1s^e_{1/2} - 1s^h_{1/2}$ exciton energy and the measured PL peaks versus edge length. Dashed green: HF energy, solid blue line: HF plus second-order MBPT energy. The experimental data are taken from Protesescu et al., Ref. [99]; Dong et al., Ref. [35]; Canneson et al., Ref. [20]; Brennan et al., Ref. [15]

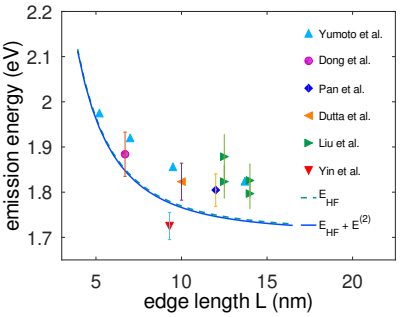

Figure 3.4.2: $CsPbI_3$, theoretical calculations for $1s^e_{1/2} - 1s^h_{1/2}$ exciton energy versus edge length. Dashed green: HF energy, solid blue line: HF plus second-order MBPT energy. The measured PL peaks are taken from Yumoto et al., Ref. [139]; Dong et al., Ref. [35]; Pan et al., Ref. [95]; Dutta et al., Ref. [36]; Liu et al., Ref. [76]; Yin et al., Ref. [135]

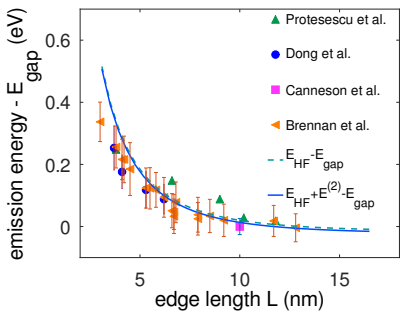

(a) $CsPbBr_3$

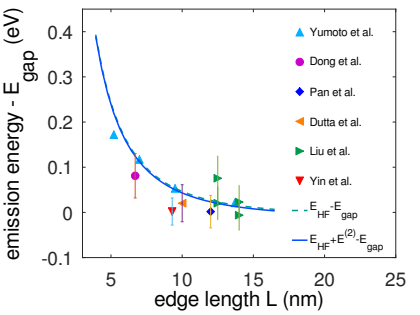

(b) $CsPbI_3$

Figure 3.4.3: The theoretical calculations and the measured excitation energy, which is the emission energy minus $E_{\rm gap}$, versus edge length L. Dashed green: HF energy, solid blue line: HF plus second-order MBPT energy. The exciton was assumed to be in the state $1s^1_{1/2} - 1s^1_{1/2}$. $E_{\rm gap}$ has been adjusted to the experimental temperature.

The adjustment of the T-dependence $E_{\rm gap}$ bridges the gap between the theoretical curves and the experimental data points for $L > 5$ nm. However, the overestimation at small size L, in fact, becomes worse. So far, we have been comparing the theoretical calculations to the experimental PL peaks. A well-known phenomenon,

called the Stokes shift [33, 71], was also observed in perovskite nanocrystals [15]. The first absorption peak has slightly higher energy (blue shift) compared to the PL peak. It remains unclear whether the emission peak or the first absorption peak is better at reflecting $1s^e_{1/2} - 1s^h_{1/2}$ single exciton energy. However, the comparison in Fig. 3.4.3 is purely due to the more abundant published experimental data on photoluminescence. Brennan et al. [15] shows a strong size-dependent Stokes shift in $CsPbBr_3$, where the shift is larger for a smaller nanocrystal. The Stokes shift ranges from $20 - 35$ meV for the biggest nanocrystals $L = 11.7 - 12.8$ nm to approximately 100 meV for the smallest sizes $L \sim 3.0 - 3.8$ nm.

In addition to the Stokes shift, one can identify two other factors that affects the theoretical calculations at small L. First, when one uses a more realistic confining potential with a finite barrier, the fermionic wave function will spill out of the nanocrystal into the external medium. This has an effect on reducing the particle energy, which is more noticeable for smaller sizes due to their higher excitation energies. Second, there may be some variation of ε_{eff} on the nanocrystal size [67], where the effective dielectric constant seems to decrease for a more strongly confined system. The calculation of how ε_{eff} potentially varies w.r.t. the size L requires careful theoretical investigation. These issues lie beyond the scope of the current thesis. We leave them as subjects for future studies.

Having discussed the issues with T-dependent E_{gap}, the Stokes shift as well as some possible dependence of ε_{eff} on the nanocrystal size L, we conclude that the HF-level calculations for the $1s^e_{1/2} - 1s^h_{1/2}$ exciton energies versus L are in reasonable agreement with the experimental data. This implies that Hartree-Fock energy works well for predicting E_{bind} of the lowest exciton state up to about 12.5 nm. In the strong to intermediate confinement regime, the second-order MBPT correction $E^{(2)}$ is relatively unimportant for the binding energy compared to the first-order energy $E^{(1)}$, as shown in Fig. 3.4.4. (See the next chapter for the detailed formalism.) For $L \lesssim 4.5$ nm, $E^{(2)}$ contribution is at most 6% of $E^{(1)}$. Up to $L \lesssim 9.0$ nm, the ratio $E^{(2)}/E^{(1)}$ between the second-order and first-order Coulomb energy is less than 10%, which indicates a still modest contribution to the total single exciton binding.

However, as one enters the weak confinement and the bulk limit, the correlation energy represents a fairly large portion of E_{bind} as the HF energy E_{HF} no longer provides a sufficient answer. Take the calculation at $L = 22.9$ nm $\gg a_B = 3.1$ nm, the Bohr radius. The first- and second-order contributions to E_{Coul} are $E^{(1)} = 33.4$ meV and $E^{(2)} = 6.3$ meV, which means $E^{(2)}$ is around 19% of $E^{(1)}$. When the size L becomes larger in approaching the bulk limit, the ratio $E^{(2)}/E^{(1)}$ will increase even further. In the bulk crystal of $CsPbBr_3$, the binding energy is $E^{\text{bulk}}_{\text{bind}} = -33 \pm 1$ meV [132], which is in agreement with Ref. [140]. We assume that the hydrogen model gives an adequate description of an exciton in the bulk. By applying the virial theorem and using the fact that $E^{\text{bulk}}_{\text{bind}} = E_{\text{kin}} + E_{\text{Coul}}$, one can arrive at the kinetic energy $E_{\text{kin}} = 33$ meV and the total Coulomb energy $E_{\text{Coul}} = -66$ meV. Assuming that the binding energy for $L = 22.9$ nm is close enough to the bulk value, the fraction of E_{Coul} that is contributed by $E^{(1)}$ approximately is

$$\eta^{(1)} = \frac{E^{(1)}}{E_{\text{Coul}}} \approx 50.6\%. \tag{3.4.12}$$

When the second-order contribution $E^{(2)}$ is included, one accounts for about

$$\eta^{(2)} = \frac{E^{(1)} + E^{(2)}}{E_{\text{Coul}}} \approx 60.1\% \tag{3.4.13}$$

of the total Coulomb energy up to second-order MBPT.

Furthermore, we note that an all-order method (in Coulomb perturbation) is needed to correctly reproduce $E_{\text{bind}}^{\text{bulk}}$. The correlation also further modifies the electron and hole correlated wave functions and their kinetic energy. The values of $\eta^{(1)}$ and $\eta^{(2)}$ above provide only a vague idea of how much of the actual correlation energy of trions and biexcitons is captured by the second-order MBPT in the intermediate to weak confinement regime ($L \gg a_B$) in the next chapter. To fully understand the effect of all-order correlation, explicit calculations are needed.

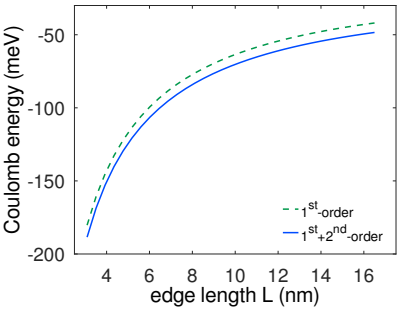

Figure 3.4.4: $1s^e_{1/2} - 1s^h_{1/2}$ single exciton binding energy versus edge length L, $CsPbBr_3$. Dashed green line: first-order MBPT (or HF), solid blue line: first-order plus second-order MBPT.

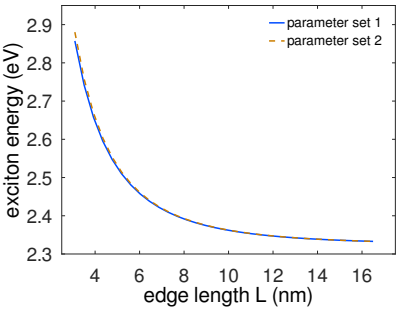

Figure 3.4.5: $1s^e_{1/2} - 1s^h_{1/2}$ exciton energy versus edge length for $CsPbBr_3$, using two parameter sets. Solid line: parameter set 1 (3.4.9), dashed line: parameter set 2 (3.4.10).

As established earlier, there are some uncertainties related to the exact value of m_h^*, m_e^* and E_{p}. Using parameter sets 1 and 2, we show the HF exciton energy E_{HF} versus the nanocrystal size L on Fig. 3.4.5. Despite having slightly different values of m_h^* and m_e^*, these parameter sets, (3.4.9) and (3.4.10), give almost identical results for the exciton energy. This leads to the suspicion that, although m_h^* and m_e^* are not known, the fact that (i) $1/\mu = 1/m_h^* + 1/m_e^*$ and (ii) the effective masses are approximately equal makes the precise values of m_h^* and m_e^* not crucial to the current approach. Additionally, after adjusting E_{gap} to the experimental temperature (Fig. 3.4.3), the good agreement between the theoretical calculations and the measured data also validates the basic assumption in the $\text{k} \cdot \text{p}$ model of using bulk values for the basic input, especially m_h^*, m_e^* and ε_{eff}.

The Kane parameter E_{p} enters the calculations of E_{bind} as a $\text{k} \cdot \text{p}$ correction of the order $\mathcal{O}((\text{k} \cdot \text{p})^2)$. As discussed before, the biggest contribution to E_{bind} comes from the direct interaction (3.3.21), which is of order $\mathcal{O}((\text{k} \cdot \text{p})^0) \equiv \mathcal{O}(1)$. Thus, E_{p} is expected to be unimportant here. An effective mass model with the same value of m_h^* an m_e^* will reproduce similar answers to those of the 4×4 $\text{k} \cdot \text{p}$

model. One problem with the $\mathrm{k}\cdot\mathrm{p}$ model is the existence of the spurious (or intra-gap) solution(s) in the case where the actual value of E_{p} is large enough [124]. In Subsection 4.2.5, we introduce a simple approach, by virtue of perturbation theory in $\mathrm{k}\cdot\mathrm{p}$ Hamiltonian, to extrapolate into the region of high E_{p} values and stay away from the problem of the intra-gap states.

3.4.3 Effect of surface polarization

Size L (nm)	E_{HF} (eV) with $\varepsilon_{\mathrm{out}} = \varepsilon_{\mathrm{eff}}$	E_{HF} (eV) with $\varepsilon_{\mathrm{out}} = 2.4$
3.1	2.857	2.858
6.0	2.4573	2.4575
9.0	2.37487	2.3749
12.3	2.34534	2.34537

Table 3.3: The HF energy E_{HF} of $1\mathrm{s}^e_{1/2} - 1\mathrm{s}^h_{1/2}$ exciton $CsPbBr_3$ nanocrystals for various sizes for two cases, without the boundary charge $\varepsilon_{\mathrm{out}} = \varepsilon_{\mathrm{eff}}$ and with the boundary charge in which $\varepsilon_{\mathrm{out}} = 2.4$. The parameter set 1, see (3.4.9), was used. The values of E_{HF} were rounded to the first decimal place where the calculations for $\varepsilon_{\mathrm{out}} = \varepsilon_{\mathrm{eff}}$ and $\varepsilon_{\mathrm{out}} = 2.4$ start to show any difference. We note that the two cases produce almost identical answers, down to a relative error of less than 0.05%.

The effect of the boundary (or surface) charges is negligible and diminishes as the size increases, see Table 3.3. The same observation about the tiny effect of the surface polarization has been reported by Bányai et al., Ref. [9], or Delerue et al., Ref. [32].

In the case of a single dielectric sphere, the interaction of a particle with the induced charge at the interface is contained in the second term of $\gamma^k(r, r')$ in (3.2.3). The self-energy V_{self}, as defined in (3.2.14), represents the interaction between a charge and its own induced surface charge and also comes from

$$\frac{(\varepsilon_{\mathrm{in}} - \varepsilon_{\mathrm{out}})(k+1)}{\varepsilon_{\mathrm{in}} k + \varepsilon_{\mathrm{out}}(k+1)} \frac{(rr')^k}{R^{2k+1}}, \tag{3.4.14}$$

of $\gamma^k(r, r')$.

In a (neutral) single exciton system, where the total charge is zero, the interaction between an electron and the surface charge of a hole cancels the self-energy of the electron almost exactly. Let us consider more explicitly the monopole $k = 0$ of a single exciton, which gives the biggest contributions to V_{HF} and V_{self}. The exchange term V_{exc} vanishes for the monopole and only V_{dir} is present in the Hartree-Fock potential V_{HF}. By making use of the identities (C.1.4) for $|a\rangle$, we can show from the results (3.3.21)-(3.3.22) and (3.3.27)-(3.3.28) that the monopole of the image charge in V_{dir} exactly cancels the $k = 0$ term of the self-energy. For the higher multipoles $k > 1$, partial cancellations still exist between V_{HF} and V_{self} due to them sharing the same term, given in (3.4.14). An identical argument applies to a hole.

Hence, the overall physical effect of the surface polarization charge induced at the interface is very small, as shown in Table 3.3.

As a result, this cancellation leads to the fact that the remaining interaction can be described by $\frac{1}{\varepsilon_{\text{in}}} \frac{r_<^k}{r_>^{k+1}}$. Heuristically, this term corresponds to the simple screening by a homogeneous medium with dielectric constant ε_{in}, which is equivalent to setting $\varepsilon_{\text{out}} = \varepsilon_{\text{eff}}$.

The simple dielectric sphere model does not capture the real situation where (i) the dielectric function changes continuously from inside the nanocrystal to the outside environment [66] and (ii) the dielectric function $\varepsilon(\vec{r})$ actually depends on the size L and other atomistic effects. The second issue (ii) can be studied via some ab initio method, which will supply useful and more complete input to the $\mathrm{k} \cdot \mathrm{p}$ theory. To understand the situation (i) above while following the current line of research, one can use the generalized Poisson equation. It permits, in combination with a more general $\mathrm{k} \cdot \mathrm{p}$ approach as outlined in Ref. [17, 18], the study of various core-shell systems. This work is left for another publication.

Since the effect of the surface charge in the dielectric sphere model seems unimportant, to minimize the number of MBPT diagrams and to simplify the subsequent calculations, we focus on the case of a homogenous medium with ε_{eff} in the next two chapters. The precise effect of the surface polarization on the correlation energy, in the case of either a dielectric sphere or a more general inhomogeneous medium, can be a subject of future study.

Chapter 4

Many-body perturbation theory: Coulomb correlation

The objective of this chapter is to construct a unified approach to study the dark-bright exciton splitting as well as the energy shifts of biexciton and trions compared to the single exciton emission. The exchange interaction that controls the previous splitting receives significant correlation correction. The enhancement factor from correlation is estimated to be about 2.5-3.5 in the intermediate confinement regime, see Subsection 4.2.5 as well as Ref. [106]. For the nanocrystal systems, the correlated effect is usually evaluated by using a variational method with a one-parameter variational ansatz [118, 121, 10]. Here, we shall instead treat the correlation via the method of many-body perturbation theory that can also be applied to the calculations of biexciton and trion shifts.

Roughly speaking, the basic idea of many-body perturbation theory (MBPT) is to look for the eigenstates of a Hamiltonian H^* knowing the exact solutions $\{|\psi\rangle, E\}$ of an approximated Hamiltonian H. A true eigenstate $|\psi^*\rangle$ of H^* will be expanded in the basis of $\{|\psi\rangle\}$. The smaller the perturbative Hamiltonian $V = H^* - H$, the faster the convergence of the MBPT. The exact form of V will be determined by which basis $\{|\psi\rangle, E\}$ is used. The technical details of this chapter follow closely the formulation in Ref. [75], especially Chapters 11-13.

The first section deals with the basic elements of MBPT that are the HF basis set and its corresponding residual Coulomb interaction V. The dark-bright exciton splitting, as discussed in Subsection 4.2.2, serves as the motivation for the open-shell formalism or the degenerate many-body perturbation theory. We start with the derivation for the short-range and long-range Coulomb interaction in subsection 4.2.1. It turns out that the long-range interaction has comparable contribution as the short-range term to the previously mentioned splitting, contrary to the conclusion in Ref. [119] for $\mathrm{k} \cdot \mathrm{p}$ theory. More recent publications [106, 121], however, have recognized that the long-range term is non-vanishing. We shall provide a clear derivation in the momentum space together with calculated results for this fact. Subsections 4.2.3 and 4.2.4 discuss the first- and second-order MBPT contributions to the long-range Coulomb interaction. The second-order diagrams Fig. 4.2.2b act as vertex corrections to the first-order diagram Fig. 4.2.6 (lowest-order in MBPT). The last part of Section 4.2 is devoted to the discussion of the

long-range exchange splitting between dark and bright excitons up to second-order MBPT.

The aim of Section 4.3 is to build a simple theory and an efficient numerical method for computing the biexciton and trion shifts. Biexciton and trion (an exciton with an additional electron or hole) emit at a different energy than the single exciton emission due to the intercarrier interaction. The difference in the emitted energy is referred to as biexciton and trion shifts. Correlation energy gives a small contribution to the single exciton binding energy, see Fig. 3.4.3. However, it has been shown that the biexciton/trion shift equals to almost zero from the Hartree-Fock (or any mean-field) calculation [113] and comes purely from correlated effects. For this purpose, we provide the basic results from the closed-shell formalism, including the relevant Feynman diagrams and their explicit expressions, in Subsection 4.3.1. The calculations of the shifts are presented in Subsection 4.3.2. Thanks to a number of available measured data [21, 52, 135], we discuss the comparison between the experiments and our theory as well as the various sources of theoretical errors.

The labelling of the orbitals goes as follows.

i) v and c denote an occupied hole (valence) and electron (conduction) respectively.

ii) $a, b, \ldots$ denote occupied states of either electron or hole.

iii) $p, q, s, r, \ldots$ denote unoccupied states.

4.1 Many-body perturbation formalism

Once again, we consider a nanocrystal with N_e and N_h confined electrons and holes respectively. To calculate the many-body corrections to the system energy, for example, one needs to construct a set $\{|\psi\rangle, E\}$ of the basis functions and their corresponding energy levels. In Subsection 4.1.1, the various possibilities of the approximated Hamiltonian H and the set of its eigenstates and eigenenergy $\{|\psi\rangle, E\}$ will be discussed. We shall argue in favor of choosing the HF Hamiltonian

$$H_{\mathrm{HF}} = H_{\mathrm{k\cdot p}} + V_{\mathrm{conf}} + V_{\mathrm{HF}} \tag{4.1.1}$$

over the non-interacting Hamiltonian $H_0 = H_{\mathrm{k\cdot p}} + V_{\mathrm{conf}}$. In Subsection 4.1.2, we write down the explicit form of the perturbative potential V related to the H_{HF} approximation of the exact Hamiltonian H^*.

4.1.1 Hartree-Fock basis set

From the discussion in Subsection 3.3.1, there are two immediate choices of $\{|\psi\rangle, E\}$ for the system with N_e electrons and N_h holes. One possibility is the non-interacting-particle basis (wave functions and energy levels) that is the solution of

$$(H_{\mathrm{k\cdot p}} + V_{\mathrm{conf}})|s\rangle^0 = E_s^0|s\rangle^0. \tag{4.1.2}$$

Eq. (4.1.2) offers the ease of generating the whole basis set including the occupied state $|a\rangle^0$ by using, for instance, the LAPACK solver '*dgeev*' for the eigenvectors and eigenvalues of a general matrix, without performing any iteration.

Another way of generating the unoccupied states is to use the HF Hamiltonian. We can obtain the full basis set (particle and hole) for MBPT calculations after iterating the equation

$$\left(H_{\mathrm{k\cdot p}} + V_{\mathrm{conf}} + V_{\mathrm{HF}}\right)|s\rangle = E_s|s\rangle \tag{4.1.3}$$

to self-consistency starting from some initial guess function and energy, for example from $\{|s\rangle^0, E_s^0\}$ of Eq. (4.1.2).

The HF basis has several advantages over the one of non-interacting-particle model. Firstly, in the intermediate or weak confinement regime or when $N_e > 1$ or $N_h > 1$, the non-interacting particle picture, Eq. (3.3.18), is rendered inadequate. Secondly, for a single exciton in its ground state, the energy of an unoccupied electron-hole pair turns out to be within a few per cent relative error from the actual HF energy. Thus, the transition energy of the higher exciton states can be well approximated once one has generated the whole basis set. This fact is particularly useful for obtaining the single-photon absorption spectrum. Lastly, the use of the HF basis minimizes the number of diagrams in higher-order MBPT, particularly at second-order [75]. This means that the second-order calculations will be simplified analytically and numerically. When one needs to go beyond second-order MBPT, for example by using configuration interaction, the HF basis usually provide faster convergence as well.

The $\mathrm{k}\cdot\mathrm{p}$ Hamiltonian $H_{\mathrm{k\cdot p}}$, the confining potential V_{conf} and the configuration-averaged HF potential V_{HF} all possess spherical symmetry. Therefore, the solution $|s\rangle$ of Eq. (4.1.3) can be separated into angular and radial parts. One has

$$|s\rangle = \frac{1}{r}\sum_{\nu} R_{s\nu}(r)|(l_{s\nu}J_{s\nu})F_sM_s\rangle. \tag{4.1.4}$$

Note that the unoccupied states $|s\rangle$ must be orthogonal to the occupied states $|a\rangle$, see the definitions in (3.2.6) for $|a\rangle$. If $|s\rangle$ has a different angular momentum than that of $|a\rangle$, the two states are orthogonal as a result of the orthogonality of their spherical harmonics. If $|s\rangle$ and $|a\rangle$ belong to the same angular momentum channel, the radial integral $\int R_{s\nu}(r)R_{a\alpha}(r)\,dr = 0$ due to the fluctuating sign of $R_{s\nu}(r)R_{a\alpha}(r)$. A Gram-Schmidt orthogonalization can be performed to ensure the orthogonality in the latter case.

For the MBPT calculations, the HF basis set has been generated up to the orbital angular momentum cut-off $l_{\text{cut-off}} = 10$ and the cut-off $n_{\text{cut-off}} = 9$ for the principal quantum number n. The computation of the correlation energy, see the later sections, converges extremely rapidly w.r.t. l and n, see Table 4.2. As a demonstration, the cut-offs ($l_{\text{cut-off}} = 1,\ n_{\text{cut-off}} = 2$) gives about 80% of the answer from ($l_{\text{cut-off}} = 10,\ n_{\text{cut-off}} = 9$) for second-order correlation energy. Putting $l_{\text{cut-off}} > 10$ or $n_{\text{cut-off}} > 9$ produces less than 0.1% difference in the calculated correlation energy.

4.1.2 Perturbative Coulomb potential

We have shown that the effective HF interaction between the N_e electrons and N_h holes is U, which is given by (3.1.1). After configuration-averaging U, one obtains the spherical HF potential $V_{\rm HF}$ in (3.1.9). In this section, we follow the formalism and convention in Ref. [75] (or Ref. [107] for a more advanced textbook). The perturbative Coulomb potential for the MBPT can be decomposed as follows

$$V = V_0 + V_1 + V_2, \tag{4.1.5}$$

where V_0, V_1 and V_0 are the zero-body, one-body and two-body parts respectively.

The zero-body term is

$$V_0 = -\sum_{a=1}^{N_v+N_c} \langle a|U^N_{\rm HF}|a\rangle + \sum_{a=1}^{N_0}\langle a|U^{(0)}_{\rm HF}|a\rangle. \tag{4.1.6}$$

In the above formula, the sum $\sum_{a=1}^{N_v,N_c}$ means summing over the N_v electrons in the VBs and N_c electrons in CBs. Similarly, $\sum_{a=1}^{N_0}$ is the sum over the 'core' states in the nanocrystal ground state. [1] We note that V_0 is just an energy constant containing no creation or annihilation operator. Thus, it gives no perturbative correction to the wave function and energy of the system since it does not connect the model space to the states outside of the model space. Only V_1 and V_2 potentially contribute to the MBPT series. [2]

Let i, j, k and l denote arbitrary electron orbitals, either occupied or unoccupied, in the VBs as well CBs. The one-body and two-body terms can be written respectively as

$$\begin{aligned} V_1 &= -\sum_{i,j} \left\{i^\dagger\ j\right\} \langle i|V_{\rm HF}|j\rangle \\ &= \sum_{i,j} \left\{i^\dagger\ j\right\} \left(-\sum_C w_C\langle i|U^c|j\rangle + \sum_V w_V\langle i|U^v|j\rangle\right), \end{aligned} \tag{4.1.7}$$

and

$$V_2 = \frac{1}{2}\sum_{ij,kl} \left\{i^\dagger\ j^\dagger\ l\ k\right\} V_{ij,kl}, \tag{4.1.8}$$

where $V_{ij,kl} = \langle ij|G_{12}|kl\rangle$ is the general Coulomb matrix elements between the states i, j, k, l. An expression for $\langle ij|G_{12}|kl\rangle$ can be found in (3.3.10). The curly

[1] Despite the rather cumbersome look, formula (4.1.6) results from the direct application of Chapter 11 of Ref. [75]. One only needs to keep in mind that the *core* particles are the N_0 electrons in the semiconductor ground state. The mean-field potential u, which has been defined in Ref. [75], is the HF potential $U^N_{\rm HF}$ of the N_e conduction and N_v valence electrons in our case. The effective potential $\langle i|v|j\rangle = \langle i|U^N_{\rm HF} - U^{N_0}_{\rm HF}|j\rangle$, which becomes exactly $\langle i|V_{\rm HF}|j\rangle$, after configuration-averaging.

[2] For the ground state exciton $1s^e_{1/2} - 1s^h_{1/2}$, in which the electron and hole states are denoted as $|c\rangle$ and $|v\rangle$ respectively, V_0 approximately equals to zero. To see this, one notes that $V_0 = -\sum_{a=1}^{N_v}\langle c|U^a|c\rangle + \sum_{a=1}^{N_v}\langle v|U^a|v\rangle$. When the electron and hole effective masses are similar, we can reasonably assume that the $1s_{1/2}$ envelope functions of $|c\rangle$ and $|v\rangle$ are the same. Thus, the terms $-\langle c|U^a|c\rangle$ and $\langle v|U^a|v\rangle$ roughly cancel. Hence, $V_0 \approx 0$.

brackets $\{\dots\}$ in (4.1.7) and (4.1.8) stand for normal ordering of the fermion operators. In a normal order, all the creation operators of valence states and annihilation operators of conduction states appear to the right.

The diagrammatic representations of V_1 and V_2 are given in Fig. 4.1.1.

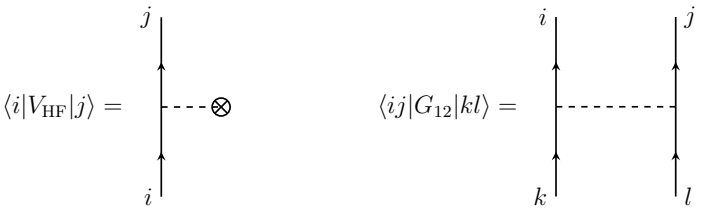

(a) one-body term (b) two-body term

Figure 4.1.1: Graphical representations of V_1 and V_2. An arrowed solid line represents a fermion (including electron and hole) where an inwards/outwards pointing arrow indicates an annihilation/a creation of the fermion. On the LHS of the graphs, we have the associated algebraic expressions when the interacting vertices appear in a given Feynman diagram.

4.2 Correlation for open-shell systems

We start this section by studying the short-range and long-range Coulomb interaction. In general, the total Coulomb interaction is the sum of the short-range and long-range terms. The derivation in Subsection 4.2.1 was inspired by the work in Ref. [119, 97] though we provide the explicit angular-radial expressions here. The energy splitting between the dark and bright excitons, as discussed in subsection 4.2.2, serves as the motivation for open-shell MBPT. In Subsections 4.2.3 and 4.2.4, we provide the first- and second-order long-range contributions to the dark-bright exciton splitting. In the final subsection, we calculate the long-range exchange splitting as an application of these results.

4.2.1 Short-range and long-range Coulomb interaction

Below, the division of the Coulomb interaction into the short-range and long-range parts will be given. Roughly speaking, this division originates from the exchanged momentum at the Coulomb vertices, which is related to either the size of the nanocrystal (mesoscopic length scale, long-range) or the size of each unit cell (atomic length scale, short-range). Despite the topic being very interesting, the technical details can be quite involved. The readers can safely take the final results, as presented in (4.2.9) and (4.2.17), and move on to the next subsections.

For the clarity of the derivation, we focus on the case of the unscreened Coulomb interaction $G_{12} = 1/|\vec{r}_1 - \vec{r}_2|$. The same method should be applicable, in principle, for the case of a more general medium. G_{12} can be rewritten as the following

Fourier integral

$$\frac{1}{|\vec{r}_1 - \vec{r}_2|} = \int \frac{4\pi}{q^2}\ \mathrm{e}^{i\vec{q}\cdot(\vec{r}_1-\vec{r}_2)}\ d\vec{q}. \tag{4.2.1}$$

In other words, $1/q^2$ is the Coulomb interaction in momentum-space representation, where $\vec{q}$ is understood to be the exchanged momentum between the particles at each Coulomb vertex.

With a bit of generalization from Chapter 2, one can express the α-component of the full wave function of the state $|\psi_a\rangle$ to be

$$\psi_{a\alpha}(\vec{r}) = \sum_{\vec{k}} c_{a\alpha}(\vec{k})\ \mathrm{e}^{i\vec{k}.\vec{r}} u_{a\alpha,k}(\vec{r}), \tag{4.2.2}$$

where the Bloch function $u_k(\vec{r})$ is periodic w.r.t. the unit cells. More generally, the envelope function is defined as

$$\xi_{a\alpha}(\vec{r}) = \sum_{\vec{k}} c_{a\alpha}(\vec{k})\ \mathrm{e}^{i\vec{k}.\vec{r}}. \tag{4.2.3}$$

By assuming that $\vec{k}$ narrowly centers around a certain $\vec{k}_0$, for instance $\vec{k}_0 = 0$, one has $\psi_{a\alpha}(\vec{r}) = \xi_{a\alpha}(\vec{r})\ u_{a\alpha,\vec{k}_0}(\vec{r})$ and we recover precisely the expression (2.2.1).

For this thesis, we follow the convention in the appendix Chapter A. After taking the Fourier transform into the momentum space, the Coulomb matrix element $\langle\psi_{a\alpha}, \psi_{b\beta}|G_{12}|\psi_{c\mu}, \psi_{d\nu}\rangle$ between the various $\mathrm{k}\cdot\mathrm{p}$ components turns into

$$\begin{aligned}\langle\psi_{a\alpha}, \psi_{b\beta}|\frac{1}{|\vec{r}_1 - \vec{r}_2|}|\psi_{c\mu}, \psi_{d\nu}\rangle = &\sum_{\vec{k}'_2\vec{k}'_1,\vec{k}_1\vec{k}_2} c^*_{b\beta}(\vec{k}'_2)\ c^*_{a\alpha}(\vec{k}'_1)\ c_{c\mu}(\vec{k}_1)\ c_{d\nu}(\vec{k}_2)\\ &\sum_{\vec{\mathsf{K}}'_1,\vec{\mathsf{K}}_1} u^*_{a\alpha,k'_1}(\vec{\mathsf{K}}'_1)\ u_{c\mu,k_1}(\vec{\mathsf{K}}_1) \sum_{\vec{\mathsf{K}}'_2,\vec{\mathsf{K}}_2} u^*_{b\beta,k'_2}(\vec{\mathsf{K}}'_2)\ u_{d\nu,k_2}(\vec{\mathsf{K}}_2)\\ &\frac{4\pi}{|\vec{k}_1 - \vec{k}'_1 + \vec{\mathsf{K}}_1 - \vec{\mathsf{K}}'_1|^2}\ \delta(\vec{k}_1 - \vec{k}'_1 + \vec{\mathsf{K}}_1 - \vec{\mathsf{K}}'_1 + \vec{k}_2 - \vec{k}'_2 + \vec{\mathsf{K}}_2 - \vec{\mathsf{K}}'_2).\end{aligned} \tag{4.2.4}$$

Note that $\vec{\mathsf{K}}_{1/2}$ and $\vec{\mathsf{K}}'_{1/2}$ are the wave vectors in the reciprocal lattice. It means that $\vec{\mathsf{K}} \sim 2\pi/a_0$, where a_0 is the averaged distance between two adjacent points in the Bravais lattice and a_0 corresponds to the atomic length scale. On the other hand, $\vec{k}_{1/2}$ or $\vec{k}'_{1/2}$ are on the order of $2\pi/R$, where R is the nanocrystal size (mesoscopic). Clearly, $R \gg a$. Therefore, $|\vec{\mathsf{K}}_1 - \vec{\mathsf{K}}'_1|$ or $|\vec{\mathsf{K}}_2 - \vec{\mathsf{K}}'_2| \gg \max(|\vec{k}_1 - \vec{k}'_1|, |\vec{k}_2 - \vec{k}'_2|)$.

If $\vec{\mathsf{K}}_1 = \vec{\mathsf{K}}'_1$, one must have $\vec{\mathsf{K}}_2 = \vec{\mathsf{K}}'_2$ for the $\delta-$function in (4.2.4) to give non-zero contribution. Or else, if $\vec{\mathsf{K}}_1 \neq \vec{\mathsf{K}}'_1$, note that unless $(\vec{\mathsf{K}}_1 - \vec{\mathsf{K}}'_1 + \vec{\mathsf{K}}_2 - \vec{\mathsf{K}}'_2) = 0$, $(\vec{k}_1 - \vec{k}'_1 + \vec{\mathsf{K}}_1 - \vec{\mathsf{K}}'_1 + \vec{k}_2 - \vec{k}'_2 + \vec{\mathsf{K}}_2 - \vec{\mathsf{K}}'_2) \neq \vec{0}$.

We claim here that the two cases ($\vec{\mathsf{K}}_1 = \vec{\mathsf{K}}'_1$) and ($\vec{\mathsf{K}}_1 \neq \vec{\mathsf{K}}'_1$) give rise to the long-range and short-range interactions respectively. The total Coulomb interaction equals to the sum of these two terms. To see it, one needs to look at (4.2.4) in further details.

For the case where $\vec{\mathsf{K}}_1 = \vec{\mathsf{K}}_1'$: $\sum_{\vec{k}_1',\vec{k}_1} \longmapsto \sum_{\vec{\mathsf{K}}_1}$ and $\sum_{\vec{k}_2',\vec{k}_2} \longmapsto \sum_{\vec{\mathsf{K}}_2}$. Therefore, this part of the Coulomb interaction in (4.2.4) is

$$\begin{aligned}
&\langle \psi_{a\alpha}, \psi_{b\beta}| \frac{1}{|\vec{r}_1 - \vec{r}_2|} |\psi_{c\mu}, \psi_{d\nu}\rangle_{LR} \\
&= \sum_{\vec{k}_2'\vec{k}_1',\vec{k}_1\vec{k}_2} c^*_{b\beta}(\vec{k}_2')\; c^*_{a\alpha}(\vec{k}_1')\; c_{c\mu}(\vec{k}_1)\; c_{d\nu}(\vec{k}_2)\; \sum_{\vec{\mathsf{K}}_1} u_{a\alpha,k_1'}^*(\vec{\mathsf{K}}_1)\; u_{c\mu,k_1}(\vec{\mathsf{K}}_1) \\
&\qquad \frac{4\pi}{|\vec{k}_1 - \vec{k}_1'|^2} \delta(\vec{k}_1 - \vec{k}_1' + \vec{k}_2 - \vec{k}_2')\; \sum_{\vec{\mathsf{K}}_2} u_{b\beta,k_2'}^*(\vec{\mathsf{K}}_2)\; u_{d\nu,k_2}(\vec{\mathsf{K}}_2).
\end{aligned} \tag{4.2.5}$$

By making the inverse Fourier transform into the position space, one has

$$\begin{aligned}
&\langle \psi_{a\alpha}, \psi_{b\beta}| \frac{1}{|\vec{r}_1 - \vec{r}_2|} |\psi_{c\mu}, \psi_{d\nu}\rangle_{LR} = \sum_{\vec{k}_2'\vec{k}_1',\vec{k}_1\vec{k}_2} c^*_{b\beta}(\vec{k}_2')\; c^*_{a\alpha}(\vec{k}_1')\; c_{c\mu}(\vec{k}_1)\; c_{d\nu}(\vec{k}_2) \\
&\sum_{\vec{\mathsf{K}}_1} \frac{1}{v_0^2} \iint_{v_0} u_{a\alpha,k_1'}^*(\tilde{r}_1')\; u_{c\mu,k_1}(\tilde{r}_1)\; \mathrm{e}^{-i\vec{\mathsf{K}}_1.(\tilde{r}_1 - \tilde{r}_1')}\; d\tilde{r}_1'\; d\tilde{r}_1 \;\; \int \frac{1}{r} \mathrm{e}^{i(\vec{k}_1 - \vec{k}_1').\vec{r}}\; d\vec{r} \\
&\int \mathrm{e}^{i(\vec{k}_1 - \vec{k}_1' + \vec{k}_2 - \vec{k}_2').\vec{r}'}\; d\vec{r}' \;\; \sum_{\vec{\mathsf{K}}_2} \frac{1}{v_0^2} \iint_{v_0} u_{b\beta,k_2'}^*(\tilde{r}_2')\; u_{d\nu,k_2}(\tilde{r}_2)\; \mathrm{e}^{-i\vec{\mathsf{K}}_2.(\tilde{r}_2 - \tilde{r}_2')}\; d\tilde{r}_2'\; d\tilde{r}_2.
\end{aligned} \tag{4.2.6}$$

In the above, $\tilde{r}_1, \tilde{r}_1', \tilde{r}_2, \tilde{r}_2'$ denote the vectors within a unit cell of the crystal lattice. We apply the identity (A.0.3) to the sums over $\vec{\mathsf{K}}_1$ and $\vec{\mathsf{K}}_2$. After regrouping the terms in the integrals w.r.t. $\vec{r}$ and $\vec{r}'$, the expression above becomes

$$\begin{aligned}
&\langle \psi_{a\alpha}, \psi_{b\beta}| \frac{1}{|\vec{r}_1 - \vec{r}_2|} |\psi_{c\mu}, \psi_{d\nu}\rangle_{LR} = \sum_{\vec{k}_2'\vec{k}_1',\vec{k}_1\vec{k}_2} c^*_{b\beta}(\vec{k}_2')\; c^*_{a\alpha}(\vec{k}_1')\; c_{c\mu}(\vec{k}_1)\; c_{d\nu}(\vec{k}_2) \\
&\qquad \iint \mathrm{e}^{-i\vec{k}_2'.\vec{r}'} \mathrm{e}^{-i\vec{k}_1'.(\vec{r}' + \vec{r})} \frac{1}{r} \mathrm{e}^{i\vec{k}_1.(\vec{r}' + \vec{r})} \mathrm{e}^{i\vec{k}_2.\vec{r}'}\; d\vec{r}\; d\vec{r}' \\
&\frac{1}{v_0} \int_{v_0} u_{a\alpha,k_1'}^*(\tilde{r}_1)\; u_{c\mu,k_1}(\tilde{r}_1)\; d\tilde{r}_1 \; \frac{1}{v_0} \int_{v_0} u_{b\beta,k_2'}^*(\tilde{r}_2)\; u_{d\nu,k_2}(\tilde{r}_2)\; d\tilde{r}_2.
\end{aligned} \tag{4.2.7}$$

To lowest order in $\mathrm{k}\cdot\mathrm{p}$ theory, the orthogonality of the Bloch functions implies that

$$\begin{aligned}
\frac{1}{v_0} \int_{v_0} u_{a\alpha,k_1'}^*(\tilde{r}_1)\; u_{c\mu,k_1}(\tilde{r}_1)\; d\tilde{r}_1 = \delta_{J_{a\alpha},J_{c\mu}}, \\
\frac{1}{v_0} \int_{v_0} u_{b\beta,k_2'}^*(\tilde{r}_2)\; u_{d\nu,k_2}(\tilde{r}_2)\; d\tilde{r}_2 = \delta_{J_{b\beta},J_{d\nu}}.
\end{aligned} \tag{4.2.8}$$

Again, the notation $\delta_{J_{a\alpha},J_{c\mu}}$ carries the selection rule for the angular momentum $\vec{L}$ and pseudo-spin $\vec{J}$ of the Bloch functions. See the expression (3.3.8) for c_χ^k and the discussion thereon. At higher-order $\mathrm{k}\cdot\mathrm{p}$ perturbation, the above orthogonality is slight corrupted, which leads to $\mathrm{k}\cdot\mathrm{p}$ corrections to the Coulomb matrix element in (4.2.7). However, the effect of these terms are not important for the current purposes and we shall omit them for now.

Let us rename the variables as $(\vec{r}' + \vec{r}) \mapsto \vec{r}_1$ and $\vec{r}' \mapsto \vec{r}_2$. By substituting the identities (4.2.3) and (4.2.8) into (4.2.7), we arrive at the following long-range Coulomb interaction

$$\begin{aligned}\langle \psi_{a\alpha}, \psi_{b\beta}| \frac{1}{|\vec{r}_1 - \vec{r}_2|} |\psi_{c\mu}, \psi_{d\nu}\rangle_{LR} &= \delta_{J_{a\alpha},J_{c\mu}}\ \delta_{J_{b\beta},J_{d\nu}} \\ \iint \xi^*_{b\beta}(\vec{r}_2)\ \xi^*_{a\alpha}(\vec{r}_1)\ \frac{1}{|\vec{r}_1 - \vec{r}_2|}\ \xi_{c\mu}(\vec{r}_1)\ \xi_{d\nu}(\vec{r}_2)\ d\vec{r}_1\ d\vec{r}_2.\end{aligned} \tag{4.2.9}$$

The integration on the second line of (4.2.9) is over the envelope functions of the total wave functions. The relevant length scale is the mesoscopic size of the nanocrystals. Thus, the part with $\vec{\mathsf{K}}_1 = \vec{\mathsf{K}}'_1$ of the total Coulomb interaction (4.2.4) is called long-range interaction. The decomposition of (4.2.9) into radial and angular parts has been given in Subsection 3.3.1. After summing over the $\mathrm{k}\cdot\mathrm{p}$ components, one can find the final result in (3.3.10).

For the case where $\vec{\mathsf{K}}_1 \neq \vec{\mathsf{K}}'_1$: As established above, the non-zero contributions only come from $\vec{\mathsf{K}}_1 - \vec{\mathsf{K}}'_1 + \vec{\mathsf{K}}_2 - \vec{\mathsf{K}}'_2 = 0$. This leads to

$$\delta(\vec{k}_1 - \vec{k}'_1 + \vec{\mathsf{K}}_1 - \vec{\mathsf{K}}'_1 + \vec{k}_2 - \vec{k}'_2 + \vec{\mathsf{K}}_2 - \vec{\mathsf{K}}'_2) = \delta(\vec{k}_1 - \vec{k}'_1 + \vec{k}_2 - \vec{k}'_2)\ \delta_{\vec{\mathsf{K}}_1-\vec{\mathsf{K}}'_1,\vec{\mathsf{K}}'_2-\vec{\mathsf{K}}_2}.$$

For the double sums over the reciprocal lattice vectors, $\sum_{\vec{\mathsf{K}}'_1,\vec{\mathsf{K}}_1} \longmapsto \sum_{\vec{\mathsf{K}}_1,\vec{\mathsf{K}}'_1\neq\vec{\mathsf{K}}_1}$ and $\sum_{\vec{\mathsf{K}}'_2,\vec{\mathsf{K}}_2} \longmapsto \sum_{\vec{\mathsf{K}}_2,\vec{\mathsf{K}}'_2\neq\vec{\mathsf{K}}_2}$. We denote $\langle \psi_{a\alpha}, \psi_{b\beta}| \frac{1}{|\vec{r}_1-\vec{r}_2|} |\psi_{c\mu}, \psi_{d\nu}\rangle_{SR}$ to be the value of (4.2.4) in the case $\vec{\mathsf{K}}_1 \neq \vec{\mathsf{K}}'_1$ and $\vec{\mathsf{K}}_2 \neq \vec{\mathsf{K}}'_2$.

Furthermore, since $|\vec{k}_1 - \vec{k}'_1| \ll |\vec{\mathsf{K}}_1 - \vec{\mathsf{K}}'_1|$, we consider $|\vec{k}_1 - \vec{k}'_1 + \vec{\mathsf{K}}_1 - \vec{\mathsf{K}}'_1| \approx |\vec{\mathsf{K}}_1 - \vec{\mathsf{K}}'_1|$ to simplify the subsequent algebraic manipulations. This approximation separates (4.2.4) into Bloch and envelope parts.

The Bloch part of $\langle \psi_{a\alpha}, \psi_{b\beta}| \frac{1}{|\vec{r}_1-\vec{r}_2|} |\psi_{c\mu}, \psi_{d\nu}\rangle_{SR}$ is

$$\begin{aligned}&\sum_{\substack{\vec{\mathsf{K}}'_1 \\ \vec{\mathsf{K}}_1\neq\vec{\mathsf{K}}'_1}} u^*_{a\alpha,k'_1}(\vec{\mathsf{K}}'_1) u_{c\mu,k_1}(\vec{\mathsf{K}}_1) \sum_{\substack{\vec{\mathsf{K}}'_2 \\ \vec{\mathsf{K}}_2\neq\vec{\mathsf{K}}'_2}} u^*_{b\beta,k'_2}(\vec{\mathsf{K}}'_2) u_{d\nu,k_2}(\vec{\mathsf{K}}_2) \frac{4\pi}{|\vec{\mathsf{K}}_1 - \vec{\mathsf{K}}'_1|^2}\ \delta_{\vec{\mathsf{K}}_1-\vec{\mathsf{K}}'_1,\vec{\mathsf{K}}'_2-\vec{\mathsf{K}}_2} \\ = &\sum_{\substack{\vec{\mathsf{K}}'_1 \\ \vec{\mathsf{K}}_1\neq\vec{\mathsf{K}}'_1}} \sum_{\substack{\vec{\mathsf{K}}'_2 \\ \vec{\mathsf{K}}_2\neq\vec{\mathsf{K}}'_2}} \frac{1}{v_0^2} \iint_{v_0} u^*_{a\alpha,k'_1}(\tilde{r}'_1) \mathrm{e}^{i\vec{\mathsf{K}}'_1.\tilde{r}'_1} u_{c\mu,k_1}(\tilde{r}_1) \mathrm{e}^{-i\vec{\mathsf{K}}_1.\tilde{r}_1}\ d\tilde{r}_1\ d\tilde{r}'_1 \int_{v_0} \frac{1}{r} \mathrm{e}^{i(\vec{\mathsf{K}}'_1-\vec{\mathsf{K}}_1).\tilde{r}}\ d\tilde{r} \\ &\frac{1}{v_0} \int_{v_0} \mathrm{e}^{i(\vec{\mathsf{K}}'_1-\vec{\mathsf{K}}_1+\vec{\mathsf{K}}'_2-\vec{\mathsf{K}}_2).\tilde{r}'}\ d\tilde{r}'\ \frac{1}{v_0^2} \iint_{v_0} u^*_{b\beta,k'_2}(\tilde{r}'_2) \mathrm{e}^{i\vec{\mathsf{K}}'_2.\tilde{r}'_2} u_{d\nu,k_2}(\tilde{r}_2) \mathrm{e}^{-i\vec{\mathsf{K}}_2.\tilde{r}_2}\ d\tilde{r}_2\ d\tilde{r}'_2.\end{aligned} \tag{4.2.10}$$

The latter expression results from inverse Fourier transforming to the position space. After summing over $\vec{\mathsf{K}}_1, \vec{\mathsf{K}}'_1, \vec{\mathsf{K}}_2, \vec{\mathsf{K}}'_2$, we have the expressions in (4.2.10) to be equal to

$$\begin{aligned}&\frac{1}{v_0^5} \underbrace{\int \cdots \int_{v_0}}_{\times 6} u^*_{b\beta,k'_2}(\tilde{r}'_2)\ u^*_{a\alpha,k'_1}(\tilde{r}'_1)\ \frac{1}{r}\ u_{c\mu,k_1}(\tilde{r}_1)\ u_{d\nu,k_2}(\tilde{r}_2) \\ &\delta(\tilde{r}'_1 + \tilde{r} + \tilde{r}')\ \delta(\tilde{r}_1 + \tilde{r} + \tilde{r}')\ \delta(\tilde{r}' + \tilde{r}_2)\ \delta(\tilde{r}' + \tilde{r}'_2)\ d\tilde{r}\ d\tilde{r}'\ d\tilde{r}_1\ d\tilde{r}'_1\ d\tilde{r}_2\ d\tilde{r}'_2 \\ =&\frac{1}{v_0} \iint_{v_0} u^*_{b\beta,k'_2}(\tilde{r}_2)\ u^*_{a\alpha,k'_1}(\tilde{r}_1) \frac{1}{|\tilde{r}_1 - \tilde{r}_2|} u_{c\mu,k_1}(\tilde{r}_1)\ u_{d\nu,k_2}(\tilde{r}_2) d\tilde{r}_1\ d\tilde{r}_2.\end{aligned}$$

The last line can be obtained by integrating over $\tilde{r}, \tilde{r}'$ and then $\tilde{r}'_1, \tilde{r}'_2$. We define the exchange α_{exch} constant as follows

$$\alpha_{\text{exch}}(a\alpha\ b\beta, c\mu\ d\nu) = \frac{1}{v_0}\iint_{v_0} u^*_{b\beta,k'_2}(\tilde{r}_2)\ u^*_{a\alpha,k'_1}(\tilde{r}_1)\frac{1}{|\tilde{r}_1 - \tilde{r}_2|}u_{c\mu,k_1}(\tilde{r}_1)\ u_{d\nu,k_2}(\tilde{r}_2). \tag{4.2.11}$$

In essence, α_{exch} is the Coulomb interaction within a unit cell normalized over its unit volume v_0. Since the relevant length scale for α_{exch} is roughly the distance between two points on the Bravais lattice, the term is called the short-range exchange constant.

Now, we return to the envelope degree of freedom. One can perform an inverse Fourier transform to $\delta(\vec{k}_1 - \vec{k}'_1 + \vec{k}_2 - \vec{k}'_2)$.

$$\begin{aligned}
&\sum_{\vec{k}'_2\vec{k}'_1,\vec{k}_1\vec{k}_2} c^*_{b\beta}(\vec{k}'_2)\ c^*_{a\alpha}(\vec{k}'_1)\ c_{c\mu}(\vec{k}_1)\ c_{d\nu}(\vec{k}_2)\ \delta(\vec{k}_1 - \vec{k}'_1 + \vec{k}_2 - \vec{k}'_2) \\
&= \int \sum_{\vec{k}'_2\vec{k}'_1,\vec{k}_1\vec{k}_2} c^*_{b\beta}(\vec{k}'_2)\ c^*_{a\alpha}(\vec{k}'_1)\ c_{c\mu}(\vec{k}_1)\ c_{d\nu}(\vec{k}_2)\ \mathrm{e}^{i(\vec{k}_1 - \vec{k}'_1 + \vec{k}_2 - \vec{k}'_2).\vec{r}}\ d\vec{r} \\
&\text{(apply the definition (4.2.3))} \\
&= \int \xi^*_{b\beta}(\vec{r})\ \xi^*_{a\alpha}(\vec{r})\ \xi_{c\mu}(\vec{r})\ \xi_{d\nu}(\vec{r})\ d\vec{r} \\
&= \iint \xi^*_{b\beta}(\vec{r}_2)\ \xi^*_{a\alpha}(\vec{r}_1)\ \delta(\vec{r}_1 - \vec{r}_2)\ \xi_{c\mu}(\vec{r}_1)\ \xi_{d\nu}(\vec{r}_2)\ d\vec{r}_1\ d\vec{r}_2 \\
&= \langle a\alpha, b\beta|\delta(\vec{r}_1 - \vec{r}_2)|c\mu, d\nu\rangle.
\end{aligned} \tag{4.2.12}$$

One combines the exchange constant (4.2.11) and the envelope part (4.2.12) and finds the short-range Coulomb interaction to be

$$\langle\psi_{a\alpha}, \psi_{b\beta}|\frac{1}{|\vec{r}_1 - \vec{r}_2|}|\psi_{c\mu}, \psi_{d\nu}\rangle_{SR} = \alpha_{\text{exch}}(a\alpha\ b\beta, c\mu\ d\nu)\ \langle a\alpha, b\beta|\delta(\vec{r}_1 - \vec{r}_2)|c\mu, d\nu\rangle. \tag{4.2.13}$$

As apparent from $\delta(\vec{r}_1 - \vec{r}_2)$, the envelope part of $\langle\psi_{a\alpha}, \psi_{b\beta}|\frac{1}{|\vec{r}_1 - \vec{r}_2|}|\psi_{c\mu}, \psi_{d\nu}\rangle_{SR}$ takes the form of a contact interaction. In 3-D, the *Dirac* δ-function carries the dimension of volume inverse. Therefore, one expects the short-range interaction to scale as $1/R^3$, instead of $1/R$ as in the long-range counterpart.

We can make use of the following multipole expansion of the *Dirac* δ-function,

$$\begin{aligned}
\delta(\vec{r}_1 - \vec{r}_2) &= \frac{\delta(r_1 - r_2)}{r_1^2}\sum_k \frac{[k]}{4\pi}\ \vec{\mathbb{C}}^k_1 \cdot \vec{\mathbb{C}}^k_2 \\
&= \frac{\delta(r_1 - r_2)}{r_1^2}\sum_k \frac{[k]}{4\pi} \times (-1)^k\sqrt{[k]}\left\{\mathbb{C}^k_1\mathbb{C}^k_2\right\}^0_0,
\end{aligned} \tag{4.2.14}$$

to decompose $\langle a\alpha, b\beta|\delta(\vec{r}_1 - \vec{r}_2)|c\mu, d\nu\rangle$ into angular and radial parts. From (4.2.14) and (3.2.5), it is clear that the contact interaction between the envelope functions should have a similar angular decomposition as for the long-range Coulomb interaction in (3.3.10).

By repeating the derivation (3.3.2)-(3.3.10) for a general Coulomb matrix element as in Subsection 3.3.1, one can obtain the angular-radial expression for the contact term. As the detailed derivation is quite tedious and fairly straightforward, we just quote the final result for the contact interaction,

$$\langle a\alpha, b\beta|\delta(\vec{r}_1-\vec{r}_2)|c\mu, d\nu\rangle = \sum_k (-1)^k \frac{[k]}{4\pi} R^k_\delta(a\alpha\ b\beta, c\mu\ d\nu)$$

$$c^k(a\alpha\ b\beta, c\mu\ d\nu) \times$$

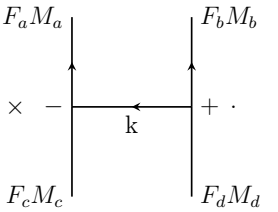

(4.2.15)

The 'contact' radial integral $R^k_\delta(a\alpha\ b\beta, c\mu\ d\nu)$ is given as follows

$$R^k_\delta(a\alpha\ b\beta, c\mu\ d\nu) = \int R_{b\beta}(r)\ R_{a\alpha}(r)\ \frac{1}{r^2}\ R_{c\mu}(r)\ R_{d\nu}(r)\ dr\ . \tag{4.2.16}$$

The full expression for the short-range interaction $\langle ab|G_{12}|cd\rangle_{SR}$ of a general Coulomb interaction G_{12} becomes

$$\langle ab|G_{12}|cd\rangle_{SR} = \textstyle\sum_k X^k_{SR}(ab, cd) \times$$

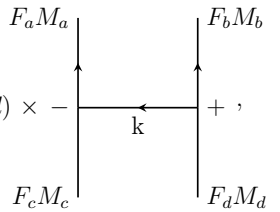

(4.2.17)

where the states $|a\rangle, |b\rangle, |c\rangle$ and $|d\rangle$ are defined in (3.2.6) and contain all the $\mathrm{k}\cdot\mathrm{p}$ components. We note from (4.2.17) that the structure of the short-range Coulomb interaction is as same as the long-range expression (3.3.10). X^k_{SR} is also called the short-range reduced matrix element and is given as

$$\begin{aligned} X^k_{SR}(ab, cd) =& (-1)^k \frac{[k]}{4\pi} \sum_{\alpha\beta,\mu\nu} R^k_\delta(a\alpha\ b\beta, c\mu\ d\nu) \\ & c^k(a\alpha\ b\beta, c\mu\ d\nu)\ \alpha_{\text{exch}}(a\alpha\ b\beta, c\mu\ d\nu). \end{aligned} \tag{4.2.18}$$

4.2.2 Single exciton: dark versus bright states

In this subsection, the reader is quickly introduced to the classification of single exciton states based on the total angular momentum of the electron-hole pair. As theoretically predicted and experimentally observed [97, 93, 121], these various exciton states with different total angular momenta have slightly different energy.

The calculation of the energy differences serves as the motivation for the first- and second-order open-shell MBPT.

For the system of N_c conduction and N_v valence electrons, the Coulomb potential V_{Coul} dictates that the true conserved quantity is the total angular momentum F_{tot}, which is the sum of all the angular momenta F's of the $N_c + N_v$ electrons. In the neutral ground state $|\varnothing\rangle$ of a nanocrystal, the N_0 electrons completely fill the energy levels up to VBM. As a consequence, each energy level is fully occupied with the electrons present in all magnetic substates and the total angular momentum of the system is $F_{\text{tot}} = 0$.

In a neutral single exciton with $N_c = 1$ electron and $N_h = 1$ hole, the electron occupies some conduction state $|c\rangle$ with the angular momentum and magnetic quantum number (F_c, M_c) while there is another electron in $|v\rangle$ missing from the valence state with (F_v, M_v). We note that for a hole, $F_h = F_v$ and $M_h = -M_v$. In second-quantization formalism, this single exciton state can be expressed as $c^\dagger v|\varnothing\rangle$, i.e. one electron has been destroyed from $|v\rangle$ and brought to $|c\rangle$. The angular state of the remaining electrons in the same shell as $|v\rangle$ is $|F_v\ (-M_v)\rangle = |F_h M_h\rangle$. Except for the shell that has total angular momentum F_v, all other energy levels in the VBs are fully occupied. Hence, for a single exciton, its total angular momentum F_{tot} is the sum of the angular momenta F_c and F_v. In other words, the angular states $|F_c M_c\rangle$ of an electron and $|F_h M_h\rangle$ of a hole, where $M_h = -M_v$, are coupled to form the exciton angular state $|F_{\text{tot}} M_{\text{tot}}\rangle$. The associated Clebsch-Gordan coefficients and their graphical representations are given as

$$C_{\text{eh}}(F_c\ M_c, F_v M_v; FM) = (-1)^{F_v - M_v}\langle F_c M_c, F_v M_v | FM\rangle$$

$$= [F]^{1/2} \times$$

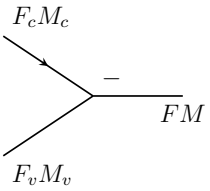

, (4.2.19)

$$C^*_{\text{eh}}(F_c M_c, F_v M_v; FM) = (-1)^{F_v - M_v}\langle FM | F_c M_c, F_v M_v\rangle$$

$$= [F]^{1/2} \times$$

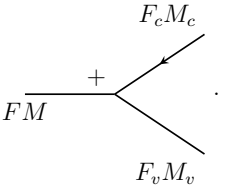

. (4.2.20)

The phase factor $(-1)^{F_v - M_v}$ stems from the fact that a hole wave function is the corresponding time-reversed (complex conjugate) electron wave function. From Ref. [37] or Ref. [14], under time-reversal symmetry, $Y^l_{-m}(\theta, \phi)^* = (-1)^{l-m} Y^l_m(\theta, \phi)$.

$$|F_{\text{tot}} M_{\text{tot}}\rangle = \sum_{M_c, M_v} C_{\text{eh}}(F_c M_c, F_v M_v; F_{\text{tot}} M_{\text{tot}})\ |F_c M_c, F_v M_v\rangle. \tag{4.2.21}$$

Upon emitting a single photon, the system makes the transition from a single exciton state with $N_e = N_h = 1$ to $|\varnothing\rangle$. A photon has its angular momentum $l_{\text{photon}} = 1$. The selection rule $\Delta F_{\text{tot}} = 1$ applies as a result of the conservation of the total angular momentum of the exciton and the photon [14]. Under the emission of a single photon, only the exciton states with $F_{\text{tot}} = 1$ can radiatively decay into the ground state $|\varnothing\rangle$ and, thus, are called the bright excitons. The other exciton state(s) with $F_{\text{tot}} \neq 1$ cannot transition to $|\varnothing\rangle$ via emitting only one photon and are called the dark exciton(s).

As a concrete example for lead halide perovskites (but not only), take the $1\text{s}^e_{1/2} - 1\text{s}^h_{1/2}$ exciton. The conduction and valence electrons have $F_c = 1/2$ and $F_v = 1/2$ respectively. When the angular momenta of the conduction and valence electron are coupled to produce an exciton with total angular momentum F_{tot}, one has the triangle inequality $0 = |F_c - F_v| \leq F_{\text{tot}} \leq |F_c + F_v| = 1$. It means $F_{\text{tot}} = 0$ or $F_{\text{tot}} = 1$. Followed from the discussion above, only the exciton $F_{\text{tot}} = 1$ can radiatively decay to $|\varnothing\rangle$ by releasing one photon. The states with $F_{\text{tot}} = 1$ are called the bright excitons while the $F_{\text{tot}} = 0$ exciton is dark.

Let $E(F_{\text{tot}})$ denote the energy of the exciton with F_{tot}. In a spherical model, the magnetic substates $|F_{\text{tot}} M_{\text{tot}}\rangle$ of the same F_{tot} are degenerate. It turns out that the exciton states with $F_{\text{tot}} = 0$ and $F_{\text{tot}} = 1$ have slightly different energy. The dark-bright exciton splitting is the energy difference $E(F_{\text{tot}} = 1) - E(F_{\text{tot}} = 0)$. The contribution from the long-range Coulomb interaction, called Δ_{LR}, to this energy splitting will be shown in Subsection 4.2.5. Subsections 4.2.3 and 4.2.4 focus on deriving the first- and second-order MBPT contributions to Δ_{LR}.

At first-order MBPT, only the exchange diagram in Fig. 4.2.2, which comes from the two-body V_2 interaction, gives non-zero splitting as will be shown in Subsection 4.2.3. At second-order MBPT, Δ_{LR} receives non-zero contributions from both the one-body V_1 and two-body V_2 interaction. It can be shown that the diagrams containing V_1 cancels some diagrams coming from only V_2. This effectively reduces the computation to a subset of second-order diagrams containing only the two-body interaction. The two exchange diagrams in Fig. 4.2.6 are the vertex corrections to the first-order exchange diagram, Fig. 4.2.2. Their contribution to the total Δ_{LR} varies depending on the confinement regime, i.e. on the size of the nanocrystal. At large sizes, the second-order vertex correction can be quite important, as seen in Fig. 4.2.9 and 4.2.10.

4.2.3 First-order correlation

We note to the readers here that there are two kinds of diagrams appearing in this thesis: the angular momentum diagrams and the Feynman diagrams. In the former case, a black solid line represents an angular momentum (integer or half-integer) and its arrow, if there is any, carries an associated phase factor. The convention used in the Feynman diagrams can be described as follows:

1) A blue or red solid line represents an electron or a hole (fermion) respectively. An inwards or outwards pointing arrow indicates respectively the annihilation or creation of the corresponding fermion. [3]

[3] Even though it is not necessary, the colouring of the fermion lines seems useful for the

2) Each horizontal dashed line represents a Coulomb interaction.

3) In Chapter 5, each photon is drawn by a wavy line. [4]

Long-range interaction

The first-order MBPT correction to the energy of $|F_{\rm tot}M_{\rm tot}\rangle$ is

$$E^{(1)}_{LR}(F_{\rm tot}) = \sum_{\substack{M_{c'}M_{v'}\\ M_cM_v}} C^*_{\rm eh}(F_{c'}M_{c'}, F_{v'}M_{v'}; F_{\rm tot}M_{\rm tot}) \\ \langle\varnothing|v'^{\dagger}c'(V_1+V_2)c^{\dagger}v|\varnothing\rangle\ C_{\rm eh}(F_cM_c, F_vM_v; F_{\rm tot}M_{\rm tot}). \tag{4.2.22}$$

Figure 4.2.1: First-order MBPT diagrams coming from V_1.

We show briefly here that the first-order diagrams from the one-body term V_1 in Fig. 4.2.1 do not contribute to the energy of an exciton and thus do not give rise to the dark-bright exciton splitting.

Consider the matrix element $\langle\varnothing|v'^{\dagger}c'\ V_1\ c^{\dagger}v|\varnothing\rangle$ for a single exciton, where V_1 is given in (4.1.7). There are two ways of performing the Wick contraction of the first-order term $(-\langle\varnothing|v'^{\dagger}c'\sum_{i,j}\{i^{\dagger}\ j\}\langle i|V_{\rm HF}|j\rangle c^{\dagger}v|\varnothing\rangle)$:

- $j \mapsto c$ and $i \mapsto c'$, $v \equiv v'$.

  The associated matrix element is $(\sum_V w_V\langle cv|G_{12}|cv\rangle)$.

- $i \mapsto v$ and $j \mapsto v'$, $c \equiv c'$.

  The matrix element, in this case, is $(-\sum_C w_C\langle vc|G_{12}|vc\rangle)$. [5]

The Wick phases coming from the two contractions above are

$$\langle\varnothing|v^{\dagger}c'\{i^{\dagger}\ j\}c^{\dagger}v|\varnothing\rangle = +1, \\ \langle\varnothing|v'^{\dagger}c\{i^{\dagger}\ j\}c^{\dagger}v|\varnothing\rangle = +1. \tag{4.2.23}$$

discussion in the next two subsections.

[4] In principle, an inwards/outwards arrow also implies the absorption/emission of a photon, as used in Fig. 5.1.1. However, in calculating the transition amplitude and the vertex correction of a one-photon process, the detail knowledge of whether it is an absorption or emission process is not very important.

[5] We note that v and v' (or c and c') are just two different magnetic substates belonging to the same valence (or conduction) energy level. Therefore, after configuration-averaging, $\sum_V w_V\langle c'v|G_{12}|cv\rangle = \sum_V w_V\langle cv|G_{12}|cv\rangle$ and $\sum_C w_C\langle vc|G_{12}|v'c\rangle = \sum_C w_C\langle vc|G_{12}|vc\rangle$.

For the single exciton $1s^e_{1/2} - 1s^h_{1/2}$, the weight factors are $w_C = w_V = \frac{1}{2}$. Therefore, the contributions of the two contractions of the one-body term V_1 have the same absolute value but opposite signs. Consequently, the sum of the diagrams in Fig. 4.2.1 gives zero and only the two-body potential V_2 gives non-zero contribution, as shown below.

Consider the two-body matrix element, in which $V_{ij,kl} = \langle ij|G_{12}|kl\rangle$,

$$\langle \varnothing|v'^\dagger c'\ V_2\ c^\dagger v|\varnothing\rangle = \frac{1}{2}\sum_{ijkl} V_{ij,kl}\ \langle \varnothing|v'^\dagger c'\left\{i^\dagger\ j^\dagger\ l\ k\right\} c^\dagger v|\varnothing\rangle. \tag{4.2.24}$$

There are two pairs of equivalent Wick contractions of $\langle \varnothing|v'^\dagger c'\left\{i^\dagger\ j^\dagger\ l\ k\right\} c^\dagger v|\varnothing\rangle$ as follows

$$\begin{cases} \langle \varnothing|v'^\dagger c'\left\{i^\dagger\ j^\dagger\ l\ k\right\} c^\dagger v|\varnothing\rangle = -\langle \varnothing|v'^\dagger c'\left\{c'^\dagger v'v^\dagger c\right\} c^\dagger v|\varnothing\rangle = -1, \\ \langle \varnothing|v'^\dagger c'\left\{i^\dagger\ j^\dagger\ l\ k\right\} c^\dagger v|\varnothing\rangle = -\langle \varnothing|v'^\dagger c'\left\{c'^\dagger v'v^\dagger c\right\} c^\dagger v|\varnothing\rangle = -1. \end{cases} \tag{4.2.25}$$

The contractions in (4.2.25) have the same Coulomb matrix element (with the Wick phase included)

$$-V_{vc',v'c} = -V_{c'v,cv'} = -\langle c'v|G_{12}|cv'\rangle.$$

Therefore, they contribute a factor of 2 that cancels with $\frac{1}{2}$ in (4.2.24). The same applies for the contractions in (4.2.26) with the Wick phases equal to 1 and their corresponding Coulomb matrix element to be

$$V_{vc',cv'} = V_{c'v,v'c} = \langle vc'|G_{12}|cv'\rangle.$$

$$\begin{cases} \langle \varnothing|v'^\dagger c'\left\{i^\dagger\ j^\dagger\ l\ k\right\} c^\dagger v|\varnothing\rangle = \ \langle \varnothing|v'^\dagger c'\left\{c'^\dagger v'v^\dagger c\right\} c^\dagger v|\varnothing\rangle = +1, \\ \langle \varnothing|v'^\dagger c'\left\{i^\dagger\ j^\dagger\ l\ k\right\} c^\dagger v|\varnothing\rangle = \ \langle \varnothing|v'^\dagger c'\left\{c'^\dagger v'v^\dagger c\right\} c^\dagger v|\varnothing\rangle = +1. \end{cases} \tag{4.2.26}$$

The two sets of equivalent Wick contractions in (4.2.25) and (4.2.26) correspond to the following two diagrams in Fig. 4.2.2, that are called *direct* and *exchange* diagrams respectively.

When the Coulomb interaction is expressed in multipole expansion, one has

$$\mathcal{D}^1_d = -V_{c'v,cv'} = -\langle c'v|G_{12}|cv'\rangle = -\sum_k X^k(cv,cv)\ D^1_d(k), \tag{4.2.27}$$

$$\mathcal{D}^1_x = \ V_{vc',cv'} = \ \langle vc'|G_{12}|cv'\rangle = \ \sum_k X^k(vc,cv)\ D^1_x(k). \tag{4.2.28}$$

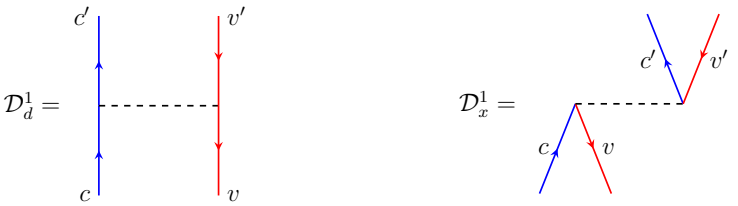

(a) Direct diagram

(b) Exchange diagram

Figure 4.2.2: The first-order MBPT diagrams coming from V_2. In contrast to $\mathcal{D}^1_d$, the 'particle type' changes at each Coulomb vertex in $\mathcal{D}^1_x$ from electron to hole, or equivalently from conduction to valence band and vice versa. These changes in 'particle type' are across-the-gap excitations.

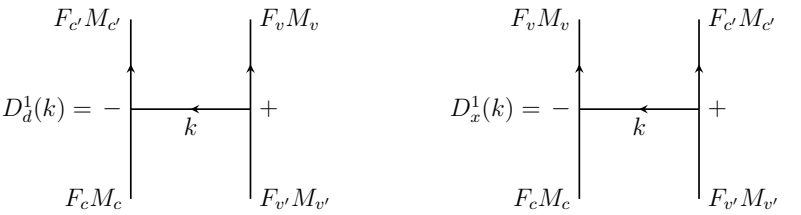

Figure 4.2.3: The angular diagrams $D^1_d(k)$ and $D^1_x(k)$ for the k-pole in the multipole decompositions of $\mathcal{D}^1_d$ and $\mathcal{D}^1_x$ given in (4.2.27) and (4.2.28).

The Coulomb reduced matrix element $X^k(ab, cd)$ was defined in (3.3.9). [6] The k-pole angular diagrams of the direct and exchange interactions can be found in Fig. 4.2.3.

For the ground state exciton $1\mathrm{s}^e_{1/2} - 1\mathrm{s}^h_{1/2}$, $F_c = F_{c'} = 1/2$ and $F_v = F_{v'} = 1/2$. Implicit in the direct and exchange angular diagrams $D_d(k)$ and $D_x(k)$ are the triangle inequalities (F_c, F_c, k) (or equivalently (F_v, F_v, k)) and (F_c, F_v, k) that require

$$|F_c - F_{c'}| = 0 \leq k \leq 1 = |F_c + F_{c'}|,$$

and

$$|F_c - F_v| = 0 \leq k \leq 1 = |F_c + F_v|.$$

Therefore, only $k = 0$ and $k = 1$ multipoles are allowed for $D_d(k)$ and $D_x(k)$ in Fig. 4.2.3.

In the direct diagram $\mathcal{D}^1_d$, the particle type (electron or hole) does not change at each interaction vertex. In order to make the reduced matrix element $\langle l_l||\mathbb{C}^k||l_r\rangle$ in (3.3.8) non-zero, $(l_l + k + l_r)$ must be an even integer. This fact together with the selection rule δ_{J_l,J_r} from c^k_χ restricts the k-poles in $\mathcal{D}^1_d$ to only the monopole $k = 0$. Once more, the direct interaction recovers the classical Coulomb interaction

[6] We note that the reduced matrix element X^k does not depend on the magnetic substates. Hence, $X^k(c'v, cv') = X^k(cv, cv)$ and $X^k(vc', cv') = X^k(vc, cv)$.

between the charge density distributions. It is this type of interaction that gives the most contribution to the binding energy of a single exciton.

At each Coulomb vertex of the exchange diagram, there is change of particle type (from electron to hole and vice versa). The Coulomb interaction scatters the particles across the gap and leads to reshuffling of the magnetic substates. This phenomenon, which has no classical analogy, contributes to the energy splitting between the dark and bright exciton. At each vertex where the particle type changes, the radial integral (3.3.3) contains twice the overlaps between the big and small components of the $\mathrm{k}\cdot\mathrm{p}$ solution of the HF Eq. (3.3.11). Each overlap of this kind brings in an extra order in $\mathrm{k}\cdot\mathrm{p}$ perturbation. Therefore, the exchange diagram in (4.2.28) is on the order of $\mathcal{O}((\mathrm{k}\cdot\mathrm{p})^2)$ and should be proportional to E_{p}.

The first-order correction (4.2.22) becomes

$$
\begin{aligned}
&\sum_{\substack{M_{c'}M_{v'}\\ M_cM_v}} C^*_{\mathrm{eh}}(F_{c'}M_{c'},F_{v'}M_{v'};F_{\mathrm{tot}}M_{\mathrm{tot}})\ \langle\varnothing|v'^{\dagger}c'\ V_2\ c^{\dagger}v|\varnothing\rangle\ C_{\mathrm{eh}}(F_cM_c,F_vM_v;F_{\mathrm{tot}}M_{\mathrm{tot}})\\
&=\sum_{\substack{M_{c'}M_{v'}\\ M_cM_v}} C^*_{\mathrm{eh}}(F_{c'}M_{c'},F_{v'}M_{v'};F_{\mathrm{tot}}M_{\mathrm{tot}})\ (\mathcal{D}^1_d+\mathcal{D}^1_x)\ C_{\mathrm{eh}}(F_cM_c,F_vM_v;F_{\mathrm{tot}}M_{\mathrm{tot}})\\
&=\sum_{\substack{M_{c'}M_{v'}\\ M_cM_v}}\sum_k \big(X^k(cv,cv)D^1_d(k)+X^k(vc,cv)D^1_x(k)\big)\\
&\qquad C^*_{\mathrm{eh}}(F_{c'}M_{c'},F_{v'}M_{v'};F_{\mathrm{tot}}M_{\mathrm{tot}})\ C_{\mathrm{eh}}(F_cM_c,F_vM_v;F_{\mathrm{tot}}M_{\mathrm{tot}}).
\end{aligned}
$$

Note that the reduced matrix elements $X^k(vc,cv)$ and $X^k(cv,cv)$ do not depend on the magnetic substates. For each k, the sums $\sum_{\substack{M_{c'}M_{v'}\\ M_cM_v}}$ can be individually performed. We define the first-order exciton angular diagrams to be

$$
\begin{aligned}
D^{exc}_{1,d}(k)&=\sum_{\substack{M_{c'}M_{v'}\\ M_cM_v}} C^*_{\mathrm{eh}}(F_{c'}M_{c'},F_{v'}M_{v'};F_{\mathrm{tot}}M_{\mathrm{tot}})\ D^1_d(k)\ C_{\mathrm{eh}}(F_cM_c,F_vM_v;F_{\mathrm{tot}}M_{\mathrm{tot}})\\
&=(-1)^{F_c+F_v+F_{\mathrm{tot}}}\begin{Bmatrix} F_{v'} & k & F_v\\ F_c & F_{\mathrm{tot}} & F_{c'}\end{Bmatrix},
\end{aligned}
\tag{4.2.29}
$$

$$
\begin{aligned}
D^{exc}_{1,x}(k)&=\sum_{\substack{M_{c'}M_{v'}\\ M_cM_v}} C^*_{\mathrm{eh}}(F_{c'}M_{c'},F_{v'}M_{v'};F_{\mathrm{tot}}M_{\mathrm{tot}})\ D^1_x(k)\ C_{\mathrm{eh}}(F_cM_c,F_vM_v;F_{\mathrm{tot}}M_{\mathrm{tot}})\\
&=\frac{(-1)^{F_c-F_v+F_{\mathrm{tot}}}}{[F_{\mathrm{tot}}]}\ \delta_{F_{\mathrm{tot}}k}.
\end{aligned}
\tag{4.2.30}
$$

The derivations for the final expressions in (4.2.29) and (4.2.30) of the angular diagrams $D^{exc}_{1,d}(k)$ and $D^{exc}_{1,x}(k)$ for a single exciton are given in Sections D.1 and D.2 of the appendix. Obviously from (4.2.29) and (4.2.30), the values of $D^{exc}_{1,d}(k)$ and $D^{exc}_{1,x}(k)$ are independent of the magnetic substates. The first-order MBPT

correction to the exciton energy is

$$E^{(1)}_{LR}(F_{\rm tot}) = \sum_k \left(-X^k(cv,cv)\ D^{exc}_{1,d}(k) + X^k(vc,cv)\ D^{exc}_{1,x}(k)\right). \tag{4.2.31}$$

Also, $X^k(vc,cv)$ and $X^k(cv,cv)$ do not depend on the total angular momentum $F_{\rm tot}$ of the exciton. As established previously, $X^k(cv,cv)$ of the $k=1$ dipole term vanishes. From (4.2.29), the values of $D^{exc}_{1,d}(k=0)$ for $F_{\rm tot}=0$ and $F_{\rm tot}=1$ are equal to $\frac{1}{2}$ for $1s^e_{1/2}-1s^h_{1/2}$ exciton. In consequence, the direct term $\sum_k X^k(cv,cv)\ D^{exc}_{1,d}(k)$ does not give rise to dark-bright exciton splitting.

In the exchange angular expression (4.2.30), due to the selection rule $\delta_{F_{\rm tot}k}$, only $k=0$ (or $k=1$) term is non-zero for the dark exciton $F_{\rm tot}=0$ (or the bright exciton $F_{\rm tot}=1$). $D^{exc}_{1,x}(k)$ receives a different value depending on whether $k=0$ or $k=1$. Therefore, the exchange interaction $X^k(vc,cv)\ D^{exc}_{1,x}(k)$ is expected to introduce some energy splitting between the dark and the bright exciton.

Short-range exchange interaction

In general, the short-range Coulomb interaction also contains direct and exchange parts, which contribute to the binding energy. The short-range coefficient $\alpha_{\rm exch}$ in (4.2.17) contains $4\pi/|\vec{\mathsf{K}}_1-\vec{\mathsf{K}}'_1|^2$, in contrast to $4\pi/|\vec{k}_1-\vec{k}'_1|^2$ in the case of long-range Coulomb interaction. Since $|\vec{k}_1-\vec{k}'_1|/|\vec{\mathsf{K}}_1-\vec{\mathsf{K}}'_1|$ is on the order of $a_0/R\ll 1$, the contribution from the short-range interaction to the exciton binding energy is of the order of $\mathcal{O}\left((a_0/R)^2\right)$ and, hence, seems unimportant in comparison with the long-range direct interaction.

As one can see from (4.2.17), the structure of the short-range term is the same as the long-range counterpart. Hence, the angular parts of the direct and exchange short-range interaction of a single exciton are precisely $D^{exc}_{1,d}(k)$ and $D^{exc}_{1,x}(k)$. The short-range contribution to the exciton energy at first-order MBPT is

$$E^{(1)}_{SR}(F_{\rm tot}) = \sum_k \left(-X^k_{SR}(cv,cv)\ D^{exc}_{1,d}(k) + X^k_{SR}(vc,cv)\ D^{exc}_{1,x}(k)\right), \tag{4.2.32}$$

where the short-range reduced matrix element X^k_{SR} is given in (4.2.18). For precisely the same reason as for long-range interaction, only the exchange interaction participates in the dark-bright exciton splitting.

The long-range exchange interaction is of the order $\mathcal{O}\left((\mathrm{k}\cdot\mathrm{p})^2\right)$, as previously established, while the short-range exchange interaction is $\mathcal{O}\left((a_0/R)^2\right)$. Therefore, we expect the two contributions to the dark-bright exciton splitting to be of equal importance. The short-range exchange interaction has been more thoroughly investigated in the literature [93, 10, 120]. The focus of our calculations in this thesis is on the long-range exchange contribution since less theoretical work has been done on the topic [48].

4.2.4 Second-order correlation

In this subsection, we aim to evaluate the second-order MBPT corrections to the exciton energy. This amounts to calculating the following matrix element

$$\sum_{\substack{M_{c'}M_{v'}\\M_cM_v}}\sum_{pq}\langle\varnothing|v'^{\dagger}c'\ (V_1+V_2)\ p^{\dagger}q|\varnothing\rangle\frac{1}{(\epsilon_c+\epsilon_v)-(\epsilon_p+\epsilon_q)}\langle\varnothing|q^{\dagger}p\ (V_1+V_2)\ c^{\dagger}v|\varnothing\rangle, \tag{4.2.33}$$

where $\epsilon_c, \epsilon_v, \epsilon_p$ and ϵ_q denote the *electron* energy levels. The energy ϵ_q of an electron in the valence state $|q\rangle$ has the opposite sign to a hole state of energy ϵ_h in the same level, i.e. $\epsilon_q = -\epsilon_h$.

We only calculate the second-order corrections that are lowest in $\mathrm{k}\cdot\mathrm{p}$ perturbation. Roughly speaking, these are the diagrams containing the lowest-order MBPT corrections to the first-order diagrams in Fig. 4.2.2. For the direct and exchange interaction, they are respectively the ladder diagram, Fig. 4.2.4a, and the vertex corrections, Fig. 4.2.6. At second-order MBPT in the perturbative Coulomb potential V, the diagrams that have higher $\mathrm{k}\cdot\mathrm{p}$ corrections are formally $\mathcal{O}((\mathrm{k}\cdot\mathrm{p})^2)$ times the lowest-order diagrams. Their total contribution is thus expected to be insignificant to the ones in Fig. 4.2.4a and Fig. 4.2.6.

We note that there exist other second-order diagrams consisting of the one-body term V_1, which has been given in (4.1.7). These diagrams can be shown to cancel partly the two-body diagrams Fig. 4.2.4a and Fig. 4.2.6 where $|p\rangle$ and $|c\rangle$ (or $|q\rangle$ and $|v\rangle$) are in the same shell. As a final result, $\sum_{pq}$ actually denotes the sum over shells P and Q and all of their magnetic substates such that $P \neq C$ and $Q \neq V$. Later, any $\sum_{F_qF_p}$ implies summing over the conduction and valence shells P and Q, with total angular momentum F_p and F_q, that are different from C and V respectively.

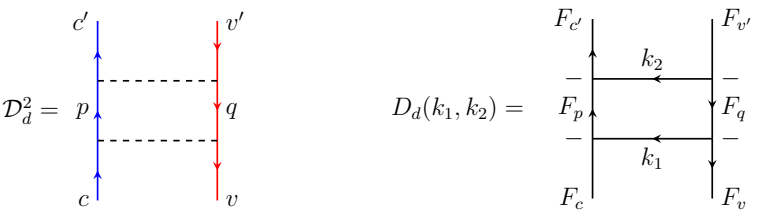

(a) Feynman diagram

(b) Angular diagram

Figure 4.2.4: Second-order MBPT direct ladder diagram, left: Feynman diagram, right: the corresponding angular diagram.

The Feynman diagram $\mathcal{D}_d^2$ in Fig. 4.2.4a provides the MBPT correction from the electron-hole pair excitation. The upward-arrowed blue lines in Fig. 4.2.4a represent the conduction electrons. The downward-arrowed red lines stand for the valence electrons, in other words the holes. The annihilation/creation of a valence electron (with an arrow going in/out of a vertex) is equivalent to creation/annihilation of a hole.

The actual process can be described in two stages: During the first stage, a conduction electron in $|c\rangle$ makes a transition to an unoccupied state $|p\rangle$ while another electron in the valence state $|q\rangle$ is destroyed and recreated in $|v\rangle$, leaving a 'hole' in $|q\rangle$. In the second stage, the electron in $|p\rangle$ comes down to $|c'\rangle$ and, at the same time, an electron moves from $|v'\rangle$ to fill the state $|q\rangle$.

The expression for the diagram $\mathcal{D}_d^2$ is

$$\mathcal{D}_d^2 = (+1) \times 4 \times \sum_{pq} \frac{\frac{1}{2}\langle c'q|G_{12}|pv'\rangle \frac{1}{2}\langle pv|G_{12}|cq\rangle}{(\epsilon_c + \epsilon_q) - (\epsilon_p + \epsilon_v)} = \sum_{pq} \frac{\langle c'q|G_{12}|pv'\rangle\langle pv|G_{12}|cq\rangle}{(\epsilon_c + \epsilon_q) - (\epsilon_p + \epsilon_v)}. \tag{4.2.34}$$

Here, the Wick phase $(+1)$ comes from the Wick contractions in (4.2.35). Since there are four equivalent ways of Wick contracting, as listed in the first two lines of (4.2.35), there should be a multiplicative factor of 4. This combines with $(\frac{1}{2})^2$ to give the overall prefactor equal to 1.

$$\begin{aligned}
&\langle \varnothing | v'^\dagger c' \{ i^\dagger \; j^\dagger \; l \; k \} \{ m^\dagger \; n^\dagger \; s \; r \} c^\dagger v | \varnothing \rangle = \langle \varnothing | v'^\dagger c' \{ i^\dagger \; j^\dagger \; l \; k \} \{ m^\dagger \; n^\dagger \; s \; r \} c^\dagger v | \varnothing \rangle \\
=&\langle \varnothing | v'^\dagger c' \{ i^\dagger \; j^\dagger \; l \; k \} \{ m^\dagger \; n^\dagger \; s \; r \} c^\dagger v | \varnothing \rangle = \langle \varnothing | v'^\dagger c' \{ i^\dagger \; j^\dagger \; l \; k \} \{ m^\dagger \; n^\dagger \; s \; r \} c^\dagger v | \varnothing \rangle \\
=&\langle \varnothing | v'^\dagger c' \{ c'^\dagger \; v' \; q^\dagger \; p \} \{ p^\dagger \; q \; v^\dagger \; c \} c^\dagger v | \varnothing \rangle = +1
\end{aligned} \tag{4.2.35}$$

After separating the angular part $D_d^2(k_1, k_2)$ by using the result in (3.3.10), $\mathcal{D}_d^2$ can be expressed compactly as [7]

$$\mathcal{D}_d^2 = \sum_{k_1 k_2} \sum_{F_q F_p} \frac{X^{k_2}(cq, pv) X^{k_1}(pv, cq)}{(\epsilon_c + \epsilon_v) - (\epsilon_p + \epsilon_q)} D_d^2(k_1, k_2). \tag{4.2.36}$$

As it will be shown in Subsection 4.2.5, even though the absolute value of the second-order direct diagram is larger than the second-order exchange diagrams, Fig. 4.2.6, the amount contributed to the dark-bright exciton splitting is surprisingly negligible.

For systems with more than one electron or one hole, apart from the direct interaction between particles in a conduction and a valence state as depicted in Fig. 4.2.4a, there exist other ladder diagrams that represent the electron-electron or the hole-hole interaction as given in Fig. 4.2.5. When c_1 is joined to c_1' and c_2 to c_2', we recover the closed-shell diagram in Fig. 4.3.1a. If the order of joining of the external legs are exchanged, i.e. c_1 to c_2' and c_2 to c_1', we get the left diagram in Fig. 4.3.3. The similar conclusions hold for the right diagram in Fig. 4.2.5 for hole-hole interaction.

[7] Again, for v and v' coming from the same shell and similarly for c, c', $X^{k_2}(c'q, pv') = X^{k_2}(cq, pv)$. An analogous situation is true in going from (4.2.37) and (4.2.38) to (4.2.41) and (4.2.42), $X^{k_2}(c'q, pv') = X^{k_2}(cq, pv)$ and $X^{k_2}(qc', pv') = X^{k_2}(qc, pv)$.

Figure 4.2.5: The second-order ladder diagrams for systems with more than one electron or hole, left: electron-electron interaction, right: hole-hole interaction. By joining the free ends, we obtain the closed-shell diagrams in Fig. 4.3.1a, 4.3.1b and 4.3.3.

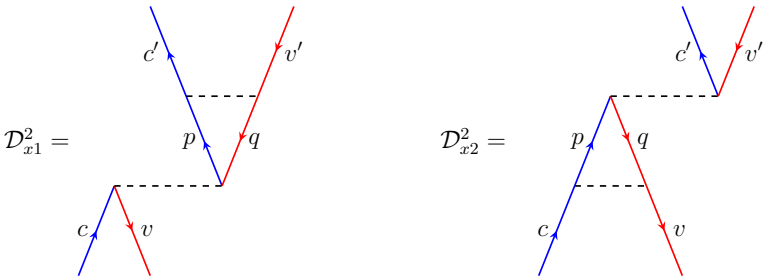

Figure 4.2.6: Second-order MBPT exchange diagrams. The two diagrams correspond to the vertex corrections for the two vertices of first-order exchange interaction.

At second-order MBPT, there are two dominant Feynman diagrams $\mathcal{D}^2_{x1}$ and $\mathcal{D}^2_{x2}$ that work as the vertex corrections to $\mathcal{D}^1_x$ on the right of Fig. 4.2.2. The expressions for these second-order corrections are

$$\mathcal{D}^2_{x1} = (-1) \times 4 \times \sum_{pq} \frac{\frac{1}{2}\langle c'q|G_{12}|pv'\rangle \frac{1}{2}\langle vp|G_{12}|cq\rangle}{(\epsilon_c + \epsilon_v) - (\epsilon_p + \epsilon_q)} = -\sum_{pq} \frac{\langle c'q|G_{12}|pv'\rangle\langle vp|G_{12}|cq\rangle}{(\epsilon_c + \epsilon_v) - (\epsilon_p + \epsilon_q)}, \tag{4.2.37}$$

$$\mathcal{D}^2_{x2} = (-1) \times 4 \times \sum_{pq} \frac{\frac{1}{2}\langle qc'|G_{12}|pv'\rangle \frac{1}{2}\langle pv|G_{12}|cq\rangle}{(\epsilon_c + \epsilon_v) - (\epsilon_p + \epsilon_q)} = -\sum_{pq} \frac{\langle qc'|G_{12}|pv'\rangle\langle pv|G_{12}|cq\rangle}{(\epsilon_c + \epsilon_v) - (\epsilon_p + \epsilon_q)}. \tag{4.2.38}$$

In (4.2.37) or (4.2.38) above, the factor 4 comes from the four equivalent Wick contractions as can be seen in (4.2.39) for $\mathcal{D}^2_{x1}$ and (4.2.40) for $\mathcal{D}^2_{x2}$. Each of the contractions gives the Wick phase equal to (-1).

$$\langle\varnothing|v'^{\dagger}c'\{i^{\dagger}\ j^{\dagger}\ l\ k\}\{m^{\dagger}\ n^{\dagger}\ s\ r\}c^{\dagger}v|\varnothing\rangle = \langle\varnothing|v'^{\dagger}c'\{i^{\dagger}\ j^{\dagger}\ l\ k\}\{m^{\dagger}\ n^{\dagger}\ s\ r\}c^{\dagger}v|\varnothing\rangle$$
$$=\langle\varnothing|v'^{\dagger}c'\{i^{\dagger}\ j^{\dagger}\ l\ k\}\{m^{\dagger}\ n^{\dagger}\ s\ r\}c^{\dagger}v|\varnothing\rangle = \langle\varnothing|v'^{\dagger}c'\{i^{\dagger}\ j^{\dagger}\ l\ k\}\{m^{\dagger}\ n^{\dagger}\ s\ r\}c^{\dagger}v|\varnothing\rangle$$
$$= -\langle\varnothing|v'^{\dagger}c'\{c'^{\dagger}\ v'\ q^{\dagger}\ p\}\{p^{\dagger}\ q\ v^{\dagger}\ c\}c^{\dagger}v|\varnothing\rangle = -1 \tag{4.2.39}$$

$$\langle\varnothing|v'^{\dagger}c'\{i^{\dagger}\ j^{\dagger}\ l\ k\}\{m^{\dagger}\ n^{\dagger}\ s\ r\}c^{\dagger}v|\varnothing\rangle = \langle\varnothing|v'^{\dagger}c'\{i^{\dagger}\ j^{\dagger}\ l\ k\}\{m^{\dagger}\ n^{\dagger}\ s\ r\}c^{\dagger}v|\varnothing\rangle$$
$$=\langle\varnothing|v'^{\dagger}c'\{i^{\dagger}\ j^{\dagger}\ l\ k\}\{m^{\dagger}\ n^{\dagger}\ s\ r\}c^{\dagger}v|\varnothing\rangle = \langle\varnothing|v'^{\dagger}c'\{i^{\dagger}\ j^{\dagger}\ l\ k\}\{m^{\dagger}\ n^{\dagger}\ s\ r\}c^{\dagger}v|\varnothing\rangle$$
$$= -\langle\varnothing|v'^{\dagger}c'\{c'^{\dagger}\ v'\ q^{\dagger}\ p\}\{p^{\dagger}\ q\ v^{\dagger}\ c\}c^{\dagger}v|\varnothing\rangle = -1 \tag{4.2.40}$$

Again, we can apply (3.3.10) and get the following angular-radial decompositions of the vertex corrections

$$\mathcal{D}^2_{x1} = -\sum_{k_1k_2}\sum_{F_pF_q}\frac{X^{k_2}(cq,pv)X^{k_1}(vp,cq)}{(\epsilon_c+\epsilon_v)-(\epsilon_p+\epsilon_q)}D^2_{x1}(k_1,k_2), \tag{4.2.41}$$

$$\mathcal{D}^2_{x2} = -\sum_{k_1k_2}\sum_{F_pF_q}\frac{X^{k_2}(qc,pv)X^{k_1}(pv,cq)}{(\epsilon_c+\epsilon_v)-(\epsilon_p+\epsilon_q)}D^2_{x2}(k_1,k_2), \tag{4.2.42}$$

where the angular diagrams $D^2_{x1}(k_1,k_2)$ and $D^2_{x2}(k_1,k_2)$ are given in Fig. 4.2.7 and Fig. 4.2.8.

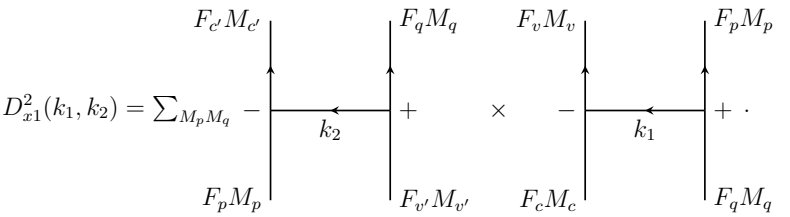

Figure 4.2.7: Angular diagram $D^2_{x1}(k_1,k_2)$ associated with $\mathcal{D}^2_{x1}$

The second-order correction to the energy of the exciton angular state $|F_{\rm tot}M_{\rm tot}\rangle$ can be written as

$$E^{(2)}_{LR}(F_{\rm tot}) = \sum_{\substack{M_{c'}M_{v'}\\M_cM_v}} C^*_{\rm eh}(F_{c'}M_{c'},F_{v'}M_{v'};F_{\rm tot}M_{\rm tot}) \\ \left(\mathcal{D}^2_d+\mathcal{D}^2_{x1}+\mathcal{D}^2_{x2}\right)\ C_{\rm eh}(F_cM_c,F_vM_v;F_{\rm tot}M_{\rm tot}). \tag{4.2.43}$$

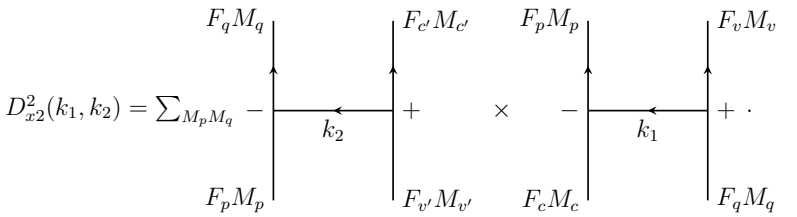

Figure 4.2.8: Angular diagram $D^2_{x2}(k_1,k_2)$ associated with $\mathcal{D}^2_{x2}$

The reduced matrix elements X^{k_1} and X^{k_2} are independent of the magnetic substates M_c, M_v, $M_{v'}$ and $M_{c'}$. Therefore, the sum over the magnetic substates are only performed on the angular parts $D^2_{x1}(k_1,k_2)$ and $D^2_{x2}(k_1,k_2)$. We define the exciton angular diagrams at second-order MBPT to be

$$\begin{aligned} D^{exc}_{2,d}(k_1,k_2) = &\sum_{\substack{M_{c'}M_{v'}\\ M_cM_v}} C^*_{\rm eh}(F_{c'}M_{c'},F_{v'}M_{v'};F_{\rm tot}M_{\rm tot}) \\ &D^2_d(k_1,k_2)\ C_{\rm eh}(F_cM_c,F_vM_v;F_{\rm tot}M_{\rm tot}), \end{aligned} \tag{4.2.44}$$

$$\begin{aligned} D^{exc}_{2,x1}(k_1,k_2) = &\sum_{\substack{M_{c'}M_{v'}\\ M_cM_v}} C^*_{\rm eh}(F_{c'}M_{c'},F_{v'}M_{v'};F_{\rm tot}M_{\rm tot}) \\ &D^2_{x1}(k_1,k_2)\ C_{\rm eh}(F_cM_c,F_vM_v;F_{\rm tot}M_{\rm tot}), \end{aligned} \tag{4.2.45}$$

$$\begin{aligned} D^{exc}_{2,x2}(k_1,k_2) = &\sum_{\substack{M_{c'}M_{v'}\\ M_cM_v}} C^*_{\rm eh}(F_{c'}M_{c'},F_{v'}M_{v'};F_{\rm tot}M_{\rm tot}) \\ &D^2_{x2}(k_1,k_2)\ C_{\rm eh}(F_cM_c,F_vM_v;F_{\rm tot}M_{\rm tot}). \end{aligned} \tag{4.2.46}$$

Interested readers can look for the derivation of (4.2.44)-(4.2.46) in section D.4 of the appendix. Here, we mention just the explicit values of the exchange angular diagrams above.

$$D^{exc}_{2,d}(k_1,k_2) = (-1)^{F_v-F_c+F_q-F_p} \begin{Bmatrix} F_{v'} & F_q & k_2 \\ F_p & F_{c'} & F_{\rm tot} \end{Bmatrix} \begin{Bmatrix} F_q & F_v & k_1 \\ F_c & F_p & F_{\rm tot} \end{Bmatrix}, \tag{4.2.47}$$

$$D^{exc}_{2,x1}(k_1,k_2) = D^{exc}_{2,x2}(k_1,k_2) = -\frac{(-1)^{F_c+F_v+F_p+F_q}}{[F_{\rm tot}]} \begin{Bmatrix} F_v & F_c & F_{\rm tot} \\ F_p & F_q & k_1 \end{Bmatrix} \delta_{k_2,F}\ . \tag{4.2.48}$$

The second-order MBPT contribution to the exciton energy takes the following final expression

$$\begin{aligned} E^{(2)}_{LR}(F_{\rm tot}) = \sum_{k_1k_2}\sum_{F_qF_p} \frac{1}{(\epsilon_c+\epsilon_v)-(\epsilon_p+\epsilon_q)} \big(&X^{k_2}(cq,pv)X^{k_1}(pv,cq)\ D^{exc}_{2,x1}(k_1,k_2) \\ -X^{k_2}(cq,pv)X^{k_1}(vp,cq)\ D^{exc}_{2,d}(k_1,k_2) &- X^{k_2}(qc,pv)X^{k_1}(pv,cq)\ D^{exc}_{2,x2}(k_1,k_2)\big)\ . \end{aligned} \tag{4.2.49}$$

The exciton angular diagrams $D^{exc}_{\cdots}$ are given in (4.2.29)-(4.2.30) and (4.2.47)-(4.2.48) as products of phase factors, fractions of integers and 6j-symbols. These expressions can be easily evaluated, even by hand. Once a subroutine for the reduced matrix element X^k exists, see (3.3.9), the evaluations of $E^{(1)}_{LR}(F_{\rm tot})$ and $E^{(2)}_{LR}(F_{\rm tot})$ become extremely straightforward and efficient. As an application of (4.2.31) and (4.2.49), we show in the next Subsection the calculations of the long-range dark-bright exciton splitting.

4.2.5 Application to dark-bright exciton splitting

Before we start the technical discussion, it is important to remark that, in this thesis, the energy splitting is between the $F_{\rm tot} = 0$ and $F_{\rm tot} = 1$ excitons. All the magnetic substates of $F_{\rm tot} = 1$ are completely degenerate. To have a more complete study of the single exciton fine structure, one needs to go beyond the spherical models. Non-spherical effects such as crystal field and shape deformation [12, 88], Rashba effect [19, 91, 60] etc. must be included. These effects will not only add to the energy difference between $F_{\rm tot} = 0$ and $F_{\rm tot} = 1$ but will also split the various magnetic substates of the bright exciton. As discussed at the end of Subsection 4.2.3, we focus on the long-range splitting in the current application.

We define the first- and second-order contributions from long-range interaction to dark-bright exciton splitting to be

$$\Delta^{(1)}_{\rm LR} = E^{(1)}_{LR}(F_{\rm tot} = 1) - E^{(1)}_{LR}(F_{\rm tot} = 0) \ , \tag{4.2.50}$$

$$\Delta^{(2)}_{\rm LR} = E^{(2)}_{LR}(F_{\rm tot} = 1) - E^{(2)}_{LR}(F_{\rm tot} = 0) \ . \tag{4.2.51}$$

The long-range (LR) splitting is defined to be the sum of the first- and second-order contributions.

$$\Delta_{\rm LR} = \Delta^{(1)}_{\rm LR} + \Delta^{(2)}_{\rm LR}. \tag{4.2.52}$$

Note that $\Delta_{\rm LR}$ does not include all of the splitting between $F_{\rm tot} = 0$ and $F_{\rm tot} = 1$ exciton. The terms that are higher-order in MBPT have been omitted.

In Fig. 4.2.9, the dark-bright exciton splitting $\Delta_{\rm LR}$ is plotted against the edge length L for a cubic nanocrystal by using the parameter set 1 (3.4.9). Most of the contribution to the splitting $\Delta_{\rm LR}$ comes from the exchange interaction. Therefore, $\Delta_{\rm LR}$ is sometimes referred to as the exchange splitting. The direct diagram $\mathcal{D}^2_d$ in Fig. 4.2.4a, despite having a bigger contribution to the exciton binding energy than the exchange diagrams $\mathcal{D}^2_{x,1}$ and $\mathcal{D}^2_{x,2}$ in Fig. 4.2.6, gives almost no splitting between the dark and the bright exciton.

The vertex correction from the second-order MBPT diagrams in Fig. 4.2.6 result in a strong enhancement of the first-order exchange diagram $\mathcal{D}^1_x$, see Fig. 4.2.2b. Let us define the vertex enhancement factor to be

$$\beta_{\rm LR} = \frac{\Delta_{\rm LR}}{\Delta^{(1)}_{\rm LR}} = 1 + \frac{\Delta^{(2)}_{\rm LR}}{\Delta^{(1)}_{\rm LR}}. \tag{4.2.53}$$

The first-order term $\Delta^{(1)}_{\rm LR}$ is the lowest-order, non-zero MBPT contribution to the dark-bright exchange splitting. $\beta_{\rm LR}$ reflects the relative importance of the

second-order contribution $\Delta_{\rm LR}^{(2)}$ over the first-order contribution $\Delta_{\rm LR}^{(1)}$ to the exchange splitting. Approximately, $\beta_{\rm LR}$ depends linearly on the size L, as shown in Fig. 4.2.10. A heuristic explanation of this linear dependence is as follows. The expressions (4.2.41) and (4.2.42) for the second-order corrections contain two Coulomb interactions G_{12} on the numerator and an excitation energy $(\epsilon_c+\epsilon_v)-(\epsilon_p+\epsilon_q)$ in the denominator. Each Coulomb term G_{12} scales as $1/L$ whereas the excitation energy is $1/L^2$. Therefore, the ratio $(\mathcal{D}_{x,1}^2+\mathcal{D}_{x,2}^2)/\mathcal{D}_x^1$ is roughly proportional to L.

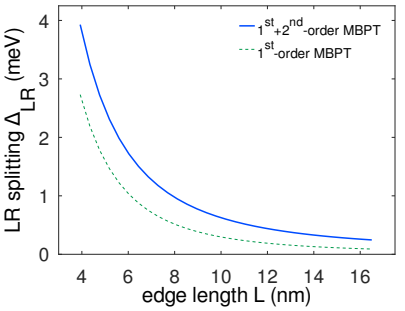

Figure 4.2.9: Long-range splitting $\Delta_{\rm LR}$ versus edge length L for $CsPbBr_3$. The calculation here uses parameter set 1 (3.4.9), where $E_{\rm p}=20.0$ eV. Generally, as L becomes smaller, the exchange splitting increases. The dependence of $\Delta_{\rm LR}^{(1)}$ and $\Delta_{\rm LR}^{(2)}$ on L can be found in (4.2.54) and (4.2.55) respectively.

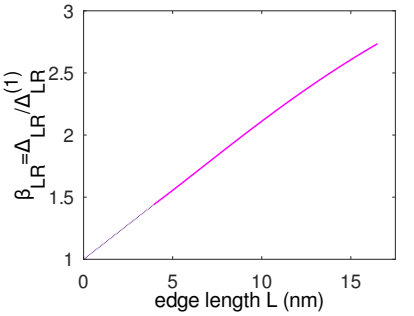

Figure 4.2.10: The long-range enhancement factor $\beta_{\rm LR}=\Delta_{\rm LR}/\Delta_{\rm LR}^{(1)}$ versus L for $CsPbBr_3$. The dotted line is a linear extrapolation into the small L region, where $\Delta_{\rm LR}$ approaches 1 in the strong confinement limit. As L increases, $\Delta_{\rm LR}^{(2)}$ becomes relatively more important compared to $\Delta_{\rm LR}^{(1)}$.

The polymonial fits of the calculated $\Delta_{\rm LR}^{(1)}$ and $\Delta_{\rm LR}^{(2)}$ w.r.t. L^{-1} shows the following dependence on the size L.

$$\Delta_{\rm LR}^{(1)}=\frac{a_3}{L^3}+\frac{a_2}{L^2}, \tag{4.2.54}$$

$$\Delta_{\rm LR}^{(2)}=\frac{b_2}{L^2}+\frac{b_1}{L}, \tag{4.2.55}$$

where $(a_3,a_2)=(-51.68,73.02)$ and $(b_2,b_1)=(-1.15,6.76)$.

In the strong confinement regime, in which $L<a_B$, the higher-order MBPT corrections are quantitatively less important. The linear extrapolation, which is represented by the dotted line in Fig. 4.2.10, indicates that $\beta_{\rm LR}\to 1$ as $L\to 0$. For the size $L\geq a_B$, (for $CsPbBr_3$, $a_B=3.1$ nm), one enters the intermediate to weak confinement regime. The enhancement factor $\beta_{\rm LR}$ is 1.5 or bigger for size $L>5.0$ nm and $\Delta_{\rm LR}^{(1)}$ alone is insufficient to describe the dark-bright exciton splitting. Most of the synthesized nanocrystals have their edge length in the range from 7.5 nm to 12 nm, for which the exciton is weakly confined. For these nanocrystals, the second-order correction $\Delta_{\rm LR}^{(2)}$ is needed, at least.

In the case of intermediate to weak confinement, to obtain a quantitative agreement with the experimental values, it seems necessary to go to an all-order method (e.g. configuration interaction) as well as to have the short-range term included. At the level $\mathcal{O}(1)$ in $\mathrm{k}\cdot\mathrm{p}$ theory, the omitted higher-order MBPT contribution corresponds to the ladder diagrams, that are the generalization of the second-order vertex corrections in Fig. 4.2.6 with more rungs of Coulomb interaction. One can sum over these diagrams by solving the particle-hole Bethe-Salpeter equation [79, 29].

As established in Subsection 3.4.1, the actual value of E_p is uncertain. Fig. 4.2.11 shows the variation of Δ_LR versus the Kane parameter. For $E_\mathrm{p} < 24.5$ eV, Δ_LR behaves linearly with respect to E_p. From our discussion in Subsection 4.2.3, the first-order exchange term $\mathcal{D}_x^1$ is $\mathcal{O}((\mathrm{k}\cdot\mathrm{p})^2)$ and thus $\Delta_\mathrm{LR}^{(1)}$ is proportional to E_p. Similarly, in the second-order exchange terms, $X^{k_1}(vp, cq)$ and $X^{k_2}(qc, pv)$ are also $\mathcal{O}((\mathrm{k}\cdot\mathrm{p})^2)$ while $X^{k_2}(cq, pv)$ and $X^{k_1}(pv, cq)$ are $\mathcal{O}(1)$ in $\mathrm{k}\cdot\mathrm{p}$. Therefore, $\mathcal{D}_{x,1}^2$ and $\mathcal{D}_{x,2}^2$ as well as $\Delta_\mathrm{LR}^{(2)}$ depend linearly on E_p. This explains the linear relationship between Δ_LR and E_p.

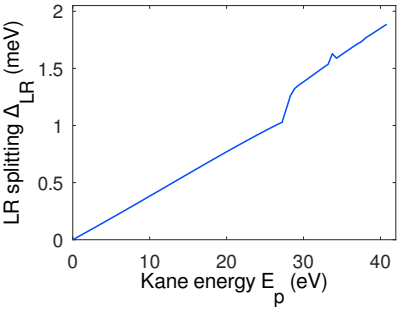

Figure 4.2.11: The long-range splitting Δ_LR versus Kane parameter E_p. The high E_p region, where $E_\mathrm{p} > 24.49$ eV, show various issues coming from the spurious solutions of the $\mathrm{k}\cdot\mathrm{p}$ model.

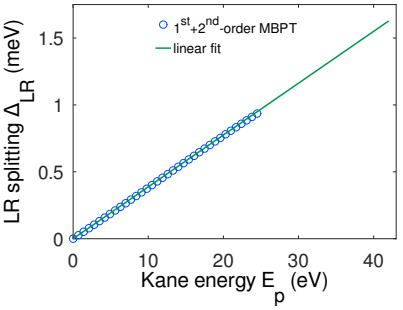

Figure 4.2.12: Δ_LR versus Kane parameter E_p with extrapolation into high E_p region (solid green line). Circles: calculated data, solid line: linear fit $\alpha_1 E_\mathrm{p}$, where $\alpha_1 = 3.87 \times 10^{-2}$.

When one reaches the high E_p region with $E_\mathrm{p} \geq 24.5$ eV, the spurious solutions of the $\mathrm{k}\cdot\mathrm{p}$ model start to appear [124]. The existence of these states seems to be rooted in some numerical instability. The spurious solutions stay inside the band gap and, unfortunately, introduce some nonsensible contribution to several physical quantities, such as Δ_LR as seen in Fig. 4.2.11. We note that Δ_LR relies on the big-small component overlap, which is a consequence of the $\mathrm{k}\cdot\mathrm{p}$ perturbation on the total wave functions. In the $E_\mathrm{p} > 24.49$ eV region, the direct calculations show that Δ_LR is $\mathcal{O}((\mathrm{k}\cdot\mathrm{p})^2)$, or in other words is linear in E_p. From the principle of perturbation theory, we expect that this relation continues to be hold beyond the E_p threshold. Linear fitting shows $\Delta_\mathrm{LR}(E_\mathrm{p}) = \alpha_1 E_\mathrm{p}$ where $\alpha_1 = 3.87 \times 10^{-2}$, see Fig. 4.2.12. It can be used to extrapolate into the high E_p region to get an insight of how much Δ_LR may be.

Using parameter set 1 with $E_{\rm p} = 20.0$ eV, one has $\Delta_{\rm LR} = 0.52$ meV at $L = 11$ nm. If we keep other parameters as in parameter set 1 but instead use $E_{\rm p} = 27.88$ eV as derived from the 4×4 k $\cdot$ p model (see Table 3.1), $\Delta_{\rm LR} = 0.72$ meV. This latter $\Delta_{\rm LR}$, which is in the general expected range, underestimates the value in Table 4 of Ref. [106] by 40%. We attribute the underestimation in our calculation to the truncation at second-order MBPT.

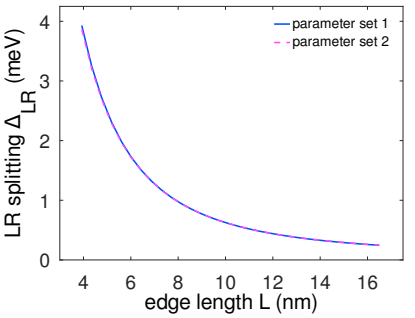

Figure 4.2.13: $\Delta_{\rm LR}$ versus edge length L using the two parameter sets (3.4.9) and (3.4.10). $E_{\rm p}$ of parameter set 2 has been rescaled to that of parameter set 1.

Fig 4.2.13 contains the calculations for two different parameter sets (3.4.9) and (3.4.10) as given in Subsection 3.4.1. Since the long-range splitting $\Delta_{\rm LR}$ depends linearly on $E_{\rm p}$, to have a fair comparison between the two choices of the parameters, one needs to use the same $E_{\rm p}$ value. The calculations using parameter set 2 have been adjusted by the factor $\frac{20.0}{16.39}$. Two parameter sets (with $E_{\rm p} = 20.0$ eV) give almost identical long-range splitting $\Delta_{\rm LR}$. This demonstrates the fact that the exact value of m_e^* and m_h^* do not influence very much the answer for $\Delta_{\rm LR}$ as long as $1/\mu = 1/m_e^* + 1/m_h^*$ and the ratio m_e^*/m_h^* is sufficiently close to 1.

Apart from the Kane parameter $E_{\rm p}$, another important quantity for $\Delta_{\rm LR}$ is the effective dielectric constant. Each reduced matrix element X^k is inversely proportional to $\varepsilon_{\rm eff}$. Hence, if $\varepsilon_{\rm eff}$ turns out to be smaller or bigger, the splitting $\Delta_{\rm LR}$ also increases or decreases respectively. A more detailed discussion of how the variation in $\varepsilon_{\rm eff}$ affects the correlation energy will be given in Subsection 4.3.2.

4.3 Second-order correlation for closed-shell systems

In this section, we aim at a pedagogic and qualitative explanation for the observed biexciton and trion shifts relative to the single exciton emission in the literature. For simplicity, we treat the electrons and holes as different types of particles here. This assumption is equivalent to accounting only for the $\mathcal{O}(1)$ (zeroth-order) diagrams in k $\cdot$ p perturbation. The higher-order k $\cdot$ p diagrams, some of which has been discussed in the previous section for open-shell MBPT formalism, contribute quantitatively a small fraction of the total shifts.

To understand why the closed-shell formalism is expected to be a good approach in this situation, we take the biexciton as an example. In its ground state, a biexciton has the two electrons and two holes occupying the various magnetic substates in the lowest conduction and valence shells respectively. For perovskites, these shells are $1{\rm s}^e_{1/2}$ and $1{\rm s}^h_{1/2}$. Each shell has a total degeneracy equal to 2 and is

fully occupied or *closed* in the biexciton ground state. The closed-shell description is, thus, exact for a biexciton in a system like perovskite nanocrystals.

Even when the shells are not fully occupied as in the case of a single exciton, the magnetic substates are degenerate and have equal chances to be occupied. From the previous subsection, when the electron and hole angular momenta are combined, the resulting exciton states with different F_{tot} have slightly different energy. This splitting is at most a few meV, even for the smallest sizes, and is much smaller than the biexciton or trion shift. It can be shown that by using the open-shell formalism and averaging over the exciton states with various F_{tot}, one recovers the results of the closed-shell formalism.

In Subsection 4.3.1, we first lay down the formulation of second-order MBPT for closed-shell systems. The theoretical foundation and other details thereon can be found in Chapter 12 of Ref. [75]. In Subsection 4.3.2, we calculate the biexciton and trion shifts, Δ_{XX} and $\Delta_{\text{X}^+}/\Delta_{\text{X}^-}$ respectively. In both cases, the second-order MBPT clearly shows a red shift, in contrast to the HF (or any other mean-field) calculation [113]. A reasonable level of agreement with experimental data is found for trion shifts. However, the agreement seems very poor for the case of Δ_{XX} of $CsPbBr_3$, where the various experiments also disagree with each other.

4.3.1 Closed-shell many-body perturbation theory

The graphical conventions for the angular momentum diagrams and Feynman diagrams have been stated at the beginning of Subsection 4.2.3. The labelling of orbitals is as mentioned at the beginning of this chapter. Similar to HF interaction, at second-order MBPT, the correction to the excitonic energy also comes from direct diagrams and their exchange variants.

There are three distinct direct diagrams $\mathcal{D}_d^{\text{h-h}}$, $\mathcal{D}_d^{\text{e-e}}$ and $\mathcal{D}_d^{\text{e-h}}$ that correspond to the electron-electron, hole-hole and electron-hole interaction. $\mathcal{D}_d^{\text{h-h}}$, for instance, requires the excitation of two particles and is only non-zero for a system with more than one hole. A similar conclusion holds for $\mathcal{D}_d^{\text{e-e}}$ for a system with more than one electron. It means also that the first two diagrams in Fig. 4.3.1 are zero for the case of a single exciton and only $\mathcal{D}_d^{\text{e-h}}$ gives non-zero contribution to correlation energy.

Here, the simplicity of the closed-shell formalism is that one can directly apply the results from chapter 12 of Ref. [75]. We remind the readers that in Fig. 4.3.1, a and b denote the occupied orbitals while r and s stand for the unoccupied states of both electrons and holes. Since the three diagrams $\mathcal{D}_d^{\text{e-e}}$, $\mathcal{D}_d^{\text{h-h}}$ and $\mathcal{D}_d^{\text{e-h}}$ share the same structure, they also have the same common expression below, called $\mathcal{D}_d$ for convenience.

$$\mathcal{D}_d = 2 \sum_{AB,RS} w_{AB} \, \frac{\frac{1}{2}\langle ab|G_{12}|rs\rangle \; \frac{1}{2}\langle rs|G_{12}|ab\rangle}{(\epsilon_a + \epsilon_b) - (\epsilon_r + \epsilon_s)}, \tag{4.3.1}$$

where the capital letters represent the shells that the orbitals belong to. Each sum, for instance $\sum_A$, means summing over all the occupied shells and all magnetic substates within each shell. Roughly speaking, the prefactor 2 comes from the two possible Wick contractions, each carries a (+1) Wick phase. The factor w_{AB} is the

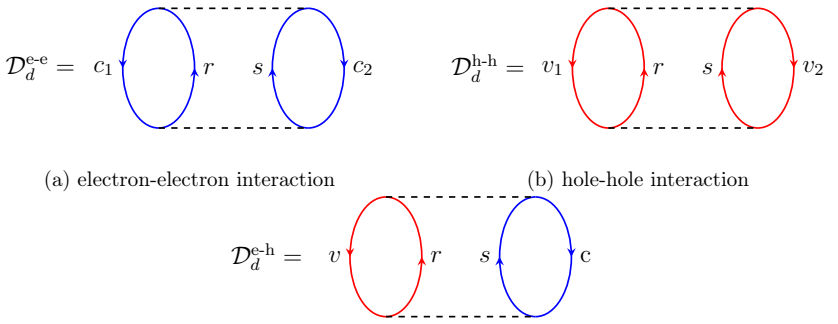

(a) electron-electron interaction

(b) hole-hole interaction

(c) electron-hole interaction

Figure 4.3.1: The three second-order direct Feynman diagrams in the closed-shell MBPT formalism. The first two diagrams in Fig. 4.3.1a and Fig. 4.3.1b are non-zero only for systems with more than one electron and one hole respectively. For a single exciton, $\mathcal{D}_d^{\text{e-e}}$ and $\mathcal{D}_d^{\text{h-h}}$ vanish. The three diagrams share the same angular diagram Fig. 4.3.2.

configuration-averaged weight factor between the two shells A and B

$$w_{AB} = \begin{cases} \frac{n_A}{N_A}\frac{n_B}{N_B}, & \text{if } A \neq B, \\ \frac{n_A}{N_A}\frac{n_B-1}{N_B-1}, & \text{if } A = B. \end{cases} \tag{4.3.2}$$

In the above, $n_{A/B}$ and $N_{A/B}$ follow the same notations as used for V_{HF}, see the discussion right below (3.1.10). From the multipole decomposition (3.3.10), the expression $\mathcal{D}_d$ can be decomposed into radial and angular parts as

$$\mathcal{D}_d = \frac{1}{2}\sum_{AB,RS} w_{AB}\, \frac{X^{k_2}(ab,rs)X^{k_1}(rs,ab)}{(\epsilon_a+\epsilon_b)-(\epsilon_r+\epsilon_s)}\; D_d^{k_2k_1}, \tag{4.3.3}$$

where $D_d^{k_2k_1}$ is the direct angular diagram in Fig. (4.3.2).

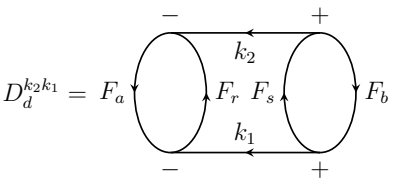

Figure 4.3.2: Direct angular diagram

The k-pole reduced matrix element $X^k(ab,cd)$ of G_{12} has been given in (3.3.9). The calculation of the expression (4.3.3) of the second-order MBPT diagrams becomes straightforward once the angular diagram $D_d^{k_2k_1}$ can be evaluated. The derivation of $D_d^{k_2k_1}$ can be easily done with the angular algebra in Ref. [75], Chapter 2-4. By applying the second theorem of Jucys, Levinson and Vanagas (the JLV2 theorem, see Chapter 4 of Ref. [75]) to the angular lines with k_1 and k_2, we

have

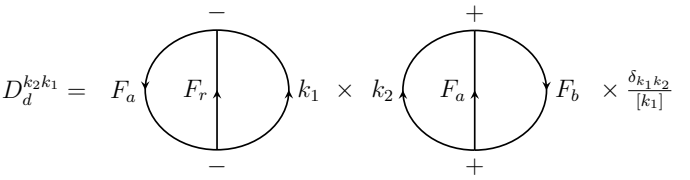

$$= (-1)^{2F_a+(F_a+F_r+k_1)}\ (-1)^{2F_b+(k_1+F_s+F_b)}\ \frac{\delta_{k_1k_2}}{[k_1]}. \tag{4.3.4}$$

One arrives at the second line of (4.3.4) after changing the sign and the direction of the arrow in each of the diagrams above, see Chapter 3 of Ref. [75].

Therefore, the value of the angular diagram $D_d^{k_2k_1}$ is

$$D_d^{k_2k_1} = \frac{(-1)^{F_r-F_a+F_s-F_b}}{[k_1]}\ \delta_{k_1k_2}. \tag{4.3.5}$$

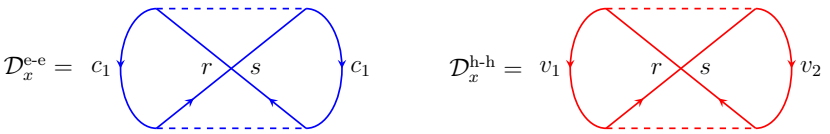

(a) electron-electron interaction

(b) hole-hole interaction

Figure 4.3.3: The two second-order exchange Feynman diagrams in the closed-shell MBPT formalism. These are non-zero only for system with more than one electron (left diagram) or one hole (right diagram) and, just as the direct diagrams, they have the same angular part called $D_x^{k_2k_1}$.

There are two second-order exchange diagrams $\mathcal{D}_x^{\text{e-e}}$ and $\mathcal{D}_x^{\text{h-h}}$ that are $\mathcal{O}(1)$ in $\mathrm{k}\cdot\mathrm{p}$ perturbation, see Fig. 4.3.3. Each of these involves only one type of particle, either electron or hole. The second-order diagrams with similar structure but contain both electron and hole lines are at least $\mathcal{O}((\mathrm{k}\cdot\mathrm{p})^2)$ and we neglect them at this level of computation, as there exist other effects that may be more important. Similar to the direct diagrams, the same expression $\mathcal{D}_x$ for $\mathcal{D}_x^{\text{e-e}}$ and $\mathcal{D}_x^{\text{h-h}}$ can be written as

$$\begin{aligned}\mathcal{D}_x &= -2\sum_{AB,RS} w_{AB}\ \frac{\frac{1}{2}\langle ab|G_{12}|sr\rangle\ \frac{1}{2}\langle rs|G_{12}|ab\rangle}{(\epsilon_a+\epsilon_b)-(\epsilon_r+\epsilon_s)} \\ &= -\frac{1}{2}\sum_{AB,RS} w_{AB}\ \frac{X^{k_2}(ab,sr)X^{k_1}(rs,ab)}{(\epsilon_a+\epsilon_b)-(\epsilon_r+\epsilon_s)}\ D_x^{k_2k_1}.\end{aligned} \tag{4.3.6}$$

Again, the prefactor (-2) results from the Wick phase equal to (-1) and from the fact that there are two equivalent Wick contractions. In (4.3.6), $D_x^{k_2k_1}$ symbolizes

the angular part of which the diagramatic representation is

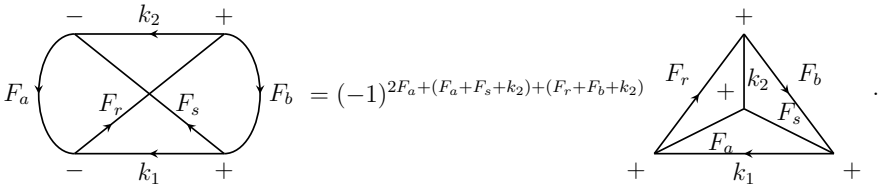

(4.3.7)

Therefore, we arrive at the following expression for the exchange angular diagram

$$D_x^{k_2 k_1} = (-1)^{F_s - F_a + F_r + F_b} \begin{Bmatrix} k_2 & F_s & F_a \\ k_1 & F_r & F_b \end{Bmatrix}. \tag{4.3.8}$$

The word 'exchange' in the case of $\mathcal{D}_x^{\text{e-e}}$ and $\mathcal{D}_x^{\text{h-h}}$ refers to the fact that r and s swap their relative places in X^{k_1} and X^{k_2}. In other words, the states r and s exchange their positions in the Coulomb interaction. The closed-shell exchange diagrams are closely related to the ladder diagrams of the open-shell formalism, Fig. 4.2.5. An explanation of this link was given in conjunction with Fig. 4.2.5. The readers should not confuse $\mathcal{D}_x^{\text{e-e}}$ and $\mathcal{D}_x^{\text{h-h}}$ with the open-shell exchange diagrams that are actually the higher-order $\mathrm{k}\cdot\mathrm{p}$ variants of $\mathcal{D}_x^{\text{e-e}}$ and $\mathcal{D}_x^{\text{h-h}}$. The electron-hole direct diagram $\mathcal{D}_d^{\text{e-h}}$, Fig. 4.3.1c, can be obtained from $\mathcal{D}_d^2$, Fig. 4.2.4a, by joining $c-c'$ and $v-v'$. In fact, the closed-shell second-order correlation energy $E_{\text{LR}}^{(2)}$ below equals to the average $\frac{3}{4}E_{LR}^{(2)}(F_{\text{tot}}=1) + \frac{1}{4}E_{LR}^{(2)}(F_{\text{tot}}=0)$ over the dark and bright exciton states of the open-shell $E_{LR}^{(2)}(F_{\text{tot}})$.

4.3.2 Appliation to trion and biexciton shifts

For an excitonic system, we defined its energy up to second-order MBPT to be

$$E = E_{\text{HF}} + E_{\text{LR}}^{(2)}, \tag{4.3.9}$$

where $E_{\text{LR}}^{(2)}$ denotes the energy contribution from the second-order diagrams in Fig. 4.3.1 and 4.3.3 and

$$E_{\text{LR}}^{(2)} = \mathcal{D}_d^{\text{e-e}} + \mathcal{D}_d^{\text{h-h}} + \mathcal{D}_d^{\text{e-h}} + \mathcal{D}_x^{\text{e-e}} + \mathcal{D}_x^{\text{h-h}}. \tag{4.3.10}$$

Let E_{X}, E_{XX}, E_{X^+} and E_{X^-} be the total energy, up to second-order MBPT, of the single exciton, biexciton, positive and negative trions respectively. A biexciton consists of two pairs of electrons and holes, which are assumed to be in their ground states. During the biexciton emission, one pair of electron and hole recombines and the system relaxes to a single exciton state. The frequency of the emitted photon is the difference between the biexciton and single exciton energy. The process can be easily generalized to describe trion emission. As a result, we define the biexciton

and trion shifts as follows.

$$\begin{aligned}\Delta_{\mathrm{XX}} &= 2E_{\mathrm{X}} - E_{\mathrm{XX}},\\ \Delta_{\mathrm{X}^+} &= (E_{\mathrm{X}} + E_{\mathrm{h}}) - E_{\mathrm{X}^+},\\ \Delta_{\mathrm{X}^-} &= (E_{\mathrm{X}} + E_{\mathrm{e}}) - E_{\mathrm{X}^-},\end{aligned} \tag{4.3.11}$$

where E_{h} and E_{e} are the non-interacting single-particle energy of an electron or a hole. Note that in a system with only a single electron or hole, there is no many-body correction.

For single exciton, only the diagram $\mathcal{D}_d^{\text{e-h}}$ gives non-zero contribution, which can be seen from the expression of the weight factor w_{AB}. The contribution of $\mathcal{D}_d^{\text{e-h}}$ to (positive or negative) trion energy is approximately twice as big as that of this diagram to a single exciton. All five diagrams, including direct and exchange, contribute to $E_{\mathrm{LR}}^{(2)}$ in the case of a biexciton. In the expression (4.3.1), since a and b are the lowest orbitals whereas r and s represent the excited levels, the denominator $(\epsilon_a + \epsilon_b) - (\epsilon_r + \epsilon_s) < 0$. Coupled to the fact that the numerator is positive, the contribution from each direct diagram is negative.

contribution	E_{X}	E_{X^*}	E_{XX}	Δ_{X^*}	Δ_{XX}
E_{HF}	2374.16	4763.48	4748.90	1.41	-0.58
$\mathcal{D}_d^{\text{e-e}}$	0.00	-8.22	-8.17	8.22	8.17
$\mathcal{D}_d^{\text{e-h}}$	-6.83	-10.07	-16.35	3.24	2.69
$\mathcal{D}_d^{\text{h-h}}$	0.00	0.00	-8.17	0.00	8.17
$\mathcal{D}_x^{\text{e-e}}$	0.00	4.11	4.08	-4.11	-4.08
$\mathcal{D}_x^{\text{h-h}}$	0.00	0.00	4.08	0.00	-4.08
total $E_{\mathrm{LR}}^{(2)}$	-6.83	-14.18	-24.53	7.36	10.87

Table 4.1: The various contributions from HF level and the second-order MBPT diagrams to the energy of single exciton E_{X}, trion E_{X^*} and biexciton E_{XX} as well as the biexciton and trion shifts, Δ_{XX} and Δ_{X^*}, for $CsPbBr_3$ nanocrystal of edge length $L = 9.0$ nm. All the values of energy are given in meV. Parameter set 1 was used for the calculation, where $m_e^* = m_h^*$ implies $\Delta_{\mathrm{X}^-} = \Delta_{\mathrm{X}^+} = \Delta_{\mathrm{X}^*}$. The HF-level shifts are almost zero. For a single exciton, only the term $\mathcal{D}_d^{\text{e-h}}$ is nonzero among the second-order diagrams. The exchange diagrams $\mathcal{D}_x^{\text{e-e}}$ and $\mathcal{D}_x^{\text{h-h}}$ have positive values but are generally smaller than their direct counterparts. Most of Δ_{XX} or Δ_{X^*} comes from second-order MBPT.

The exchange diagrams are expected to give positive contribution due to the additional minus sign. However, the absolute value of an exchange diagram is generally smaller than its direct counterpart, as shown in Table 4.1. So in general, $\mathcal{D}_d^{\text{e-e}} + \mathcal{D}_x^{\text{e-e}} < 0$ and $\mathcal{D}_d^{\text{h-h}} + \mathcal{D}_x^{\text{h-h}} < 0$ for the systems with more than one electron or more than one hole respectively. Therefore, one expects that the trion emission, via recombination of an electron-hole pair to a single charge state, has smaller energy than that of a single exciton. For the same reason, the biexciton emission is also

red-shifted w.r.t. the single exciton emission. For biexciton, the contribution from $\mathcal{D}_d^{\text{e-h}}$ is roughly twice and four times that for trions and single exciton respectively. Both $\mathcal{D}_d^{\text{e-e}} + \mathcal{D}_x^{\text{e-e}}$ and $\mathcal{D}_d^{\text{h-h}} + \mathcal{D}_x^{\text{h-h}}$ contribute to the biexciton $E_{LR}^{(2)}$ in comparison with trions. As a consequence, one generally expects also that $\Delta_{\text{XX}} > \Delta_{\text{X}^+}$ or Δ_{X^-}, see Table 4.1 and Fig. 4.3.4.

In Fig. 4.3.4, we plot the biexciton shift Δ_{XX} and trion shifts, Δ_{X^+} for positive trion and Δ_{X^-} for negative trion. Under the assumption that $m_e^* = m_h^*$, Δ_{X^+} and Δ_{X^-} are identical. Since there is no distinction needed to be made between Δ_{X^+} and Δ_{X^-}, sometimes we shall commonly refer to them as Δ_{X^*} when no confusion arises.

size (nm)		$L = 6.0$		$L = 9.0$		$L = 12.0$	
$l_{\text{cut-off}}$	$n_{\text{cut-off}}$	X^*	XX	X^*	XX	X^*	XX
0	9	1.16	2.24	1.13	2.18	1.12	2.16
1	9	12.94	22.54	11.39	19.40	10.31	17.30
2	9	14.94	26.22	13.20	22.67	11.99	20.29
4	9	15.77	27.80	13.96	24.09	12.69	21.61
7	9	15.98	28.22	14.14	24.44	12.86	21.94
10	9	16.03	28.32	14.18	24.53	12.90	22.01
10	1	11.47	19.23	9.63	15.41	8.27	12.68
10	2	15.18	26.51	13.27	22.53	11.90	19.74
10	3	15.78	27.79	13.93	23.96	12.62	21.36
10	6	16.01	28.27	14.16	24.47	12.88	21.96
10	9	16.03	28.32	14.18	24.53	12.90	22.01
1	2	12.85	22.36	11.30	19.18	10.20	17.02

Table 4.2: Convergence of the second-order MBPT energy $E_{\text{LR}}^{(2)}$ for biexciton XX and for trion X^* w.r.t. the angular momentum and principal quantum number cut-off, $l_{\text{cut-off}}$ and $n_{\text{cut-off}}$ respectively. All values $E_{\text{LR}}^{(2)}$ for XX and X^* are given in meV. When the carries stay in the states $1\text{s}_{1/2}^e$ and $1\text{s}_{1/2}^h$, the dominant contribution comes from the p-wave channel, which constitutes about 70% of the total $E_{\text{LR}}^{(2)}$ depending on the size (with $n_{\text{cut-off}} = 9$). By fixing $l_{\text{cut-off}} = 10$, the convergence w.r.t. $n_{\text{cut-off}}$ is extremely rapid with $n_{\text{cut-off}} = 3$ giving more than 95% of the total result.

The dashed green curves on Fig. 4.3.4 give the biexciton and trion shifts at HF level. Δ_{X^*} is slightly positive but remains less than about 1.5 meV. Δ_{XX} is almost identically zero for size $L \geq 6$ nm and becomes slightly negative for small L. Evidently, there is no difference in the emission of biexciton or trions compared to that of single exciton at HF level. The results here are in accordance with Ref.

[113]. We conclude also that to obtain the biexciton or trion shift, one has to go beyond mean-field level.

The second-order MBPT results in Fig. 4.3.4 demonstrate that trion and biexciton emission is at a lower energy than that of a single exciton. Since the Coulomb interaction $\langle ab|G_{12}|rs\rangle$ scales as L^{-1}, the second-order energy $E_{\mathrm{LR}}^{(2)}$ increases as L decreases. Δ_{XX} and Δ_{X^*} become bigger as L goes smaller, a fact that is also observed experimentally as shown in Fig. 4.3.5. However, it does not mean that the system is more correlated at small L. The ratio $E_{\mathrm{LR}}^{(2)}/E_{\mathrm{HF}}$ becomes smaller when L decreases, which implies that for small sizes, the correlation energy is less important in the total energy of the system.

The biexciton receives a bigger shift than trions, which has been argued for earlier. The difference between Δ_{XX} and Δ_{X^*} becomes less significant at large L. This may already be an indication that the current second-order MBPT is not sufficient since at large L, the system becomes more and more correlated and a higher-order method seems needed.

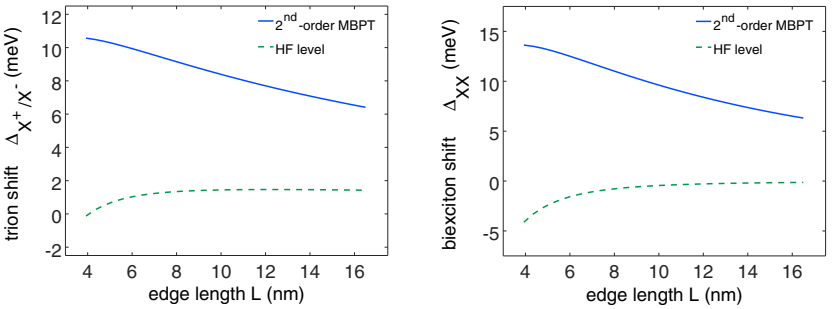

(a) Trion shifts Δ_{X^*} (or $\Delta_{\mathrm{X}^+/\mathrm{X}^-}$) (b) Biexciton shift Δ_{XX}

Figure 4.3.4: The calculated biexciton and trion shifts versus edge length L for $CsPbBr_3$. Dashed green line: HF level, solid blue line: second-order MBPT. The dashed lines show that the biexciton or trion shifts equal to almost zero at HF level, which remains true for any mean-field method [113]. The nonzero Δ_{X^*} and Δ_{XX} are essentially the result of correlation energy.

Regarding the trion data, the theoretical curves show a reasonable agreement with the measurements, see Fig. 4.3.5a for $CsPbBr_3$ and Fig. 4.3.6a for $CsPbI_3$. The theoretical values are about 1.5 to 2.0 times less than the experimental ones. By truncating at second-order MBPT, we have underestimated the true correlation energy. From the calculation of Δ_{LR} in the previous section, the first- plus second-order MBPT captures about 60% of the correlation energy that was obtained by using variational method [106]. Thus, we expect the same level of underestimation for the trion shift, and perhaps biexciton shift.

The biexciton shifts for $CsPbI_3$ also show some qualitative agreement between the theoretical prediction and the experimental data [135, 80]. The theoretical values are about half of the measured Δ_{XX}, which means that the ratio between experiments and theory is a bit bigger than for trions. With more particles present,

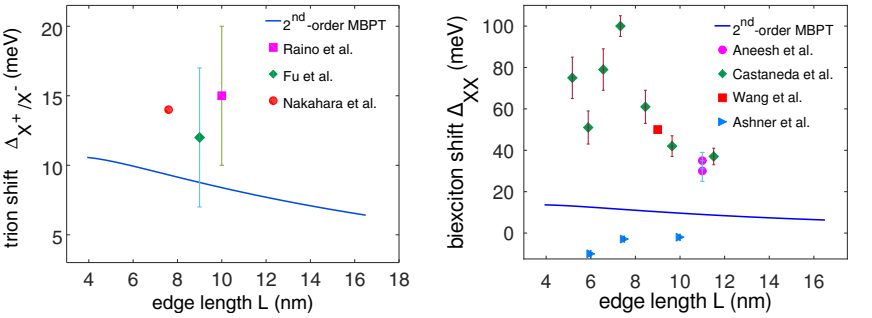

(a) Trion shift (b) Biexciton shift

Figure 4.3.5: Biexciton Δ_{XX} and trion Δ_{X^+/X^-} shifts versus edge length L for $CsPbBr_3$. Solid blue line: theoretical calculation at second-order MBPT. Experimental data for trion: Raino et al., Ref. [100]; Fu et al., Ref. [52]; Nakahara et al., Ref. [86]. Experimental data for biexciton: Aneesh et al., Ref. [3]; Castaneda et al., Ref. [21]; Wang et al., Ref. [126]; Ashner et al., Ref. [5].

the many-body correlation may be more important for the biexciton system. Therefore, a second-order method seems even more insufficient. To achieve a quantitative prediction for Δ_{XX} as well as Δ_{X^*}, one will need an all-order MBPT method (e.g. configuration interaction).

The second-order MBPT does not work very well in the case of $CsPbBr_3$ biexciton shifts. Before moving on to discuss other sources of theoretical errors, we wish to make some remarks regarding the experimental data. The values for L of Castaneda et al., Ref. [21], were estimated from a linear relationship between the nanocrystal volume L^3 and the one-photon absorption cross-section $\sigma^{(1)}$. The actual L values at small $\sigma^{(1)}$ could have been underestimated or overestimated. This may explain the extreme fluctuation of Δ_{XX} in the range $L < 8$ nm.

Schulenberger et al. [112] claimed that the upper bound for Δ_{XX} should be around 20 meV for $CsPbBr_3$ nanocrystals of averaged edge length $L = 7.5 \pm 1$ nm. In a recent publication by Ashner et al. [5], the biexciton shifts were determined to be some small blue shifts on the order of a few meV by using some novel fitting method published in Ref. [6]. While the experimental Δ_{XX} values are in contradiction with one another, we would like to note that the extraction of the biexciton shifts from the transient absorption (TA) or time-resolved photoluminescence (TRPL) spectra relies heavily on post-measurement fitting methods. The results for Δ_{XX} of $CsPbBr_3$, Fig. 4.3.5b, were not direct observations from the high-resolution PL spectra (low-temperature single-dot spectroscopy). As a result, they may be prone to some errors in the fitting methods.

Here, all the calculated energy shifts Δ_{XX} and $\Delta_{X^+}/\Delta_{X^-}$ are under the basic assumption that the biexciton and trions have relaxed to their ground state. As suggested in the literature by Yumoto et al. [139], the formation of hot excitons may have an effect on enhancing the observed red-shift.

Katan et al. [67] pointed out, from first-principle calculations, that the high-

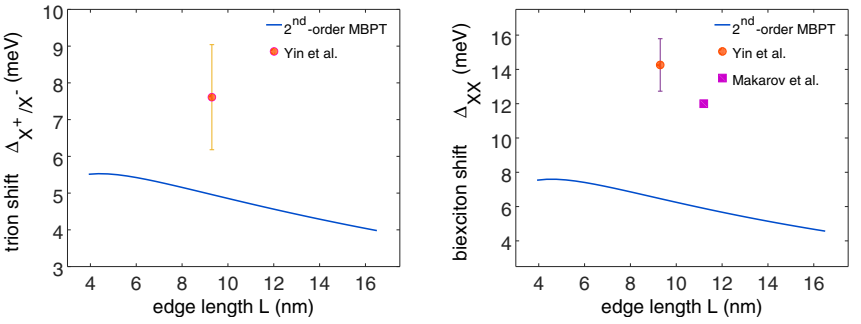

(a) Trion shift (b) Biexciton shift

Figure 4.3.6: Biexciton Δ_{XX} and trion Δ_{X^+/X^-} shifts versus edge length L for $CsPbI_3$. Solid blue line: theoretical calculation at second-order MBPT. Experimental data: Yin et al., Ref. [135]; Makarov et al., Ref. [80].

frequency dielectric 'constant' depends on the thickness z of the quantum well when z varies from one to eight atomic layers. Generally speaking, ε_∞ becomes smaller when there are fewer atomic layers. An increase in thickness naturally leads to more screening and, thus, a higher value of the dielectric function. Perovskites are rather ionic materials of which the dielectric function $\varepsilon(\vec{r},\omega)$ depends greatly on the frequency. It brings about the fact that the high-frequency dielectric constant ε_∞ is much smaller than the static dielectric constant ε_0.

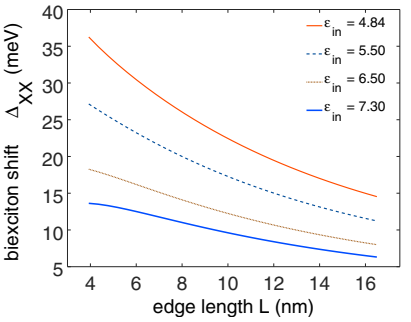

Figure 4.3.7: Biexciton shift versus edge length L. The various curves correspond to the different choices of ε_{in}.

Instead of just taking the bulk effective dielectric constant ε_{eff}, we speculate that there possibly is some dependence of ε_{in} on the size L of the nanocrystal and on the excitation energy involved in the second-order diagrams in Fig. 4.3.1 and Fig. 4.3.3. Each reduced matrix element X^k is inversely proportional to ε_{in}. From the expressions (4.3.1) and (4.3.6) for the direct and exchange interaction, we have the proportionality between $E^{(2)}_{LR}$ and $1/\varepsilon^2_{in}$. A variation of $x\%$ error in ε_{in} results in $2x\%$ error in $E^{(2)}_{LR}$.

In Fig. 4.3.7, we demonstrate how the biexciton shift Δ_{XX} changes as ε_{in} varies. The optical dielectric constant $\varepsilon_{opt} = 4.84$, see Ref. [34], was taken to be the lower limit for ε_{in}. Even though the same value of ε_{in} has been used for all sizes, in general, the current version of our code allows the calculations with ε_{in} as a function of L.

As the last topic of this section, we provide the calculations of Δ_{XX} and $\Delta_{X^+}/\Delta_{X^-}$

by using two parameter sets for $CsPbBr_3$ in Subsection 3.4.1. Unless $m_e^* = m_h^*$, one generally expects Δ_{X^+} and Δ_{X^-} to differ from each other. This is seen in Fig. 4.3.8a, notably at the small sizes $L < 6$ nm. The unequal effective masses ($m_e^* \neq m_h^*$) of parameter set 2 also make Δ_{X^+} and Δ_{X^-} to deviate from Δ_{X^*}, which was calculated using parameter set 1. However, the average $(\Delta_{X^+} + \Delta_{X^-})/2$ (parameter set 2) turns out to be very close to Δ_{X^*}. The biexciton shifts Δ_{XX} are also very similar between the two sets. At $L = 9$ nm, Δ_{XX} values are within 5% of one another. With these observations in mind, we conclude that, once the reduced mass μ is known [132], the exact values of effective masses do not greatly affect the basic outcomes of the theory, with the assumption that m_e^* and m_h^* are approximately equal.

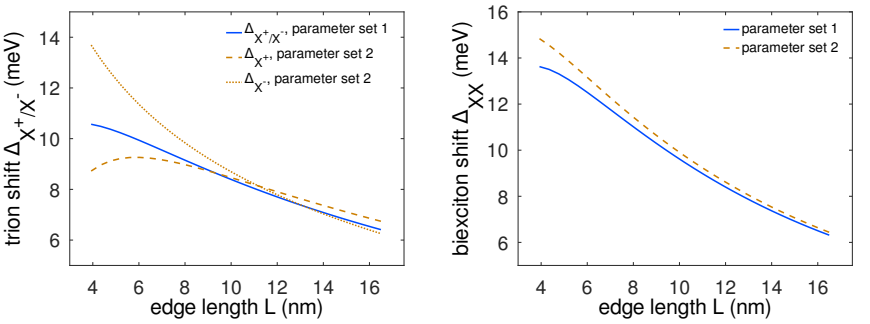

(a) Trion shifts (b) Biexciton shift

Figure 4.3.8: Biexciton and trion shifts versus edge length L. The calculations were done at second-order MBPT by using the two parameter sets (3.4.9) and (3.4.10). We note the small difference between the two parameter sets, especially for $L > 6$ nm. For trion shifts, Δ_{X^+} (positive trion) and Δ_{X^-} (negative trion) deviate from one another, more at the small sizes. This fact, however, does not change the conclusion when the theory is compared to experiments.

Together with the inconsistency of the measured Δ_{XX}, the uncertainty of the basic parameters, such as the correct effective dielectric constant and the effective masses, makes it difficult to determine the appropriateness of using the second-order MBPT. However, when an all-order method for calculating correlation energy is in place, one will be in better position to judge the correctness of the parameters used. This all-order method will also help us assess any experimental-theoretical discrepancy, which we leave for future research.

Chapter 5

Electron-photon interaction

This chapter is motivated by the available published experimental results on the radiative lifetime τ of a single exciton and the one-photon absorption (OPA) cross-section $\sigma^{(1)}$ of perovskite nanocrystals. It turns out that, for the perovskite materials, the lifetime τ stays in the sub nanosecond range, which is much shorter compared to the more conventional semiconductors [71]. It means that the gap between radiative rate and other non-radiative rates is reduced, which may be one of the contributing factors for the bright emission of the perovskite nanocrystal. Their large OPA cross-section $\sigma^{(1)}$ may also have some important implication for being a good solar cell absorber [24].

By using the electron-photon Hamiltonian in the second-quantized form, see Section 5.1, we derive in Section 5.2 the electron-photon matrix elements and their corresponding Feynman diagrams for the interband and intraband transitions. The amplitudes and transition rates at Hartree-Fock (HF) level will be given in Section 5.3. From these quantities, one obtains the lifetime τ_{HF} and the OPA cross-section $\sigma^{(1)}_{\mathrm{HF}}$. It is rather obvious that the HF-level calculations are not sufficient for describing nanocrystals in the intermediate or weak confinement regime. Due to the intercarrier Coulomb interaction, the electron and hole become strongly correlated. Section 5.4 focuses on the lowest-order MBPT corrections to the single-photon processes. These lowest-order corrections turn out to be analogous to the second-order vertex correction to the exchange interaction in Fig. 4.2.6. The relevant Feynman diagrams and their expressions are provided in Subsection 5.4.1. The calculations of the lifetime $\tau^{(1)}$ and cross-section $\sigma^{(1)}$ up to first-order MBPT will be compared against the measurements in the last two subsections. There, we shall also discuss the enhancement from the vertex corrections as well as the variation of $\tau^{(1)}$ and $\sigma^{(1)}$ w.r.t. the size L and the Kane parameter E_{p}.

5.1 Electron-photon Hamiltonian

In minimal coupling [14], the Hamiltonian of electron-photon interaction takes the following form

$$H_{e-p} = -\frac{q_e}{m_0}\vec{A}(\vec{r})\cdot\vec{p} + \frac{q_e^2}{2m_0^2}\vec{A}^2(\vec{r}), \tag{5.1.1}$$

where $\vec{A}(\vec{r})$ is the electromagnetic vector potential in a given medium. Here, q_e and m_0 represent the electron charge and free mass. In atomic units, $m_0 = 1$ and $q_e = 1$. Hence, we shall omit the prefactor q_e/m_0 for now. The first term in H_{e-p},

$$H_{A\cdot p} = -\vec{A}(\vec{r}) \cdot \vec{p}, \tag{5.1.2}$$

contains the momentum operator $\vec{p}$ and dominates the electron-photon transition. A discussion on the second term $\frac{1}{2}\vec{A}^2(\vec{r})$ can be found in Chapter 13 of Ref. [69].

To calculate the transition amplitude, we choose the second-quantized approach. In a general medium, the vector potential is a solution of the generalized Helmholtz equation. In treating the dielectric screening, we consider the case of a single dielectric sphere surrounded by a homogenous medium. The electromagnetic field inside the sphere stays parallel to the field at infinity but differs by a multiplicative factor f_ε, which we call the screening factor. Given that ε_{out} is the dielectric constant of the medium around the dielectric sphere of dielectric constant ε_{in}, one has

$$f_\varepsilon = \frac{3\varepsilon_{\text{out}}}{\varepsilon_{\text{in}} + 2\varepsilon_{\text{out}}}. \tag{5.1.3}$$

For perovskites, the dielectric function varies dramatically with respect to the frequency of the incoming light [47, 103]. Since light sources used in most of the relevant experiments (e.g. pump-probe spectroscopy) are in optical range, the dielectric 'constant' ε_{in} in the screening factor f_ε in (5.1.3) is taken to be the optical value ε_{opt}. Therefore,

$$f_\varepsilon = \frac{3\varepsilon_{\text{out}}}{\varepsilon_{\text{opt}} + 2\varepsilon_{\text{out}}}. \tag{5.1.4}$$

The dielectric screening factor of a cube, when averaged over its orientation and a number of test wave functions, shows about 6% difference from that of a sphere [127]. A perfect cube or sphere is an idealized geometry of an actual nanoparticle. In reality, nanocrystals always come with some surface roughness and other sources of shape deformation. For this reason, we shall continue to use the dielectric screening f_ε of a sphere as an estimate for that of a synthesized nanocrystal.

The vector potential $\vec{A}(\vec{r})$ in second-quantized form is

$$\vec{A}(\vec{r}) = \sum_{\vec{k},\sigma} f_\varepsilon \; A_0(\omega) \; \left(e^{i\vec{k}\cdot\vec{r}} \hat{e}_\sigma b_{\vec{k},\sigma} + e^{-i\vec{k}\cdot\vec{r}} \hat{e}^*_\sigma b^\dagger_{\vec{k},\sigma} \right), \tag{5.1.5}$$

where $b_{\vec{k},\sigma}/b^\dagger_{\vec{k},\sigma}$ represents the annihilation/creation of a photon with wave vector $\vec{k}$ and polarization σ. The positive real function $A_0(\omega)$ is the magnitude of the vector potential.

The Hamiltonian $H_{A\cdot p}$ can be written in second-quantized form as

$$H_{A\cdot p} = -\sum_{ij,\vec{k}\sigma} f_\varepsilon A_0(\omega) \left(\langle i| e^{i\vec{k}\cdot\vec{r}} \hat{e}_\sigma \cdot \vec{p} |j\rangle \; i^\dagger j \; b_{\vec{k}\sigma} + \langle i| e^{-i\vec{k}\cdot\vec{r}} \hat{e}^*_\sigma \cdot \vec{p} |j\rangle \; b^\dagger_{-\vec{k}\sigma} i^\dagger j \right). \tag{5.1.6}$$

The states $|i\rangle$ and $|j\rangle$ are n-component (n=2 or 4) $\mathrm{k}\cdot\mathrm{p}$ total wave functions, which are the solutions of the radial HF Eqs. (3.3.11)-(3.3.12). However, we shall focus this chapter on the 4×4 $\mathrm{k}\cdot\mathrm{p}$ model (where n=2) for perovskites.

The first term in (5.1.6) contains $i^\dagger j\, b_{\vec{k}\sigma}$ describes the absorption of a photon of frequency $\omega = c|\vec{k}|$ and polarization σ during which an electron makes a transition from the state $|j\rangle$ to $|i\rangle$. Here $c = c_0/n_{\text{ref}}$ where $n_{\text{ref}} = \sqrt{\varepsilon_{\text{out}}}$ is the refractive index. The second term is conjugated to the first and describes de-excitation of an electron from $|j\rangle$ to $|i\rangle$ by emitting a photon with $\omega = c|\vec{k}|$ and σ. These two terms can be depicted graphically in the following Feynman diagrams (omitting the prefactor $-f_\varepsilon A_0(\omega)$).

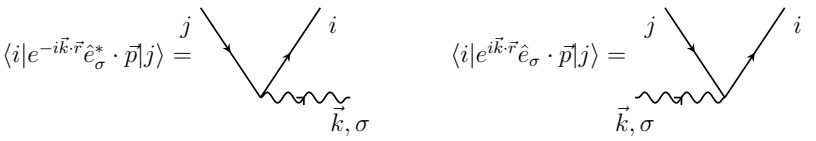

(a) emission (b) absorption

Figure 5.1.1: Feynman diagrams corresponding to the two terms in (5.1.6). The photon has wave vector $\vec{k}$ and polarization σ. The letters i and j denote any arbitrary valence and conduction states, occupied or unoccupied.

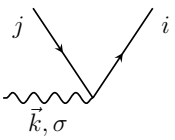

Figure 5.1.2: The electron-photon interaction vertex.

Each of the diagrams in Fig. 5.1.1 can be called an electron-photon vertex. These diagrams describe the transition of an electron from an initial state $|j\rangle$ to a final state $|i\rangle$ via either absorbing or emitting a photon. They are among the basic ingredients to build Feynman diagrams for HF-level or higher-order one-photon processes or for multi-photon interactions. Whether a photon is being absorbed or emitted, the absolute value of the transition amplitude is the same. In what follows, we shall omit the arrow on the photon propagator for simplicity and an electron-photon interacting vertex is denoted as in Fig. 5.1.2.

5.2 Electron-photon matrix element

In the optical range, the wavelength of light $\lambda = 2\pi/|\vec{k}|$ is about several hundreds nanometers and is much larger than the size of a nanocrystal, which typically comes out at most around 20 nm. This fact justifies the electric dipole approximation $e^{i\vec{k}\cdot\vec{r}} = 1$. With this, we define the electron-photon matrix element as

$$\mathcal{M}^{e-p}_{i,j} = \begin{cases} -f_\varepsilon A_0(\omega)\ \langle i|\hat{e}_\sigma \cdot \vec{p}|j\rangle, & \text{for absorption,} \\ -f_\varepsilon A_0(\omega)\ \langle i|\hat{e}^*_\sigma \cdot \vec{p}|j\rangle, & \text{for emission,} \end{cases} \tag{5.2.1}$$

in which an electron makes a transition from $|j\rangle$ to $|i\rangle$. The states $|i\rangle$ and $|j\rangle$ are the solutions of Eq. (4.1.3). Their total wave functions can be expressed as

$$\begin{aligned} |i\rangle &= \frac{1}{r}\sum_{\mu} R_\mu(r)|(l_\mu J_\mu)F_i M_i\rangle, \\ |j\rangle &= \frac{1}{r}\sum_{\nu} R_\nu(r)|(l_\nu J_\nu)F_j M_j\rangle. \end{aligned} \tag{5.2.2}$$

In this chapter, we also perform the angular-radial separation for all electron-photon matrix elements. It proves extremely useful for reducing the computational time of the vertex correction in Section 5.4 by one to two orders of magnitude. The two expressions in (5.2.1) are identical except for the polarization vectors $\hat{e}_\sigma$ versus $\hat{e}^*_\sigma$. Hence, we demonstrate the angular-radial separation only for $\langle i|\hat{e}_\sigma \cdot \vec{p}|j\rangle$ of the absorption vertex. In the spherical tensor coordinates, the dot product $\hat{e}_\sigma \cdot \vec{p}$ can be expressed as

$$\hat{e}_\sigma \cdot \vec{p} = \sum_{m=-1}^{1} e^*_{\sigma,m}\ p_m = \sum_{m=-1}^{1} (-1)^m e_{\sigma,-m}\ p_m. \tag{5.2.3}$$

If the momentum operator $\vec{p}$ acts on the Bloch functions, which are implicit in $\vec{J}$ of the angular states $|(l_\mu J_\mu)F_i M_i\rangle$ and $|(l_\nu J_\nu)F_j M_j\rangle$, it gives rise to the interband type matrix element $\mathcal{M}^{\text{inter}}_{i,j}$. When $\vec{p}$ acts on the envelope parts of the total wave functions in (5.2.2), the matrix element, $\mathcal{M}^{\text{intra}}_{i,j}$, is called intraband type.

$$\mathcal{M}^{e-p}_{i,j} = \mathcal{M}^{\text{inter}}_{i,j} + \mathcal{M}^{\text{intra}}_{i,j}, \tag{5.2.4}$$

where the interband and intraband type transition matrix elements are given as

$$\mathcal{M}^{\text{inter}}_{i,j} = -f_\varepsilon A_0(\omega) \sum_{\mu\nu,m} \int R_\mu(r) R_\nu(r)\ dr\ \ \hat{e}^*_{\sigma,m}\langle(l_\mu \underline{J_\mu})F_i M_i|p_m|(l_\nu \underline{J_\nu})F_j M_j\rangle, \tag{5.2.5}$$

$$\mathcal{M}^{\text{intra}}_{i,j} = -f_\varepsilon A_0(\omega) \sum_{\mu\nu,m} \int \frac{1}{r} R_\mu(r)\ \hat{e}^*_{\sigma,m}\langle(\underline{l_\mu} J_\mu)F_i M_i|p_m|(\underline{l_\nu} J_\nu)F_j M_j\rangle\ \frac{1}{r} R_\nu(r)\ r^2 dr. \tag{5.2.6}$$

The underlined angular components in (5.2.5) and (5.2.6) mark the ones that p^1_q operates on. Additionally, the term $\langle(\underline{l_\mu} J_\mu)F_i M_i|p_m|(\underline{l_\nu} J_\nu)F_j M_j\rangle$ in (5.2.6) is a radial operator in the space of envelope functions.

5.2.1 Interband type transition

In this subsection, we analyze the matrix element $\mathcal{M}_{i,j}^{\text{inter}}$ in (5.2.5). Applying Wigner-Eckart Theorem leads to

$$\langle (l_\mu \underline{J_\mu}) F_i M_i | p_m | (l_\nu \underline{J_\nu}) F_j M_j \rangle = \begin{array}{c} F_i M_i \quad + \quad F_j M_j \\ \longleftarrow \quad | \\ \qquad\quad 1, m \end{array} \times \langle (l_\mu \underline{J_\mu}) F_i || \vec{p} || (l_\nu \underline{J_\nu}) F_j \rangle. \tag{5.2.7}$$

By making use of the results in Section B.3 of the appendix, we have

$$\langle (l_\mu \underline{J_\mu}) F_i || \vec{p} || (l_\nu \underline{J_\nu}) F_j \rangle = \chi_2(l_\mu J_\mu F_i, l_\nu J_\nu F_j)\ \langle J_\mu || \vec{p} || J_\nu \rangle, \tag{5.2.8}$$

where the coefficient $\chi_2(l_\mu J_\mu F_i, l_\nu J_\nu F_j)$ can be found in (B.3.6).

Note that when $\vec{p}$ acts on the pseudo-spin $\vec{J}$ of the Bloch part, it only operates on the Bloch orbital angular momentum $\vec{L}$, not the spin $\vec{S}$. This means that

$$\langle J_\mu || \vec{p} || J_\nu \rangle = \langle (S_\mu \underline{L_\mu}) J_\mu || \vec{p} || (S_\nu \underline{L_\nu}) J_\nu \rangle = \chi_2(S_\mu L_\mu J_\mu, S_\nu L_\nu J_\nu)\ \langle L_\mu || \vec{p} || L_\nu \rangle. \tag{5.2.9}$$

Implicit in $\chi^2(S_\mu L_\mu J_\mu, S_\nu L_\nu J_\nu)$ is the spin selection rule.

The interband matrix element (5.2.5) can be written explicitly in radial-angular decomposition as

$$\mathcal{M}_{i,j}^{\text{inter}} = -f_\varepsilon A_0(\omega)\ \textstyle\sum_m \hat{e}^*_{\sigma,m} \begin{array}{c} F_i M_i \quad + \quad F_j M_j \\ \longleftarrow \quad | \\ \qquad\quad 1, m \end{array} \times \quad \mathcal{R}_{i,j}^{\text{inter}}. \tag{5.2.10}$$

In the above, the radial part is

$$\mathcal{R}_{i,j}^{\text{inter}} = \sum_{\mu\nu} \int R_\mu(r) R_\nu(r)\ dr \quad \chi_2(l_\mu J_\mu F_i, l_\nu J_\nu F_j)\ \chi_2(S_\mu L_\mu J_\mu, S_\nu L_\nu J_\nu)\ \langle L_\mu || \vec{p} || L_\nu \rangle. \tag{5.2.11}$$

If L_μ and L_ν are the Bloch angular momenta of the conduction and valence states, $\langle L_\mu || \vec{p} || L_\nu \rangle = \langle c || \vec{p} || v \rangle$ can be expressed in terms of the Kane parameter E_{p} as

$$|\langle L_\mu || \vec{p} || L_\nu \rangle| = \sqrt{\frac{3}{2} E_{\text{p}}}. \tag{5.2.12}$$

The radial term $\mathcal{R}_{i,j}^{\text{inter}}$ and, therefore, $\mathcal{M}_{i,j}^{\text{inter}}$ are proportional to $\sqrt{E_{\text{p}}}$. As a result, the interband transition strength, which is proportional to $|\mathcal{M}_{i,j}^{\text{inter}}|^2$, depends linearly on E_{p}.

In the effective mass model, i.e. the wave function has no $\mathrm{k}\cdot\mathrm{p}$ mixing, the selection rule $l_\mu = l_\nu$ that is contained in $\chi^2(l_\mu J_\mu F_i, l_\nu J_\nu F_j)$ means that only transition such as $1\mathrm{s}^e - 1\mathrm{s}^h$, $1\mathrm{p}^e - 1\mathrm{p}^h$ etc. are allowed. When the $\mathrm{k}\cdot\mathrm{p}$ mixing is taken into account, the selection rule no longer holds due to the presence of the small $\mathrm{k}\cdot\mathrm{p}$ components. However, as one will see later, the dominant transitions are still the ones with $l_\mu = l_\nu$.

5.2.2 Intraband type transition

Now, let us consider the intraband matrix element $\mathcal{M}^{\rm intra}_{i,j}$.

By using the results in (B.3.2)-(B.3.3), one has

$$\langle(\underline{l_\mu}J_\mu)F_iM_i|p_m|(\underline{l_\nu}J_\nu)F_jM_j\rangle = \underbrace{F_iM_i \quad + \quad F_jM_j}_{1,m} \times\langle(\underline{l_\mu}J_\mu)F_i||\vec{p}||(\underline{l_\nu}J_\nu)F_j\rangle, \tag{5.2.13}$$

where, on the RHS of the above expression,

$$\langle(\underline{l_\mu}J_\mu)F_i||\vec{p}||(\underline{l_\nu}J_\nu)F_j\rangle = \chi_1(l_\mu J_\mu F_i, l_\nu J_\nu F_j)\langle l_\mu||\vec{p}||l_\nu\rangle. \tag{5.2.14}$$

As, defined in (B.1.6), the reduced matrix element $\langle l_\mu||\vec{p}||l_\nu\rangle = -i\langle l_\mu||\vec{\nabla}||l_\nu\rangle$, is a radial operator acting on $R_\mu(r)$ and $R_\nu(r)$ in (5.2.6). The coefficient $\chi_1(l_\mu J_\mu F_i, l_\nu J_\nu F_j)$ carries the selection rule δ_{J_μ,J_ν} for the $\mathrm{k}\cdot\mathrm{p}$ components.

We define the following radial integral

$$\mathcal{R}^{\rm intra}_{\mu i,\nu j} = \gamma_\mu \int \frac{1}{r}R_\mu(r)\ \langle l_\mu||\vec{p}||l_\nu\rangle\ \frac{1}{r}R_\nu\ r^2dr. \tag{5.2.15}$$

Depending on which band is involved in the intraband matrix element, $\gamma_\mu = \gamma_\nu$ is equal to either γ_h if $\mu = \nu = 1$ or γ_e if $\mu = \nu = 2$. The parameters γ_e and γ_h also appear in (2.2.32). In the effective mass approximation, γ_μ should be the inverse effective mass, $1/m^*_e$ or $1/m^*_h$, of the corresponding band. This is the basic result from Ref. [69], Chapter 13. Essentially, the factors $1/m^*_e$ and $1/m^*_h$ represent the $\mathrm{k}\cdot\mathrm{p}$ corrections from other bands to the momentum matrix element. The 2-component solutions of Eq. (4.1.3), where $H_{\mathrm{k}\cdot\mathrm{p}}$ is given in (2.2.32), have already contained the $\mathrm{k}\cdot\mathrm{p}$ correction from the $s_{1/2}$ to the $p_{1/2}$ band and vice versa. Therefore, we have to exclude their contributions to get the prefactor γ_μ to be γ_e (for $s_{1/2}$ band) or γ_h (for $p_{1/2}$ band) in the $\mathrm{k}\cdot\mathrm{p}$ model.

Based on the form of $\langle l_\mu||\vec{\nabla}||l_\nu\rangle$ in (B.1.6), we have $l_\mu = l_\nu \pm 1$, which is the usual selection rule for an atomic transition. Depending on the exact relation between l_μ and l_ν, there are two explicit forms for $\mathcal{R}^{\rm intra}_{\mu i,\nu j}$ in (5.2.15).

$$\mathcal{R}^{\rm intra}_{\mu i,\nu j} = \begin{cases} i\sqrt{l_\nu}\gamma_\nu \displaystyle\int \left(-R_\mu(r)\frac{dR_\nu}{dr} - \frac{l_\nu}{r}R_\mu(r)R_\nu(r)\right)dr, & \text{if } l_\mu = l_\nu - 1, \\ i\sqrt{l_\mu}\gamma_\mu \displaystyle\int \left(\ R_\mu(r)\frac{dR_\nu}{dr} - \frac{l_\mu}{r}R_\mu(r)R_\nu(r)\right)dr, & \text{if } l_\mu = l_\nu + 1. \end{cases} \tag{5.2.16}$$

The intraband matrix element is thus

$$\mathcal{M}^{\rm intra}_{i,j} = -f_\varepsilon A_0(\omega)\ \sum_m \hat{e}^*_{\sigma,m} \underbrace{F_iM_i \quad + \quad F_jM_j}_{1,m} \times \quad \mathcal{R}^{\rm intra}_{i,j}, \tag{5.2.17}$$

where the radial part of (5.2.17) is given to be

$$\mathcal{R}^{\rm intra}_{i,j} = \sum_{\mu\nu} \chi_1(l_\mu J_\mu F_i, l_\nu J_\nu F_j)\ \mathcal{R}^{\rm intra}_{\mu i,\nu j}. \tag{5.2.18}$$

The interband term (5.2.10) and intraband terms (5.2.17) have the same angular part. Let

$$\mathcal{R}^{e-p}_{i,j} = \mathcal{R}^{\rm inter}_{i,j} + \mathcal{R}^{\rm intra}_{i,j}. \tag{5.2.19}$$

In fact, $\mathcal{R}^{e-p}_{i,j}$ can be treated as the reduced matrix element of $\vec{p}$ between the two coupled state $|i\rangle$ and $|j\rangle$.

The radial-angular decomposition of the electron-photon matrix element is

$$\mathcal{M}^{e-p}_{i,j} = -f_\varepsilon A_0(\omega,\vec{r})\ \sum_m \hat{e}^*_{\sigma,m}$$

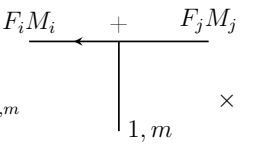

$$\times\quad \mathcal{R}^{e-p}_{i,j}. \tag{5.2.20}$$

With $\mathcal{M}^{e-p}_{i,j}$ and $\mathcal{R}^{e-p}_{i,j}$ as established in (5.2.20) and (5.2.19), we can now proceed to calculate the radiative lifetime τ and the one-photon absorption cross-section $\sigma^{(1)}$.

5.3 One-photon processes at Hartree-Fock level

We consider in this subsection the spontaneous emission and one-photon absorption (OPA). The two physical quantities of interest are the radiative lifetime τ and the OPA cross-section $\sigma^{(1)}$. To calculate τ and $\sigma^{(1)}$, we make use of the results of Subsection 5.2 for the transition amplitudes of the electron-photon Hamiltonian $H_{A\cdot p}$ in (5.1.6). At the current level, we note that the total wave functions $|i\rangle$ and $|j\rangle$ that enter the matrix element in (5.2.20) are the solutions of the HF Eq. (4.1.3). Hence, the transition amplitudes in (5.3.5) and (5.3.14), which are depicted graphically in Fig. 5.3.1, are also at HF level. The lowest-order MBPT corrections to the HF calculations will be shown in Section 5.4. By using Fermi golden rule, one can obtain the expressions for the lifetime τ and one-photon cross-section $\sigma^{(1)}$, which will be given in Subsections 5.3.1 and 5.3.2 respectively.

(a) emission (b) absorption

Figure 5.3.1: Single-photon interband transitions: absorption (left diagram) and emission (right diagram). Here, c and v denote an electron (conduction) state and a hole (valence) state respectively.

Similar to the previous chapters, we also sum over the angular part analytically. Doing this leads to reducing from the full 3-D problem to a 1-D radial problem and significantly improve the numerical efficiency, which is particularly advantageous in the calculations of the vertex corrections in Section 5.4.

5.3.1 Spontaneous emission

During spontaneous emission, an electron interacts with the vacuum electromagnetic (EM) field in a medium with dielectric constant ε_{out}. The second-quantized form of the EM field has

$$A_0(\omega) = A_{EM} = \sqrt{\frac{\hbar}{2V_0\varepsilon_0}}\ \frac{1}{\sqrt{\omega\varepsilon_{\text{out}}}}. \tag{5.3.1}$$

The polarization $\hat{e}_\sigma$ is transversal, i.e. there are two modes indexed by $\sigma = 1, 2$ and each polarization vector $\hat{e}_\sigma$ is perpendicular to $\vec{k}$.

Let $|J\rangle$ and $|I\rangle$ be the initial and final quantum states of the total excitonic system. In considering the spontaneous emission of a single exciton, the exciton state $|J\rangle$ has its total angular momentum and magnetic quantum number $(F_{\text{tot}}, M_{\text{tot}})$ and the final state $|I\rangle = |\varnothing\rangle$, which is the ground state of a nanocrystal. The transition from $|J\rangle$ to $|I\rangle$ is accompanied by the creation of a photon.

Using the Fermi golden rule [27, 102], we can define the transition rate Γ_{IJ}, i.e. the transition probability per unit time, from $|J\rangle$ to $|I\rangle$ to be

$$\Gamma_{IJ} = \frac{2\pi}{\hbar}\sum_\sigma \iint |\mathcal{A}_{I,J}|^2\ \delta(E - E_{JI})\ \rho(E)\ d\Omega\ dE. \tag{5.3.2}$$

In (5.3.2), $\mathcal{A}_{I,J}$ stands for the transition amplitude from $|J\rangle$ to $|I\rangle$. The integrals over E and Ω together with the sum over the polarization σ means summing over the possible states of the emitted photon. The density of states $\rho(E)$ of photons can be written as

$$\rho(E) = \frac{V_0}{(2\pi)^3}\frac{E^2}{\hbar^3 c^3}. \tag{5.3.3}$$

The *Dirac* δ-function, $\delta(E - E_{JI})$, guarantees the energy conservation of the entire system of the electrons plus the photon. The emitted photon carries away the energy difference $E_{JI} = \hbar\omega_{JI} = \hbar(\omega_J - \omega_I)$.

The radiative lifetime of the exciton state $|J\rangle$ having the angular state $|F_{\text{tot}}M_{\text{tot}}\rangle$ is defined as

$$\tau_J = 1/\Gamma_J = \left(\sum_I \Gamma_{IJ}\right)^{-1}. \tag{5.3.4}$$

Generally, one must sum over the final states $|I\rangle$ to get the decay rate of $|J\rangle$. However, in the case of the spontaneous emission of a single exciton, $|I\rangle = |\varnothing\rangle$ has only one state.

Another way of describing the spontaneous emission is by using the fermion picture. In a single exciton, an electron relaxes from $|c\rangle$ to $|v\rangle$, as depicted by the

diagram $\mathcal{D}^{ep,0}_{\rm emi}$ in Fig. 5.3.1a. At HF level, the transition amplitude $\mathcal{A}^{\rm HF}_{v,c}$ of this process is described by the matrix element $\mathcal{M}^{e-p}_{v,c}$ in (5.2.20).

$$\mathcal{A}^{\rm HF}_{v,c} = \mathcal{D}^{ep,0}_{\rm emi} = \mathcal{M}^{e-p}_{v,c}. \tag{5.3.5}$$

Let $\mathcal{A}^{\rm HF}_{I,J}$ denote the Hartree-Fock transition amplitude from $|J\rangle$ with angular state $|F_{\rm tot}M_{\rm tot}\rangle$ to $|I\rangle = |\varnothing\rangle$. From the electron-hole coupling coefficients in (4.2.19) and (4.2.20), the transition amplitudes $\mathcal{A}^{\rm HF}_{I,J}$ and $\mathcal{A}^{\rm HF}_{v,c}$ are related by

$$\begin{aligned} \mathcal{A}^{\rm HF}_{I,J} &= C_{\rm eh}(F_cM_c, F_vM_v; F_{\rm tot}M_{\rm tot})\ \mathcal{A}^{\rm HF}_{v,c}, \\ \mathcal{A}^{\rm HF*}_{I,J} &= C^*_{\rm eh}(F_cM_c, F_vM_v; F_{\rm tot}M_{\rm tot})\ \mathcal{A}^{\rm HF*}_{v,c}. \end{aligned} \tag{5.3.6}$$

To perform the integration over Ω in (5.3.2), note that $\hat{e}_{\sigma=1,2}$ and $\vec{k}$ form a basis for the position space. The completeness relation for the polarization vector $\hat{e}_\sigma$ means that, (see Complement A_I of Ref. [27],)

$$\sum_{\sigma=1,2} e^*_{\sigma,m_1} e_{\sigma,m_2} = \delta_{m_1m_2} - \frac{k_{m_1}k_{m_2}}{k^2}, \tag{5.3.7}$$

where m_1 and m_2 denote the components in a given coordinate system. After integrating over the solid angle Ω, the expression on the RHS of (5.3.7) can be easily shown to give

$$\int \left(\delta_{m_1m_2} - \frac{k_{m_1}k_{m_2}}{k^2}\right) d\Omega = \frac{8\pi}{3}\delta_{m_1m_2}, \tag{5.3.8}$$

which we leave the readers to verify. The results in (5.2.20) and (5.3.8) leads to

$$\int \sum_\sigma |\mathcal{A}^{\rm HF}_{v,c}|^2\ d\Omega = f^2_\varepsilon A^2_{EM} \times \tfrac{8\pi}{3} \times \left(\begin{array}{ccc} F_vM_v & + & F_cM_c \\ & 1 & \\ F_vM_v & - & F_cM_c \end{array}\right) \times |\mathcal{R}^{e-p}_{v,c}|^2. \tag{5.3.9}$$

In going from $\mathcal{A}^{\rm HF}_{v,c}$ to $\mathcal{A}^{\rm HF}_{I,J}$, one needs to couple the angular diagram above to the electron-hole Clebsch-Gordan angular diagrams in (4.2.19) and (4.2.20). By applying the angular algebra in Chapter 3 of Ref. [75], we have

$$\int \sum_\sigma |\mathcal{A}^{\rm HF}_{I,J}|^2\ d\Omega = f^2_\varepsilon A^2_{EM} \times \frac{8\pi}{3}\frac{1}{[F_J]}\ |\mathcal{R}^{e-p}_{v,c}|^2\ \delta_{F_{\rm tot},1}. \tag{5.3.10}$$

The selection rule $\delta_{F_{\rm tot},1}$ implies that the transition rate (5.3.10) for the singlet state with $(F_{\rm tot} = 0, M_{\rm tot} = 0)$ indeed equals to zero and the $|F_{\rm tot} = 0, M_{\rm tot} = 0\rangle$ exciton is 'dark'.

For the spontaneous emission of a single exciton, we set $\hbar\omega_{IJ}$ equal to the single exciton HF energy $E_{\rm HF}(N_e = 1, N_h = 1)$, which has been calculated in Chapter

3. In fact, a better choice for $\hbar\omega_{IJ}$ can be $E_{\rm X} = \hbar\omega_{\rm X}$ that includes the second-order correlation energy. However, Fig. 3.4.1 and Fig. 3.4.2 demonstrate that the second-order energy does not seem to be very important in predicting the emission peaks of the nanocrystal sizes of interest. The HF energy $E_{\rm HF}$ shows to be a good approximation for $\hbar\omega_{IJ}$ for the current purpose. The transition rate $\Gamma_{IJ}^{\rm HF}$, after integrating over the photon energy E, becomes

$$\Gamma_{IJ}^{\rm HF} = \frac{2\pi}{\hbar}\ \rho(E_{\rm X}) \times f_\varepsilon^2 A_{EM}^2 \times \frac{8\pi}{3}\frac{1}{[F_J]}\ |\mathcal{R}_{v,c}^{e-p}|^2\ \delta_{F_{\rm tot},1}. \tag{5.3.11}$$

Note that $\hbar = 1$ and $4\pi\varepsilon_0 = 1$ in atomic units. By using the photon density of state in (5.3.3), the above expression can be simplified into

$$\Gamma_{IJ}^{\rm HF} = \frac{4}{3[F_J]}\ \frac{\omega_{\rm X}}{c_0^3} \times \varepsilon_{\rm out}^{1/2}\ f_\varepsilon^2 \times\ |\mathcal{R}_{v,c}^{e-p}|^2\ \delta_{F_{\rm tot},1}. \tag{5.3.12}$$

Since there is only one final state that is the semiconductor ground state $|I\rangle = |\varnothing\rangle$, one has that the exciton lifetime $\tau_{\rm HF} = 1/\Gamma_{IJ}^{\rm HF}$.

Strictly speaking, when $F_{\rm tot} = 1$, $\hbar\omega_{IJ}$ should be the bright exciton energy. From the calculations of $\Delta_{\rm LR}$ in Subsection 4.2.5, the dark-bright exciton splitting comes out at typically 1 meV or at most a few meV and is much smaller than the second-order correlation energy. Therefore, $E_{\rm HF}$ or $E_{\rm X}$ remains a good approximation for the energy of the bright exciton $F_{\rm tot} = 1$.

When the temperature T is high enough (e.g. at room T), the exciton may be in a thermal distribution between the dark and bright states or even excited to some higher-energy configurations that lie close enough to the $1{\rm s}_{1/2}^e - 1{\rm s}_{1/2}^h$ state. Other processes such as phonon scattering may also take place at high temperature. Therefore, the high-T lifetime can be significantly different from (or, in fact, larger than) the low-T lifetime. For this reason, we shall compare the transition rate $\Gamma_{IJ}^{\rm HF}$ in (5.3.12) and the lifetime $\tau_{\rm HF}$ of the bright exciton $F_{\rm tot} = 1$ against the measurements at low-T.

In the formula (5.3.12) for the transition rate $\Gamma_{IJ}^{\rm HF}$, the radial term $\mathcal{R}_{v,c}^{e-p}$ contains the momentum matrix element, which gives rise to the electron-photon interaction. For the transition between a conduction state $|c\rangle$ and a valence state $|v\rangle$, the dominant contribution to $\mathcal{R}_{v,c}^{e-p}$ comes from the interband matrix element $\mathcal{R}_{v,c}^{\rm inter}$. The intraband term $\mathcal{R}_{v,c}^{\rm intra}$ is proportional to the overlap between the big component of $|c\rangle$ and the small component of $|v\rangle$ (in 4×4 k$\cdot$p model) and vice versa. Therefore, we expect the contribution from $\mathcal{R}_{v,c}^{\rm intra}$ to be less significant compared to $\mathcal{R}_{v,c}^{\rm inter}$.

As established earlier in Subsection 5.2.1, $\mathcal{R}_{v,c}^{\rm inter}$ scales linearly w.r.t. $\sqrt{E_{\rm p}}$, which makes the decay rate $\Gamma_{IJ}^{\rm HF}$ depend linearly on $E_{\rm p}$. This result is shown with the dashed green line on Fig. 5.3.2.

From the interband radial term (5.2.11), we conclude that $\mathcal{R}_{v,c}^{\rm inter}$ as well as $\mathcal{R}_{v,c}^{e-p}$ do not have any explicit dependence on the size L. For the transition rate $\Gamma_{IJ}^{\rm HF}$ in (5.3.12), the only term that has an L-dependence is the energy $\omega_{\rm X}$. Generally, the smaller the size L, the bigger the energy $\omega_{\rm X}$. Note, however, that $\omega_{\rm X}$ does not depend strongly on L, see Fig. 5.4.4, and stays always in the optical range. Therefore, at HF level, $\Gamma_{IJ}^{\rm HF}$ is slightly bigger and the lifetime $\tau_{\rm HF}$ becomes slightly smaller for smaller L, as shown by the dashed green line on Fig. 5.4.4.

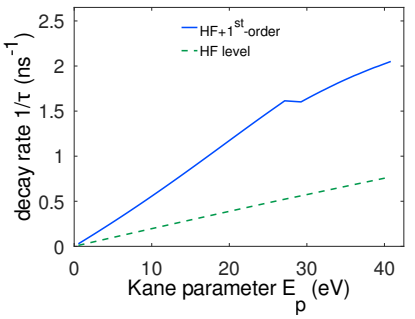

Figure 5.3.2: Decay rate $1/\tau$ versus the Kane parameter E_{p} for $CsPbBr_3$. The two curves correspond to the HF-level lifetime τ_{HF} (dashed green line) and HF plus first-order MBPT vertex correction $\tau^{(1)}$ (solid blue line). The kink on the solid curve for $\tau^{(1)}$ comes from the spurious solution of the $\mathrm{k}\cdot\mathrm{p}$ model [124].

There are two problems with the radiative lifetime τ_{HF} from the HF calculations. First, the behaviour of τ_{HF} w.r.t. L does not agree with the variational method by Takagahara [118] or Efros et al. [38]. The actual lifetime τ should become smaller as the size of the nanocrystal increases. Second, the theoretical calculations at the Hartree-Fock level overestimate the measured lifetime by a large factor, see the experimental data in Fig. 5.4.4.

We speculate the biggest source of error here to be the usage of the mean-field wave functions. In other words, the correlation effect is very important for the computation of the exciton lifetime. In Section 5.4, we perform the first-order (lowest-order) correction in MBPT to the spontaneous emission process in Fig. 5.3.1a.

As it will be shown later, the lowest-order correction to the electron-photon interaction is the same for both emission and absorption. Before delving into the MBPT correction to the electron-photon vertex, we shall derive and calculate in the next subsection the one-photon absorption cross-section at HF level.

5.3.2 One-photon cross-section

In this subsection, let us consider the creation of a single exciton in a nanocrystal via the absorption of a single photon, as depicted in Fig. 5.3.1b. We assume that the incoming field has a fixed polarization of magnitude E_0 of the electric field. The magnitude of the vector potential is

$$A_0(\omega) = \frac{E_0}{\omega}, \tag{5.3.13}$$

where ω denotes the photon frequency of the incoming field.

The electronic system makes a transition from the nanocrystal ground state $|J\rangle = |\varnothing\rangle$ (initial state) to the single exciton state $|I\rangle$ with $(F_{\mathrm{tot}}, M_{\mathrm{tot}})$ (final state). Let $\mathcal{A}^{\mathrm{HF}}_{I,J}$ be the transition amplitude of this process at HF level. In analogy with the spontaneous emission, another description of the absorption can be that of an electron going from a valence state $|v\rangle$ to a conduction state $|c\rangle$. We denote the amplitude of this process by $\mathcal{A}^{\mathrm{HF}}_{c,v}$, where

$$\mathcal{A}^{\mathrm{HF}}_{c,v} = \mathcal{D}^{ep,0}_{\mathrm{abs}} = \mathcal{M}^{e-p}_{c,v}. \tag{5.3.14}$$

Following the same argument that leads to (5.3.6), we have

$$\begin{aligned} \mathcal{A}^{\mathrm{HF}}_{I,J} &= C_{\mathrm{eh}}(F_c M_c, F_v M_v; F_{\mathrm{tot}} M_{\mathrm{tot}})\ \mathcal{A}^{\mathrm{HF}}_{c,v}, \\ \mathcal{A}^{\mathrm{HF}*}_{I,J} &= C^*_{\mathrm{eh}}(F_c M_c, F_v M_v; F_{\mathrm{tot}} M_{\mathrm{tot}})\ \mathcal{A}^{\mathrm{HF}*}_{c,v}. \end{aligned} \tag{5.3.15}$$

Under the same selection rule as for the spontaneous emission, only the bright exciton state $F_{\text{tot}} = 1$ is created. The HF transition rate from $|J\rangle = |\varnothing\rangle$ to the exciton $|I\rangle$, which has the angular state $|F_{\text{tot}} M_{\text{tot}}\rangle$, is

$$\Gamma_{IJ}^{\text{HF}} = \frac{2\pi}{\hbar}\, f_\varepsilon^2 \left(\frac{E_0}{\omega}\right)^2 |\mathcal{A}_{I,J}^{\text{HF}}|^2\, \delta(E - E_{IJ}). \tag{5.3.16}$$

To arrive at the final expression for the absorption rate Γ_{IJ}^{HF}, we need to sum over the magnetic substates of the final state $|I\rangle$ and average over the magnetic substates of the initial state $|J\rangle$. After performing the same angular reduction as in Subsection 5.3.1, we arrive at

$$\Gamma_{IJ}^{\text{HF}} = \frac{2\pi}{\hbar}\, f_\varepsilon^2 \left(\frac{E_0}{\omega}\right)^2 \frac{1}{3[F_J]} |\mathcal{R}_{c,v}^{e-p}|^2\, \delta(E - E_{IJ}). \tag{5.3.17}$$

Regarding the vector potential (5.1.5) with its magnitude given in (5.3.13), the corresponding electric and magnetic fields are

$$\begin{aligned} \vec{E} &= 2E_0 \sin(\vec{k}\cdot\vec{r} - \omega t)\ \hat{e}, \\ \vec{B} &= \frac{2E_0}{c} \cos(\vec{k}\cdot\vec{r} - \omega t)\ \hat{k}\times\hat{e}. \end{aligned} \tag{5.3.18}$$

Inside a solvent, the nanocrystals behave as point-like (or atom-like) defects. At a macroscopic level, the entire medium can be treated as having the dielectric constant ε_{out} of the outside solvent. The time-averaged electromagnetic energy density is

$$\bar{u} = \frac{1}{2}\left(\varepsilon_0\varepsilon_{\text{out}} E^2 + \frac{1}{\mu_0\mu_{\text{out}}} B^2\right) = 2\varepsilon_0\varepsilon_{\text{out}} E_0^2 \tag{5.3.19}$$

and the corresponding photon density can be derived to be

$$\bar{\rho} = \frac{\bar{u}}{\hbar\omega} = \frac{2\varepsilon_0\varepsilon_{\text{out}} E_0^2}{\hbar\omega}. \tag{5.3.20}$$

For the incoming laser field of frequency ω, we define the particle flux $\phi(\omega)$ per unit area per unit time to be the product between the density of the particles and their speed. One has

$$\phi(\omega) = \bar{\rho} \times \frac{c_0}{n} = 2\varepsilon_{\text{out}}^{1/2} \frac{c_0\varepsilon_0 E_0^2}{\hbar\omega}. \tag{5.3.21}$$

The OPA cross-section $\sigma^{(1)}$ of the incoming light at frequency ω for the transition $|J\rangle \to |I\rangle$ is defined as

$$\sigma^{(1)}(\omega) = \frac{\Gamma_{IJ}}{\phi(\omega)}. \tag{5.3.22}$$

$\sigma^{(1)}(\omega)$ has the correct unit of area. For the calculation of the transition rate at HF level, we let the rate Γ_{IJ} in (5.3.22) equal to Γ_{IJ}^{HF}. The explicit expression for $\sigma_{\text{HF}}^{(1)}$ becomes

$$\sigma_{\text{HF}}^{(1)}(\omega) = \frac{4\pi^2}{3[F_J]}\ \frac{f_\varepsilon^2}{\varepsilon_{\text{out}}^{1/2} c_0 \omega} |\mathcal{R}_{c,v}^{e-p}|^2\, \delta(E - E_{IJ}). \tag{5.3.23}$$

Apart from the *Dirac* δ-function, we call the remaining expression of the OPA cross-section $\sigma^{(1)}_{\rm HF}$ above,

$$\Xi_{\rm HF} = \frac{4\pi^2}{3[F_J]} \frac{f_\varepsilon^2}{\varepsilon_{\rm out}^{1/2} c_0 \omega} |\mathcal{R}_{c,v}^{e-p}|^2, \tag{5.3.24}$$

the *transition strength*. Here, $\Xi_{\rm HF}$ is independent of the broadening mechanisms, which will be shown in the next paragraph.

The $\delta-$function, $\delta(E - E_{IJ})$, in (5.3.23) has dimension of $[E]^{-1}$ and can be considered as a distribution in the case where the excitonic system only interacts with photons. When other decay channel(s) exist, for example via interacting with phonons, or when there is some size variation within an ensemble of nanocrystals, $\delta(E - E_{IJ})$ is 'broadened' into an actual probability distribution $g(E - E_{IJ})$ that peaks around E_{IJ}. This broadening can be viewed as a consequence of the master equation formalism [16]. The width of $g(E - E_{IJ})$ (unit: eV^{-1}) depends on the coupling strength of the other decay pathways and the size variance of the ensemble of synthesized nanocrystals.

At this level of our microscopic theory, the exact functional form of $g(E - E_{IJ})$ is unknown since it depends on various factors such as the details of the coupling to the external environment. The determination of the exact functional form of $g(E - E_{IJ})$ can be rather involved and lies beyond the scope of the current thesis. Here, we assume that each $g(E - E_{IJ})$ is a *Gaussian* distribution of a certain width ΔE_{IJ},

$$g(\eta - \eta_0) = \sqrt{\frac{1}{\pi \Delta \eta^2}}\, \mathrm{e}^{-\frac{(\eta-\eta_0)^2}{\Delta\eta^2}}. \tag{5.3.25}$$

We shall give a simple way of estimating ΔE_{IJ} assuming that there are two independent contributions to the total width, which will be shortly explained. One has

$$\Delta E_{IJ} = \sqrt{\Delta E_0^2 + \Delta E_{\rm size}^2}, \tag{5.3.26}$$

where ΔE_0 denotes the homogeneous broadening, in the sense that it takes the same value for all transitions $|J\rangle \to |I\rangle$. The second term $\Delta E_{\rm size}$ stands for the inhomogeneous broadening that depends on the size variation within an ensemble of nanocrystals. For dephasing mechanism such as via phonon interaction, a Lorentzian is more appropriate for describing the broadening of the transition lines. However, for the inhomogeneous broadening coming from the size fluctuation, for instance, a Gaussian function seems more reasonable. We note that the inhomogeneous width is often bigger than the homogenous one. Hence, we consider the overall Gaussian profile to be a better choice for the broadening.

The broadening ΔE_0 receives various contributions from the interaction with phonons ($10 - 30$ meV), the deformation of the nanocrystals from a perfect sphere, the lattice crystal field etc. We take ΔE_0 to be in the range $90-120$ meV. The exact value of ΔE_0 will be chosen so that the theoretical $\sigma^{(1)}$ reproduces approximately the various absorption features of the experimental OPA cross-section versus ω.

Let ΔL represent the variance of edge length L that can be determined experimentally using transmission-electron microscope (TEM). Here, we provide a simple model for the inhomogeneous broadening $\Delta E_{\rm size}$ coming from the size distribution.

There are two size-dependence contributions to ΔE_{size}. The first one results from the L-dependence kinetic energy, which we denote as ΔE_{kin}. The second contribution, called the Coulomb broadening ΔE_{Coul}, comes from the Coulomb interaction.

$$\Delta E_{\text{size}} = \Delta E_{\text{kin}} + \Delta E_{\text{Coul}}. \tag{5.3.27}$$

ΔE_{kin} is the variation in the kinetic energy of a confined particle in a nanocrystal and receives different values for different transitions. Roughly speaking, the kinetic energy E_{kin} of a confined particle is proportional to $1/L^2$. Thus,

$$\Delta E_{\text{kin}} \propto 2\frac{\Delta L}{L^3} \Rightarrow \Delta E_{\text{kin}} = 2\frac{\Delta L}{L} E_{\text{kin}}. \tag{5.3.28}$$

For a more highly excited exciton having higher kinetic energy E_{kin}, the transition becomes broader as the width ΔE_{kin} increases.

The Coulomb energy $E_{\text{Coul}} = E_{\text{dir}} + E_{\text{exc}}$ depends on the charge densities and does not have a strong dependence on the various transitions. Since E_{Coul} is roughly proportional to $1/L$, the width from Coulomb interaction can be approximated as

$$\Delta E_{\text{Coul}} = \frac{\Delta L}{L} E_{\text{Coul}}. \tag{5.3.29}$$

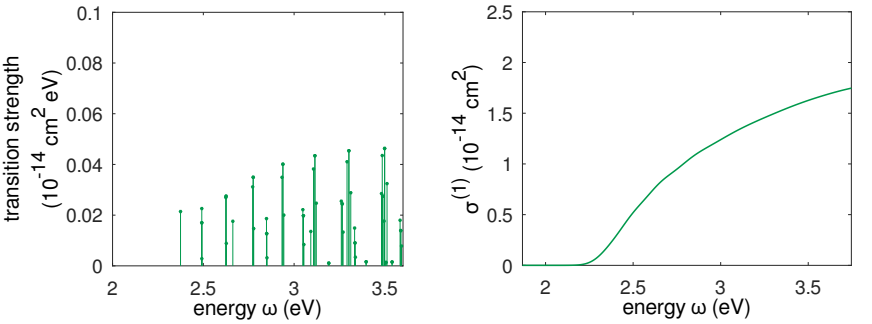

(a) Transition strength (10^{-14}cm^2 eV) (b) OPA cross-section $\sigma^{(1)}$ (10^{-14}cm^2)

Figure 5.3.3: Transition strength and one-photon absorption cross-section versus photon energy ω (eV) at HF level for edge length $L = 9.0$ nm. The calculations were done by using the parameter set 1. For the broadening of the transition lines, $\Delta E_0 = 0.1$ eV and $\Delta L/L = 12\%$.

We give some example calculations of the transition strength and OPA cross-section $\sigma^{(1)}$ in Fig. 5.3.3 for edge length $L = 9.0$ nm. For the one-photon calculations, the angular momentum and principal quantum number cut-off are $l_{\text{cut-off}} = 12$ and $n_{\text{cut-off}} = 10$.

The most prominent lines on Fig. 5.3.3a correspond to the absorption of a photon accompanied by the transition from $|\varnothing\rangle$ to the exciton state $nl_{F_c} - nl_{F_v}$ where l goes from 0 to 8. The value $l_{\text{cut-off}} = 12$ leads to an energy cut-off at around 4.5 eV for $L = 9.0$ nm. Many transitions such as $1\text{p}^e_{3/2} - 1\text{s}^h_{1/2}$ are forbidden in the

effective mass model but become allowed in the 4×4 k $\cdot$ p model. These non-zero transitions, which have small transition strength as seen in Fig. 5.3.3a, result from intraband type matrix elements between the k $\cdot$ p components in the same band.

The cross-section $\sigma^{(1)}$, Fig. 5.3.3b, can be obtained by multiplying the transition strength in Fig. 5.3.3a with a Gaussian distribution $g(E-E_{IJ})$ of total width ΔE_{IJ}. The homogenous width ΔE_0 has been chosen to be 100 meV as estimated from the Gaussian peak decomposition in Ref. [15]. The ratio $\Delta L/L$ that expresses the size distribution was set at about 12%. In other words, ΔL is around 0.6 nm, which is in accordance with various experimental figures [15, 23].

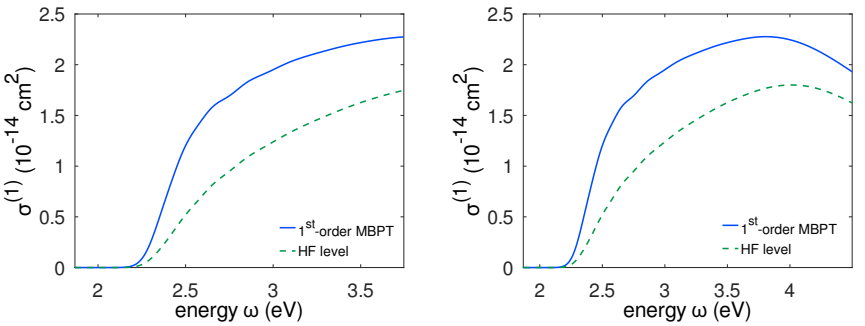

(a) Energy cut-off at $\omega_{\text{cut-off}} = 3.75$ eV (b) Energy cut-off at $\omega_{\text{cut-off}} = 4.50$ eV

Figure 5.3.4: The theoretical one-photon absorption cross-section $\sigma^{(1)}$ versus photon energy ω at HF level (green dashed line) and HF plus first-order vertex correction (blue solid line). The calculations were performed for edge length $L = 9.0$ nm using the parameters from parameter set 1 for $CsPbBr_3$. There is a big enhancement for $\sigma^{(1)}$, especially for the absorption near the band edge. The one-photon cross-section $\sigma^{(1)}$ bends over at around $\omega \gtrsim 4.0$ eV. This effect is attributed to the angular momentum cut-off $l_{\text{cut-off}} = 12$.

Similar to the case of radiative decay rate, the correlation effect is also very important here. We give an example of the HF plus first-order vertex correction versus the HF-level calculations in Fig. 5.3.4. The first-order vertex correction significantly increases the absorption cross-section, more notably for the transitions closer to the band edge. More details on the first-order vertex correction will be discussed in the next section.

Generally, $\sigma^{(1)}$ should grow as the transition energy becomes larger due to an increased density of exciton final states at higher ω. This phenomenon is observed from the absorption onset at around 2.25 eV up to about 3.75 eV in Fig. 5.3.4a. The current 4×4 k$\cdot$p model does not take into account the $p_{3/2}$ band that lies at roughly 1.0 eV above the band edge [101, 138]. Therefore, one expects the absorption cross-section to be underestimated starting from approximately the energy of the $p_{3/2}$ band upwards.

However, Fig. 5.3.4b shows a reduction in $\sigma^{(1)}$ for $\omega \gtrsim 4.0$ eV. We attribute this decrease in $\sigma^{(1)}$ to the numerical effect of the angular momentum cut-off at $l_{\text{cut-off}} = 12$, which is the maximum $l_{\text{cut-off}}$ allowed in the current version of the code. It means that the highest energy of the created exciton $1l_{F_c} - 1l_{F_v}$ is around

4.5 eV (for $L = 9.0$ nm). The Gaussian distributions $g(E - E_{IJ})$ for the exciton states with $l \geq 12$ have $\Delta E_{\text{kin}} > 0.5$ eV due to their large E_{kin}. Since these states were not computed, their contribution to $\sigma^{(1)}(\omega \gtrsim 4.0 \text{ eV})$ were not accounted for. Furthermore, the higher bands such as the $p_{3/2}$ band and the transitions at, for example, the M point of the Brillouin zone have been excluded so far. Therefore, the cross-section at $\omega \gtrsim 4.0$ eV is underestimated.

5.4 Correlation correction to electron-photon vertex

The Hartree-Fock calculations overestimate the radiative lifetime [10, 52] and underestimate the OPA cross-section $\sigma^{(1)}$ [23] by several times. The aim of this section is to go beyond the HF (mean-field) level by including the lowest-order correlated effect, which we expect to bring substantial corrections to the expressions in (5.3.12) and (5.3.24). First, we provide the readers with the formalism of the first-order MBPT correction to the electron-photon vertex in Subsection 5.4.1. Afterwards, we shall discuss the effect of the vertex correction on the shortening of the exciton lifetime in Subsection 5.4.2. The one-photon absorption cross-section will be the subject of Subsection 5.4.3. After applying the formalism in Subsection 5.4.1 to calculate $\sigma^{(1)}$, we discuss the dependence of the cross-section on the size L and the Kane parameter E_{p} as well as the effects of using 4×4 $\text{k} \cdot \text{p}$ model against the effective mass model. Comparisons with the various experimental data will also be provided.

5.4.1 Formalism

Since the spontaneous emission and the absorption across the band gap are dominated by the interband type transitions in Fig. 5.3.1, we focus in this section on the correction to these processes.

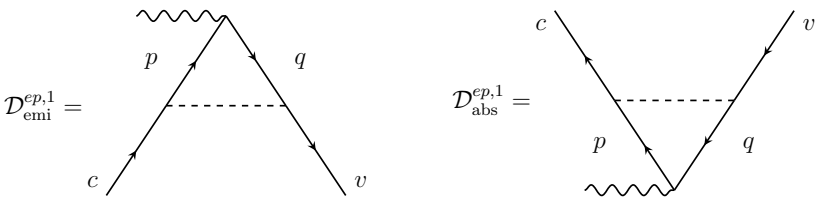

(a) emission (b) absorption

Figure 5.4.1: The first-order vertex corrections for the interband absorption and emission. These diagrams are also lowest-order in $\text{k} \cdot \text{p}$ theory and, therefore, give the biggest contributions. They come from the two-body potential V_2 of the perturbative Coulomb interaction V, see Subsection 4.1.2.

In Fig. 5.4.1, we list the Feynman diagrams that are lowest-order in both Coulomb perturbative potential and $\text{k} \cdot \text{p}$ perturbation. $\mathcal{D}^{ep,1}_{\text{abs}}$ and $\mathcal{D}^{ep,1}_{\text{emi}}$ contain

one perturbative Coulomb potential V_2 and, thus, are first-order in Coulomb perturbative potential (4.1.5). Consequently, they are also called first-order vertex corrections to the electron-photon interacting vertices in Fig. 5.3.1. The internal lines p and q in Fig. 5.4.1 denote a conduction state and a valence state respectively. There is no change of particle type (or band index) at each vertex of the Coulomb interaction. It implies that the processes in Fig. 5.4.1 are of order $\mathcal{O}(1)$ in $\mathrm{k}\cdot\mathrm{p}$ perturbation. The diagrams that are higher-order in $\mathrm{k}\cdot\mathrm{p}$ theory can be found in Fig. 5.4.2 for absorption process. These diagrams are formally $\mathcal{O}((\mathrm{k}\cdot\mathrm{p})^2)$. Since their values rely on the big-small $\mathrm{k}\cdot\mathrm{p}$ components overlap, we expect them to be at most within several percent of $\mathcal{D}^{ep,1}_{\mathrm{abs}}$. As their contributions are insignificant for the current interest, we shall omit them in the thesis for the sake of simplicity.

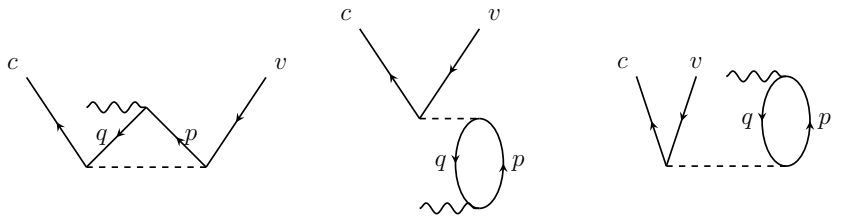

Figure 5.4.2: Feynman diagrams for absorption that are $\mathcal{O}((\mathrm{k}\cdot\mathrm{p})^2)$ in $\mathrm{k}\cdot\mathrm{p}$ theory.

We note that the shells containing p and q in the diagrams in Fig. 5.4.1 have to differ from the shells containing c and v respectively. In other words, the sum $\sum_{PQ}$ means summing over all conduction levels with F_p and all valence levels with F_q as well as all the magnetic substates with M_p and M_q, where the shell P containing $|p\rangle$ is different from C and, similarly, $Q \neq V$. The diagrams with either $|p\rangle$ contained in shell C or $|q\rangle$ in shell V cancel with the first-order diagrams involving the one-body potential V_1 of the perturbative Coulomb potential V.

Let us consider the absorption process in Fig. 5.4.1b for example. The algebraic expression of the diagram Fig. 5.4.1a can be easily obtained from the one of the absorption diagram Fig. 5.4.1b. The algebraic expression for $\mathcal{D}^{ep,1}_{\mathrm{abs}}$ can be written as

$$\mathcal{D}^{ep,1}_{\mathrm{abs}} = \sum_{PQ} \langle \varnothing | q^\dagger p \left\{ i^\dagger \; j^\dagger \; l \; k \right\} c^\dagger v | \varnothing \rangle \; \frac{\frac{1}{2}\langle cq | G_{12} | pv \rangle}{(\epsilon_c + \epsilon_v) - (\epsilon_p + \epsilon_q)} \; \mathcal{M}^{e-p}_{p,q}. \tag{5.4.1}$$

$\mathcal{M}^{e-p}_{p,q}$ represents the creation of an intermediate exciton state $n_p l_{p F_p} - n_q l_{q F_q}$, which differs from the final state $n_c l_{c F_c} - n_v l_{v F_v}$, after absorbing a photon. Via Coulomb excitation, the electron in $|p\rangle$ and the hole in $|q\rangle$ are scattered into the states $|c\rangle$ and $|v\rangle$ respectively. Similar to the calculations of correlation energy, $(\epsilon_c + \epsilon_v) - (\epsilon_p + \epsilon_q)$ describes the excitation energy involved in the Coulomb interaction. After Wick contracting, the term $\langle \varnothing | q^\dagger p \left\{ i^\dagger \; j^\dagger \; l \; k \right\} c^\dagger v | \varnothing \rangle$ in (5.4.1) gives rise to a Wick phase and a multiplicative factor from the number of possible contractions.

There are two equivalent ways of contracting $\langle \varnothing | q^\dagger p \left\{ i^\dagger \; j^\dagger \; l \; k \right\} c^\dagger v | \varnothing \rangle$, each of

which results in the Wick phase equal to -1.

$$\begin{aligned}
\langle\varnothing|q^\dagger p\{i^\dagger\ j^\dagger\ l\ k\}c^\dagger v|\varnothing\rangle &= \langle\varnothing|q^\dagger p\{p^\dagger\ v^\dagger\ q\ c\}c^\dagger v|\varnothing\rangle = -1 \\
\langle\varnothing|q^\dagger p\{i^\dagger\ j^\dagger\ l\ k\}c^\dagger v|\varnothing\rangle &= \langle\varnothing|q^\dagger p\{v^\dagger\ p^\dagger\ c\ q\}c^\dagger v|\varnothing\rangle = -1
\end{aligned} \tag{5.4.2}$$

The angular-radial expressions of $\langle cq|G_{12}|pv\rangle$ and $\mathcal{M}^{e-p}_{p,q}$ are given in (3.3.10) and (5.2.20). The product of the angular part of the multipole k of $\langle cq|G_{12}|pv\rangle$ and the angular part of $\mathcal{M}^{e-p}_{p,q}$ can be analytically summed over M_q and M_p. By applying the JVL3 theorem (see Chapter 3, Ref. [75]), we have

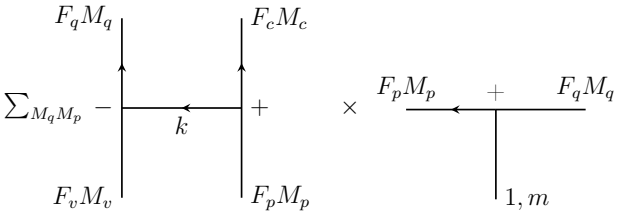

(5.4.3)

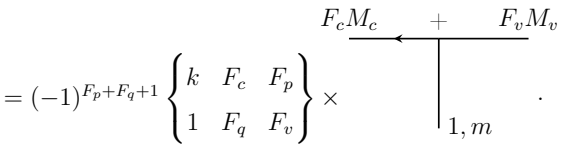

The last diagram in (5.4.3) is, in fact, the angular part of $\mathcal{D}^{ep,1}_{\rm abs}$. The factor (-2) combines with the phase $(-1)^{F_p+F_q+1}$ and the factor $\frac{1}{2}$ to give $(-1)^{F_p+F_q}$. The expression for the first-order vertex correction $\mathcal{D}^{ep,1}_{\rm abs}$ to electron-photon vertex $\mathcal{D}^{ep,0}_{\rm abs}$ is

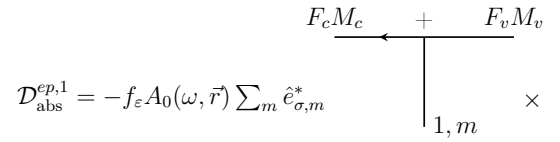

(5.4.4)

In the above formula, the radial part of the first-order vertex correction can be written as

$$\mathcal{R}^{(1)}_{c,v} = \sum_{F_pF_q}\sum_k (-1)^{F_p+F_q}\begin{Bmatrix} k & F_c & F_p \\ 1 & F_q & F_v \end{Bmatrix}\frac{X^k(qc,vp)\ \mathcal{R}^{e-p}_{p,q}}{(\epsilon_c+\epsilon_q)-(\epsilon_p+\epsilon_v)}. \tag{5.4.5}$$

$\mathcal{R}^{(1)}_{c,v}$ can be thought of as a first-order MBPT version of the radial function $\mathcal{R}^{e-p}_{c,v}$ in (5.2.20). The computation of this term and of $\mathcal{D}^{ep,1}_{\rm abs}$, thanks to the angular reduction, is very efficient.

The first-order vertex correction $\mathcal{D}^{ep,1}_{\rm emi}$ for emission is almost as same as $\mathcal{D}^{ep,1}_{\rm abs}$ by exchanging $c \leftrightarrow v$ and $p \leftrightarrow q$. The energy denominator $(\epsilon_c+\epsilon_v)-(\epsilon_p+\epsilon_q)$

results from the first-order MBPT and is, therefore, the same for both $\mathcal{D}^{ep,1}_{\rm abs}$ and $\mathcal{D}^{ep,1}_{\rm emi}$. By making use of (5.4.4), one can immediately obtain the explicit formula for $\mathcal{D}^{ep,1}_{\rm emi}$ as follows.

$$\mathcal{D}^{ep,1}_{\rm emi} = -f_\varepsilon A_0(\omega,\vec{r}) \sum_m \hat{e}^*_{\sigma,m} \quad \times \quad \mathcal{R}^{(1)}_{v,c}, \tag{5.4.6}$$

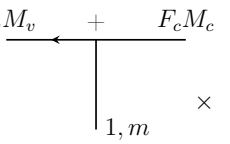

where the radial part is

$$\mathcal{R}^{(1)}_{v,c} = \sum_{F_p F_q} \sum_k (-1)^{F_p+F_q} \begin{Bmatrix} k & F_v & F_q \\ 1 & F_p & F_c \end{Bmatrix} \frac{X^k(pv,cq)\ \mathcal{R}^{e-p}_{q,p}}{(\epsilon_c+\epsilon_q)-(\epsilon_p+\epsilon_v)}. \tag{5.4.7}$$

Due to the symmetry of the 6j-symbol, of the reduced matrix elements X^k and $\mathcal{R}^{\rm inter}_{i,j}$, we have that $\mathcal{R}^{(1)}_{v,c} = \mathcal{R}^{(1)}_{c,v}$. Therefore, the correction ratio between the first-order MBPT and the HF diagram is identical for both absorption and emission processes.

5.4.2 Exciton lifetime

Up to first-order vertex correction, the decay rate $\Gamma^{(1)}_{IJ}$ in (5.3.2) can be calculated by using the transition amplitude $\mathcal{A}^{(1)}_{I,J}$ where

$$\mathcal{A}^{(1)}_{I,J} = \mathcal{D}^{ep,0}_{\rm emi} + \mathcal{D}^{ep,1}_{\rm emi}. \tag{5.4.8}$$

From (5.4.4) and (5.4.6), $\mathcal{D}^{ep,1}_{\rm emi}$ has the same angular part as $\mathcal{D}^{ep,0}_{\rm emi}$ of the HF-level calculations. Therefore, the result of the angular manipulation is clearly identical. One can immediately write down

$$\Gamma^{(1)}_{IJ} = \frac{4}{3[F_J]}\ \frac{\omega_{\rm X}}{c_0^3} \times \varepsilon^{1/2}_{\rm out}\ f^2_\varepsilon \times\ |\mathcal{R}^{e-p}_{v,c} + \mathcal{R}^{(1)}_{v,c}|^2\ \delta_{F_{\rm tot},1}. \tag{5.4.9}$$

In other words, the transition rates $\Gamma^{(1)}_{IJ}$ and $\Gamma^{\rm HF}_{IJ}$, see (5.3.12), differ only in their radial parts.

Let $\tau^{(1)}$ be the radiative lifetime of the bright state $F_{\rm tot} = 1$ calculated at HF plus first-order MBPT correction, see also (5.3.4). In the rest of this subsection, we shall discuss the behaviour of $\tau^{(1)}$ versus the Kane parameter $E_{\rm p}$ and the size L of a nanocrystal.

The Kane parameter is proportional to the square of the momentum matrix element, please refer to (5.2.12). As previously established, it is an important parameter for the electron-photon interaction. At HF level, $\tau^{-1}_{\rm HF}$ has a linear relationship w.r.t $E_{\rm p}$, which is shown by the dashed green line in Fig. 5.3.2.

The calculation of $\tau^{(1)}$ versus $E_{\rm p}$, where $E_{\rm p}$ varies in the range $[0, 40]$ eV, is presented with the solid blue line in Fig. 5.3.2. For $E_{\rm p} < 27$ eV, the calculation converges and the resulting decay rate $1/\tau^{(1)}$ versus ω is well behaved. As $E_{\rm p}$

increases, the bright exciton radiatively decays to the ground state much more rapidly. At the value E_p around 27 eV and higher, the curve starts showing some strange behaviour due to the spurious intra-gap states in the $\mathrm{k}\cdot\mathrm{p}$ model [124]. The HF iterations manage to converge for high value of E_p and the resulting wave functions and energy levels still seem sensible.

Despite this fact, the existence of the spurious states proves detrimental to the calculations of correlation effects. These states stay inside the energy gap and have significant but unphysical contributions to the correlation correction. Their presence explains the appearance of a kink at approximately $E_\mathrm{p} = 27$ eV in Fig. 5.3.2. Nonetheless, the brute-force removal of the spurious states leads to the incompleteness of the basis set, which poses a foundational problem.

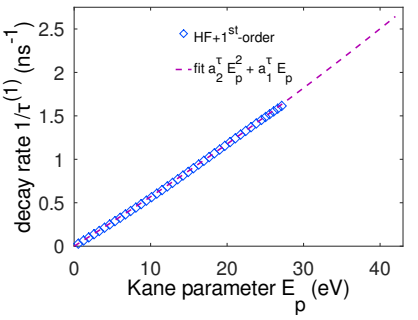

Figure 5.4.3: Decay rate $1/\tau^{(1)}$ versus the Kane parameters E_p for edge length $L = 9.0$ nm. Open diamonds: calculated data at HF level plus first-order vertex correction, dashed line: fitting function $\tau^{(1)} = \mathrm{a}_1^\tau E_\mathrm{p} + \mathrm{a}_2^\tau E_\mathrm{p}^2$ where $\mathrm{a}_1^\tau = 5.51\times10^{-2}$ and $\mathrm{a}_2^\tau = 1.87\times10^{-4}$. Polynomial fitting shows that the dependence of $1/\tau^{(1)}$ on E_p is almost linear with some quadratic correction.

When p and q describe a conduction and a valence state, $\mathcal{R}_{q,p}^{e-p}$ is dominated by the interband type term $\mathcal{R}_{q,p}^{\mathrm{inter}}$. $\mathcal{R}_{v,c}^{(1)}$ contains $\mathcal{R}_{q,p}^{e-p}$ and, thus, is also proportional to $\sqrt{E_\mathrm{p}}$. The sum over F_p and F_q, however, may have some dependence on E_p due to the density of states of the nonzero $\mathcal{R}_{q,p}^{\mathrm{inter}}$ transitions. Many of these transitions that are rather small come from the $\mathrm{k}\cdot\mathrm{p}$ corrections of the total wave functions $|p\rangle$ and $|q\rangle$. One expects the resulting polynomial fit of $1/\tau^{(1)}$ versus E_p to be dominantly a linear function in E_p with some higher power corrections w.r.t. E_p. Fig. 5.4.3 shows that

$$\tau^{(1)} = \mathrm{a}_1^\tau E_\mathrm{p} + \mathrm{a}_2^\tau E_\mathrm{p}^2$$

with $\mathrm{a}_1^\tau = 5.51\times10^{-2}$ and $\mathrm{a}_2^\tau = 1.87\times10^{-4}$ produces an excellent fit for the data when E_p stays in the interval $[0, 27]$ eV. By means of $\mathrm{k}\cdot\mathrm{p}$ perturbation theory, the polynomial fit above can be used to extrapolate into the region with higher E_p. In this way, one can extract the answer for the case where the high E_p values cause the spurious-state problems in $\mathrm{k}\cdot\mathrm{p}$ model.

Now, we move on to discuss the variation of the lifetime versus the nanocrystal size. The first-order vertex correction alters the behaviour of τ w.r.t. the edge length L in comparison to HF-level calculation. With the correction $\mathcal{D}_{\mathrm{emi}}^{ep,1}$ included, the lifetime becomes shorter for the more weakly confined exciton, which was also observed by using variational method in [10, 118]. Let us define the enhancement factor coming from the first-order vertex correction to be

$$\beta_\tau = \frac{\tau_{\mathrm{HF}}}{\tau^{(1)}}. \tag{5.4.10}$$

A plot of β_τ versus edge length L can be found on Fig. 5.4.5. The ratio β_τ for a given size L encapsulates the importance of the MBPT correlation in the exciton radiative

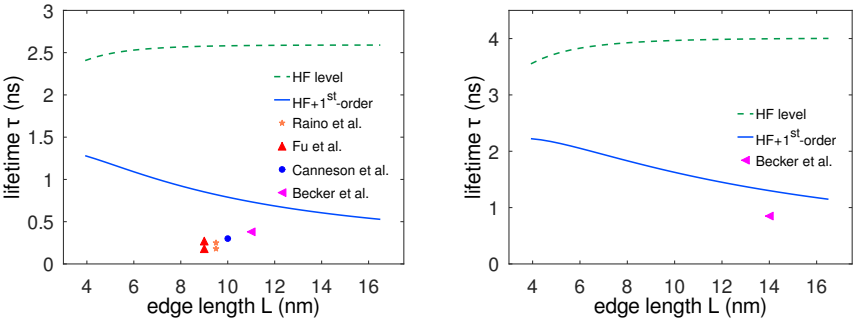

(a) $CsPbBr_3$ (b) $CsPbI_3$

Figure 5.4.4: Exciton lifetime τ versus edge length L for $CsPbBr_3$ and $CsPbI_3$. The calculations were done using parameter set 1 (3.4.9) for $CsPbBr_3$ and parameter set 3 (3.4.11) for $CsPbI_3$. The two theoretical curves correspond to the HF lifetime τ_{HF} (dashed green line) and $\tau^{(1)}$ for HF plus first-order vertex correction (solid blue line). Experimental data: Raino et al., Ref. [100]; Fu et al., Ref. [52]; Canneson et al., Ref. [20]; Becker et al., Ref. [10].

lifetime. As $L \to 0$, β_τ is expected to converge towards 1. It is equivalent to say that, in the strong confinement limit, the HF transition amplitude $\mathcal{D}^{ep,0}_{\mathrm{emi}}$ sufficiently describes spontaneous emission of a single exciton. When the nanocrystal size increases and one enters the intermediate to eventually weak confinement regime, the system becomes more and more correlated as evidenced by an increasing β_τ. The enhancement of the lifetime, from first-order vertex correction, helps to explain the fast sub-nanosecond decay of the single exciton in the perovskite nanocrystals.

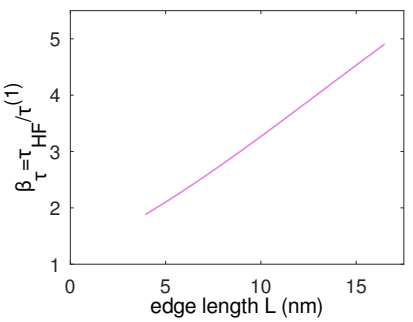

Figure 5.4.5: The enhancement factor $\beta_\tau = \tau_{\mathrm{HF}}/\tau^{(1)}$ for the $1s^e_{1/2} - 1s^h_{1/2}$ transition of $CsPbBr_3$ from first-order vertex correction. As L becomes bigger, β_τ increases, which reflects the fact that the correlation becomes more important when one goes from the strong to the weak confinement regime.

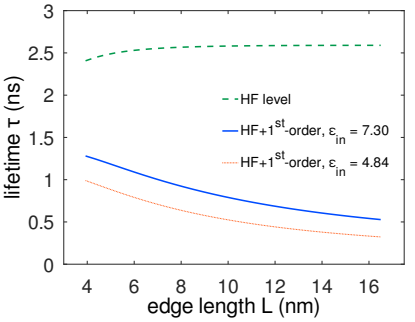

Figure 5.4.6: Calculated lifetime τ versus edge length L for $CsPbBr_3$. Dashed curve: HF level; solid curve: HF plus first-order MBPT using $\varepsilon_{\mathrm{in}} = \varepsilon_{\mathrm{eff}} = 7.30$ (effective dielectric constant); dotted curve: HF plus first-order MBPT using $\varepsilon_{\mathrm{in}} = \varepsilon_{\mathrm{opt}} = 4.84$ (optical value).

Fig. 5.4.5 demonstrates that β_τ grows approximately linearly with L. However, Takagahara [118] shows, via variational calculations, that the enhancement should be proportional to the volume L^3 provided that L is sufficiently large but not approaching the bulk limit. We note that our MBPT method stops at first-order while the variational method, in principle, includes all-order correlation. Therefore, we do not expect a quantitative agreement at the current level of MBPT, especially for weak confinement. We consider this to be one of the main reasons for the overestimation of the experimentally measured lifetime in Fig. 5.4.4. Nonetheless, it is important to emphasize that the current approach requires the same level of complexity to treat the MBPT corrections to the higher exciton states as compared to the ground state $1\mathrm{s}^e_{1/2}-1\mathrm{s}^h_{1/2}$. This is in contrast to the variational approach that requires orthogonalization of the variational wave functions [118, 119]. Therefore, one can easily improve the single-photon absorption cross-section with the first-order vertex correction.

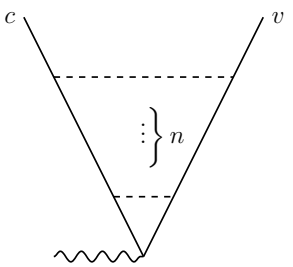

Figure 5.4.7: Higher-order MBPT corrections (ladder diagrams) for electron-photon vertex.

In the effective mass model, one way of including all-order MBPT in the bulk limit is to use the *final state interactions,* as described in Chapter 9 of Ref. [79]. Another more general all-order approach via Bethe-Salpeter equations allows the treatment of intermediately as well as weakly confined systems. These topics go beyond the scope of this thesis and are left as future research problems.

Instead of embarking on a full all-order calculation here, we can have a rough estimate of the all-order MBPT correction to the electron-photon vertex $\mathcal{D}^{ep,0}_{\mathrm{emi}}$. To lowest order in $\mathrm{k}\cdot\mathrm{p}$ perturbation, the important higher-order diagrams will be the ladder diagrams as shown in Fig. 5.4.7, in which $n = 2, 3, \ldots$ denotes the number of Coulomb interactions. Let $\mathcal{D}^{ep,2+}_{\mathrm{emi}}$ be the sum of contributions corresponding to $n = 2, \ldots, \infty$. We surmise that the ratio $\mathcal{D}^{ep,2+}_{\mathrm{emi}}/\mathcal{D}^{ep,1}_{\mathrm{emi}}$, which is controlled by the ratio of the Coulomb interaction over the excitation energy, to be around $1/\eta^{(1)} - 1$. We remind ourselves that $\eta^{(1)}$ is the percentage of the total correlation energy that comes from first-order Coulomb interaction, see (3.4.12) in subsection 3.4.2. One can roughly estimate the enhancement coming from the sum of all ladder diagrams to be $\beta_\tau/\eta^{(1)}$. For edge length $L = 11$ nm, the estimated 'total' enhancement $\beta_\tau/\eta^{(1)}$ comes to around 7. Ideally, one needs to carry out an explicit calculation up to all-order MBPT, which provides a much more reliable answer to the vertex enhancement than the estimate above. Again, we leave this for future work.

Apart from the error of truncating at first order, another source of uncertainty of the current theory could be the dielectric constant $\varepsilon_{\mathrm{in}}(\vec{r}, \omega)$ that depends on the length scale and excitation energy, in principle. Fig. 5.4.6 demonstrates the first-order MBPT correction using two different values of $\varepsilon_{\mathrm{in}}$ for $CsPbBr_3$. These are

the effective dielectric constant $\varepsilon_{\rm in} = \varepsilon_{\rm eff} = 7.30$ and the optical dielectric constant $\varepsilon_{\rm in} = \varepsilon_{\rm opt} = 4.84$. Clearly, with a smaller $\varepsilon_{\rm in}$, the correlation correction becomes relatively more important. The ratio $\mathcal{D}^{ep,1}_{\rm emi}/\mathcal{D}^{ep,0}_{\rm emi}$ is proportional to $1/\varepsilon_{\rm in}$, i.e. an $x\%$ change in $\varepsilon_{\rm in}$ leads to the same relative error in $\mathcal{D}^{ep,1}_{\rm emi}/\mathcal{D}^{ep,0}_{\rm emi}$. We suspect that $\varepsilon_{\rm opt}$ acts as the lower bound for the correct value of $\varepsilon_{\rm in}$ used for each size L and excitation energy.

5.4.3 Single-photon absorption

To calculate the absorption cross-section, we need to consider all the allowed transitions. For each transition from the ground state $|J\rangle = |\varnothing\rangle$ to the final state $|I\rangle$, the transition rate at HF plus first-order vertex correction is defined as

$$\Gamma^{(1)}_{IJ} = \frac{2\pi}{\hbar}\, f_\varepsilon^2 \left(\frac{E_0}{\omega}\right)^2 |\mathcal{A}^{(1)}_{I,J}|^2\, \delta(E + E_{IJ}). \tag{5.4.11}$$

Similarly to the emission, the transition amplitude $\mathcal{A}^{(1)}_{I,J}$ in (5.4.11) contains both the HF contribution and the first-order correction.

$$\mathcal{A}^{(1)}_{I,J} = \mathcal{D}^{ep,0}_{\rm abs} + \mathcal{D}^{ep,1}_{\rm abs}. \tag{5.4.12}$$

Again, $\mathcal{D}^{ep,0}_{\rm abs}$ and $\mathcal{D}^{ep,1}_{\rm abs}$ differ only in their radial parts $\mathcal{R}^{e-p}_{I,J}$ and $\mathcal{R}^{(1)}_{I,J}$, see (5.2.20) and (5.4.4). This implies that the results of the angular reduction in Subsection 5.3.2 can be directly applied here. One just needs to add the radial part of the first-order vertex correction to the radial term in the HF-level expression.

Let $\sigma^{(1)}$ and $\Xi^{(1)}$ denote the one-photon absorption cross-section and transition strength up to first-order MBPT. From the formula (5.3.24) for the transition strength at HF level, we have

$$\Xi^{(1)}_{IJ} = \frac{4\pi^2}{3[F_J]}\, \frac{f_\varepsilon^2}{\varepsilon_{\rm out}^{1/2} c_0 \omega} |\mathcal{R}^{e-p}_{c,v} + \mathcal{R}^{(1)}_{c,v}|^2. \tag{5.4.13}$$

Here, we have simply replaced $\mathcal{R}^{e-p}_{c,v}$ of the HF formula by $\mathcal{R}^{e-p}_{c,v} + \mathcal{R}^{(1)}_{c,v}$. This leads to the cross-section

$$\sigma^{(1)}(\omega) = \sum_I \Xi^{(1)}_{IJ}\; g(\omega_{IJ} - \omega), \tag{5.4.14}$$

where the broadening functions $g(\omega_{IJ} - \omega)$ of the transition lines are taken to be the Gaussian distributions as given in (5.3.25). See (5.3.26) and the discussion thereon for the choices of the widths ΔE_{IJ} of $g(\omega_{IJ} - \omega)$. With these definitions in mind, we first show in Fig. 5.4.8 an example calculation for $\Xi^{(1)}$ and $\sigma^{(1)}$ up to first-order vertex correction.

In the expression (5.4.5) for the first-order correction, we note that the lowest transition $1{\rm s}^e_{1/2} - 1{\rm s}^h_{1/2}$ has its energy well separated from other transitions. Therefore, the energy denominator in (5.4.5) is always guaranteed to be far from zero and the MBPT calculation converges to a finite answer. When higher transitions $n_c l_{c_{F_c}} - n_v l_{v_{F_v}}$ are considered, some intermediate states $n_p l_{p_{F_p}} - n_q l_{q_{F_q}}$ that have

nearly equal energy to the final state (c, v) may exist. The near-zero energy denominator $(\epsilon_c + \epsilon_v) - (\epsilon_p + \epsilon_q)$ causes some catastrophic effect on the results from first-order MBPT. One quick solution to this problem of the nearly degenerate states (p, q) is to remove their contributions of from the sum $\sum_{F_p F_q}$ in (5.4.5) if $(\epsilon_c + \epsilon_v) - (\epsilon_p + \epsilon_q) < \delta E_{\min}$ for a given choice of the energy lower bound $\delta E_{\min}$.

Depending on the exact choice of $\delta E_{\min}$, the positions and the values of the transition strength $\Xi^{(1)}$, for instance in Fig. 5.4.8a, may change. However, the final answer for the cross-section $\sigma^{(1)}$ does not depend that much on the choice of $\delta E_{\min}$. This fact also validates the current approach using first-order MBPT vertex correction. In the calculation below, we set $\delta E_{\min} = 20$ meV, which is about the phonon broadening. The problem with the nearly degenerate states will disappear when one implements an all-order MBPT method, for instance the Bethe-Salpeter equation for a confined system or the final state interaction in the bulk [79]. For now, we focus on some of the basic properties of the transition strength and the one-photon absorption cross-section at the level of first-order MBPT.

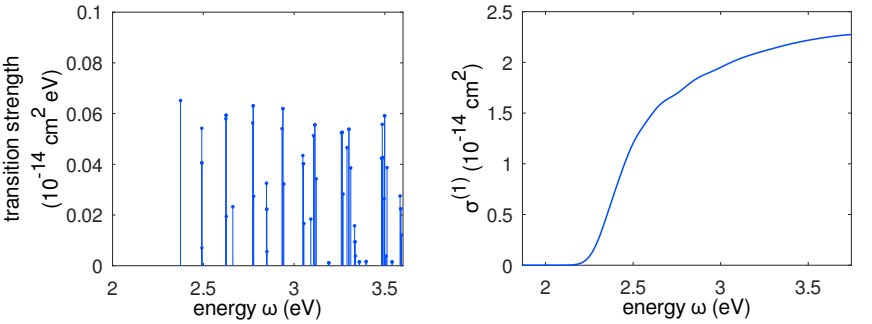

(a) Transition strength

(b) cross-section $\sigma^{(1)}$

Figure 5.4.8: Transition strength and cross-section $\sigma^{(1)}$ versus transition energy ω for $CsPbBr_3$ nanocrystal with edge length $L = 9.0$ nm in the 4×4 k·p model. The calculations were done at HF level plus first-order vertex correction with $\delta E_{\min} = 20$ meV. The basic parameters are given in parameter set 1.

Some transitions that were vanishing at HF level, for instance $1s^e_{1/2} - 1d^h_{5/2}$, may become non-zero, in principle, as a result of the Coulomb excitation in Fig. 5.4.1b. These new peaks, however, are rather small due to their existence owing only to the k-pole excitation (where $k \geq 1$) of the Coulomb matrix element. Therefore, they do not bring about significant contributions to $\sigma^{(1)}$. Most of the enhancement of the cross-section $\sigma^{(1)}$ in (5.4.14) compared to the HF-level cross-section $\sigma^{(1)}_{\rm HF}$ comes from the increase of the transition strength $\Xi^{(1)}$ of the $nl_{F_c} - nl_{F_v}$ transition with higher n and l ($n = n_c = n_v$ and $l = l_c = l_v$). The calculations of $\Xi^{(1)}$ for the various transitions for edge length $L = 9.0$ nm are shown in Fig. 5.3.3a at HF level and Fig. 5.4.8a up to first-order MBPT.

We note that the enhancement from MBPT for the first peak, which correspond to $1s^e_{1/2} - 1s^h_{1/2}$ transition, comes out about 3 in accordance with the emission calculation. The lowest state $1s^e_{1/2} - 1s^h_{1/2}$ receives the largest correcting factor.

Similar to the transition strength in Fig. 5.3.3a, the most prominent peaks on Fig. 5.4.8a correspond to the $nl_{F_c} - nl_{F_v}$ transitions with higher principal quantum number n or orbital angular momentum l. These transitions with higher n or l have smaller correcting factors from first-order MBPT, see Table 5.1 for the enhancement factor for various n and l values. This is somewhat expected from expression (5.4.7) due to the fluctuating contributions, see Table 5.2 for more details, from the intermediate states (p, q) with higher and lower energy than (c, v). The plot of both $\sigma^{(1)}$ and $\sigma^{(1)}_{\text{HF}}$ versus ω in Fig. 5.3.4 also provides the reader a sense of the enhancement from first-order vertex correction. Let us define the enhancement factor for the OPA cross-section at frequency ω to be

$$\beta_\sigma(\omega) = \frac{\sigma^{(1)}(\omega)}{\sigma^{(1)}_{\text{HF}}(\omega)}. \tag{5.4.15}$$

For ω ranging between 3.10 eV and 3.75 eV, $\beta_\sigma(\omega)$ varies from 1.52 to 1.30. From the results in Table 5.1, we generally expect $\beta_\sigma(\omega)$ to be smaller than β_τ, which equals to $\beta_{n=1\ l=0}$. Intuitively, the electron and hole of an excited exciton stay further apart. This makes its effective Bohr radius larger and, in the same volume of a nanocrystal, an excited exciton seems more strongly confined than a ground state exciton.

n	l	$\lvert\mathcal{R}^{e-p}_{c,v}\rvert^2$	$\lvert\mathcal{R}^{e-p}_{c,v} + \mathcal{R}^{(1)}_{c,v}\rvert^2$	β_{nl}
1	0	0.710	2.159	3.042
2	0	0.653	0.779	1.193
3	0	0.585	0.663	1.133
1	1	0.786	1.888	2.402
2	1	0.741	1.365	1.843
1	2	1.073	2.037	1.899
2	2	0.956	1.926	2.014
1	4	1.429	2.128	1.489
1	6	1.886	2.592	1.375
1	8	2.348	3.052	1.300

Table 5.1: n and l correspond to the principal and orbital quantum number of the transitions $nl_{F_c} - nl_{F_v}$. The radial parts $|\mathcal{R}^{e-p}_{c,v}|^2$ and $|\mathcal{R}^{e-p}_{c,v} + \mathcal{R}^{(1)}_{c,v}|^2$ in the transition strength Ξ_{HF} and $\Xi^{(1)}$ are shown in atomic units. We defined the enhancement factor β_{nl} to be the ratio $|\mathcal{R}^{e-p}_{c,v} + \mathcal{R}^{(1)}_{c,v}|^2 / |\mathcal{R}^{e-p}_{c,v}|^2$. β_{nl} becomes smaller for higher n and l, i.e. the excited states receive smaller corrections compared to the ground state $1\text{s}^e_{1/2} - 1\text{s}^h_{1/2}$.

Fig. 5.4.8b shows that $\sigma^{(1)}$ increases w.r.t. ω. However, the curve of $\sigma^{(1)}$ versus ω tends to flatten out at high energy due to the angular momentum cut-off at $l_{\text{cut-off}} = 12$, see the discussion in subsection 5.3.2. The general shape of

the curve and the value of the cross-section $\sigma^{(1)}(\omega)$ will further change when one accounts completely for the correlation to all-order MBPT. The first-order vertex correction brings an enhancement to the cross-section and an all-order method will increase $\beta_\sigma(\omega)$ even further. Hence, we expect that the cross-section has been so far underestimated. Another source of underestimation of $\sigma^{(1)}$ comes from neglecting the $p_{3/2}$ band. The first absorption peak from the $p_{3/2}$ band lies approximately 1 eV above the $1s^e_{1/2} - 1s^h_{1/2}$ [101, 138]. Since the $p_{3/2}$ and $p_{1/2}$ conduction bands are both connected to the $s_{1/2}$ valence band via the same momentum matrix element $\langle L_c||\vec{p}||L_v\rangle$, the optical absorption from $s_{1/2}$ to $p_{3/2}$ is also expected to be strong. This fact leads one to expect a clear rise in $\sigma^{(1)}$ at about $\Delta_{\rm soc}$ above the first transition $1s^e_{1/2} - 1s^h_{1/2}$, see the discussion in Ref. [90]. It means that for $CsPbBr_3$ nanocrystals with averaged edge length $L = 9.0$ nm, we may have a notably higher $\sigma^{(1)}$ around $\omega = 3.3 - 3.4$ eV. To systematically include the $p_{3/2}$ band, we need to resort to electron-photon interaction in the 8×8 $k \cdot p$ model. For this reason, we leave this issue for future study.

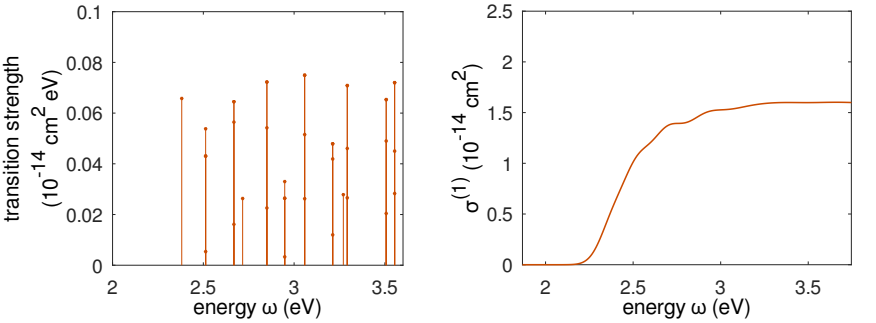

(a) Transition strength (b) cross-section $\sigma^{(1)}$

Figure 5.4.9: Transition strength and cross-section $\sigma^{(1)}$ versus transition energy ω for $CsPbBr_3$ nanocrystal with edge length $L = 9.0$ nm in the effective mass model. The basic parameters are given in parameter set 1, except there is no $k \cdot p$ coupling between the conduction and valence bands by setting $E_p = 0.0$ eV. The energy lower bound for vertex correction is $\delta E_{\rm min} = 20$ meV.

Before moving on to discuss the theoretical calculations and the measurements of $\sigma^{(1)}$ for various sizes, a comparison between the 4×4 $k \cdot p$ and the effective mass models is useful to understand the role of the $k \cdot p$ corrections to the single-photon absorption.

At both HF level and at first-order MBPT, there are two most obvious consequences of the $k \cdot p$ model against effective mass model. Firstly, the $k \cdot p$ mixing reduces the energy of the conduction states, especially for the states with higher angular momentum, while raises the energy of the valence (electron) states. In other words, the energy of the $nl_{F_e} - nl_{F_h}$ transition coming out of the $k \cdot p$ model is smaller than the effective mass model, particularly for bigger l and n. Secondly, some forbidden transitions in the effective mass model become non-zero in the $k \cdot p$ model. In fact, these transitions may be further enhanced after the vertex correc-

	β_{nl}			
$l_{\text{cut-off}}$	$l=0$ (s-wave)	$l=1$ (p-wave)	$l=6$	$l=8$
HF level	1	1	1	1
0	1.089	0.813	0.993	0.983
1	2.015	0.873	1.005	0.976
2	2.399	1.546	0.971	0.936
3	2.603	1.841	0.935	0.927
4	2.729	2.008	0.878	0.880
5	2.814	2.116	0.614	0.997
6	2.875	2.193	0.634	0.926
7	2.920	2.250	0.978	0.663
8	2.956	2.294	1.133	0.680
9	2.984	2.329	1.226	1.005
10	3.007	2.358	1.290	1.151
11	3.026	2.382	1.338	1.239
12	3.042	2.402	1.375	1.300

Table 5.2: The enhancement factor from first-order MBPT $\beta_{nl} = |\mathcal{R}^{e-p}_{c,v} + \mathcal{R}^{(1)}_{c,v}|^2/|\mathcal{R}^{e-p}_{c,v}|^2$ for the transition $nl_{F_c} - nl_{F_v}$, where $n = 1$. The HF-level calculations have β_{nl} set equal to 1 as a reference. As $l_{\text{cut-off}}$ increases, for instance from $l_{\text{cut-off}} = 1$ to $l_{\text{cut-off}} = 2$, the angular momentum channel with $l' = 2$ (d-wave) has been included. The corresponding change in β_{nl} reflects the effect of the added l' channel. We note that, for a given l value, the value of β_{nl} w.r.t. $l_{\text{cut-off}}$, where $l_{\text{cut-off}} < l$, may fluctuate depending on whether the contribution from a lower angular momentum channel is negative or positive. The higher angular momentum channels always contribute a positive amount, which is evident by the fact that β_{nl} keeps growing if $l_{\text{cut-off}}$ increases and $l_{\text{cut-off}} > l$.

tion and contribute a small but finite amount to the cross-section $\sigma^{(1)}$. Generally, the $\mathrm{k}\cdot\mathrm{p}$ model results in a higher density of states within a certain energy range compared with the effective mass model. One thus expects a slightly higher value of $\sigma^{(1)}$ at a given ω from the $\mathrm{k}\cdot\mathrm{p}$ model, see Fig. 5.4.8b and Fig. 5.4.9b.

Next, we focus on the variation of the one-photon absorption cross-section $\sigma^{(1)}$ versus L and how the computation up to first-order vertex correction looks in comparison to the available experimental data.

The cross-sections $\sigma^{(1)}$ (with vertex correction) and $\sigma^{(1)}_{\text{HF}}$ (Hartree-Fock) are assumed to depend on some power of the edge length L. Using a least-square linear fit to the log-log relation between $\sigma^{(1)}$ or $\sigma^{(1)}_{\text{HF}}$ and L, one obtains $\log(\sigma^{(1)}) =$

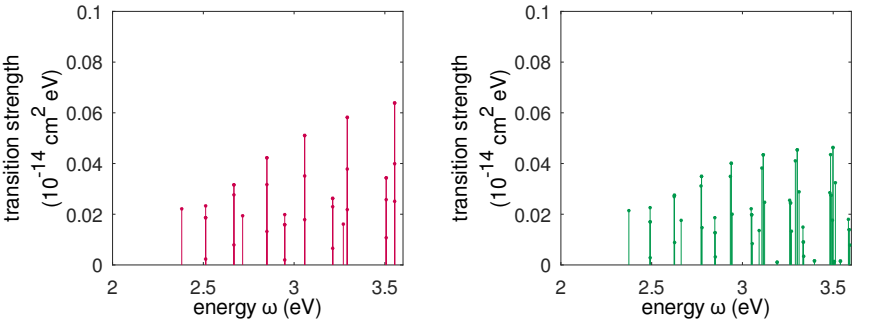

(a) Effective mass model

(b) 4×4 k $\cdot$ p model

Figure 5.4.10: Transition strength at HF level versus transition energy ω for $CsPbBr_3$ of edge length $L = 9.0$ nm in the effective mass model (left) and 4×4 k $\cdot$ p model (right). The basic parameters are from parameter set 1. Note the higher density of the transitions in the case of 4×4 k $\cdot$ p model.

$A_1 \log(L) + A_0$, where $A_1 = 2.88$, and $\log(\sigma^{(1)}_{\rm HF}) = B_1 \log(L) + B_0$, where $B_1 = 3.02$. See Fig. 5.4.11 for further details. The experimental data from Chen et al., Ref. [23], and Makarov et al., Ref. [80], show that the slope of the log-log plot ranges from 2.94 to 3.36, which is in accordance with our theoretical values.

As the nanocrystals become bigger, the density of states that controls the absorption of the system grows proportionally to the volume in which the particles are confined. Regarding the ground state $1s^e_{1/2} - 1s^h_{1/2}$, the enhancement factor β_τ has a strong L-dependence as shown in Fig. 5.4.5. For the higher states $nl_{F_c} - nl_{F_v}$, the enhancement factors β_{nl} get closer to unity, see Table 5.1, and are less dependent on L owning to stronger effective confinement. At $\omega = 3.1$ eV, for instance, the density of final exciton states become the dominant contribution to the one-photon cross-section. Hence, $\sigma^{(1)}$ at this value of ω is expected to depend approximately linearly on the volume L^3. The cubic functions aL^3 and bL^3 in Fig. 5.4.12, where $a = 2.6 \times 10^{-3}$ and $b = 1.9 \times 10^{-3}$ (unit: 10^{-14}cm^2 nm^{-3}), describe reasonably the theoretical data for $\sigma^{(1)}$ and $\sigma^{(1)}_{\rm HF}$ respectively. We use these cubic fits to compare with the measurements in Fig. 5.4.12. Large discrepancies exist between experimental data and the theoretical calculations as well as among the various experiments themselves.

On the theoretical side, there are several reasons for an underestimation of the true one-photon absorption cross-section. Since we stop at first-order correction for the electron-photon vertex, some error undoubtedly comes from the truncation of the MBPT. The discussion at the end of the previous subsection suggests a substantially larger correcting factor when the correlation is taken into account up to all-order. From the current theoretical point of view, the truncation at first-order MBPT is regarded as one of the biggest sources of theoretical error.

The angular momentum cut-off $l_{\text{cut-off}}$ not only affects the high-energy end of $\sigma^{(1)}(\omega)$ but also the amount of MBPT correction at first-order. One must note that the vertex correction of which the radial part is given in (5.4.5) for a more

highly excited exciton contains many terms with varying signs. The contributions in $\mathcal{R}_{c,v}^{\text{inter}}$ from the lower states fluctuate and partly cancel the contributions from the higher states than (c, v). The transitions with high l closer to $l_{\text{cut-off}} = 12$ tend to receive lower first-order correction factors β_{nl} compared to the actual values by using a higher $l_{\text{cut-off}}$, see Table 5.2 for some example calculations.

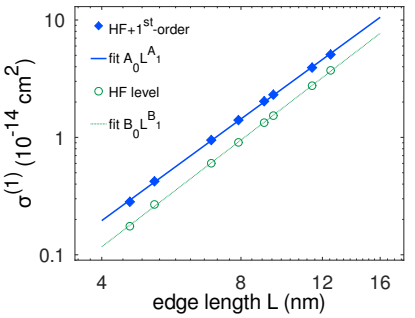

Figure 5.4.11: The calculated $\sigma^{(1)}$ (filled blue diamonds) and $\sigma_{\text{HF}}^{(1)}$ (empty green circles) (unit: 10^{-14}cm^2) for $CsPbBr_3$ at $\omega = 3.1$ eV versus edge length L(nm) in logarithmic scale. The least-square linear fits show the slope of the log-log curves to be $A_1 = 2.88$ for $\sigma^{(1)}$ (blue solid line) and $B_1 = 3.02$ for $\sigma_{\text{HF}}^{(1)}$ (dashed green line). The almost cubic dependence on L is attributed to the proportionality between the density of states (for large sizes) and the nanocrystal volume L^3. The calculated data points were done with $\varepsilon_{\text{out}} = 2.4$ (toluene).

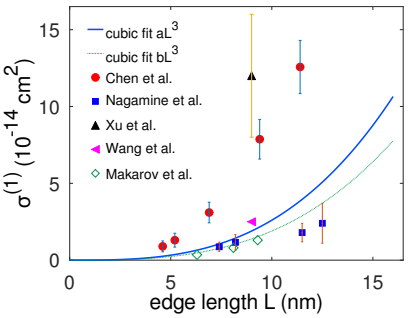

Figure 5.4.12: Cubic fits of theoretical data and the measured $\sigma^{(1)}$ versus edge length L for $CsPbBr_3$. The fitting coefficients are a $= 2.6 \times 10^{-3}$ and b $= 1.9 \times 10^{-3}$ (unit: $10^{-14}\text{cm}^2\ \text{nm}^{-3}$) The experimental data are taken from Chen et al., Ref. [23]; Nagamine et al., Ref. [85]; Xu et al., Ref. [130]; Wang et al., Ref. [126]; Makarov et al., Ref. [80]. All the measurements were done at excitation energy $\omega = 3.1$ eV, which is equivalent to 400 nm. We did not include the theoretical data for the clarity of the plots. Note that $\varepsilon_{\text{out}} = 2.4$ in our calculations, assuming the solvent is toluene.

As we have discussed in Subsection 3.4.1, the actual value of E_{p} is unknown with the estimated values ranging from $E_{\text{p}}^{8\times8} = 16.39$ eV to $E_{\text{p}}^{4\times4} = 27.88$ eV for $CsPbBr_3$ depending on the various $\mathbf{k}\cdot\mathbf{p}$ model, see Table 3.2 and Table 3.1. In the calculations of the cross-section and the transition strength, the value $E_{\text{p}} = 20.0$ eV, which is intermediate between $E_{\text{p}}^{8\times8}$ and $E_{\text{p}}^{4\times4}$, was selected. In Fig. 5.4.13, we provide the calculated $\sigma^{(1)}$ at two different frequencies $\omega = 3.1$ eV (orange circles) and $\omega = 2.65$ eV (green diamonds) for various E_{p} such that 8 eV $< E_{\text{p}} <$ 24.5 eV. The explicit formulas of the polynomial fits can be found in the caption of Fig. 5.4.13.

We note to the readers that no linear function serves as a good fit for the theoretical data, for example at $\omega = 3.1$ eV, and a quadratic function such as $\text{a}_2^{\sigma}E_{\text{p}}^2 + \text{a}_1^{\sigma}E_{\text{p}}$ must be used to obtain a reasonable description. Compared to the case of spontaneous emission, the one-photon absorption cross-section $\sigma^{(1)}$, as a series expansion w.r.t. E_{p}, contains higher power of E_{p}. This reflects the two ways in which $\sigma^{(1)}$ depends on E_{p}: via the transition strength in (5.4.13) and via the sum

over the final states $|I\rangle$ that implicitly contains the density of states at a given ω.

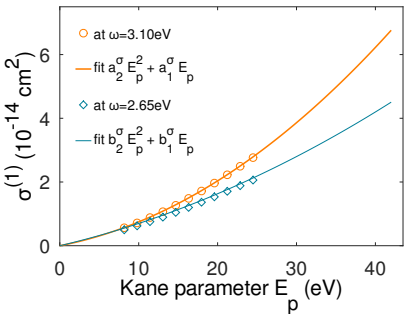

Figure 5.4.13: The calculated one-photon absorption cross-section versus E_p for $CsPbBr_3$ of edge length $L = 9.0$ nm at two different energies, $\omega = 3.1$ eV (orange circles) and $\omega = 2.65$ eV (green diamonds). Their respective fits are the two solid lines, $\mathrm{a}_2^\sigma E_\mathrm{p}^2 + \mathrm{a}_1^\sigma E_\mathrm{p}$ where $\mathrm{a}_2^\sigma = 2.69 \times 10^{-3}$ and $\mathrm{a}_1^\sigma = 4.79 \times 10^{-2}$ and $\mathrm{b}_2^\sigma E_\mathrm{p}^2 + \mathrm{b}_1^\sigma E_\mathrm{p}$ where $\mathrm{b}_2^\sigma = 1.17 \times 10^{-3}$ and $\mathrm{b}_1^\sigma = 5.82 \times 10^{-2}$. The deviation from a linear relationship between E_p and $\sigma^{(1)}$ is considered to be due to the density of states that depends on the $\mathrm{k} \cdot \mathrm{p}$ correction, which in turn depends on E_p.

On the one hand, $\Xi_{IJ}^{(1)}$ is proportional to $|\mathcal{R}_{c,v}^{e-p} + \mathcal{R}_{c,v}^{(1)}|^2$, which scales almost linearly in E_p with a small quadratic dependence, see the discussion for the decay rate $1/\tau^{(1)}$. It explains the fairly linear part of $\sigma^{(1)}$ for small E_p. On the other hand, the $\mathrm{k} \cdot \mathrm{p}$ corrections that are proportional to E_p increase the density of states, especially further away from the band edge, as discussed above. Consequently, $\sigma^{(1)}(E_\mathrm{p})$ deviates more from a linear relationship w.r.t. E_p.

The polynomial fits in Fig. 5.4.13 allow the ability to extrapolate into higher E_p region, where one faces the problem of spurious solution of the $\mathrm{k} \cdot \mathrm{p}$ model. Once a better knowledge of E_p is obtained via an *ab initio* method or some measurements, the resulting cross-section can be calculated by using, for instance

$$\sigma^{(1)}(E_\mathrm{p}) = \mathrm{a}_2^\sigma E_\mathrm{p}^2 + \mathrm{a}_1^\sigma E_\mathrm{p}$$

for the exciting laser of wavelength 400 nm (i.e. $\omega = 3.1$ eV).

So far, the effective dielectric constant from the bulk has been used. Similar to the discussion in Subsection 4.3.2, some uncertainty exists related to the potential dependence of ε_in on the size of the nanocrystals. Due to the lack of knowledge of $\varepsilon_\mathrm{in}(\vec{r}, \omega)$, the error coming from the size-dependent ε_in remains undetermined. The dielectric screening of the electron-photon interaction, as reflected by the ratio $f_\varepsilon^2/\varepsilon_\mathrm{out}^{1/2}$, also depends on the dielectric constant of the external medium. The specific experimental conditions may introduce some variation for ε_out.

The various solvents, among which toluene [23, 130] and hexane [85] are the most common, may have different dielectric constants. Toluene has $\varepsilon_\mathrm{out} = 2.4$ whereas the dielectric constant of hexane is approximately $\varepsilon_\mathrm{out} = 1.9$. The change of ε_out from 2.4 to 1.9 gives rise to about 14% relative error in the cross-section [23, 85]. When the nanocrystals are closely packed into a thin film [126] instead of being dispersed in solutions [80, 23], the ε_out should perhaps be treated as having the same value as the optical dielectric constant of the semiconductor ε_opt. Depending on the material of the nanocrystals, these detailed experimental set-ups can also introduce a variation in $\sigma^{(1)}$ up to 45%.

Another source of experimental error is the estimation of the concentration of nanocrystals, especially in solutions. This may explain the big factors between the measured cross-sections $\sigma^{(1)}$, for instance between the data by Chen et al. [23] and by Makarov et al. [80].

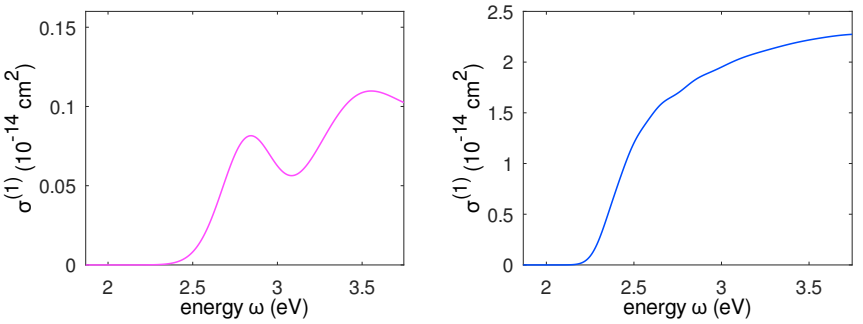

(a) $L = 3.2$ nm (b) $L = 9.0$ nm

Figure 5.4.14: The calculated one-photon absorption cross-section $\sigma^{(1)}$ (with first-order vertex correction) versus energy ω for two radii, $L = 3.2$ nm and $L = 9.0$ nm, of $CsPbBr_3$ nanocrystals. The basic band parameters are from parameter set 1 with $E_p = 20.0$ eV. The outside medium has dielectric constant $\varepsilon_{out} = 2.4$. The same lower bound $\delta E_{min} = 20$ meV for the energy denominator was used for both radii. $\varepsilon_{out} = 2.4$ and $\delta E_{min} = 20$ meV were used for both radii. The homogeneous broadening ΔE_0 and the size variation $\Delta L/L$ were chosen to appropriate various experimental values [35, 15]. For $D = 3.7$ nm, $\Delta E_0 = 120$ meV and $\Delta L/L = 16\%$ are estimated from Dong et al., Ref. [35]. The edge length $L = 3.2$ nm is equivalent to a diameter $D = 3.7$ nm. For $L = 9.0$ nm, $\Delta E_0 = 100$ meV and $\Delta L/L = 12\%$ are taken from Brennan et al., Ref. [15]. The width of the PL peak from Dong et al., Ref. [35], basically agrees with the width of the first absorption peak from Brennan et al., Ref. [15].

As the last part of the discussion on one-photon absorption, we give example calculations of $\sigma^{(1)}$ for $CsPbBr_3$ versus ω for two different edge lengths of nanocrystals, $L = 3.2$ nm and $L = 9.0$ nm. The point here is to show how the $\sigma^{(1)}(\omega)$ curves as functions of the energy ω would behave when the size changes. The parameters used for these calculations were as before, see the description of Fig. 5.4.14. Apart from the uncertainty with the basic parameters for the $\mathbf{k}\cdot\mathbf{p}$ theory and the dielectric functions, one needs to also estimate the parameters ΔE_0 for homogeneous broadening and $\Delta L/L$ for the size broadening. The homogeneous broadening ΔE_0 can be estimated from either the width of the PL peak or the first absorption peak (if available) for a given size. The size variation is specific to the method of synthesis and various experimental conditions such as temperature etc. A good reference of $\Delta L/L$ can be taken from Fig. S1 in Ref. [15].

For the size $L = 9.0$ nm, $\Delta E_0 = 100$ meV and $\Delta L/L = 12\%$, i.e. $\Delta L = 1.1$ nm, which are intermediate between the corresponding values for $L = 8.5$ nm and $L = 9.2$ nm from table S2 in Ref. [15]. The numbers in the supplementary information of Ref. [15] are in general agreement with other experimental reported values [100, 23, 133]. The homogeneous width was taken to be $\Delta E_0 = 120$ meV for $L = 3.2$ nm [15] whereas the size distribution is $\Delta L/L = 16\%$, which implies $\Delta L = 0.5$ nm. The high monodispersity was chosen for a direct comparison with the measurement in Fig. 5.4.15a from Ref. [35] for the diameter $D = 3.7$ nm. Note that in Ref. [35], the synthesis gives the nanocrystals roughly spherical shape. So

the size $D = 3.7$ nm should be interpreted as the diameter of the nanocrystals, which is equivalent to cubic edge length $L = 3.2$ nm in the current modelling.

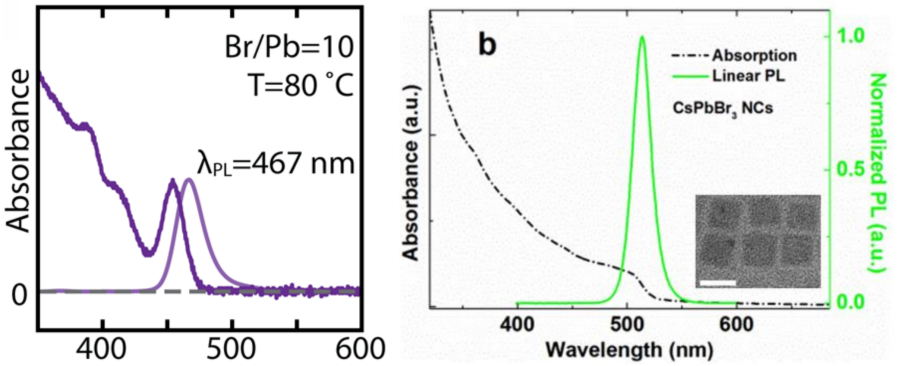

(a) $D = 3.7$ nm (b) $L = 9.0$ nm

Figure 5.4.15: Experimental absorption curves for $CsPbBr_3$ for two different sizes. $D = 3.7$ nm and $L = 9.0$ nm were taken from Dong et al., Ref. [35], and Chen et al., Ref. [25] respectively.

The smaller nanocrystals $D = 3.7$ nm have more clearly observed absorption features than $L = 9.0$ nm nanocrystals and the theory correctly reproduces this phenomenon. The $1s^e_{1/2} - 1s^h_{1/2}$ transition energy is around $\omega = 2.82$ eV, which corresponds to the first absorption peak as seen in Fig. 5.4.14a. This transition energy stays slightly above the emission frequency $\omega = 2.65$ eV ($\lambda_{\mathrm{PL}} = 467$ nm in Fig. 5.4.15a). The comparison for other sizes between the theoretical calculations and the data by Dong et al., Ref. [35], can be found in Fig. 3.4.3a. The first absorption local maximum in Fig. 5.4.15a happens around $\omega = 2.76$ eV, which is equivalent to $\lambda_{\mathrm{abs}} = 450$ nm, and is much closer to our calculated transition energy. The difference between the PL and the first absorption peaks is the Stokes shift [71], which may depend on the size of the nanocrystals [15].

The various absorption shoulders as observed in Fig. 5.4.15a between 2.75 eV and 3.1 eV are missing from the current theory Fig. 5.4.14a. While a similar remark is true also for $L = 9.0$ nm, we also note that the steep rise of $\sigma^{(1)}$ for energy above 400 nm that does not show also on Fig. 5.4.14b.

As the last note, we would like to conclude that the need for a better assessment of the absorption features and of the correct curvature of the curves $\sigma^{(1)}$ w.r.t. ω necessitates the theoretical calculations where (i) the Coulomb interaction should be accounted for completely by using an all-order method and (ii) the $p_{3/2}$ band is preferably included in the $\mathrm{k} \cdot \mathrm{p}$ model.

Chapter 6

Conclusion

In this work, we have developed a theoretical approach to study the correlation effects in the systems of semiconductor nanocrystals. The basic assumption of spherical symmetry has been made throughout the entire thesis. The angular-radial separation, which was allowed by the underlying spherical symmetry, improves considerably the computational efficiency. There are two essential elements of the system that one needs to take care of: the Coulomb interaction and the effect of confinement on the kinetic energy. The Hamiltonian for the particle kinetic energy in a confining potential can be described using the well-established $\mathrm{k} \cdot \mathrm{p}$ model.

The Coulomb interaction was treated in two steps. First, we incorporated into the non-interacting single-particle model the Hartree-Fock approximation for describing the intercarrier interaction. This produces a mean-field level theory, which has been shown to provide a satisfactory description of the single exciton energy. The second step involves constructing the two building blocks of many-body perturbation theory: a perturbative potential V and a basis set. In this thesis, they correspond to the configuration-averaged Hartree-Fock approximation and together they allow one to go beyond this mean-field theory via using the many-body perturbation theory. The calculations of the correlation energies and of the correlated electron-photon interaction were performed up to the lowest-order, nonzero contributions in many-body perturbation theory. We shall summarize our main results and basic conclusions in Section 6.1. A discussion of some future research directions will be provided in Section 6.2.

6.1 Summary of basic findings

In Chapter 3, the configuration-averaged Hartree-Fock potential V_{HF}, which is spherically symmetric, was used to calculate the single exciton binding energy of perovskite nanocrystals of various sizes. After careful literature research, we concluded that many of the fundamental parameters of the perovskite band structures are still poorly known. The values of these parameters from density functional theory, such as the reduced mass, differ by a factor of two from the measured reduced mass [99, 132]. We claim that more thorough calculations that go beyond density functional theory must be used instead, such as the GW calculations in Ref. [122].

The band gap E_{gap} of many perovskite materials have a clear dependence on the

temperature T. After adjusting the exciton energy with $E_{\text{gap}}(T)$, the theoretical single exciton energies match excellently the experimental data, as shown in Fig. 3.4.3, except for some small deviation at $L < 5.0$ nm. The Hartree-Fock potential, which is first-order in many-body perturbation theory, captures most of the exciton binding energy. We attribute the overestimation at small L to three factors: the Stokes shift, the use of an infinite barrier in the confining potential and the probable size-dependence of the dielectric constant ε_{eff}.

Chapter 4 was concerned with the correlation energy of the single exciton, trions and biexciton. We used the degenerate, open-shell MBPT to calculate the long-range exchange splitting between the dark and bright excitons. Section 4.2 reasserts the fact that the long-range exchange contribution is nonzero for the ground state exciton [106]. Up to second-order MBPT, the exchange contribution to the dark-bright exciton splitting varies from approximately 0.5 meV to a few milielectronvolts. The second-order term is shown to be rather important compared to the first-order term for the large nanocrystals, as reflected in the enhancement factor β_{LR}.

Section 4.3 confirms the previous observation that the biexciton and trion shifts are essentially zero at mean-field level [113]. However, by using closed-shell formalism of nondegenerate MBPT, we demonstrated that the biexciton or trion emission is clearly red-shifted up to second-order (lowest-order) MBPT. The biexciton shifts are bigger than those of trions for all sizes. Nonetheless, the theoretical values at this level come out about 1.5-2.0 times smaller than the experimental data. We ascribe the major cause of this rather unsatisfactory result to the truncation at second order in our theory and the inconsistency among the different measurements. Another source of errors may come from the variation of the dielectric function $\varepsilon(\vec{r}, \omega)$ on the excitation frequency ω involved in the many-body Feynman diagrams and the size of the nanocrystal.

In Chapter 5, we studied the electron-photon interaction, both at Hartree-Fock level and up to first-order vertex correction. The radiative decay rate $1/\tau$ and the one-photon absorption cross-section $\sigma^{(1)}$ were calculated and discussed. The Kane parameter E_{p} and the dielectric screening factor f_ε are among the most important parameters for the one-photon processes. The rate $1/\tau$ and the cross-section $\sigma^{(1)}$ show an approximate linear dependence on E_{p} and f_ε^2. The precise value of E_{p} is unknown, as established in Section 3.4.1. Therefore, we have also performed calculations of τ and $\sigma^{(1)}$ while letting E_{p} vary in some conservative range in Section 5.3 and Section 5.4. These calculations make it easier for extracting the corresponding lifetime and cross-section once the true value of E_{p} will be known in the future.

By comparing the results at Hartree-Fock level and at HF plus first-order vertex correction, it is clearly shown that the vertex correction plays a fundamental role in the electron-photon interaction. Regarding the spontaneous emission from the exciton ground state, the vertex correction increases the radiative decay rate by a factor β_τ equal to 2 up to 4 as the nanocrystal size varies from 5.0 nm to 13.0 nm. The more weakly confined the exciton, which is equivalent to a bigger nanocrystal, the more important the correlation effect. However, the enhancement factor becomes smaller as the energy of an exciton state gets higher. Hence, further

away from the band edge, the vertex correction to the cross-section $\sigma^{(1)}$ is not as large as that for the radiative lifetime.

With the first-order vertex correction included, we note that the calculated lifetime still remains about 2 to 3 times bigger than the measured values. We argued that, in this case, the overestimation comes from the truncation at first-order many-body perturbation theory. A method that takes care of the Coulomb correlation up to all orders is strictly necessary, especially in the weak confinement limit. Our theory also underestimates the experimental cross-section in Ref. [23] by a sizable ratio. Surely, an all-order approach would further enhance the theoretical results of $\sigma^{(1)}$. Additionally, we speculate that the $p_{3/2}$ band, which stays about 1.0 eV above the band edge in perovskites, potentially increases the final answer for the cross-section.

6.2 Outlook

Many directions for future research can be taken from the theoretical formulation of the current work. Below, we list a number of possibilities that one can pursue.

From the discussions in Chapter 4 and Chapter 5, the dominant contribution to the theoretical errors is the truncation at the first nonzero (or lowest order) term of the MBPT series. The Bethe-Salpeter equation offers a way to treat the correlation correction to electron-photon vertex up to all orders. This technique can be used, in principle, for the single exciton binding energy, from which we can derive nonperturbatively the long-range exchange contribution to the true dark-bright exciton splitting. To obtain an all-order correction for the biexciton and trion shifts, the many-body perturbative approach, such as configuration interaction, can be employed. Considering the electron-photon interaction in particular, many measurements of the multiphoton absorption cross-section are available in the literature [23, 85, 25]. The current second-quantization technique used in Chapter 5 can be extended to treat the case of multiphoton absorption [81].

To more accurately model the system, one should take into account the fact that the surface barrier is, in fact, never infinite. Hence, the use of a more realistic confining potential with a finite barrier is expected to further improve the theoretical prediction of, for example, the single exciton energy. A finite barrier allows the particle wave function to extend into the outer region. This will likely reduce the total kinetic energy of the particles and also modify the intercarrier Coulomb interaction. The potential barrier can be known if the band misalignment between the nanocrystal material and the outside medium can be either calculated or measured. One can make use of a well-chosen confining potential to describe the situation of a core-shell nanoparticle. Here, the core nanocrystal is covered inside one semiconducting shell or even multishells. Upon knowing the details of the band structure of all involved semiconductors, the boundary condition given in Ref. [17] can be deployed to construct a kinetic model for the core-shell systems.

The Auger recombination depletes the multicarriers created in an excitonic system with more than one electron and one hole and, thus, is proved to be detrimental to the multiexciton generation process [59, 108, 143]. With the current $\mathbf{k} \cdot \mathbf{p}$ approach, one can easily compute the Coulomb matrix element that is involved in the

relevant Auger process. The Auger recombination rate can be calculated using the Fermi golden rule. Other decay channels, such as electron-phonon interaction [31], should also be taken into consideration for a more complete description. Instead of Fermi golden rule, one can also build a quantum-dynamical model with these decay pathways included in the Lindblad master equations for describing the open quantum systems of nanocrystals [16].

With these open problems, and many more that were not even listed here, we would like to conclude this thesis with the ending remark that one expects semiconductor nanocrystals to continue to be a productive area of future research, both experimentally and theoretically.

Appendices

Appendix A

Coulomb interaction in momentum space

The Bloch functions $u_{a\alpha,k}(\tilde{r})$, which correspond to the α-component of the k · p wave function $|a\rangle$, are periodic w.r.t. the Bravais lattice vectors $\vec{R}$. We define the Fourier transformation as follows.

$$\begin{aligned} u_{a\alpha,k}(\tilde{r}) &= \sum_{\vec{\mathsf{K}}} u_{a\alpha k}(\vec{\mathsf{K}}) \mathrm{e}^{i\vec{\mathsf{K}}.\tilde{r}} \\ \Leftrightarrow u_{a\alpha k}(\vec{\mathsf{K}}) &= \frac{1}{v_0} \int_{v_0} u_{a\alpha,k}(\vec{r}) \mathrm{e}^{-i\vec{\mathsf{K}}.\tilde{r}}\ d\tilde{r}, \end{aligned} \tag{A.0.1}$$

where $\vec{\mathsf{K}}$ is a reciprocal lattice vector with $\mathrm{e}^{i\vec{\mathsf{K}}.\vec{R}} = 1$ and $\int_{v_0}$ denotes integrating over a unit cell v_0, where the position $\tilde{r}$ lives.

The completeness relation of the Bloch functions says that

$$\frac{1}{v_0} \int_{v_0} \mathrm{e}^{-i(\vec{\mathsf{K}}-\vec{\mathsf{K}}').\tilde{r}}\ d\tilde{r} = \delta_{\vec{\mathsf{K}}\vec{\mathsf{K}}'}, \tag{A.0.2}$$

$$\sum_{\vec{\mathsf{K}}} \mathrm{e}^{i\vec{\mathsf{K}}.(\tilde{r}-\tilde{r}')} = \delta(\tilde{r}-\tilde{r}'). \tag{A.0.3}$$

With the definition above of the Fourier transform, the product of two Bloch functions in position space can be written as

$$u^*_{a\alpha,k'}(\tilde{r})\ u_{c\mu,k}(\tilde{r}) = \sum_{\vec{\mathsf{K}}\vec{\mathsf{K}}'} \mathrm{e}^{i(\vec{\mathsf{K}}-\vec{\mathsf{K}}').\tilde{r}}\ u^*_{a\alpha,k'}(\vec{\mathsf{K}}')\ u_{c\mu,k}(\vec{\mathsf{K}}). \tag{A.0.4}$$

The Fourier identity (A.0.4) means that

$$\int \mathrm{e}^{i(\vec{k}-\vec{k}'+\vec{q}).\vec{r}} u^*_{a\alpha,k'}(\vec{r})\ u_{c\mu,k}(\vec{r})\ d\vec{r} = \sum_{\vec{\mathsf{K}}'\vec{\mathsf{K}}} u^*_{a\alpha,k'}(\vec{\mathsf{K}}')\ u_{c\mu,k}(\vec{\mathsf{K}})\ \delta(\vec{k}-\vec{k}'+\vec{\mathsf{K}}-\vec{\mathsf{K}}'+\vec{q}), \tag{A.0.5}$$

where $\delta(\vec{k}-\vec{k}'+\vec{\mathsf{K}}-\vec{\mathsf{K}}'+\vec{q})$ is a Dirac-δ since the integral $\int \ldots d\vec{r}$ above is over the whole space, not within a unitcell. Note that $\vec{k}$, $\vec{k}'$ and $\vec{q}$ are general wave vectors that need not belong to the reciprocal space.

Let $|\psi_a\rangle,\ |\psi_b\rangle,\ |\psi_c\rangle$ and $|\psi_d\rangle$ be the full wave functions, i.e. they contain also the Bloch functions $u_k(\vec{r})$, corresponding to the k · p wave functions $|a\rangle,\ |b\rangle, |c\rangle$ and $|d\rangle$ respectively.

$$\begin{aligned} |\psi_a\rangle &= \textstyle\sum_\alpha |\psi_{a\alpha}\rangle, \quad |\psi_c\rangle = \sum_\mu |\psi_{c\mu}\rangle, \\ |\psi_b\rangle &= \textstyle\sum_\beta |\psi_{b\beta}\rangle, \quad |\psi_d\rangle = \sum_\nu |\psi_{d\nu}\rangle, \end{aligned} \tag{A.0.6}$$

where the position representation of, for instance, $|\psi_{a\alpha}\rangle$ is

$$\psi_{a\alpha}(\vec{r}) = \sum_{\vec{k}} \mathrm{e}^{i\vec{k}.\vec{r}} c_{a\alpha}(\vec{k})\ u_{a\alpha,k}(\vec{r}). \tag{A.0.7}$$

The sums over $\alpha,\ \beta,\ \mu$ and ν also correspond to the k · p components of the total wave functions $|a\rangle,\ |b\rangle, |c\rangle$ and $|d\rangle$.

With the full wave functions given in (A.0.6), the general Coulomb matix element $\langle\psi_a\psi_b|G_{12}|\psi_c\psi_d\rangle$ is

$$\langle\psi_a\psi_b|G_{12}|\psi_c\psi_d\rangle = \sum_{\alpha\beta,\mu\nu} \langle\psi_{a\alpha},\psi_{b\beta}|G_{12}|\psi_{c\mu},\psi_{d\nu}\rangle. \tag{A.0.8}$$

In this part, we shall derive the momentum-space representation of the Coulomb interaction. We start with the simple, unscreened Coulomb interaction $G_{12} = r_{12}^{-1}$. The momentum representation of G_{12} in this case is

$$\frac{1}{r} = \int \mathrm{e}^{i\vec{q}\cdot\vec{r}}\ \frac{4\pi}{q^2}\ d\vec{q}. \tag{A.0.9}$$

Therefore, one has

$$\begin{aligned} \langle\psi_{a\alpha},\psi_{b\beta}|G_{12}|\psi_{c\mu},\psi_{d\nu}\rangle &= \iint \psi^*_{b\beta}(\vec{r}_2)\psi^*_{a\alpha}(\vec{r}_1)\frac{1}{|\vec{r}_1-\vec{r}_2|}\psi_{c\mu}(\vec{r}_1)\psi_{d\nu}(\vec{r}_2)\ d\vec{r}_1\ d\vec{r}_2 \\ &= \sum_{\vec{k}'_2\vec{k}'_1,\vec{k}_1\vec{k}_2} \iint c^*_{b\beta}(\vec{k}'_2)u^*_{b\beta,\vec{k}'_2}(\vec{r}_2)\ c^*_{a\alpha}(\vec{k}'_1)u^*_{a\alpha,\vec{k}'_1}(\vec{r}_1) \\ \mathrm{e}^{i(\vec{k}_1-\vec{k}'_1).\vec{r}_1}\mathrm{e}^{i(\vec{k}_2-\vec{k}'_2).\vec{r}_2} &\int \frac{4\pi}{q^2}\ \mathrm{e}^{i\vec{q}\cdot(\vec{r}_1-\vec{r}_2)}\ d\vec{q}\ c_{c\mu}(\vec{k}_1)u_{c\mu,k_1}(\vec{r}_1)\ c_{d\nu}(\vec{k}_2)u_{d\nu,k_2}(\vec{r}_2)\ d\vec{r}_1\ d\vec{r}_2. \end{aligned} \tag{A.0.10}$$

After making the Fourier transform of the Bloch functions $u_{b\beta,\vec{k}'_2},\ u_{a\alpha,\vec{k}'_1},\ u_{c\mu,k_1}$ and $u_{d\nu,k_2}$ into the space of the reciprocal lattice vectors $\vec{\mathsf{K}}'_2,\ \vec{\mathsf{K}}'_1,\ \vec{\mathsf{K}}_1$ and $\vec{\mathsf{K}}_2$, we

arrive at

$$
\begin{aligned}
&\langle \psi_{a\alpha}, \psi_{b\beta} | G_{12} | \psi_{c\mu}, \psi_{d\nu} \rangle \\
&= \sum_{\vec{k}_2' \vec{k}_1', \vec{k}_1 \vec{k}_2} \iint c^*_{b\beta}(\vec{k}_2') c^*_{a\alpha}(\vec{k}_1')\ c_{c\mu}(\vec{k}_1) c_{d\nu}(\vec{k}_2)\ \mathrm{e}^{i(\vec{k}_1 - \vec{k}_1').\vec{r}_1} \mathrm{e}^{i(\vec{k}_2 - \vec{k}_2').\vec{r}_2} \int \frac{4\pi}{q^2}\ \mathrm{e}^{i\vec{q}.(\vec{r}_1 - \vec{r}_2)}\ d\vec{q} \\
&\sum_{\vec{\mathsf{K}}_1', \vec{\mathsf{K}}_1} \mathrm{e}^{i(\vec{\mathsf{K}}_1 - \vec{\mathsf{K}}_1').\vec{r}_1} u^*_{a\alpha, k_1'}(\vec{\mathsf{K}}_1')\ u_{c\mu, k_1}(\vec{\mathsf{K}}_1) \sum_{\vec{\mathsf{K}}_2', \vec{\mathsf{K}}_2} \mathrm{e}^{i(\vec{\mathsf{K}}_2 - \vec{\mathsf{K}}_2').\vec{r}_2} u^*_{b\beta, k_2'}(\vec{\mathsf{K}}_2')\ u_{d\nu, k_2}(\vec{\mathsf{K}}_2)\ d\vec{r}_1\ d\vec{r}_2 \\
&= \sum_{\vec{k}_2' \vec{k}_1', \vec{k}_1 \vec{k}_2} c^*_{b\beta}(\vec{k}_2')\ c^*_{a\alpha}(\vec{k}_1')\ c_{c\mu}(\vec{k}_1)\ c_{d\nu}(\vec{k}_2) \sum_{\vec{\mathsf{K}}_1', \vec{\mathsf{K}}_1} u^*_{a\alpha, k_1'}(\vec{\mathsf{K}}_1')\ u_{c\mu, k_1}(\vec{\mathsf{K}}_1) \\
&\sum_{\vec{\mathsf{K}}_2', \vec{\mathsf{K}}_2} u^*_{b\beta, k_2'}(\vec{\mathsf{K}}_2')\ u_{d\nu, k_2}(\vec{\mathsf{K}}_2) \int \frac{4\pi}{q^2}\ \delta(\vec{k}_1 - \vec{k}_1' + \vec{\mathsf{K}}_1 - \vec{\mathsf{K}}_1' + \vec{q})\ \delta(\vec{k}_2 - \vec{k}_2' + \vec{\mathsf{K}}_2 - \vec{\mathsf{K}}_2' - \vec{q})\ d\vec{q}.
\end{aligned}
\tag{A.0.11}
$$

The last expression can be obtained by integrating the exponential functions w.r.t. the position vectors $\vec{r}_1$ and $\vec{r}_2$

$$
\begin{aligned}
\int \mathrm{e}^{i(\vec{k}_1 - \vec{k}_1').\vec{r}_1}\ \mathrm{e}^{i\vec{q}.\vec{r}_1}\ \mathrm{e}^{i(\vec{\mathsf{K}}_1 - \vec{\mathsf{K}}_1').\vec{r}_1}\ d\vec{r}_1 &= \delta(\vec{k}_1 - \vec{k}_1' + \vec{\mathsf{K}}_1 - \vec{\mathsf{K}}_1' + \vec{q}), \\
\int \mathrm{e}^{i(\vec{k}_2 - \vec{k}_2').\vec{r}_2}\ \mathrm{e}^{-i\vec{q}.\vec{r}_2}\ \mathrm{e}^{i(\vec{\mathsf{K}}_2 - \vec{\mathsf{K}}_2').\vec{r}_2}\ d\vec{r}_2 &= \delta(\vec{k}_2 - \vec{k}_2' + \vec{\mathsf{K}}_2 - \vec{\mathsf{K}}_2' - \vec{q}).
\end{aligned}
\tag{A.0.12}
$$

The integral over $\vec{q}$ gives

$$
\int \ldots\ d\vec{q} = \frac{4\pi}{|\vec{k}_1 - \vec{k}_1' + \vec{\mathsf{K}}_1 - \vec{\mathsf{K}}_1'|^2}\ \delta(\vec{k}_1 - \vec{k}_1' + \vec{\mathsf{K}}_1 - \vec{\mathsf{K}}_1' + \vec{k}_2 - \vec{k}_2' + \vec{\mathsf{K}}_2 - \vec{\mathsf{K}}_2'), \tag{A.0.13}
$$

which immediately brings us to the expression (4.2.4).

Appendix B

Angular algebra

Wigner-Eckart theorem says that for a spherical tensor $\mathbf{t}^k_q$,

$$\langle j'm'|\mathbf{t}^k_q|jm\rangle = (-1)^{j'-m'} \begin{pmatrix} j' & k & j \\ -m' & q & m \end{pmatrix} \times \langle j'||\mathbf{t}^k||j\rangle$$

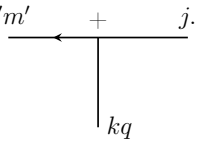

(B.0.1)

B.1 Reduced matrix element of $\vec{\nabla}$

Considering the spherical harmonics, we have (see Ref. [14])

$$|lm\rangle = Y^l_m(\theta,\phi) = (-1)^m \sqrt{\frac{2l+1}{4\pi}} \sqrt{\frac{(l-m)!}{(l+m)!}}\, P^l_m(\cos\theta)\, \mathrm{e}^{im\phi}. \tag{B.1.1}$$

Given that $\nabla^1_0 = \nabla_z = \cos\theta \frac{\partial}{\partial r} - \frac{\sin\theta}{r}\frac{\partial}{\partial\theta}$ and by letting $x = \cos\theta$, one has

$$\begin{aligned} \nabla^1_0 P^l_{|m|}(x) &= \cos\theta P^l_{|m|}(x)\frac{\partial}{\partial r} + \frac{1}{r}(1-x^2)\frac{dP^l_{|m|}(x)}{dx} \\ &= \left(\frac{l-|m|+1}{2l+1}P^{l+1}_{|m|}(x) + \frac{l+|m|}{2l+1}P^{l+1}_{|m|}(x)\right)\frac{\partial}{\partial r} \\ &+ \left(-\frac{l(l-|m|+1)}{2l+1}P^{l+1}_{|m|}(x) + \frac{(l+1)(l+|m|)}{2l+1}P^{l-1}_{|m|}(x)\right)\frac{1}{r}. \end{aligned} \tag{B.1.2}$$

More generally, ∇^1_q connects $Y^l_m(\theta,\phi)$ to $Y^{l\pm1}_{m+1}(\theta,\phi)$.
From the action of ∇^1_0 on to the Legendre polynomials, which essentially is the

angular part of a spherical wave function, one can deduce its radial operator to be

$$\begin{aligned}\nabla_0^1 = Y_m^{l+1}(\theta,\phi)\sqrt{\frac{(l+m+1)(l-m+1)}{(2l+1)(2l+3)}}\left(\frac{\partial}{\partial r} - l\,\frac{1}{r}\right)\\ +Y_m^{l-1}(\theta,\phi)\sqrt{\frac{(l-m)(l+m)}{(2l+1)(2l-1)}}\left(\frac{\partial}{\partial r} + (l+1)\frac{1}{r}\right).\end{aligned} \tag{B.1.3}$$

Using the Wigner-Eckart theorem, we can derived from (B.1.3) the two non-zero reduced matrix elements of $\vec{\nabla}$: $\langle l||\vec{\nabla}||l-1\rangle$ and $\langle l||\vec{\nabla}||l+1\rangle$.

For the case $\langle l||\vec{\nabla}||l-1\rangle$ $(l \geq 1)$:

$$\begin{aligned}\langle l\ l-1|\nabla_0^1|l-1\ l-1\rangle &= -\begin{pmatrix} l & 1 & l-1 \\ -(l-1) & 0 & l-1\end{pmatrix}\ \langle l||\vec{\nabla}||l-1\rangle \\ \Rightarrow \frac{1}{\sqrt{[l]}}\left(\frac{\partial}{\partial r} - (l-1)\frac{1}{r}\right) &= \frac{1}{\sqrt{l[l]}}\ \langle l||\vec{\nabla}||l-1\rangle.\end{aligned} \tag{B.1.4}$$

For the case $\langle l||\vec{\nabla}||l+1\rangle$ $(l \geq 0)$:

$$\begin{aligned}\langle l\ l|\nabla_0^1|l+1\ l\rangle &= \begin{pmatrix} l & 1 & l+1 \\ -l & 0 & l\end{pmatrix}\ \langle l||\vec{\nabla}||l+1\rangle \\ \Rightarrow \frac{1}{\sqrt{[l+1]}}\left(\frac{\partial}{\partial r} + (l+2)\frac{1}{r}\right) &= -\frac{1}{\sqrt{(l+1)[l+1]}}\ \langle l||\vec{\nabla}||l+1\rangle.\end{aligned} \tag{B.1.5}$$

In summary, the nonzero reduced matrix elements $\langle l||\vec{\nabla}||l'\rangle$ are

$$\langle l||\vec{\nabla}||l'\rangle = \begin{cases}\sqrt{l}\left(\frac{\partial}{\partial r} - (l-1)\frac{1}{r}\right), & \text{if } l = l'+1, \\ \sqrt{l+1}\left(\frac{\partial}{\partial r} + (l+2)\frac{1}{r}\right), & \text{if } l = l'-1.\end{cases} \tag{B.1.6}$$

B.2 Reduced matrix element of $\left\{\vec{\nabla}\vec{\nabla}\right\}^2$

$\left\{\vec{\nabla}\vec{\nabla}\right\}^2 \equiv \{\nabla^1\nabla^1\}^2$ denotes the rank-two spherical tensor that is a sum of two spherical rank-one tensor $\vec{\nabla} \equiv \nabla^1$. The notation ∇^1 for $\vec{\nabla}$ means to emphasize its rank.

From the previous subsection, we know that $\vec{\nabla}$ connects $Y_m^l(\theta,\phi)$ to $Y_{m'}^{l'}(\theta,\phi)$ where $l' = l \pm 1$. As a result, $\left\{\vec{\nabla}\vec{\nabla}\right\}^2$ connects $Y_m^l(\theta,\phi)$ to $Y_{m'}^{l'}(\theta,\phi)$. For the rank-two tensor, it is noted that $l' = l$ or $l \pm 2$.

For the case $\langle l||\left\{\vec{\nabla}\vec{\nabla}\right\}^2||l+2\rangle$:

By using the Wigner-Eckart theorem for $\langle l\ l|\left\{\vec{\nabla}\vec{\nabla}\right\}^2_{-2}|l+2\ l+2\rangle$, one has

$$\langle l\ l|\left\{\vec{\nabla}\vec{\nabla}\right\}^2_{-2}|l+2\ l+2\rangle = \underset{2,\ -2}{\overset{l,\ l \quad + \quad l+2,\ l+2}{\overset{\longleftarrow}{\Big|}}} \times\langle l||\left\{\vec{\nabla}\vec{\nabla}\right\}^2||l+2\rangle \tag{B.2.1}$$

$$= \frac{1}{\sqrt{[l+2]}} \times \langle l||\left\{\vec{\nabla}\vec{\nabla}\right\}^2||l+2\rangle.$$

On the other hand, the action of each $\vec{\nabla} \equiv \nabla^1$ on the angular momentum states gives

$$\langle l\ l|\left\{\vec{\nabla}\vec{\nabla}\right\}^2_{-2}|l+2\ l+2\rangle = \langle l\ l|\nabla^1_{-1}|l+1\ l+1\rangle \times \langle l+1\ l+1|\nabla^1_{-1}|l+2\ l+2\rangle$$

$$= \langle l||\vec{\nabla}||l+1\rangle\times \underset{1\ -1}{\overset{l,\ l \quad + \quad l+1,\ l+1}{\overset{\longleftarrow}{\Big|}}} \times$$

$$\langle l+1||\vec{\nabla}||l+2\rangle\times \underset{1,\ -1}{\overset{l+1,\ l+1 \quad + \quad l+2,\ l+2}{\overset{\longleftarrow}{\Big|}}} .$$

(B.2.2)

The angular diagrams above can be easily evaluated by noting that

$$\underset{1\ -1}{\overset{l,\ l \quad + \quad l+1,\ l+1}{\overset{\longleftarrow}{\Big|}}} = (-1)^{l-l}\begin{pmatrix} l & 1 & l+1 \\ -l & -1 & l+1 \end{pmatrix} = (-1)^{l+1+(l+1)}\begin{pmatrix} l & 1 & l+1 \\ l & 1 & -(l+1) \end{pmatrix}$$

$$= (-1)^{l+1+(l+1)}\begin{pmatrix} l & 1 & l+1 \\ -(l+1) & 1 & l \end{pmatrix} = \frac{1}{\sqrt{[l+1]}}.$$

(B.2.3)

The last expresion in (B.2.2) becomes

$$\langle l\ l|\left\{\vec{\nabla}\vec{\nabla}\right\}^2_{-2}|l+2\ l+2\rangle = \frac{1}{\sqrt{[l+1]}}\langle l||\vec{\nabla}||l+1\rangle\times\frac{1}{\sqrt{[l+2]}}\langle l+1||\vec{\nabla}||l+2\rangle. \tag{B.2.4}$$

Therefore,

$$\langle l||\left\{\vec{\nabla}\vec{\nabla}\right\}^2||l+2\rangle = \sqrt{\frac{(l+1)(l+2)}{2l+3}}\times\left(\frac{1}{r^2}\frac{\partial}{\partial r}(r^2\frac{\partial}{\partial r}) + (2l+3)\frac{1}{r}\frac{\partial}{\partial r} + (l+1)(l+3)\frac{1}{r^2}\right). \tag{B.2.5}$$

Similarly, by applying the same procedure to $\langle l+2\ l+2|\left\{\vec{\nabla}\vec{\nabla}\right\}^2_2|l\ l\rangle$, we have

$$\langle l{+}2||\left\{\vec{\nabla}\vec{\nabla}\right\}^2||l\rangle = \sqrt{\frac{(l+1)(l+2)}{2l+3}}\times\left(\frac{1}{r^2}\frac{\partial}{\partial r}(r^2\frac{\partial}{\partial r}) - (2l+3)\frac{1}{r}\frac{\partial}{\partial r} + l(l+2)\frac{1}{r^2}\right). \tag{B.2.6}$$

For the case $\langle l||\left\{\vec{\nabla}\vec{\nabla}\right\}^2||l\rangle$:

$$\begin{aligned}\langle l\ l|\left\{\vec{\nabla}\vec{\nabla}\right\}^2_0|l\ l\rangle &= \langle l\ l|\sum_{q,q'}\nabla^1_q\nabla^1_{q'}\sqrt{[2]}\begin{pmatrix}1 & 1 & 2\\ q & q' & 0\end{pmatrix}|l\ l\rangle\\ &= \frac{1}{\sqrt{6}}\left(2\langle l\ l|\nabla^1_0\nabla^1_0|l\ l\rangle + \langle l\ l|\nabla^1_{-1}\nabla^1_1|l\ l\rangle + \langle l\ l|\nabla^1_1\nabla^1_{-1}|l\ l\rangle\right)\\ &= \frac{1}{\sqrt{6}}\left(3\langle l\ l|\nabla^1_0\nabla^1_0|l\ l\rangle - \langle l\ l|\nabla^2|l\ l\rangle\right).\end{aligned} \tag{B.2.7}$$

From Wigner-Eckart theorem, the LHS of Eq. (B.2.7) turns into

$$\langle l\ l|\left\{\vec{\nabla}\vec{\nabla}\right\}^2_0|l\ l\rangle = \quad \times\langle l||\left\{\vec{\nabla}\vec{\nabla}\right\}^2||l\rangle \tag{B.2.8}$$

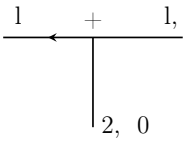

$$= \sqrt{\frac{(2l-1)l}{(2l+3)(l+1)}}\times\langle l||\left\{\vec{\nabla}\vec{\nabla}\right\}^2||l\rangle.$$

The terms on the RHS can be evaluated explicitly to be

$$\begin{aligned}\langle l\ l|\nabla^1_0\nabla^1_0|l\ l\rangle &= \langle l\ l|\nabla^1_0|l+1\ l\rangle\langle l+1\ l|\nabla^1_0|l\ l\rangle\\ &= \frac{1}{2l+3}\left(\frac{\partial}{\partial r}+(l+2)\frac{1}{r}\right)\left(\frac{\partial}{\partial r}-l\frac{1}{r}\right)\\ &= \frac{1}{2l+3}\left(\frac{1}{r^2}\frac{\partial}{\partial r}(r^2\frac{\partial}{\partial r}) - l(l+1)\frac{1}{r^2}\right)\end{aligned} \tag{B.2.9}$$

and

$$\langle l\ l|\nabla^2|l\ l\rangle = \frac{1}{r^2}\frac{\partial}{\partial r}(r^2\frac{\partial}{\partial r}) - l(l+1)\frac{1}{r^2}. \tag{B.2.10}$$

The RHS of (B.2.7) can be expressed as

$$\frac{1}{\sqrt{6}}\left(3\langle l\ l|\nabla^1_0\nabla^1_0|l\ l\rangle - \langle l\ l|\nabla^2|l\ l\rangle\right) = -\sqrt{\frac{2}{3}}\frac{l}{2l+3}\left(\frac{1}{r^2}\frac{\partial}{\partial r}(r^2\frac{\partial}{\partial r}) - l(l+1)\frac{1}{r^2}\right). \tag{B.2.11}$$

Therefore, the reduce matrix element $\langle l||\left\{\vec{\nabla}\vec{\nabla}\right\}^2||l\rangle$ is

$$\langle l||\left\{\vec{\nabla}\vec{\nabla}\right\}^2||l\rangle = -\sqrt{\frac{2}{3}}\sqrt{\frac{l(l+1)(2l+1)}{(2l-1)(2l+3)}}\left(\frac{1}{r^2}\frac{\partial}{\partial r}(r^2\frac{\partial}{\partial r}) - l(l+1)\frac{1}{r^2}\right) \tag{B.2.12}$$

B.3 Reduced matrix element of coupled angular momenta

In this section of the appendix, we shall derive the reduced matrix element of $\langle (j_1, j_2)\, J||\mathbf{t}^k||\, (j_1, j_2)\, J\rangle$ where $\vec{j_1}+\vec{j_2}=\vec{J}$ and $\vec{j_1'}+\vec{j_2'}=\vec{J'}$. The spherical operator $\mathbf{t}^k$ acts on either j_1 or j_2.

In the derivation below, the part where $\mathbf{t}^k$ acts on will be written in bold letters. For instance, $\langle(\mathbf{j_1}j_2)JM|\mathbf{t}^k|(\mathbf{j_1'}j_2')J'M'\rangle$ means the reduced matrix element between the coupled states $|JM\rangle$ and $|J'M'\rangle$ of $\mathbf{t}^k$ where $\mathbf{t}^k$ atcs on the first spherical tensor $\mathbf{j_1}$ and $\mathbf{j_1'}$.

Let us consider the case where $\mathbf{t}^k$ acts on the first angular momentum j_1 and j_1'.

$\langle(\mathbf{j_1}j_2)JM|\mathbf{t}^k|(\mathbf{j_1'}j_2')J'M'\rangle$

$$= \sqrt{[J][J']}\times$$

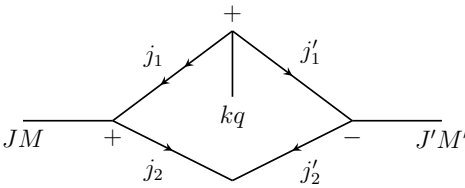

$$\times\langle j_1||\mathbf{t}^k||j_1'\rangle \tag{B.3.1}$$

$$\langle(\mathbf{j_1}j_2)JM|\mathbf{t}^k|(\mathbf{j_1'}j_2')J'M'\rangle = \sqrt{[J][J']}\ \ \delta_{j_2,j_2'}\times$$

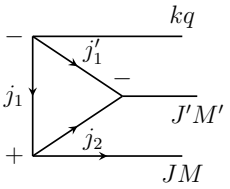

$$\times\ \langle j_1||\mathbf{t}^k||j_1'\rangle$$

$$= \sqrt{[J][J']}\ \ \delta_{j_2,j_2'}\ \langle j_1||\mathbf{t}^k||j_1'\rangle\times$$

$$(-1)^{(j_1+j_2+J)+(J+k+J')+2j_1+2j_2}\times$$

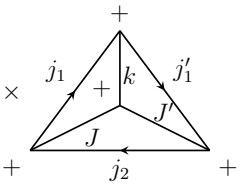

$$\times$$

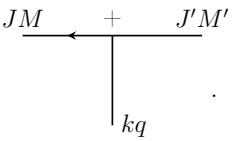

.

Again, by using Wigner-Eckart Theorem, one arrives at

$$\langle(\mathbf{j_1}j_2)JM|\mathbf{t}^{kq}|(\mathbf{j_1'}j_2')J'M'\rangle = \langle(\mathbf{j_1}j_2)J||\mathbf{t}^k||(\mathbf{j_1'}j_2')J'M'\rangle\times$$

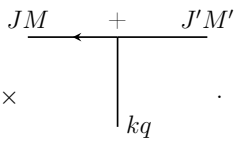

.

Since (j_1, j_2, J) forms a triangle, $(-1)^{2(j_1+j_2+J)}=1$ and the phase factor $(-1)^{(j_1+j_2+J)+(J+k+J')+2j_1+2j_2}=(-1)^{j_1+j_2+J'+k}$.

Therefore, the desired reduced matrix element can be written as

$$\langle(\mathbf{j_1}, j_2)\, J||\mathbf{t}^k||\,(\mathbf{j'_1}, j'_2)\, J'\rangle = \chi_1(j_1 j_2 J, j'_1 j'_2 J')\ \langle j_1||\mathbf{t}^k||j'_1\rangle, \tag{B.3.2}$$

where the coefficient $\chi_1(j_1 j_2 J, j'_1 j'_2 J')$ represents the effect of the coupled angular momenta and is equal to

$$\chi_1(j_1 j_2 J, j'_1 j'_2 J') = (-1)^{j_1+j_2+J'+k}\ \sqrt{[J][J']}\ \begin{Bmatrix} k & J & J' \\ j_2 & j'_1 & j_1 \end{Bmatrix}\ \delta_{j_2, j'_2}\ . \tag{B.3.3}$$

For the other case in which $\mathbf{t}^k$ acts on j_2 and j'_2, we can quickly arrive at the final results by noting the identity

$$\langle j_1 m_1, j_2 m_2|JM\rangle = (-1)^{j_1+j_2-J}\langle j_2 m_2, j_1 m_1|JM\rangle = (-1)^{J-j_1-j_2}\langle j_2 m_2, j_1 m_1|JM\rangle.$$

See Chapter 2 of Ref. [75] for more details. This identity leads to

$$\langle(j_1, \mathbf{j_2})\, JM|\mathbf{t}^{k_q}|\,(j'_1, \mathbf{j'_2})\, J'M'\rangle = (-1)^{J-j_1-j_2+j'_2+j'_1-J'}\times$$

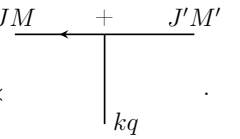

$$\langle(\mathbf{j_2}, j_1)\, JM||\mathbf{t}^k||\,(\mathbf{j'_2}, j'_1)\, J'M'\rangle\times \qquad .$$

(B.3.4)

Therefore, the previous results can be transformed into, by using the relation (B.3.4),

$$\langle(j_1, \mathbf{j_2})\, J||\mathbf{t}^{k_|}|\,(j'_1, \mathbf{j'_2})\, J'\rangle = \chi_2(j_1 j_2 J, j'_1 j'_2 J')\ \langle j_2||\mathbf{t}^k||j'_2\rangle, \tag{B.3.5}$$

where the coefficient χ_2 is defined to be

$$\chi_2(j_1 j_2 J, j'_1 j'_2 J') = (-1)^{j'_1+j'_2+J+k}\ \sqrt{[J][J']}\ \begin{Bmatrix} k & J & J' \\ j_1 & j'_2 & j_2 \end{Bmatrix}\ \delta_{j_1, j'_1}. \tag{B.3.6}$$

B.4 Matrix elements of the dot product of two spherical tensors

Here, we give the derivation of the matrix element $\langle(j_1 j_2)JM|\mathbf{t}^k(1)\cdot\mathbf{t}^k(2)|(j'_1 j'_2)J'M'\rangle$, where $\mathbf{t}^k(1)$ and $\mathbf{t}^k(2)$ act on the first and second angular momentum respectively.

To more conveniently operate using the angular-momentum algebra given in Ref. [75], we use the following identity

$$\begin{aligned}\langle(j_1 j_2)JM|\mathbf{t}^k(1)\cdot\mathbf{t}^k(2)|(j'_1 j'_2)J'M'\rangle = \\ (-1)^k\sqrt{[k]}\times\langle(j_1 j_2)JM|\{\mathbf{t}^k(1)\mathbf{t}^k(2)\}^0_0|(j'_1 j'_2)J'M'\rangle.\end{aligned} \tag{B.4.1}$$

The matrix element on the RHS can be expressed as

$$\langle (j_1 j_2) JM | \{ \mathbf{t}^k(1) \mathbf{t}^k(2) \}^0_0 | (j_1' j_2') J'M' \rangle$$

$$= \sqrt{[J][J']} \times$$

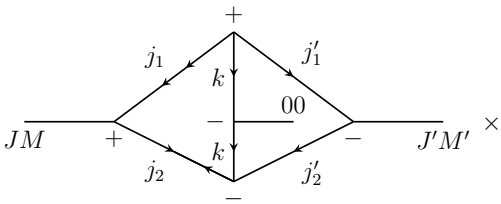

$$\times \langle j_1 || \mathbf{t}_1^k || j_1' \rangle \langle j_2 || \mathbf{t}_2^k || j_2' \rangle$$

$$= \sqrt{\tfrac{[J][J']}{[k]}} \times$$

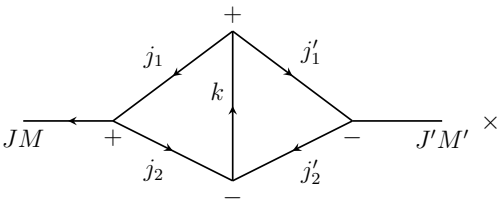

$$\times \langle j_1 || \mathbf{t}_1^k || j_1' \rangle \langle j_2 || \mathbf{t}_2^k || j_2' \rangle$$

To evaluate the angular diagram above, we apply JLV2 theorem (please refer to Chapter 4, Ref. [75]) to the free lines JM and $J'M'$. Together with some phases to change the direction of some arrows and the two vertices with $(-)$ sign to $(+)$ sign, we get

$$\langle (j_1 j_2) JM | \{ \mathbf{t}^k(1) \mathbf{t}^k(2) \}^0_0 | (j_1' j_2') J'M' \rangle = (-1)^{2j_1+2J+2k+(j_1'+j_2'+J)+(k+j_2'+j_2)} \, \delta_{JJ'} \delta_{MM'} \times \frac{1}{\sqrt{[k]}} \begin{Bmatrix} j_2' & j_2 & k \\ j_1 & j_1' & J \end{Bmatrix} \times \langle j_1 || \mathbf{t}_1^k || j_1' \rangle \langle j_2 || \mathbf{t}_2^k || j_2' \rangle. \tag{B.4.2}$$

The total phase factor of $\langle (j_1 j_2) JM | \mathbf{t}^k(1) \cdot \mathbf{t}^k(2) | (j_1' j_2') J'M' \rangle$ can be simplified into

$$(-1)^{2j_1+3J+4k+j_1'+2j_2'+j_2} = \underbrace{(-1)^{2(j_1+k+j_1')}}_{=1} \underbrace{(-1)^{2(J+j_2'-j_1')}}_{=1} \underbrace{(-1)^{2k}}_{=1} (-1)^{j_1'+j_2+J} \tag{B.4.3}$$

since both (j_1, k, j_1') and (J, j_2', j_1') satisfy the triangle condition and k is an integer.

Therefore, combining (B.4.1), (B.4.2) and (B.4.3) gives

$$\langle (j_1 j_2) JM | \mathbf{t}^k(1) \cdot \mathbf{t}^k(2) | (j_1' j_2') J'M' \rangle = (-1)^{j_1'+j_2+J} \, \delta_{JJ'} \delta_{MM'} \begin{Bmatrix} j_2' & j_2 & k \\ j_1 & j_1' & J \end{Bmatrix} \times \langle j_1 || \mathbf{t}_1^k || j_1' \rangle \langle j_2 || \mathbf{t}_2^k || j_2' \rangle. \tag{B.4.4}$$

Appendix C

Configuration-averaged Hartree-Fock approximation: derivation

For simplicity of notations, l/J_a is used synonymously for $l/J_{a\alpha}$ provided that its meaning is clear under a given context.

The direct (3.3.13) and exchange (3.3.14) contains the sums over the magnetic quantum number M_b of the substates in shell B. We perform these sums in this chapter of the appendix.

Note that the only part of the Coulomb interaction that depends on the magnetic quantum number M_b (and also M_a) is the H-shape angular diagram that appears in (3.3.6) and (3.3.10).

C.1 Direct interaction

For the direction interaction, $|F_c M_c\rangle = |F_a M_a\rangle$ and $|F_d M_d\rangle = |F_b M_b\rangle$. The sum over M_b means that one joins the free ends on the right hand side into a closed loop.

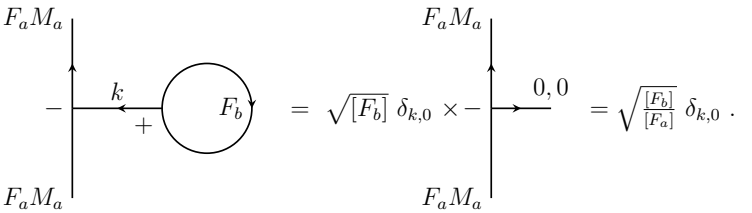

(C.1.1)

The Kronecker-δ means that only the mono-pole term is non-zero, as claimed in the main text. Using that fact that $k = 0$, we can further simplify the expression for the coefficients $c^k_\chi(lJ_{a\alpha}F_a; lJ_{a\mu}F_a)$ and $c^k_\chi(lJ_{b\beta}F_b; lJ_{b\nu}F_b)$ defined in (3.3.8).

As an example, we explicitly evaluate the coefficient $c^k_\chi(lJ_{a\alpha}F_a; lJ_{a\mu}F_a)$. The

6j-symbol is

$$\begin{Bmatrix} F_a & F_a & k \\ l_{a\mu} & l_{a\alpha} & J_{a\alpha} \end{Bmatrix} \equiv$$

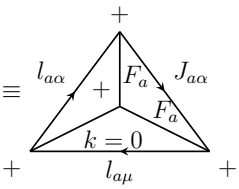

$$= (-1)^{l_{a\alpha}+J_{a\alpha}+F_a} \frac{1}{\sqrt{[l_{a\alpha}]}} \frac{1}{\sqrt{[F_a]}} \delta_{l_{a\alpha},l_{a\mu}} \,. \tag{C.1.2}$$

Given that $\langle l||\mathbb{C}^k||l'\rangle = (-1)^l \sqrt{[l][l']} \begin{pmatrix} l & k & l' \\ 0 & 0 & 0 \end{pmatrix}$ and $\begin{pmatrix} l & 0 & l' \\ 0 & 0 & 0 \end{pmatrix} = (-1)^l \, \delta_{l,l'} [l]^{-1/2}$, (see Chapter 2 of Ref. [75]), we have

$$\langle l_{a\alpha}||0||l_{a\mu}\rangle = \sqrt{[l_{a\alpha}]} \, \delta_{l_{a\alpha},l_{a\mu}}. \tag{C.1.3}$$

Together with (3.3.8), the coefficient $c^k_\chi(lJ_{a\alpha}F_a; lJ_{a\mu}F_a)$ can be simplified, for $k = 0$, into

$$c^k_\chi(lJ_{a\alpha}F_a; lJ_{a\mu}F_a) = \delta_{J_{a\alpha},J_{a\mu}} \, \delta_{l_{a\alpha},l_{a\mu}} \, \frac{1}{\sqrt{[F_a]}} \tag{C.1.4}$$

and, similarly, $c^k_\chi(lJ_{b\beta}F_b; lJ_{b\nu}F_b)$ is

$$c^k_\chi(lJ_{b\beta}F_b; lJ_{b\nu}F_b) = \delta_{J_{b\beta},J_{b\nu}} \, \delta_{l_{b\beta},l_{b\nu}} \, \frac{1}{\sqrt{[F_b]}}. \tag{C.1.5}$$

Note that $\delta_{J_{a\alpha},J_{a\mu}} \, \delta_{l_{a\alpha},l_{a\mu}} = \delta_{\alpha,\mu}$ and $\delta_{J_{b\beta},J_{b\nu}} \, \delta_{l_{b\beta},l_{b\nu}} = \delta_{\beta,\nu}$.

The sum over M_b, i.e. over all magnetic substates of shell B, yields,

$$\sum_{M_b} \langle ab|G_{12}|ab\rangle = [F_b] \times \sum_\alpha R_{a\alpha}(r) R_{a\alpha}(r) \, \mathcal{Y}^0[\sum_\beta R_{b\beta} R_{b\beta}](r). \tag{C.1.6}$$

Taking the functional derivative of (C.1.6) w.r.t. $\langle a|$, we arrive at (3.3.21) for $(V^b_{\rm dir}|a\rangle)_\alpha$.

C.2 Exchange interaction

Consider the exchange matrix element $\langle ab|G_{12}|ba\rangle$. In the exchange diagram, $|F_cM_c\rangle = |F_bM_b\rangle$ and $|F_dM_d\rangle = |F_aM_a\rangle$. The sum over M_b lead to

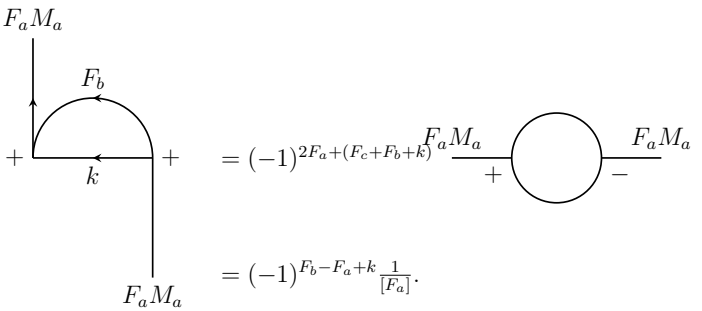

(C.2.1)

The phase factor $(-1)^k$ combines with $(-1)^k$ in (3.3.9). Summing the exchange interaction $\langle ab|G_{12}|ba\rangle$ over the magnetic substates M_b gives

$$\sum_{M_b}\langle ab|G_{12}|ba\rangle = (-1)^{F_b-F_a}[F_b]\times\sum_k \mathcal{Y}^k[\sum_{\beta,\nu} c^k_\chi(lJ_{b\beta}F_b;lJ_{a\nu}F_a)\ R_{b\beta}R_{a\nu}](r) \left(\sum_{\alpha,\mu} c^k_\chi(lJ_{a\alpha}F_a;lJ_{b\mu}F_b)\ R_{a\alpha}(r)R_{b\mu}(r)\right). \tag{C.2.2}$$

C.3 Self-energy

The H-shape angular diagram in (3.3.6) with $F_b = F_c = F_d = F_a$ and $M_b = M_c = M_d = M_a$ can be written in terms of 3j-symbol as

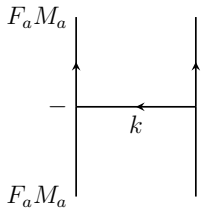

$$= (-1)^k\sum_m \begin{pmatrix} F_a & k & F_a \\ -M_a & m & M_a\end{pmatrix}^2 = (-1)^k \begin{pmatrix} F_a & k & F_a \\ -M_a & 0 & M_a\end{pmatrix}^2. \tag{C.3.1}$$

The last equality comes from the selection rule $(-M_a + m + M_a) = 0$ for the magnetic quantum numbers. Note the following identity for 3j-symbols

$$\sum_{m_1m_2}\begin{pmatrix} j_3 & j_1 & j_2 \\ m_3 & m_1 & m_2\end{pmatrix}\begin{pmatrix} j_3' & j_1 & j_2 \\ m_3' & m_1 & m_2\end{pmatrix} = \frac{1}{[j_3]}\ \delta_{j_3j_3'}\ \delta_{m_3m_3'}. \tag{C.3.2}$$

Averaging over the magnetic substate $|F_aM_a\rangle$ and using the identity (C.3.2) leads us to

$$\frac{1}{[F_a]}\sum_{M_a}\begin{pmatrix} F_a & k & F_a \\ -M_a & 0 & M_a\end{pmatrix}^2 = \sum_{M_aM_a'}\begin{pmatrix} k & F_a & F_a \\ 0 & M_a & M_a'\end{pmatrix}^2 = \frac{1}{[F_a]}\ \frac{1}{[k]}. \tag{C.3.3}$$

The coefficient c^k for self-energy, where with $|b\rangle = |c\rangle = |d\rangle = |a\rangle$, is

$$c^k(a\alpha\ a\beta, a\mu\ a\nu) = [F_a]^2\ c^k_\chi(lJ_{a\alpha}F_a;lJ_{a\mu}F_a)\ c^k_\chi(lJ_{a\beta}F_a;lJ_{a\nu}F_a). \tag{C.3.4}$$

Combining the results in (C.3.1), (C.3.3) and (C.3.4) leads one to the final expression (3.3.27) in the main text.

With this, the derivation for the radial formulas for $V_{\rm dir}$, $V_{\rm exc}$ and $V_{\rm self}$ is completed.

Appendix D

Single exciton angular diagrams

In this chapter of the appendix, we give the derivation of the expressions for the angular diagrams concerning the many-body perturbation theory corrections to the single exciton energy. These include the first-order direct $D^{exc}_{1,d}(k)$ and exchange $D^{exc}_{1,x}(k)$ angular diagrams of the multipole k in (4.2.29) and (4.2.30) as well as the second-order angular diagrams as defined in (4.2.44) and (4.2.46).

D.1 First-order direct angular diagram

Starting with the definition of $D^{exc}_{1,d}(k)$ as in (4.2.29),

$$D^{exc}_{1,d}(k) = \sum_{\substack{M_{c'}M_{v'} \\ M_cM_v}} C^*_{\rm eh}(F_{c'}M_{c'}, F_{v'}M_{v'}; F'_{\rm tot}M'_{\rm tot})\; D^1_d(k)\; C_{\rm eh}(F_cM_c, F_vM_v; F_{\rm tot}M_{\rm tot})$$

with the first-order direct angular diagram $D^1_d(k)$ given on the left of Fig. 4.2.3. The electron-hole Clebsch-Gordan coupling coefficients $C_{\rm eh}(F_cM_c, F_vM_v; F_{\rm tot}M_{\rm tot})$ and $C^*_{\rm eh}(F_{c'}M_{c'}, F_{v'}M_{v'}; F_{\rm tot}M_{\rm tot})$, of which their angular representations are in (4.2.19) and (4.2.20).

$D^{exc}_{1,d}(k) = \sqrt{[F'_{\rm tot}][F_{\rm tot}]} \times$

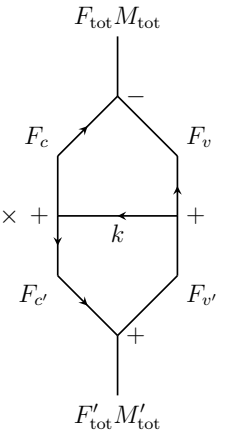

$= \sqrt{[F'_{\rm tot}][F_{\rm tot}]} \times$

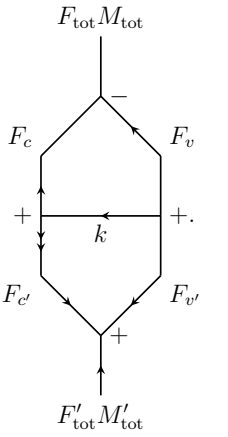

(D.1.1)

Applying the JLV2 theorem described in Chapter 4 of Ref. [75] to the free lines with $F_{\rm tot}M_{\rm tot}$ and $F'_{\rm tot}M'_{\rm tot}$ transforms the previous expression into

$$D^{exc}_{1,d}(k) = \sqrt{[F'_{\rm tot}][F_{\rm tot}]}\times$$

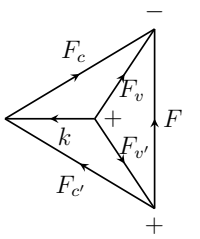

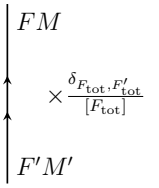

(D.1.2)

$$= (-1)^{F_c+F_v+F_{\rm tot}} \begin{Bmatrix} F_{v'} & k & F_v \\ F_c & F_{\rm tot} & F_{c'} \end{Bmatrix} \delta_{F_{\rm tot},F'_{\rm tot}}\ \delta_{M_{\rm tot},M'_{\rm tot}}.$$

Note the selection rule $\delta_{F_{\rm tot},F'_{\rm tot}}\ \delta_{M_{\rm tot},M'_{\rm tot}}$ in the expression (D.1.2) above. This unambiguously shows that the total angular momentum $F_{\rm tot}$ of the exciton is indeed conserved by the Coulomb interaction. The reader should bare in mind that $F_{\rm tot} \equiv F'_{\rm tot}$ also holds for the first-order exchange interaction and all the second-order corrections. For notational simplicity in the manipulations of these diagrams, we implicity assume that $F'_{\rm tot} = F_{\rm tot}$ in sections D.2- D.4 below.

D.2 First-order exchange angular diagram

Here, we give the derivation for $D^{exc}_{1,x}(k)$ in equation (4.2.30) for an exciton in angular state $|F_{\rm tot}M_{\rm tot}\rangle$.

$$D^{exc}_{1,x}k = [F_{\rm tot}] \times$$

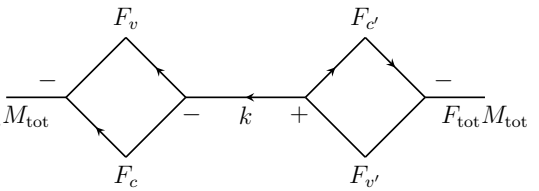

(D.2.1)

By applying the JVL2 theorem, again see Ref. [75], to the free lines with $F_{\rm tot}M_{\rm tot}$, we arrive at

$$D^{exc}_{1,x}k = [F_{\rm tot}] \times$$

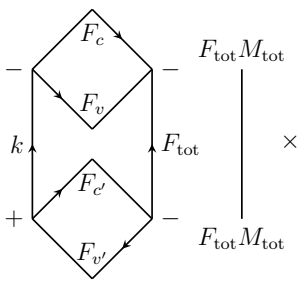

(D.2.2)

The value of the line on the right of (D.2.2) is 1 (Eq. (3.4) of Ref. [75].) Another application of JLV2 theorem (see problem 4.2 in Ref. [75]) for the lines k and $F_{\rm tot}$ in the above equation gives

$$\begin{aligned} D^{exc}_{1,x}k &= (-1)^{2F_{v'}+F_v+F_c+F_{\rm tot}}\ \frac{1}{[F_{\rm tot}]}\ \delta_{kF_{\rm tot}} \\ &= \frac{(-1)^{F_c-F_v+F_{\rm tot}}}{[F_{\rm tot}]}\ \delta_{F_{\rm tot}k}\ \ (F_v = F_{v'}). \end{aligned} \tag{D.2.3}$$

D.3 Second-order direct angular diagrams

The second-order direct angular diagram $D_d(k_1, k_2)$ Fig. 4.2.4b is coupled with the electron-hole Clebsch-Gordan coefficients $C_{\rm eh}(F_cM_c, F_vM_v; F_{\rm tot}M_{\rm tot})$ and $C^*_{\rm eh}(F_{c'}M_{c'}, F_{v'}M_{v'}; F_{\rm tot}M$ into $D^{exc}_{1,d}(k_1, k_2)$.

The JLV2 theorem in Ref. [75] leads us to

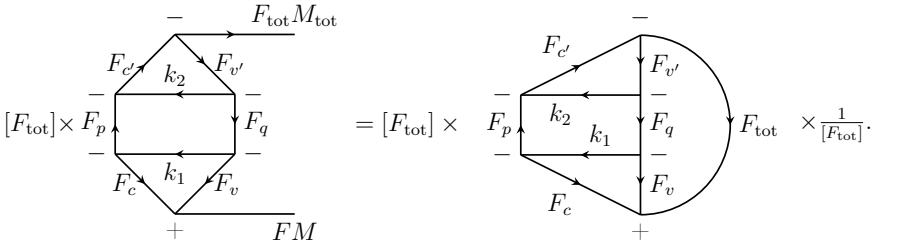

(and by using the JLV3 theorem of Ref. [75] for the three lines F_p, F_q and $F_{\rm tot}$)

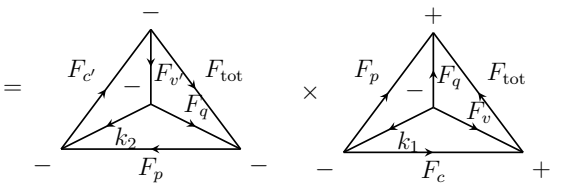

$$= (-1)^{2F_p} \begin{Bmatrix} F_{v'} & F_q & k_2 \\ F_p & F_{c'} & F_{\rm tot} \end{Bmatrix} \times (-1)^{(F_p+k_1+F_c)+(k_1+F_q+F_v)+2F_c+2F_{\rm tot}} \begin{Bmatrix} F_q & F_v & k_1 \\ F_c & F_p & F_{\rm tot} \end{Bmatrix}$$

One arrives at the last line by adding some phase factor to change the diagrams into the ones for 6j-symbols.

Note that $(-1)^{2k_1} = (-1)^{2F_{\rm tot}} = 1$ since k_1 and $F_{\rm tot}$ are both integers. Since F_c and F_p are half-integers, $(-1)^{3F_c} = (-1)^{-F_c}$ and $(-1)^{3F_p} = (-1)^{-F_p}$. Finally, with $F_{v'} = F_v,\ F_{c'} = F_c$, one can put the last expression into its final form in (4.2.47).

D.4 Second-order exchange angular diagrams

Our aim in this subsection is to calculate the exciton angular diagrams $D^{exc}_{2,x1}(k_1,k_2)$ and $D^{exc}_{2,x2}(k_1,k_2)$, as defined in (4.2.45) and (4.2.46).

Consider first the coupling between the direct diagram in $D^2_{x1}(k_1,k_2)$ on the left of Fig. 4.2.7 and the electron-hole Clebsch-Gordan coupling coefficient $C^*_{\rm eh}(F_{c'}M_{c'},F_{v'}M_{v'};F_{\rm tot}M_{\rm tot})$.

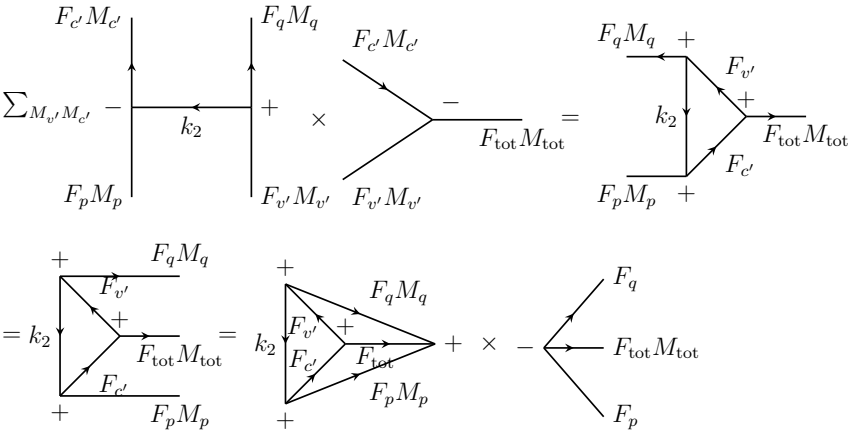

$$= (-1)^{2k_2+2F_{c'}+2F_p} \begin{Bmatrix} F_v & F_c & F_{\rm tot} \\ F_p & F_q & k_2 \end{Bmatrix} \times (-1)^{F_p+F_q+F_{\rm tot}}$$

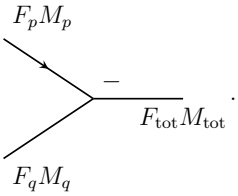

$$= (-1)^{F_p+F_q+F_{\rm tot}} \begin{Bmatrix} F_v & F_c & F_{\rm tot} \\ F_p & F_q & k_2 \end{Bmatrix} C^*_{\rm eh}(F_pM_p,F_qM_q;F_{\rm tot}M_{\rm tot})$$

Therefore, $D^{exc}_{2,x1}(k_1,k_2)$ is equal to

$$\sum_{\substack{M_{v'}M_{c'}\\ M_pM_q}} C_{\rm eh}(F_cM_c,F_vM_v;F_{\rm tot}M_{\rm tot}) \times$$

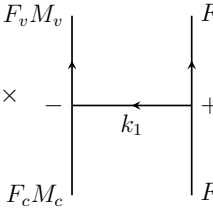

$$\times C^*_{\rm eh}(F_pM_p,F_qM_q;F_{\rm tot}M_{\rm tot})$$

$$\times (-1)^{F_p+F_q+F_{\rm tot}} \begin{Bmatrix} F_v & F_c & F_{\rm tot} \\ F_p & F_q & k_2 \end{Bmatrix}.$$

By making use of the results in subsection D.2,

$$D^{exc}_{2,x1}(k_1,k_2) = \frac{(-1)^{F_c+F_v+F_p-F_q}}{[F_{\rm tot}]} \begin{Bmatrix} F_v & F_c & F_{\rm tot} \\ F_p & F_q & k_2 \end{Bmatrix} \delta_{k_1,F}. \tag{D.4.1}$$

Either by repeating the calculation above, which is too tedious to be done again here, or by using the fact that $D^2_{x2}(k_1,k_2)$ can be transformed into $D^2_{x1}(k_1,k_2)$, we immediately have

$$D^{exc}_{2,x2}(k_1,k_2) = \frac{(-1)^{F_c-F_v+F_p+F_q}}{[F_{\rm tot}]} \begin{Bmatrix} F_v & F_c & F_{\rm tot} \\ F_p & F_q & k_1 \end{Bmatrix} \delta_{k_2,F}. \tag{D.4.2}$$

Note that $2F_q$ and $2F_v$ are odd intergers. Hence,

$$(-1)^{F_c-F_v+F_p+F_q} = (-1)^{F_c+F_v+F_p-F_q} = -(-1)^{F_c+F_v+F_p+F_q}.$$

This finishes the derivation for the expressions (4.2.47) and (4.2.48).

Bibliography

[1] Anna Amat, Edoardo Mosconi, Enrico Ronca, Claudio Quarti, Paolo Umari, Md. K. Nazeeruddin, Michael Grätzel, and Filippo De Angelis. Cation-induced band-gap tuning in organohalide perovskites: Interplay of spin–orbit coupling and octahedra tilting. *Nano Letters*, 14(6):3608–3616, 2014. PMID: 24797342.

[2] J. M. An, A. Franceschetti, S. V. Dudiy, and Alex Zunger. The peculiar electronic structure of pbse quantum dots. *Nano Letters*, 6(12):2728–2735, 2006. PMID: 17163696.

[3] J. Aneesh, Abhishek Swarnkar, Vikash Kumar Ravi, Rituraj Sharma, Angshuman Nag, and K. V. Adarsh. Ultrafast exciton dynamics in colloidal cspbbr3 perovskite nanocrystals: Biexciton effect and auger recombination. *The Journal of Physical Chemistry C*, 121(8):4734–4739, 2017.

[4] N. W. Ashcroft. *Solid State Physics*. Thomson Press, 1st edition edition, 2003.

[5] M Ashner, K. E. Shulenberger, F. Krieg, E. R. Powers, M. V. Kovalenko, M. G. Bawendi, and W. A. Tisdale. Size-dependent biexciton spectrum in cspbbr3 perovskite nanocrystals. *ACS Energy Letters*, 4(11):2639–2645, 2019.

[6] Matthew N. Ashner, Samuel W. Winslow, James W. Swan, and William A. Tisdale. Markov chain monte carlo sampling for target analysis of transient absorption spectra. *The Journal of Physical Chemistry A*, 123(17):3893–3902, 2019. PMID: 30900887.

[7] Maryam Azizi and Pawel Machnikowski. Interband coulomb coupling in narrow-gap semiconductor nanocrystals: $\mathbf{k} \cdot \mathbf{p}$ theory. *Phys. Rev. B*, 91:195314, May 2015.

[8] A. Baldereschi and Nunzio O. Lipari. Spherical model of shallow acceptor states in semiconductors. *Phys. Rev. B*, 8:2697–2709, Sep 1973.

[9] L. Bányai, P. Gilliot, Y. Z. Hu, and S. W. Koch. Surface-polarization instabilities of electron-hole pairs in semiconductor quantum dots. *Phys. Rev. B*, 45:14136–14142, Jun 1992.

[10] Michael A. Becker, Roman Vaxenburg, Georgian Nedelcu, Peter C. Sercel, Andrew Shabaev, Michael J. Mehl, John G. Michopoulos, Samuel G. Lambrakos, Noam Bernstein, John L. Lyons, Thilo Stöferle, Rainer F. Mahrt,

Maksym V. Kovalenko, David J. Norris, Gabriele Rainò, and Alexander L. Efros. Bright triplet excitons in caesium lead halide perovskites. *Nature*, 553(1):189–193, 2018.

[11] J. Bellessa, V. Voliotis, R. Grousson, X. L. Wang, M. Ogura, and H. Matsuhata. Quantum-size effects on radiative lifetimes and relaxation of excitons in semiconductor nanostructures. *Phys. Rev. B*, 58:9933–9940, Oct 1998.

[12] R. Ben Aich, I. Saïdi, S. Ben Radhia, K. Boujdaria, T. Barisien, L. Legrand, F. Bernardot, M. Chamarro, and C. Testelin. Bright-exciton splittings in inorganic cesium lead halide perovskite nanocrystals. *Phys. Rev. Applied*, 11:034042, Mar 2019.

[13] Riley E. Brandt, Vladan Stevanović, David S. Ginley, and Tonio Buonassisi. Identifying defect-tolerant semiconductors with high minority-carrier lifetimes: beyond hybrid lead halide perovskites. *MRS Communications*, 5(2):265–275, 2015.

[14] B. H. Bransden and C. J. Joachain. *Quantum Mechanics*. Pearson, 2nd edition edition, 1999.

[15] Michael C. Brennan, John E. Herr, Triet S. Nguyen-Beck, Jessica Zinna, Sergiu Draguta, Sergei Rouvimov, John Parkhill, and Masaru Kuno. Origin of the size-dependent stokes shift in cspbbr3 perovskite nanocrystals. *Journal of the American Chemical Society*, 139(35):12201–12208, 2017. PMID: 28772067.

[16] H. Breuer and F. Petruccione. *The Theory of Open Quantum Systems*. Oxford University Press, 2002.

[17] M G Burt. The justification for applying the effective-mass approximation to microstructures. *Journal of Physics: Condensed Matter*, 4(32):6651–6690, aug 1992.

[18] M G Burt. The evaluation of the matrix element for interband optical transitions in quantum wells using envelope functions. *Journal of Physics: Condensed Matter*, 5(24):4091–4098, jun 1993.

[19] Y. A. Bychkov and E. I. Rashba. Properties of a 2d electron gas with lifted spectral degeneracy. *Zh. Eksp. Teor. Fiz.*, 39:66–69, Jan 1984.

[20] Damien Canneson, Elena V. Shornikova, Dmitri R. Yakovlev, Tobias Rogge, Anatolie A. Mitioglu, Mariana V. Ballottin, Peter C. M. Christianen, Emmanuel Lhuillier, Manfred Bayer, and Louis Biadala. Negatively charged and dark excitons in cspbbr3 perovskite nanocrystals revealed by high magnetic fields. *Nano Letters*, 17(10):6177–6183, 2017. PMID: 28820601.

[21] J. A. Castañeda, G. Nagamine, E. Yassitepe, L. G. Bonato, O. Voznyy, S. Hoogland, A. F. Nogueira, E. H. Sargent, C. H. Brito Cruz, and L. A. Padilha. Efficient biexciton interaction in perovskite quantum dots under

weak and strong confinement. *ACS Nano*, 10(9):8603–8609, 2016. PMID: 27574807.

[22] J. Chen, Q. Zhang, J. Shi, S. Zhang, W. Du, Y. Mi, Q. Shang, P. Liu, X. Sui, X. Wu, R. Wang, B. Peng, H. Zhong, G. Xing, X. Qiu, T. C. Sum, and X. Liu. Room temperature continuous-wave excited biexciton emission in perovskite nanoplatelets via plasmonic nonlinear fano resonance. *Communications Physics*, 2, 2019.

[23] Junsheng Chen, Karel Žídek, Pavel Chábera, Dongzhou Liu, Pengfei Cheng, Lauri Nuuttila, Mohammed J. Al-Marri, Heli Lehtivuori, Maria E. Messing, Keli Han, Kaibo Zheng, and Tõnu Pullerits. Size- and wavelength-dependent two-photon absorption cross-section of cspbbr3 perovskite quantum dots. *The Journal of Physical Chemistry Letters*, 8(10):2316–2321, 2017. PMID: 28480702.

[24] Qi Chen, Nicholas De Marco, Yang (Michael) Yang, Tze-Bin Song, Chun-Chao Chen, Hongxiang Zhao, Ziruo Hong, Huanping Zhou, and Yang Yang. Under the spotlight: The organic–inorganic hybrid halide perovskite for optoelectronic applications. *Nano Today*, 10(3):355 – 396, 2015.

[25] W. Chen, S. Bhaumik, S. A. Veldhuis, G. Xing, Q. Xu, M. Grätzel, S. Mhaisalkar, N. Mathews, and T. C. Sum. Giant five-photon absorption from multidimensional core-shell halide perovskite colloidal nanocrystals. *Nat. Commun.*, 8:1–9, 2017.

[26] X. Y. Chin, D. Cortecchia, J. Yin, A. Bruno, and C. Soci. Lead iodide perovskite light-emitting field-effect transistor. *Nature Communications*, 6(1), 2015.

[27] C. Cohen-Tannoudji, J. Dupont-Roc, and G. Grynberg. *Atom-Photon Interactions: Basic Processes and Applications*. Wiley-VCH, 1998.

[28] M. Combescot and S.-Y. Shiau. *Excitons and Cooper Pairs: Two Composite Bosons in Many-Body Physics*. Oxford University Press, 1st edition edition, 2016.

[29] Monique Combescot and Roland Combescot. Optical stark effect of the exciton: Biexcitonic origin of the shift. *Phys. Rev. B*, 40:3788–3801, Aug 1989.

[30] Riccardo Comin, Grant Walters, Emmanuel Sol Thibau, Oleksandr Voznyy, Zheng-Hong Lu, and Edward H. Sargent. Structural, optical, and electronic studies of wide-bandgap lead halide perovskites. *J. Mater. Chem. C*, 3:8839–8843, 2015.

[31] C. Delerue and M. Lannoo. *Nanostructure Theory and Modeling*. Springer, 2004.

[32] C. Delerue, M. Lannoo, and G. Allan. Excitonic and quasiparticle gaps in si nanocrystals. *Phys. Rev. Lett.*, 84:2457–2460, Mar 2000.

[33] D. O. Demchenko and Lin-Wang Wang. Optical transitions and nature of stokes shift in spherical cds quantum dots. *Phys. Rev. B*, 73:155326, Apr 2006.

[34] Dmitry N. Dirin, Ihor Cherniukh, Sergii Yakunin, Yevhen Shynkarenko, and Maksym V. Kovalenko. Solution-grown cspbbr3 perovskite single crystals for photon detection. *Chemistry of Materials*, 28(23):8470–8474, 2016.

[35] Yitong Dong, Tian Qiao, Doyun Kim, David Parobek, Daniel Rossi, and Dong Hee Son. Precise control of quantum confinement in cesium lead halide perovskite quantum dots via thermodynamic equilibrium. *Nano Letters*, 18(6):3716–3722, 2018. PMID: 29727576.

[36] A. Dutta, S. K. Dutta, S. D. Adhikari, and N. Pradhan. Phase-stable $cspbi_3$ nanocrystals: The reaction temperature matters. *Angew. Chem. Int. Ed.*, 57:9083–9087, 2018.

[37] A. R. Edmonds. *Angular Momentum in Quantum Mechanics*. Princeton University Press, 1957.

[38] Al. L. Efros and A. L. Efros. Interband absorption of light in a semiconductor sphere. *Sov. Phys. Semicond.*, 16:772–775, 1982.

[39] Al. L. Efros and M. Rosen. The electronic structure of semiconductor nanocrystals. *Annu. Rev. Mat. Sci.*, 30(1):475–521, 2000.

[40] Thomas Eißfeller. *Theory of the Electronic Structure of Quantum Dots in External Fields*. PhD thesis, Technische Universität München, 2012.

[41] A. I. Ekimov, F. Hache, M. C. Schanneklein, D. Ricard, C. Flytzanis, I. A. Kudryavtsev, T. V. Yazeva, A. V. Rodina, and A. L. Efros. Absorption and intensity-dependent photoluminescence measurements on cdse quantum dots – assignment of the 1st electronic-transitions. *J. Opt. Soc. Am. B*, 10(1):100–107, 1993.

[42] R. J. Elliott. Intensity of optical absorption by excitons. *Phys. Rev.*, 108:1384–1389, Dec 1957.

[43] R. J. Elliott. *Introduction to the Theory of Excitons*, pages 271–292. Springer US, 1984.

[44] Giles E. Eperon, Tomas Leijtens, Kevin A. Bush, Rohit Prasanna, Thomas Green, Jacob Tse-Wei Wang, David P. McMeekin, George Volonakis, Rebecca L. Milot, Richard May, Axel Palmstrom, Daniel J. Slotcavage, Rebecca A. Belisle, Jay B. Patel, Elizabeth S. Parrott, Rebecca J. Sutton, Wen Ma, Farhad Moghadam, Bert Conings, Aslihan Babayigit, Hans-Gerd Boyen, Stacey Bent, Feliciano Giustino, Laura M. Herz, Michael B. Johnston, Michael D. McGehee, and Henry J. Snaith. Perovskite-perovskite tandem photovoltaics with optimized band gaps. *Science*, 354(6314):861–865, 2016.

[45] Jacky Even, Laurent Pedesseau, Jean-Marc Jancu, and Claudine Katan. Importance of spin–orbit coupling in hybrid organic/inorganic perovskites for photovoltaic applications. *The Journal of Physical Chemistry Letters*, 4(17):2999–3005, 2013.

[46] Jacky Even, Laurent Pedesseau, and Claudine Katan. Analysis of multivalley and multibandgap absorption and enhancement of free carriers related to exciton screening in hybrid perovskites. *The Journal of Physical Chemistry C*, 118(22):11566–11572, 2014.

[47] A. Filippetti and A. Mattoni. Hybrid perovskites for photovoltaics: Insights from first principles. *Phys. Rev. B*, 89:125203, Mar 2014.

[48] A. Franceschetti, L. W. Wang, H. Fu, and A. Zunger. Short-range versus long-range electron-hole exchange interactions in semiconductor quantum dots. *Phys. Rev. B*, 58:R13367–R13370, Nov 1998.

[49] J. Frenkel. On the transformation of light into heat in solids. i. *Phys. Rev.*, 37:17–44, Jan 1931.

[50] J. Frenkel. On the transformation of light into heat in solids. ii. *Phys. Rev.*, 37:1276–1294, May 1931.

[51] J. Fu, Q. Xu, G. Han, B. Wu, C. H. A. Huan, M. L. Leek, and T. C. Sum. Hot carrier cooling mechanisms in halide perovskites. *Nat. Commun.*, 8:1–9, 2017.

[52] Ming Fu, Philippe Tamarat, He Huang, Jacky Even, Andrey L. Rogach, and Brahim Lounis. Neutral and charged exciton fine structure in single lead halide perovskite nanocrystals revealed by magneto-optical spectroscopy. *Nano Letters*, 17(5):2895–2901, 2017. PMID: 28240910.

[53] Krzysztof Galkowski, Anatolie Mitioglu, Atsuhiko Miyata, Paulina Plochocka, Oliver Portugall, Giles E. Eperon, Jacob Tse-Wei Wang, Thomas Stergiopoulos, Samuel D. Stranks, Henry J. Snaith, and Robin J. Nicholas. Determination of the exciton binding energy and effective masses for methylammonium and formamidinium lead tri-halide perovskite semiconductors. *Energy Environ. Sci.*, 9:962–970, 2016.

[54] K G Hambleton, C Hilsum, and B R Holeman. Determination of the effective ionic charge of gallium arsenide from direct measurements of the dielectric constant. *Proceedings of the Physical Society*, 77(6):1147–1148, jun 1961.

[55] H. Haug and S. W. Koch. *Quantum Theory Of The Optical And Electronic Properties Of Semiconductors*. World Scientific Publishing Co., 4th edition edition, 2003.

[56] Jin Hyuck Heo and Sang Hyuk Im. Ch3nh3pbbr3-ch3nh3pbi3 perovskite-perovskite tandem solar cells with exceeding 2.2 v open circuit voltage. *Advanced Materials*, 28(25):5121–5125, 2016.

[57] Masakatsu Hirasawa, Teruya Ishihara, and Takenari Goto. Exciton features in 0-, 2-, and 3-dimensional networks of [pbi6]4- octahedra. *Journal of the Physical Society of Japan*, 63(10):3870–3879, 1994.

[58] Shunsuke Hirotsu, Jimpei Harada, Masashi Iizumi, and Kazuo Gesi. Structural phase transitions in cspbbr3. *Journal of the Physical Society of Japan*, 37(5):1393–1398, 1974.

[59] Fengrui Hu, Chunyang Yin, Huichao Zhang, Chun Sun, William W. Yu, Chunfeng Zhang, Xiaoyong Wang, Yu Zhang, and Min Xiao. Slow auger recombination of charged excitons in nonblinking perovskite nanocrystals without spectral diffusion. *Nano Letters*, 16(10):6425–6430, 2016. PMID: 27689439.

[60] Maya Isarov, Liang Z. Tan, Maryna I. Bodnarchuk, Maksym V. Kovalenko, Andrew M. Rappe, and Efrat Lifshitz. Rashba effect in a single colloidal cspbbr3 perovskite nanocrystal detected by magneto-optical measurements. *Nano Letters*, 17(8):5020–5026, 2017. PMID: 28657325.

[61] Tadashi Itoh, Tsuyoshi Ikehara, and Yasuo Iwabuchi. Quantum confinement of excitons and their relaxation processes in cucl microcrystals. *Journal of Luminescence*, 45(1):29 – 33, 1990.

[62] J. D. Jackson. *Classical Electrodynamics*. Wiley, 3rd edition edition, 1998.

[63] Qi Jiang, Zema Chu, Pengyang Wang, Xiaolei Yang, Heng Liu, Ye Wang, Zhigang Yin, Jinliang Wu, Xingwang Zhang, and Jingbi You. Planar-structure perovskite solar cells with efficiency beyond 21%. *Advanced Materials*, 29(46):1703852, 2017.

[64] Inuk Kang and Frank W. Wise. Electronic structure and optical properties of pbs and pbse quantum dots. *J. Opt. Soc. Am. B*, 14(7):1632–1646, Jul 1997.

[65] Jun Kang and Lin-Wang Wang. High defect tolerance in lead halide perovskite cspbbr3. *The Journal of Physical Chemistry Letters*, 8(2):489–493, 2017. PMID: 28071911.

[66] A Karpulevich, H Bui, Z Wang, S Hapke, C Palencia Ramirez, H Weller, and G Bester. Dielectric response function for colloidal semiconductor quantum dots. *J. Chem. Phys.*, 151:224103, 2019.

[67] Claudine Katan, Nicolas Mercier, and Jacky Even. Quantum and dielectric confinement effects in lower-dimensional hybrid perovskite semiconductors. *Chemical Reviews*, 119(5):3140–3192, 2019. PMID: 30638375.

[68] K. H. Khoo, A. T. Zayak, H. Kwak, and James R. Chelikowsky. First-principles study of confinement effects on the raman spectra of si nanocrystals. *Phys. Rev. Lett.*, 105:115504, Sep 2010.

[69] M. Kira and S. W. Koch. *Semiconductor Quantum Optics*. Cambridge University Press, 1st edition edition, 2011.

[70] C. Kittel. *Quantum theory of solids*. John Wiley & Sons, 2nd edition edition, 1987.

[71] Victor I. Klimov. Spectral and dynamical properties of multiexcitons in semiconductor nanocrystals. *Annual Review of Physical Chemistry*, 58(1):635–673, 2007. PMID: 17163837.

[72] Piotr Kowalski, Lukasz Marcinowski, and Pawel Machnikowski. Coulomb matrix elements for the impact ionization process in nanocrystals: An envelope function approach. *Phys. Rev. B*, 87:075309, Feb 2013.

[73] Franziska Krieg, Stefan T. Ochsenbein, Sergii Yakunin, Stephanie ten Brinck, Philipp Aellen, Adrian Süess, Baptiste Clerc, Dominic Guggisberg, Olga Nazarenko, Yevhen Shynkarenko, Sudhir Kumar, Chih-Jen Shih, Ivan Infante, and Maksym V. Kovalenko. Colloidal cspbx3 (x = cl, br, i) nanocrystals 2.0: Zwitterionic capping ligands for improved durability and stability. *ACS Energy Letters*, 3(3):641–646, 2018. PMID: 29552638.

[74] Landolt-Börnstein. *Semiconductors-Group III Condensed Matter*. Springer, subvolume c 'non-tetrahedrally bonded elements and binary compounds i', volume 41 edition.

[75] I. Lindgren and J. Morrison. *Atomic Many-Body Theory*. Springer-Verlag, 1982.

[76] Feng Liu, Yaohong Zhang, Chao Ding, Syuusuke Kobayashi, Takuya Izuishi, Naoki Nakazawa, Taro Toyoda, Tsuyoshi Ohta, Shuzi Hayase, Takashi Minemoto, Kenji Yoshino, Songyuan Dai, and Qing Shen. Highly luminescent phase-stable cspbi3 perovskite quantum dots achieving near 100% absolute photoluminescence quantum yield. *ACS Nano*, 11(10):10373–10383, 2017. PMID: 28910074.

[77] M. Liu, M. B. Johnston, and H. J. Snaith. Efficient planar heterojunction perovskite solar cells by vapour deposition. *Nature*, 501:395–398, 2013.

[78] C. Lew Yan Voon Lok and Morten Willatzen. *The k·p Method*. Springer-Verlag, 2009.

[79] G. D. Mahan. *Many-Particle Physics*. Springer, 3rd edition edition, 2000.

[80] Nikolay S. Makarov, Shaojun Guo, Oleksandr Isaienko, Wenyong Liu, István Robel, and Victor I. Klimov. Spectral and dynamical properties of single excitons, biexcitons, and trions in cesium–lead-halide perovskite quantum dots. *Nano Letters*, 16(4):2349–2362, 2016. PMID: 26882294.

[81] F Mandl and G. Shaw. *Quantum Field Theory*. Wiley, 1st edition edition, 1984.

[82] R. M. Martin. *Electronic Structure: Basic Theory and Practical Methods*. Cambridge University Press, 1st edition edition, 2008.

[83] E. Menéndez-Proupin, P. Palacios, P. Wahnón, and J. C. Conesa. Self-consistent relativistic band structure of the $CH_3NH_3PbI_3$ perovskite. *Phys. Rev. B*, 90:045207, Jul 2014.

[84] A. Miyata, A. Mitioglu, P. Plochocka, O. Portugall, J. T. Wang, S. D. Stranks, H. J. Snaith, and R. J. Nicholas. Direct measurement of the exciton binding energy and effective masses for charge carriers in organic–inorganic tri-halide perovskites. *Nature Physics*, 11:582–587, 2015.

[85] Gabriel Nagamine, Jaqueline O. Rocha, Luiz G. Bonato, Ana F. Nogueira, Zhanet Zaharieva, Andrew A. R. Watt, Carlos H. de Brito Cruz, and Lazaro A. Padilha. Two-photon absorption and two-photon-induced gain in perovskite quantum dots. *The Journal of Physical Chemistry Letters*, 9(12):3478–3484, 2018. PMID: 29882410.

[86] S. Nakahara, H. Tahara, G. Yumoto, T. Kawawaki, M. Saruyama, R. Sato, T. Teranishi, and Y. Kanemitsu. Suppression of trion formation in cspbbr3 perovskite nanocrystals by postsynthetic surface modification. *The Journal of Physical Chemistry C*, 122(38):22188–22193, 2018.

[87] S. B. Nam, D. C. Reynolds, C. W. Litton, R. J. Almassy, T. C. Collins, and C. M. Wolfe. Free-exciton energy spectrum in gaas. *Phys. Rev. B*, 13:761–767, Jan 1976.

[88] M. O. Nestoklon, S. V. Goupalov, R. I. Dzhioev, O. S. Ken, V. L. Korenev, Yu. G. Kusrayev, V. F. Sapega, C. de Weerd, L. Gomez, T. Gregorkiewicz, Junhao Lin, Kazutomo Suenaga, Yasufumi Fujiwara, L. B. Matyushkin, and I. N. Yassievich. Optical orientation and alignment of excitons in ensembles of inorganic perovskite nanocrystals. *Phys. Rev. B*, 97:235304, Jun 2018.

[89] T. P. T. Nguyen, S. A. Blundell, and C. Guet. Calculation of the biexciton shift in nanocrystals of inorganic perovskites. *Phys. Rev. B*, 101:125424, Mar 2020.

[90] T. P. T. Nguyen, S. A. Blundell, and C. Guet. One-photon absorption by inorganic perovskite nanocrystals: a theoretical study. 2020.

[91] Daniel Niesner, Max Wilhelm, Ievgen Levchuk, Andres Osvet, Shreetu Shrestha, Miroslaw Batentschuk, Christoph Brabec, and Thomas Fauster. Giant rashba splitting in $ch_3nh_3pbbr_3$ organic-inorganic perovskite. *Phys. Rev. Lett.*, 117:126401, Sep 2016.

[92] Susumu Ninomiya and Sadao Adachi. Optical properties of wurtzite cds. *Journal of Applied Physics*, 78(2):1183–1190, 1995.

[93] M. Nirmal, D. J. Norris, M. Kuno, M. G. Bawendi, Al. L. Efros, and M. Rosen. Observation of the "dark exciton" in cdse quantum dots. *Phys. Rev. Lett.*, 75:3728–3731, Nov 1995.

[94] Shintaro Nomura and Takayoshi Kobayashi. Nonparabolicity of the conduction band in cdse and cds_xse_{1-x} semiconductor microcrystallites. *Solid State Communications*, 78(8):677 – 680, 1991.

[95] Jun Pan, Yuequn Shang, Jun Yin, Michele De Bastiani, Wei Peng, Ibrahim Dursun, Lutfan Sinatra, Ahmed M. El-Zohry, Mohamed N. Hedhili, Abdul-Hamid Emwas, Omar F. Mohammed, Zhijun Ning, and Osman M. Bakr. Bidentate ligand-passivated cspbi3 perovskite nanocrystals for stable near-unity photoluminescence quantum yield and efficient red light-emitting diodes. *Journal of the American Chemical Society*, 140(2):562–565, 2018. PMID: 29249159.

[96] R. G. Parr and W. Yang. *Density-Functional Theory of Atoms and Molecules*. Oxford University Press, 1989.

[97] G. E. Pikus and G. L. Bir. Exchange interaction in excitons in semiconductors. *Zh. Eksp. Teor. Fiz.*, 33:195–208, 1971.

[98] E. P. Pokatilov, V. A. Fonoberov, V. M. Fomin, and J. T. Devreese. Development of an eight-band theory for quantum dot heterostructures. *Phys. Rev. B*, 64:245328, Dec 2001.

[99] Loredana Protesescu, Sergii Yakunin, Maryna I. Bodnarchuk, Franziska Krieg, Riccarda Caputo, Christopher H. Hendon, Ruo Xi Yang, Aron Walsh, and Maksym V. Kovalenko. Nanocrystals of cesium lead halide perovskites (cspbx3, x = cl, br, and i): Novel optoelectronic materials showing bright emission with wide color gamut. *Nano Letters*, 15(6):3692–3696, 2015. PMID: 25633588.

[100] Gabriele Rainò, Georgian Nedelcu, Loredana Protesescu, Maryna I. Bodnarchuk, Maksym V. Kovalenko, Rainer F. Mahrt, and Thilo Stöferle. Single cesium lead halide perovskite nanocrystals at low temperature: Fast single-photon emission, reduced blinking, and exciton fine structure. *ACS Nano*, 10(2):2485–2490, 2016. PMID: 26771336.

[101] Julien Ramade, Léon Marcel Andriambariarijaona, Violette Steinmetz, Nicolas Goubet, Laurent Legrand, Thierry Barisien, Frédérick Bernardot, Christophe Testelin, Emmanuel Lhuillier, Alberto Bramati, and Maria Chamarro. Fine structure of excitons and electron–hole exchange energy in polymorphic cspbbr3 single nanocrystals. *Nanoscale*, 10:6393–6401, 2018.

[102] J. J. Sakurai. *Modern Quantum Mechanics*. Addison Wesley, 1993.

[103] Daniel Sapori, Mikaël Kepenekian, Laurent Pedesseau, Claudine Katan, and Jacky Even. Quantum confinement and dielectric profiles of colloidal nanoplatelets of halide inorganic and hybrid organic–inorganic perovskites. *Nanoscale*, 8:6369–6378, 2016.

[104] Michael Sendner, Pabitra K. Nayak, David A. Egger, Sebastian Beck, Christian Müller, Bernd Epding, Wolfgang Kowalsky, Leeor Kronik, Henry J. Snaith, Annemarie Pucci, and Robert Lovrinčić. Optical phonons in methylammonium lead halide perovskites and implications for charge transport. *Mater. Horiz.*, 3:613–620, 2016.

[105] Peter C. Sercel and Alexander L. Efros. Band-edge exciton in cdse and other ii-vi and iii-v compound semiconductor nanocrystals-revisited. *Nano Lett.*, 18(7):4061–4068, 2018. PMID: 29927610.

[106] Peter C. Sercel, John L. Lyons, Darshana Wickramaratne, Roman Vaxenburg, Noam Bernstein, and Alexander L. Efros. Exciton fine structure in perovskite nanocrystals. *Nano Lett.*, 19(6):4068–4077, 2019. PMID: 31088061.

[107] I. Shavitt and R. J. Bartlett. *Many-Body Methods in Chemistry and Physics: MBPT and Coupled-Cluster Theory*. Cambridge University Press, 2009.

[108] Jimmy-Xuan Shen, Xie Zhang, Suvadip Das, Emmanouil Kioupakis, and Chris G. Van de Walle. Unexpectedly strong auger recombination in halide perovskites. *Advanced Energy Materials*, 8(30):1801027, 2018.

[109] Weidong Sheng, Shun-Jen Cheng, and Pawel Hawrylak. Multiband theory of multi-exciton complexes in self-assembled quantum dots. *Phys. Rev. B*, 71:035316, Jan 2005.

[110] Zhifeng Shi, Sen Li, Ying Li, Huifang Ji, Xinjian Li, Di Wu, Tingting Xu, Yongsheng Chen, Yongtao Tian, Yuantao Zhang, Chongxin Shan, and Guotong Du. Strategy of solution-processed all-inorganic heterostructure for humidity/temperature-stable perovskite quantum dot light-emitting diodes. *ACS Nano*, 12(2):1462–1472, 2018. PMID: 29323874.

[111] Y. Shirasaki, G. J. Supran, M. G. Bawendi, and V. Bulović. Emergence of colloidal quantum-dot light-emitting technologies. *Nature*, 7:1, 2013.

[112] Katherine E. Shulenberger, Matthew N. Ashner, Seung Kyun Ha, Franziska Krieg, Maksym V. Kovalenko, William A. Tisdale, and Moungi G. Bawendi. Setting an upper bound to the biexciton binding energy in cspbbr3 perovskite nanocrystals. *The Journal of Physical Chemistry Letters*, 10(18):5680–5686, 2019. PMID: 31502848.

[113] J. Shumway, A. Franceschetti, and Alex Zunger. Correlation versus mean-field contributions to excitons, multiexcitons, and charging energies in semiconductor quantum dots. *Phys. Rev. B*, 63:155316, Mar 2001.

[114] Olivier Stier. *Electronic and optical properties of quantum dots and wires*. PhD thesis, Technischen Universität Berlin, 2000.

[115] Ireneusz Strzalkowski, Sharad Joshi, and C. R. Crowell. Dielectric constant and its temperature dependence for gaas, cdte, and znse. *Applied Physics Letters*, 28(6):350–352, 1976.

[116] Tze Chien Sum and Nripan Mathews. Advancements in perovskite solar cells: photophysics behind the photovoltaics. *Energy Environ. Sci.*, 7:2518–2534, 2014.

[117] Tze Chien Sum, Marcello Righetto, and Swee Sien Lim. Quo vadis, perovskite emitters? *The Journal of Chemical Physics*, 152(13):130901, 2020.

[118] T. Takagahara. Excitonic optical nonlinearity and exciton dynamics in semiconductor quantum dots. *Phys. Rev. B*, 36:9293–9296, Dec 1987.

[119] T. Takagahara. Effects of dielectric confinement and electron-hole exchange interaction on excitonic states in semiconductor quantum dots. *Phys. Rev. B*, 47:4569–4584, Feb 1993.

[120] T. Takagahara. Theory of exciton doublet structures and polarization relaxation in single quantum dots. *Phys. Rev. B*, 62:16840–16855, Dec 2000.

[121] P. Tamarat, M. I. Bodnarchuk, J.-B. Trebbia, R. Erni, M. V. Kovalenko, J. Even, and B. Lounis. The ground exciton state of formamidinium lead bromide perovskite nanocrystals is a singlet dark state. *Nat. Mater.*, 18:717–724, Sep 2019.

[122] Paolo Umari, Edoardo Mosconi, and Filippo De Angelis. Relativistic gw calculations on ch3nh3pbi3 and ch3nh3sni3 perovskites for solar cell applications. *Scientific Reports*, 4:4467, 2014.

[123] Hendrik Utzat, Weiwei Sun, Alexander E. K. Kaplan, Franziska Krieg, Matthias Ginterseder, Boris Spokoyny, Nathan D. Klein, Katherine E. Shulenberger, Collin F. Perkinson, Maksym V. Kovalenko, and Moungi G. Bawendi. Coherent single-photon emission from colloidal lead halide perovskite quantum dots. *Science*, 363(6431):1068–1072, 2019.

[124] Lin-Wang Wang. Real and spurious solutions of the 8×8 k·p model for nanostructures. *Phys. Rev. B*, 61:7241–7244, Mar 2000.

[125] Lin-Wang Wang and Alex Zunger. Pseudopotential calculations of nanoscale cdse quantum dots. *Phys. Rev. B*, 53:9579–9582, Apr 1996.

[126] Y. Wang, X. Li, J. Song, L. Xiao, H. Zeng, and Sun H. All-inorganic colloidal perovskite quantum dots: A new class of lasing materials with favorable characteristics. *Adv. Mater.*, 27:7101–7108, 2015.

[127] Zhe Wang. *private communication.* 2019.

[128] Gregory H. Wannier. The structure of electronic excitation levels in insulating crystals. *Phys. Rev.*, 52:191–197, Aug 1937.

[129] G. Xing, N. Mathews, S. S. Lim, N. Yantara, X. Liu, D. Sabba, M. Grätzel, S. Mhaisalkar, and T. C. Sum. Low-temperature solution-processed wavelength-tunable perovskites for lasing. *Nature Materials*, 13:476–480, 2014.

[130] Yanqing Xu, Qi Chen, Chunfeng Zhang, Rui Wang, Hua Wu, Xiaoyu Zhang, Guichuan Xing, William W. Yu, Xiaoyong Wang, Yu Zhang, and Min Xiao. Two-photon-pumped perovskite semiconductor nanocrystal lasers. *Journal of the American Chemical Society*, 138(11):3761–3768, 2016. PMID: 26938656.

[131] Miki Yamanaka, Hiromitsu Itoh, Masato Morifuji, and Chihiro Hamaguchi. Thermal dissociation of excitons in a type-i gaas/alas superlattice studied by time-resolved photoluminescence measurements. *Physica E: Low-dimensional Systems and Nanostructures*, 7(3):581 – 585, 2000.

[132] Z. Yang, A. Surrente, K. Galkowski, A. Miyata, O. Portugall, R. J. Sutton, A. A. Haghighirad, H. J. Snaith, D. K. Maude, P. Plochocka, and R. J. Nicholas. Impact of the halide cage on the electronic properties of fully inorganic cesium lead halide perovskites. *ACS Energy Letters*, 2(7):1621–1627, 2017.

[133] Naoki Yarita, Tomoko Aharen, Hirokazu Tahara, Masaki Saruyama, Tokuhisa Kawawaki, Ryota Sato, Toshiharu Teranishi, and Yoshihiko Kanemitsu. Observation of positive and negative trions in organic-inorganic hybrid perovskite nanocrystals. *Phys. Rev. Materials*, 2:116003, Nov 2018.

[134] Gurivi Reddy Yettapu, Debnath Talukdar, Sohini Sarkar, Abhishek Swarnkar, Angshuman Nag, Prasenjit Ghosh, and Pankaj Mandal. Terahertz conductivity within colloidal cspbbr3 perovskite nanocrystals: Remarkably high carrier mobilities and large diffusion lengths. *Nano Letters*, 16(8):4838–4848, 2016. PMID: 27367476.

[135] Chunyang Yin, Liyang Chen, Nan Song, Yan Lv, Fengrui Hu, Chun Sun, William W. Yu, Chunfeng Zhang, Xiaoyong Wang, Yu Zhang, and Min Xiao. Bright-exciton fine-structure splittings in single perovskite nanocrystals. *Phys. Rev. Lett.*, 119:026401, Jul 2017.

[136] Wan-Jian Yin, Tingting Shi, and Yanfa Yan. Unusual defect physics in ch3nh3pbi3 perovskite solar cell absorber. *Applied Physics Letters*, 104(6):063903, 2014.

[137] M. Yu, G. W. Fernando, R. Li, F. Papadimitrakopoulos, N. Shi, and R. Ramprasad. First principles study of cdse quantum dots: Stability, surface unsaturations, and experimental validation. *Applied Physics Letters*, 88(23):231910, 2006.

[138] Z. G. Yu. Effective-mass model and magneto-optical properties in hybrid perovskites. *Scientific Reports*, 6:28576, 2016.

[139] Go Yumoto, Hirokazu Tahara, Tokuhisa Kawawaki, Masaki Saruyama, Ryota Sato, Toshiharu Teranishi, and Yoshihiko Kanemitsu. Hot biexciton effect on optical gain in cspbi3 perovskite nanocrystals. *The Journal of Physical Chemistry Letters*, 9(9):2222–2228, 2018. PMID: 29644864.

[140] Qing Zhang, Rui Su, Xinfeng Liu, Jun Xing, Tze Chien Sum, and Qihua Xiong. High-quality whispering-gallery-mode lasing from cesium lead halide perovskite nanoplatelets. *Advanced Functional Materials*, 26(34):6238–6245, 2016.

[141] D. Zhao, Y. Yu, C. Wang, W. Liao, N. Shrestha, C. R. Grice, A. J. Cimaroli, L. Guan, R. J. Ellingson, K. Zhu, X. Zhao, R.-G. Xiong, and Y. Yan. Low-bandgap mixed tin–lead iodide perovskite absorbers with long carrier lifetimes for all-perovskite tandem solar cells. *Nature Energy*, 2, 2017.

[142] X.-G. Zhao, G. M. Dalpian, Z. Wang, and A. Zunger. Polymorphous nature of cubic halide perovskites, *accepted*. *Phys. Rev. B*, Mar 2020.

[143] Gal Zohar, Roi Baer, and Eran Rabani. Multiexciton generation in iv–vi nanocrystals: The role of carrier effective mass, band mixing, and phonon emission. *The Journal of Physical Chemistry Letters*, 4(2):317–322, 2013. PMID: 26283441.

[144] Alex Zunger. Pseudopotential theory of semiconductor quantum dots. *physica status solidi (b)*, 224(3):727–734, 2001.